## Distribution Agreement

Signature:

________________________ ________________

Guibo Zhu Date

# Transition-metal-substituted polyoxometalates as Water Oxidation Catalysts

By

Guibo Zhu
Doctor of Philosophy

Chemistry

Craig L. Hill
Advisor

Vincent Conticello
Committee Member

Cora E. MacBeth
Committee Member

Accepted:

Lisa A. Tedesco, Ph.D.
Dean of the James T. Laney School of Graduate Studies

Date

# Transition-metal-substituted polyoxometalates as Water Oxidation Catalysts

By

Guibo Zhu
Bachelor of Science, Southwest University, China, 2002
Master of Science, Fudan University, China, 2005

Advisor: Craig L. Hill, Ph.D.

An abstract of
a dissertation submitted to the Faculty of the
James T. Laney School of Graduate Studies of Emory University
in partial fulfillment of the requirements for the degree of
Doctor of Philosophy in Chemistry
2013

# Abstract

## Transition-metal-substituted polyoxometalates as Water Oxidation Catalysts

By Guibo Zhu

Several new polysilicotungstates substituted with earth-abundant elements (Co and Ni), $K_{10.2}Na_{0.8}[\{Co_4(\mu\text{-}OH)(H_2O)_3\}(Si_2W_{19}O_{70})]\cdot 31H_2O$, $K_5Na_4H_4[\{Na_3(\mu\text{-}OH_2)_2Co_2(\mu\text{-}OH)_4\}(Si_2W_{18}O_{66})]\cdot 37H_2O$, $K_6Na_3[Na(H_2O)\{Co(H_2O)_3\}_2\{Co(H_2O)_2\}(Si_2W_{18}O_{66})]\cdot 22H_2O$ and $K_{10}H_2[Ni_5(OH)_6(OH_2)_3(Si_2W_{18}O_{66})]\cdot 34H_2O$, have been synthesized and characterized by X-ray crystallography, infrared, elemental analysis, UV-vis spectroscopy and cyclic voltammetry. They can effectively catalyze water oxidation in a photo-driven system with $[Ru(bpy)_3]^{2+}$ as photosensitizer and $Na_2S_2O_8$ as the sacrificial electron acceptor. Several lines of evidence show that none of these complexes decompose to insoluble metal oxide under the harsh catalytic conditions. Although $[\{Co_4(\mu\text{-}OH)(H_2O)_3\}(Si_2W_{19}O_{70})]^{11-}$ slowly hydrolyzes in aqueous solution, it is quite probable that the initial complex is the real catalyst, because the isolated hydrolysis products show lower WOC activity. Because of their low solubility in aqueous solution, $[\{Na_3(\mu\text{-}OH_2)_2Co_2(\mu\text{-}OH)_4\}(Si_2W_{18}O_{66})]^{13-}$, $[Na(H_2O)\{Co(H_2O)_3\}_2\{Co(H_2O)_2\}(Si_2W_{18}O_{66})]^{9-}$, and $[Ni_5(OH)_6(OH_2)_3(Si_2W_{18}O_{66})]^{12-}$ form solution $\rightleftharpoons$ $[Ru(bpy)_3]^{n+}$-POM complex equilibria and remain molecular during the catalytic process.

A dodecazinc silicotungstate $K_{20}Na_2[Zn_6(OH)_7(H_2O)(Si_2W_{18}O_{66})]_2\cdot 34H_2O$ has been synthesized and characterized. DFT B3LYP calculations give HOMO–LUMO and (HOMO-1)–LUMO energy gaps of ~3.65 and 3.91 eV, which are larger than in ZnO (band gap = 3.35 eV).

The catalytic activity of tetra-*n*-butylammonium salt of $[\{Ru_4O_4(OH)_2(H_2O)_4\}(\gamma\text{-}SiW_{10}O_{36})_2]^{10-}$, whose water soluble salt is a water oxidation catalyst, was explored in oxidation of 3,5,3',5'-tetrabutyl-biphenyl-4,4'-diol by dioxygen. Alcohols are stoichiometricaly oxidized under Ar by this compound to aldehydes/ketones in acetonitrile solution. The reaction kinetics and stoichiometry were studied by GC, NMR and UV-vis spectroscopies. The reaction kinetics are very complex, the reaction proceeds in two steps with the second step being significantly slower. Several reaction mechanisms were analyzed by fitting of the reaction kinetic curves obtained from changes of UV-Vis spectra versus time.

# Transition-metal-substituted polyoxometalates as Water Oxidation Catalysts

By

Guibo Zhu
Bachelor of Science, Southwest University, China, 2002
Master of Science, Fudan University, China, 2005

Advisor: Craig L. Hill, Ph.D.

A dissertation submitted to the Faculty of the
James T. Laney School of Graduate studies of Emory University
in partial fulfillment of the requirements for the degree of
Doctor of Philosophy in Chemistry
2013

# Acknowledgments

I would like to acknowledge many people for their help during my doctoral work.

I would like to give my most earnest acknowledgment to my advisor, Professor Craig L. Hill. I thank him for offering me the opportunity to work with him, and all the unconditional support and help during my PhD study. He is not only a distinguished scientist, but also a great mentor. I learned a lot from him both in scientific research area and many other skills, such as communication skills and presentation skills. I am always encouraged by his optimism, and I would like to learn this virtue throughout the rest of my life.

I am also very grateful for the advice I have received from my research committee, Professors Vincent Conticello and Cora E. MacBeth.

I would like to thank Yurii V. Geletii for his guidance in my early research, and I very appreciate his valuable comments after each discussion; I thank Jie Song for his constructive suggestions on my research; I thank Claire Besson for her patience in explaining basic ideas to me when I was new to the lab, and thank her for setting up a model as an excellent chemistry graduate student; I thank Yu Hou for her help in obtaining $^{24}$Si NMR data at Sandia National Laboratory and many others.

I extend my many thanks to my colleagues who collaborate on my research. I thank John Bacsa and Kenneth I. Hardcastle in the X-ray center, Drs. Shaoxiong Wu and Bin Wang in the NMR center at Emory University, Elliot N. Glass and James Vickers in Hill group.

I would like to thank all other previous and current Hill group members: Dr. Haiyan An, Dr. Yong Ding, Dr. Huiyuan Ma, Dr. John Fielden, Dr. Ibram Ganesh, Zhen Luo,

Daniel A. Hillesheim, Rui Cao, Kevin O'Halloran, Hongjin Lv, Jordan Sumliner, Weiwei Guo, Kevin Sullivan, Sarah M. Lauinger, Juan Cardenas Saavedra, Chongchao Zhao, Daniel T. Kim, and Evan T. Huang. I would like to thank Leslie Chauvin and Cindee K. Yates for their kind help.

Last but not least, my thanks go to my husband, my son, my parents and elder sister, for their love and support over all these past years.

# Table of Contents

# List of Figures

# List of Tables

# List of Schemes

# List of Abbreviations

| | |
|---|---|
| Å | Angstrom |
| *a, b, c* | unit cell axial lengths |
| $BPH_2$ | 3,5,3’,5’-tetra-*t*-butyl-biphenyl-4,4’-diol |
| ℃ | degrees Celsius |
| C | carbon |
| calcd | calculated |
| CCD | charge-coupled device |
| CEES | 2-chloroethyl ethyl sulfide |
| CIF | crystallographic information file |
| $cm^{-1}$ | reciprocal centimeter |
| CV | cyclic voltammetry |
| DBP | 2,6-di-*t*-butylpyridine |
| DPQ | 3,5,3’,5’-tetra-*t*-butyl-diphenoquinone |
| eq | equation |
| F.W. | formula weight |
| *F(000)* | structure factor for the unit cell; it is equal to the total number of electrons in the unit cell |
| FT-IR | Fourier transform infrared spectroscopy |
| g | gram(s) |
| GC | gas chromatography |
| hr | hour(s) |
| H | hydrogen |
| Hz | Hertz |
| $^{o}K$ | degrees Kelvin |
| L | ligand |
| m | medium intensity stretch (FT-IR) |
| M | molarity |
| mg | milligram(s) |
| MHz | megahertz |
| M.W. | molecular weight |
| min | minute(s) |
| mL | milliliter(s) |
| mmol | millimole |
| mol | mole |
| nm | nanometer |
| NMR | nuclear magnetic resonance spectroscopy |
| O | oxygen |
| OAc | acetate |
| P | phosphorus |
| pH | potential of hydrogen, a measure of the acidity or alkalinity of a solution |
| Ph | phenyl, $C_6H_5$ |
| POM | polyoxometalate |

| | |
|---|---|
| ppm | part per million |
| R | discrepancy index for crystal structure refinement |
| s | strong intensity stretch (FT-IR) |
| s, sec | second(s) |
| sh | shoulder (FT-IR) |
| TBA | tetra-*n*-butylammonium |
| TEA | triethylamine |
| TGA | thermogravimetric analysis |
| THT | tetrahydrothiophene |
| TMSPs | transition-metal-substituted polyoxometalates |
| UV | ultraviolet |
| *V* | volume of the unit cell |
| vs | very strong intensity stretch (FT-IR) |
| W | tungsten |
| w | weak intensity stretch (FT-IR) |
| WOC | water oxidation catalyst |
| Z | number of molecules per unit cell |
| *α, β, γ* | interaxial angles between unit cell vector b and c, a and c, and a and b, respectively |
| δ | chemical shift (expressed in ppm for NMR) |
| ε | molar extinction (or absorption) coefficient |
| θ | the glancing angle of the X-ray beam to the “reflecting plane” |
| λ | wavelength |
| μ | the total linear absorption coefficient (with unit of cm-1) |
| μL | microliter |

# *Chapter 1*

## Chapter 1 : Introduction to Transition-metal-Substituted Polyoxometalates (TMSPs) and TMSP-Catalyzed Water Oxidation

## 1.1 General Information about POMs

Polyoxometalates (POMs) are composed of transition metals in their highest oxidation states ($d^0$) bridged by oxygen atoms. They are molecular structures formed by the condensation of mononuclear oxometalates $[MO_4]^{n-}$ under acidic conditions. The common transition metals in POMs are tungsten, vanadium, molybdenum, niobium, and tantalum, and they are referred as *addenda* atoms. If the POMs only consist of addenda and oxygen atoms, they are called *isopolyanions*. If a main group element (such as Si, P, Ge, As, B… termed "the heteroatom") is added during the condensation process, it usually acts as a template in the center of the structure, and this type of POM is called a *heteropolyanion*. In this introduction, we will mainly discuss one type of heteropolyanion, the polysilicotungstates.

Scheme 1.1 describes the synthesis and isomerization of silicatungstates as an example. We examine this scheme from the left to the right. When the mixture of tungstate and silicate solution is acidified, species having multiple open sites ("unsaturated" or "lacunary") will be formed, frequently the 9-tungstopolyoxometalates. These open sites are highly reactive because of their nucleophilic oxygen atoms. In the presence of tungstate or transition metal cations at lower pH, these lacunary species transform into their closed ("plenary") structures, or into dimerized, tetramerized or more complex structures with additional open sites by linking the tungsten atoms. The transformations between these species are controlled by many factors, such as pH, the tungsten/heteroatom ratio and the counterions ($Na^+$ or $K^+$). Therefore, the plenary structures decompose, reversibly, into the lacunary structure(s) when the pH increases.

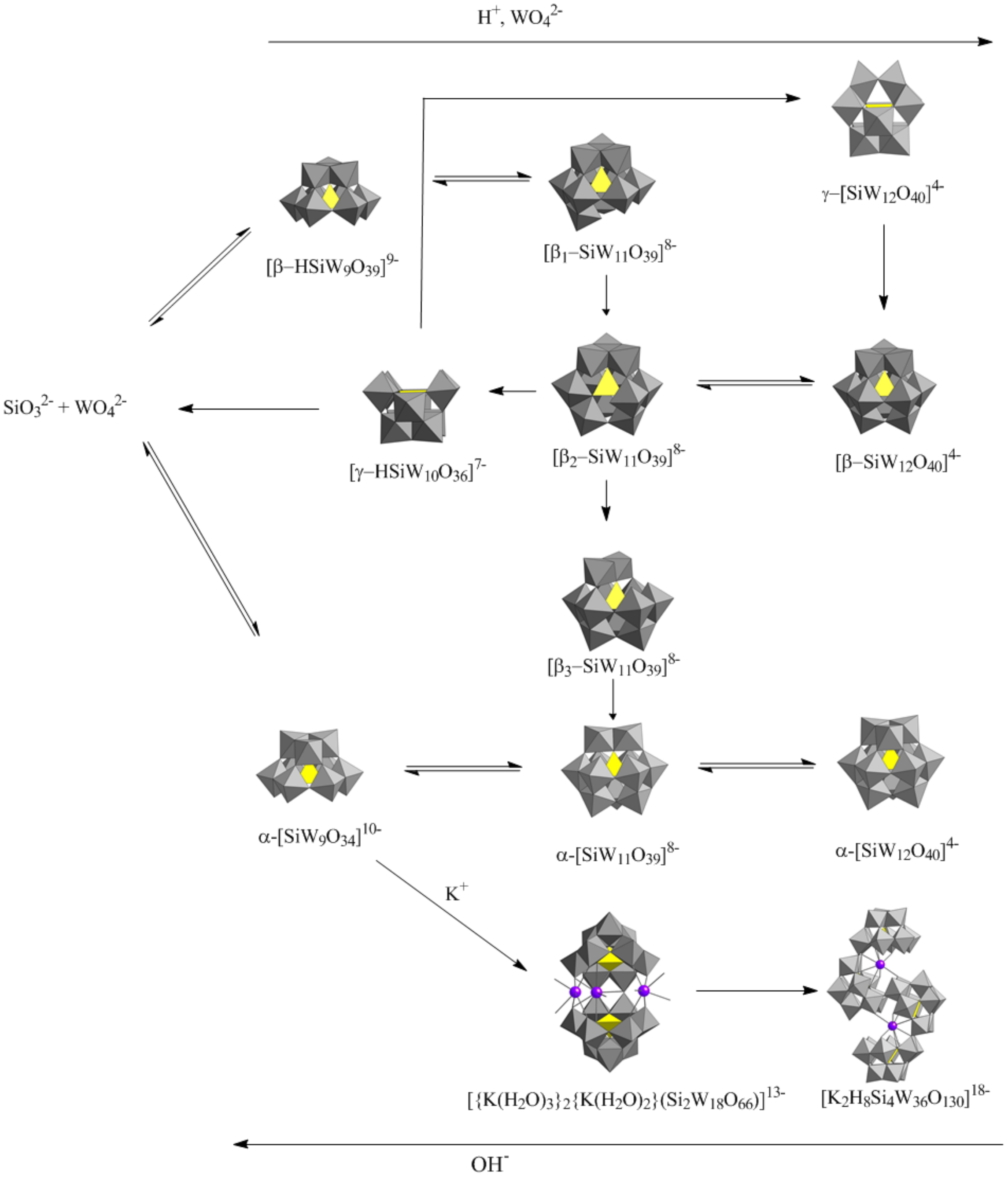

**Scheme 1.1** General route for the formation of polysilicotungstates (color code: W, gray; Si, yellow; K, purple).

Trivacant lacunary POMs can be formed when sodium tungstate and sodium silicate is acidified to about pH 9. Usually, there are two types of 9-tungstosilicates, the A type and the B type (Figure 1.1). The A-type is formed by the association of three $\{W_2O_8\}$ groups and one $\{W_3O_{10}\}$ group around the central atom, and the B-type is formed by the association of three $\{W_3O_{10}\}$ groups around the central heteroatom. The trivacant Keggin POMs mentioned in Scheme 1.1 are all A-type lacunary Keggin species. A B-type trivacant Keggin $\{SiW_9\}$ POM has never been isolated to my knowledge, but these structures can be stabilized by transition metal ions through the hydrolysis of other Keggin structures. For example, the "sandwich-type" complexes, $[M_4(H_2O)(B\text{-}\alpha\text{-}SiW_9O_{34})_2]^{12-}$ ($M=Mn^{2+}$, $Cu^{2+}$, $Zn^{2+}$), were synthesized using $\gamma\text{-}[SiW_{10}O_{36}]^{8-}$ as the precursor;[1] and $[Co_4(H_2O)(B\text{-}\alpha\text{-}SiW_9O_{34})_2]^{12-}$ was obtained using the sodium salt of $\alpha\text{-}[SiW_9O_{34}]^{10-}$.[2] However, the phosphorus analogue, B-type $[PW_9O_{34}]^{9-}$, can be obtained by heating $[A\text{-}PW_9O_{34}]^{9-}$ at 150 ℃ for 2 days to a week.

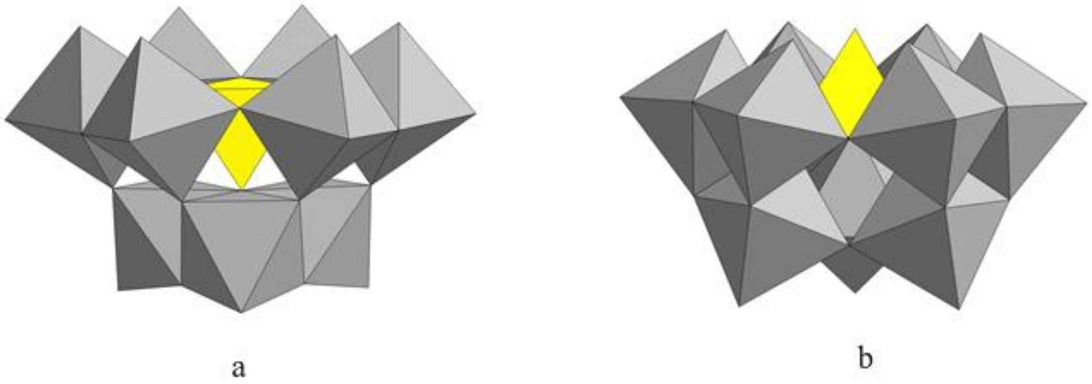

**Figure 1.1** A-type (A-α-isomer) and B-type (B-α-isomer) trivacant Keggin polytungstosilicates.

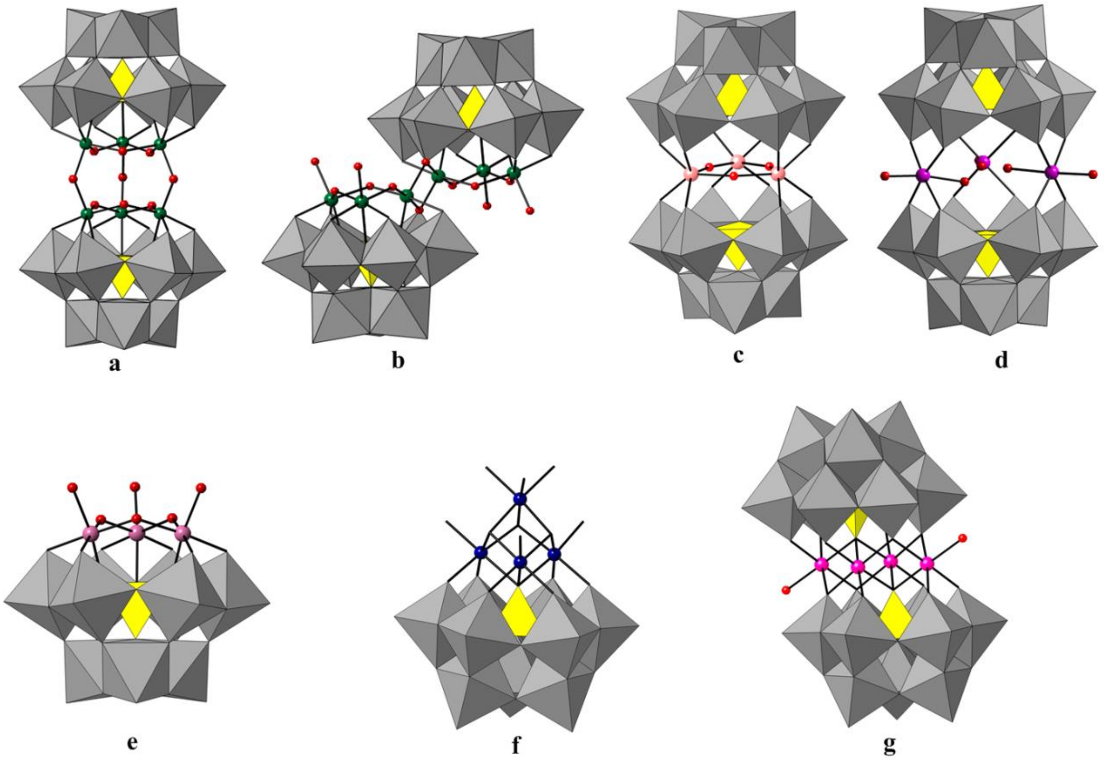

**Figure 1.2** Polyhedral and ball-and-stick representation of compounds that form by reaction of trivacant Keggin polysilicotungstates with transition metals. $[(\alpha\text{-SiFe}_3\text{W}_9(\text{OH})_3\text{O}_{34})_2(\text{OH})_3]^{11-}$ (a),[3] and $[(\alpha\text{-Si}(\text{FeOH}_2)_2\text{FeW}_9(\text{OH})_3\text{O}_{34})_2]^{8-}$ (b),[3] $[\text{Zr}_3\text{O}(\text{OH})_2(\text{SiW}_9\text{O}_{34})_2]^{12-}$ (c),[4] $[\{\text{Co}(\text{H}_2\text{O})_2\}_3(\text{SiW}_9\text{O}_{34})_2]^{14-}$ (d),[5] $[\text{A-}\alpha\text{-SiO}_4\text{W}_9\text{M}_3(\text{OH}_2)_3\text{O}_{33}]^{7-}$ (M = Ru, Cr, Co, Fe, Cu, Mn, Ni) (e),[2,6,7] $[\text{Ru}_4(\text{H}_2\text{O})_3\text{Cl}_3(\text{B-}\alpha\text{-SiW}_9\text{O}_{37})]^{7-}$(f),[8] $[\text{M}_4(\text{H}_2\text{O})_2(\text{Si W}_9\text{O}_{34})_2]^{12-}$ (M = Ni, Co) (g).[2] Color code: W, gray; Si, yellow; Fe, dark teal; Zr, light salmon; Co, magenta; Ru, dark blue.

Several transition-metal-substituted POMs (TMSPs) prepared using A-α-SiW$_9$ (sodium or potassium salt) as precursors are shown in Figure 1.2 (only TMSPs without organic ligands are discussed in this chapter). The A-type structure is maintained (Figure 1.2 a-e), or undergoes isomerization to B-type SiW$_9$ (Figure 1.2 f, g). The trivacant POM units react with transition metal cations to form structures with single substituted POMs (such as Figure 1.2 e and f), or sandwich-type structures (such as Figure 1.2 a, b, c, d, and g). It should be noted that different structures, $[Ru_4(H_2O)_3Cl_3(B\text{-}\alpha\text{-}SiW_9O_{37})]^{7-}$ (Figure 1.2 f)[8] and B-α-$[\{Ru_3O_3(H_2O)Cl_2\}(SiW_9\ O_{34})]^{7-}$,[2] have been obtained by different research group by using the same precursor (A-α-$SiW_9$); when β-$SiW_9$ was used, $[Ru_4(H_2O)_3Cl_3(B\text{-}\beta\text{-}SiW_9O_{37})]^{7-}$ has been obtained.[8] No single crystals were obtained for $[Ru_4(H_2O)_3Cl_3(B\text{-}\alpha\text{-}SiW_9O_{37})]^{7-}$ (Figure 1.2f) or $[M_4(H_2O)_2(SiW_9O_{34})_2]^{12-}$ (M = Ni, Co) (Figure 1.2g), suggesting that these open Keggin POMs are generally challenging to synthesize or hard to crystallize.

By addition of two equivalents of $WO_4^{2-}$ per equivalent of trivacant Keggin POM $\{SiW_9\}$ at around pH 5, monovacant tungstosilicate $\{SiW_{11}\}$ can be formed. These 11-tungstosilicate anions transform to the plenary $\{SiW_{12}\}$ anions when the pH is lower to 4 and tungstate is added. For the monolacunary Keggin polytungstosilicates, all the β isomers are unstable in solution and transform to the α isomer slowly, except when the pH <4, when the β isomers react with tungstate to give the plenary β-$[SiW_{12}O_{40}]^{4-}$. Similarly, α-$[SiW_{12}O_{40}]^{4-}$ can be obtained by acidifying α-$[SiW_{11}O_{39}]^{8-}$ in the presence tungstate. The plenary structure is called Keggin type POM, and has the general formula as $[XW_{12}O_{40}]^{n-}$, where X is the heteroatom. The structure is constituted by a central $XO_4$ tetrahedron surrounded by four $M_3O_{13}$ triads at each of its vertices. These triads are linked with each other and the central tetrahedron by corner-sharing contacts (bonds). Geometrically, five isomers can be formed by successive 60 ° rotation of the $M_3O_{13}$ groups (Figure 1.3). The α-Keggin isomer ($T_d$ symmetry) is the most thermodynamic stable species.

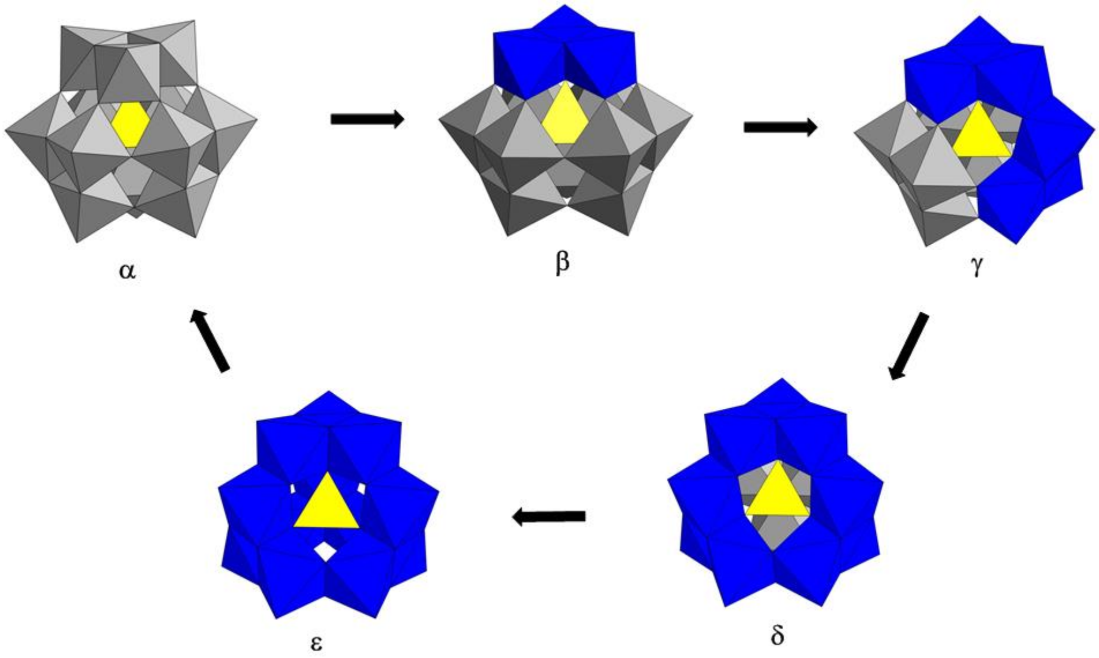

**Figure 1.3** The five isomers of the Keggin structure. The rotated $M_3O_{13}$ group(s) are shown in blue.

γ-$[SiW_{10}O_{36}]^{8-}$ cannot be obtained by condensation reactions (lowering of pH) starting with α-$SiW_9$ or β-$SiW_9$. It can only be synthesized by hydrolysis (increase of pH) of $β_2$-$SiW_{11}$ at ~pH 9. Neither α and β-$[SiW_{10}O_{37}]^{10-}$ have been isolated, in agreement with the "Lipscomb rule". According to this rule, $\{MO_6\}$ units are not stable in POMs if they have three or more terminal oxygen atoms. However, like B-α-$SiW_9$, they can be stabilized by incorporation of transition metals. Complexes as α-$[Fe_4O_4([SiW_{10}O_{37}])_2]^{16-}$,[9] [α-$Mn_2SiW_{10}O_{38}]^{7-}$,[10] $[Mn^{II}_{19}(OH)_{12}(α\text{-}SiW_{10}O_{37})_6]^{34-}$ (Figure 1.4 a),[11] $[\{β\text{-}SiCo_2W_{10}O_{36}(OH)_2(H_2O)\}_2]^{12-}$,[12] $[[\{β\text{-}SiNi_2 W_{10}O_{36}(OH)_2(H_2O)\}_2]^{12-}$,[13] and $[Ln^{III}_6Fe^{III}_6(H_2O)_{12}(α\text{-}SiW_{10}O_{38})_6]^{36-}$ (Ln=Tb, Dy) (Figure 1.4b) [14] have been synthesized. γ-$[SiW_{12}O_{40}]^{4-}$ is not stable in aqueous solution, and can only be obtained as a tetrabutylammonium (TBA) salt in aqueous-organic mixed solution from the condensation of γ-$SiW_{10}$.

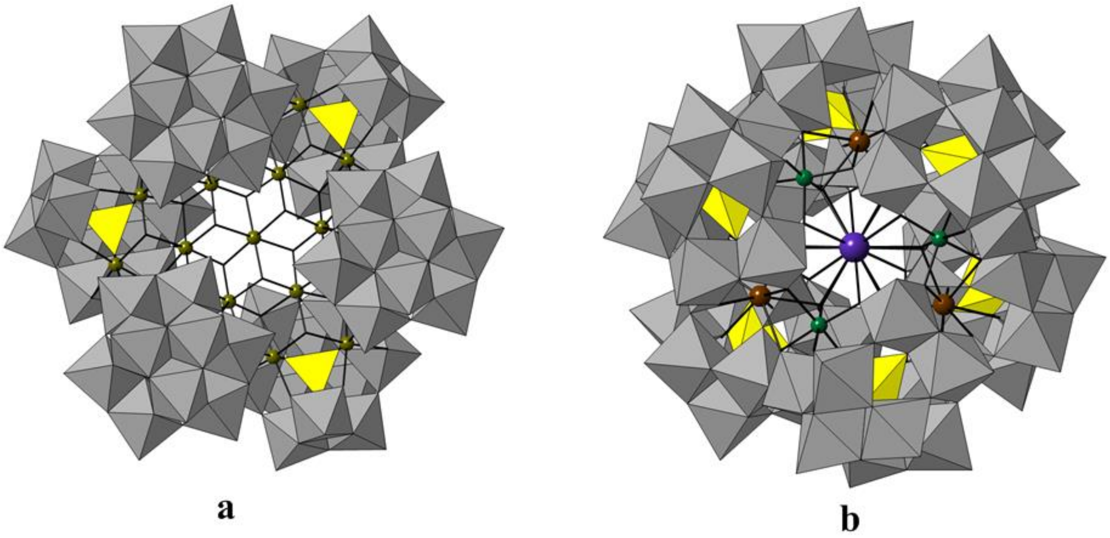

**Figure 1.4** Polyhedral and ball-and-stick representation of compounds $[Mn^{II}_{19}(OH)_{12}(\alpha\text{-}SiW_{10}O_{37})_6]^{34-}$ (Figure 1.4 a),[11] and $[Ln^{III}_6\,Fe^{III}_6(H_2O)_{12}(\alpha\text{-}SiW_{10}O_{38})_6]^{36-}$ (Ln = Tb, Dy) (Figure 1.4b).[14] Color code: W, gray; Si, yellow; Mn, olive; Ln, Brown; Fe, dark teal.

γ-$SiW_{10}$ can react with electrophiles at the lacunary sites. Because γ-$SiW_{10}$ is metastable in aqueous solution, and it is sensitive to synthetic conditions, such as pH, temperature, cation size, ionic strength, the nature of the transition metal, and buffer capacity, it is hard to predict the products of these reactions. The structure of γ-$SiW_{10}$ can be maintained, undergo isomerization, or decompose. Figure 1.5 shows several examples with the intact γ-$SiW_{10}$ structure, while Figure 1.6a shows an example of an isomerized γ-$SiW_{10}$. Figure 1.6 b-g shows loss of tungsten atoms during the reaction, and Figure 1.6 h is an example of γ-$SiW_{10}$ gaining an extra tungsten atoms. The trend in thermodynamic stability with respect to isomerization and gain or loss of tungsten atoms is as follows: γ-isomer (least stable) < β-isomer < α- isomer (most stable). It is interesting to note that to obtain the sandwich-type structure, $[M_4(H_2O)_2(B\text{-}\alpha\text{-}SiW_9O_{34})_2]^{12-}$, $\gamma$-$SiW_{10}$ is needed for reactions involving Mn, Cu, Zn (Figure 1.6g), but A-$\alpha$-$SiW_9$ is needed for reactions involving Ni, Co (Figure 1.2g).

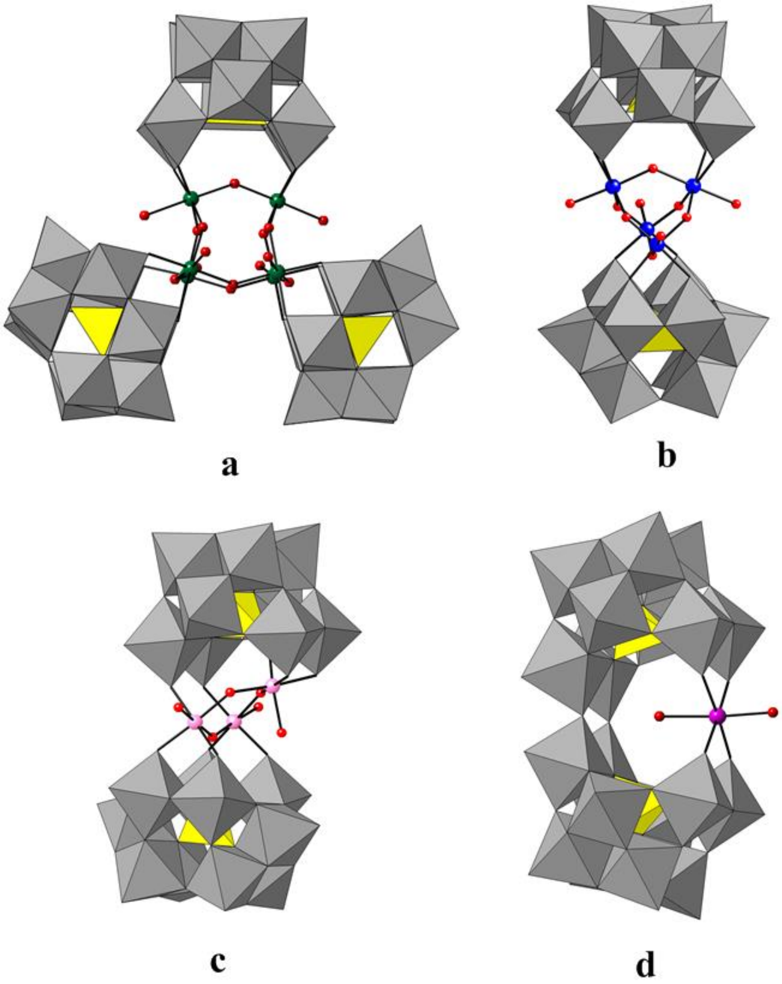

**Figure 1.5** Polyhedral and ball-and-stick representation of compounds that were formed by $\gamma$-$[SiW_{10}O_{36}]^{8-}$ with its structure intact. $[\{Fe_2(OH)_3(H_2O)_2\}_3(\gamma\text{-}SiW_{10}O_{36})_3]^{15-}$ (a),[15] $[\{Ru_4O_4(OH)_2(H_2O)_4\}(\gamma\text{-}SiW_{10}O_{36})_2]^{10-}$ (b)[16,17] $[(\gamma\text{-}SiW_{10}O_{36})_2(Cr(OH)(H_2O))_3]^{10-}$ (c),[18] $([K(H_2O)\}_2\{(\mu_3\text{-}H_2O)M(H_2O)\}(\gamma\text{-}Si_2W_{20}O_{70})]^{8-}$ (M = $Mn^{2+}$; $Co^{2+}$; $Ni^{2+}$) (d).[19,20] Color code: W, gray; Si, yellow; Fe, dark teal; Ru, blue; Cr, pink; Co, magenta.

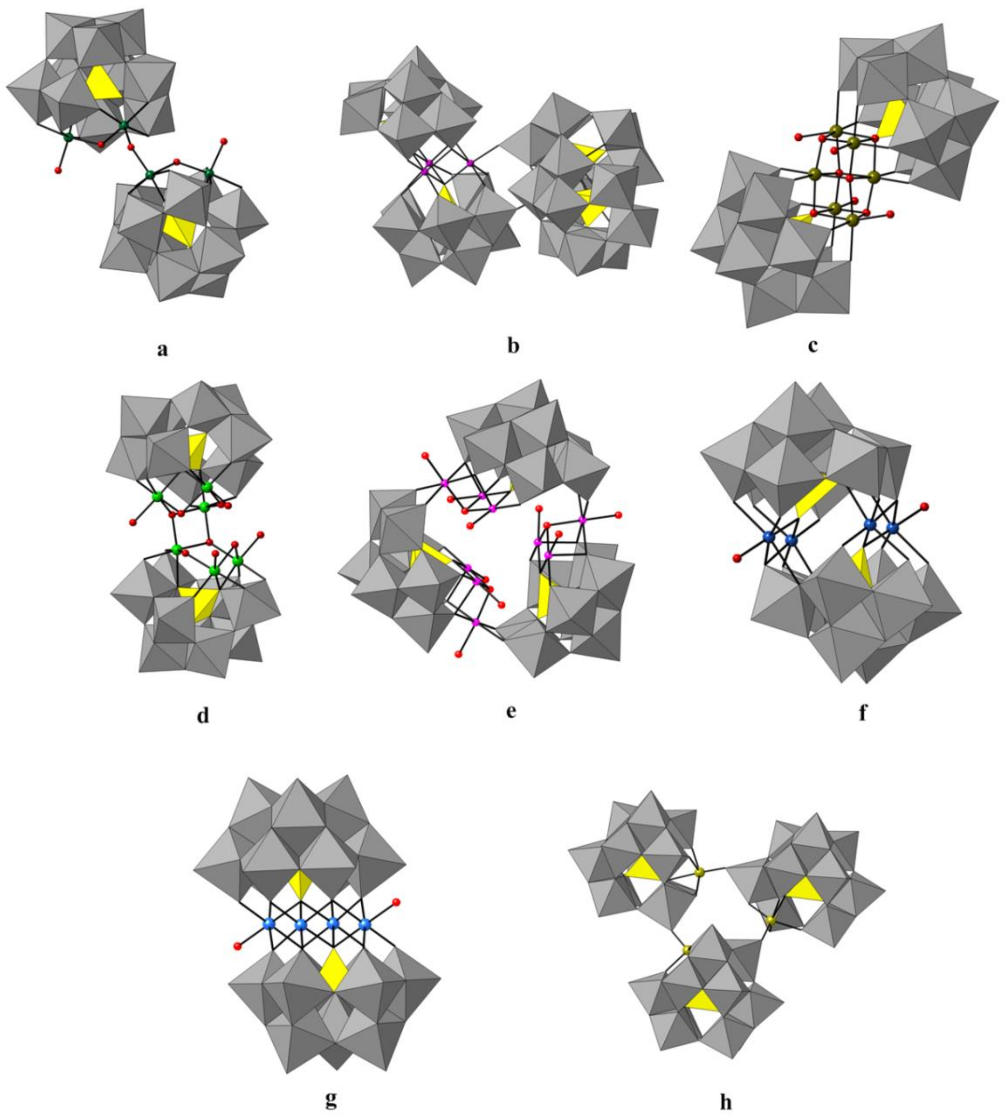

**Figure 1.6** Polyhedral and ball-and-stick representation of compounds that were formed by reaction of γ-$[SiW_{10}O_{36}]^{8-}$ after skeletal isomerization. $[\{(\beta\text{-}SiFe_2W_{10}O_{37}(OH)(H_2O)\}_2(\mu\text{-}OH)]^{12-}$ (a),[15] $[\{Co_3(B\text{-}\beta\text{-}SiW_9O_{33}(OH))(B\text{-}\beta\text{-}SiW_8O_{29}(OH)_2)\}_2]^{22-}$ (b),[21,22] $\{[SiW_9O_{34}]_2[Mn^{III}_4Mn^{II}_2O_4(H_2O)_4]\}^{12-}$ (c),[23] $[\{Ni_6(H_2O)_4(\mu_2\text{-}H_2O)_4(\mu_3\text{-}OH)_2\}(x\text{-}SiW_9O_{34})_2]^{10-}$ (d),[24] $[Co_9Cl_2(OH)_3(H_2O)_9(B\text{-}\beta\text{-}SiW_8O_{31})_3]^{17-}$ (e),[22,25] $[Cu_4(H_2O)_2(OH)_4Si_2W_{16}O_{58}]^{8-}$ (f),[26,27] $[\{SiM_2W_9O_{34}(H_2O)\}_2]^{12-}$ (M = $Mn^{2+}$, $Cu^{2+}$, $Zn^{2+}$) (g),[1] $[(\beta_2\text{-}SiW_{11}MnO_{38}OH)_3]^{18-}$ (only one enantiomer is shown here) (h).[28] Color code: W, gray; Si, yellow; Fe, dark teal; Co, magenta; Mn, olive; Ni, gree; Cu, royal blue.

Another polysilicotungstate structure that forms at lower pH is the open Wells-Dawson one, α-$[Si_2W_{18}O_{66}]^{16-}$. Compounds with the α-Wells-Dawson common "closed" motif, α-$[P_2W_{18}O_{62}]^{6-}$, involve binding of two A-α-$[PW_9]$ units (Figure 1.7a). The silicon analogue of the Wells-Dawson polyanion has never been obtained, and α-$[Si_2W_{18}O_{66}]^{16-}$ (with the open Wells-Dawson structure) can be isolated if an excess of $K^+$ cations are present. The molecular anion comprises two A-α-$[SiW_9O_{34}]^{10-}$ subunits linked through two oxygen atoms (Figure 1.7b). The W atoms which participate in the two W–O–W bonds are linked by edge junctions. The cavities of the polyanion are good binding sites for metal cations: either through four terminal oxygen atoms on each $SiW_9$ half unit, or through two junction oxygen atoms (shown in Figure 1.8). Complexes involving α-$[Si_2W_{18}O_{66}]^{16-}$ include $[\{M(H_2O)\}(\mu\text{-}H_2O)_2K(Si_2W_{18}O_{66})]^{13-}$ (M = Co, Ni, Cu),[29] $[\{M(H_2O)\}(\mu\text{-}H_2O)_2K\{[M(H_2O)_4(Si_2W_{18}O_{66})]^{13-}$ (M = Mn, Co, Ni),[29] $[Cu_5(OH)_4(H_2O)_2(A\text{-}\alpha\text{-}SiW_9O_{33})_2]^{10-}$,[30,31] $[\{KV_2O_3(H_2O)_2\}(Si_2W_{18}O_{66})]^{11-}$,[32] $[\{Fe_4(OH)_6\}(Si_2W_{18}O_{66})]^{10-}$,[32] $[Ln_2(H_2O)_7Si_2W_{18}O_{66}]^{10-}$ (Ln = $Gd^{III}$, $Tb^{III}$, $Ho^{III}$, $Eu^{III}$, $Tb^{III}$),[33,34] $[K\{UO_2(H_2O)_2\}(Si_2W_{18}O_{66})]^{11-}$,[35] and α-$[\{[K(H_2O)][K(H_2O)_4]\}_2Si_8W_{36}O_{136}]^{22-}$,[36] shown in Figure 1.9. The open Wells-Dawson structure dimerizes into a tetramer of $SiW_9$ units (α-$[K_2Li_2H_8Si_4W_{36}O_{130}]^{16-}$) when pH drops below 2.4 (Scheme 1.1). The formation of the tetramer still requires a high concentration of $K^+$.

Examination of Scheme 1.1 from the right to the left shows that as the pH increases, the plenary Keggin POMs undergo series of hydrolysis processes, and form mono-, bi- and tri-lacunary species successively.

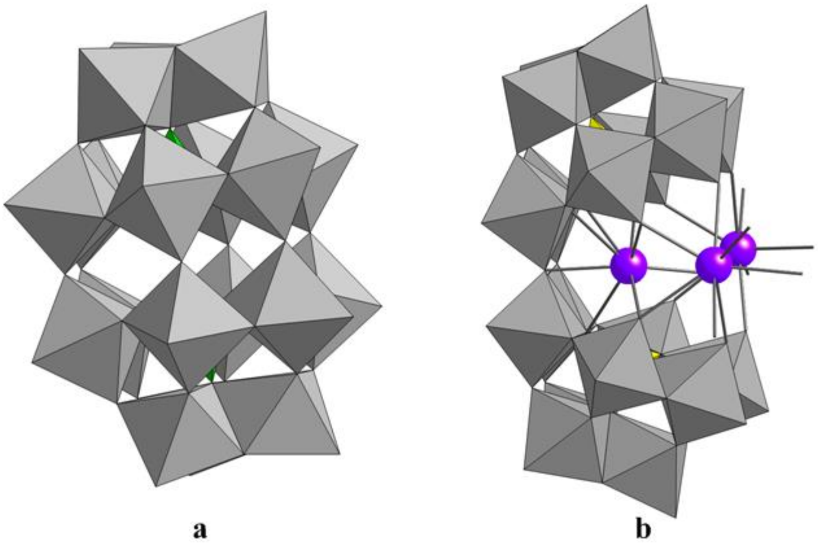

**Figure 1.7** Polyhedral representation of the Wells–Dawson polyanion α-$[P_2W_{18}O_{62}]^{6-}$ (a) and the open Wells-Dawson polynanion $[\{K(H_2O)_3\}_2\{K(H_2O)_2\}(Si_2W_{18}O_{66})]^{13-}$ (b). Color code: W, gray; Si, yellow; K, purple; P, green.

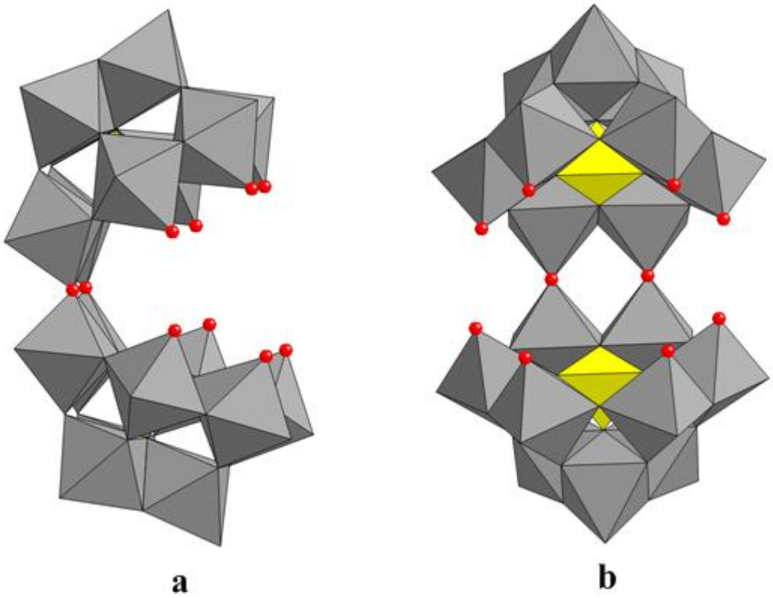

**Figure 1.8** The binding sites of α-$[Si_2W_{18}O_{66}]^{16-}$ (oxygen atoms shown in red are lacunary binding sites for transition metals) from different views.

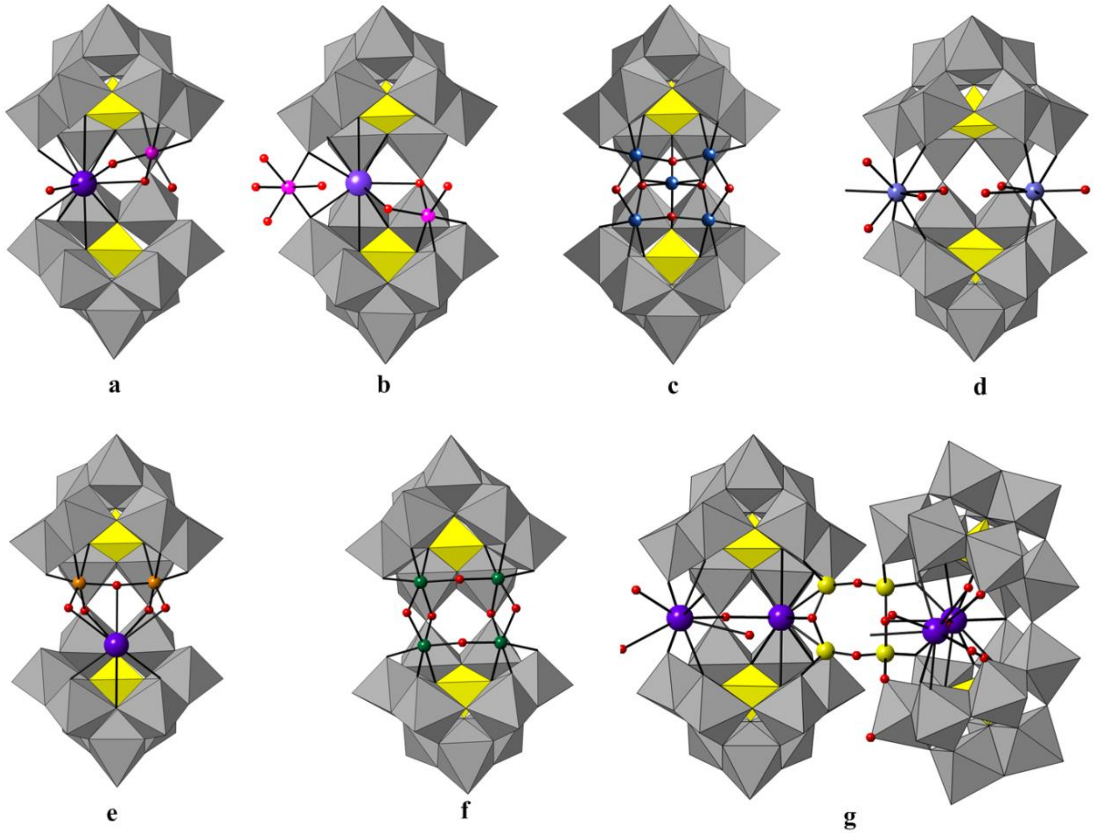

**Figure 1.9** Complexes containing α-$[Si_2W_{18}O_{66}]^{16-}$ units: $[\{M(H_2O)\}(\mu\text{-}H_2O)_2K(Si_2W_{18}O_{66})]^{13-}$(M=Co, Ni, Cu) (a),[29] $[\{M(H_2O)\}(\mu\text{-}H_2O)_2K\{[M(H_2O)_4(Si_2W_{18}O_{66})]^{13-}$ (M=Mn, Co, Ni) (b),[29] $[Cu_5(OH)_4(H_2O)_2(A\text{-}\alpha\text{-}SiW_9O_{33})_2]^{10-}$ (c),[30,31] $[Ln_2(H_2O)_7Si_2W_{18}O_{66}]^{10-}$ (Ln = $Gd^{III}$, $Tb^{III}$, $Ho^{III}$, $Eu^{III}$, $Tb^{III}$) (d), [33,34] $[\{KV_2O_3(H_2O)_2\}(Si_2W_{18}O_{66})]^{11-}$ (e),[32] $[\{Fe_4(OH)_6\}(Si_2W_{18}O_{66})]^{10-}$ (f),[32] and α-$\{[K(H_2O)][K(H_2O)_4]\}_2Si_8W_{36}O_{136}]^{22-}$ (g). Color code: K, purple; W, grey; Co, pink; Cu, blue; Si, yellow; V, orange; Fe, green.

## 1.2 Catalytic applications of POMs

### 1.2.1 POMs as Water oxidation catalysts (WOCs)

Solar energy is the most abundant renewable energy on the planet. Solar fuel can be realized by water splitting or $CO_2$ reduction (eqs 1.1 and 1.2, respectively). Both these reactions include water oxidation (eq 1.3), a four-electron process, that is both kinetically and thermodynamically challenging.

$$2H_2O + h\nu \rightarrow O_2 + 2H_2 \qquad (1.1)$$

$$2CO_2 + 4H_2O + h\nu \rightarrow 2CH_3OH + 3O_2 \qquad (1.2)$$

$$2H_2O \rightarrow O_2 + 4H^+ + 4e^- \qquad E^0 = 1.23\ \text{V vs. NHE} \qquad (1.3)$$

A variety of homogeneous and heterogeneous WOCs have been developed. A useful WOC must meet several requirements, and one of them is that the WOC has to be stable in the catalytic processes.[37] Organic ligands in the WOCs can be oxidized under harsh oxidizing conditions, resulting in loss of catalytic activity. To this end, a compound with a POM-ligated $Ru_4O_4$ core, $[Ru_4O_4(OH)_2(H_2O)_4(\gamma\text{-}SiW_{10}O_{36})_2]^{10-}$ (Figure 1.5b), was developed as a carbon-free yet soluble (homogeneous) WOC.[16,17] The phosphorus analogue of this compound was also recently made by our group, and shown to have WOC activity.[38] Subsequently, our group reported another POM WOC, $[Co_4(H_2O)_2(\alpha\text{-}PW_9O_{34})_2]^{10-}$ (phosphorus analogue of Figure 1.2g), which is based on all earth-abundant elements.[39] Since then, many additional POM WOCs have been studied and this area of research has recentlhy been reviewed.[37] However, there has yet to be any insightful structure-reactivity relationship information on involving these popular catalysts. Although cubane or cubical-core-like structures such as the $CaMn_3O_4$ core of the water oxidizing complex of *Photosystem II* tend to have higher water oxidation activity, many other factors are also important, including the overall molecular charge (which relate directly to the $pK_a$ values of the catalyst), the accessibility of the active sites to the reactants and the number of the active core metal atoms. It is also highly problematical to compare the reactivities of all WOCs, because the catalytic conditions vary in the different published studies. In addition, each POM WOC has its own pH range of hydrolytic stability.

### 1.2.2 POMs as catalysts for other oxidation processes

POMs, especially TMSPs, are good candidates for oxidation catalysis, because they are stable under oxidative conditions. They are also self-adjusting and self-repairing under appropriate conditions (pH and ionic strength). The chemical properties (redox potentials, solubility in different solvents, etc.) of POMs are also tunable by changing the component elements and counter-cations. Therefore, besides water oxidation, POMs are also good catalysts for the oxidation of organic pollutants, such as sulfide and alkenes, using green oxidants such as $O_2$ and $H_2O_2$. Scheme 1.2 shows the general mechanism for POM-catalyzed oxidation of organic compounds. Once the POM is reduced, it can be re-oxidized to form a catalytic cycle. Usually, the reoxidation step is the rate limiting step.

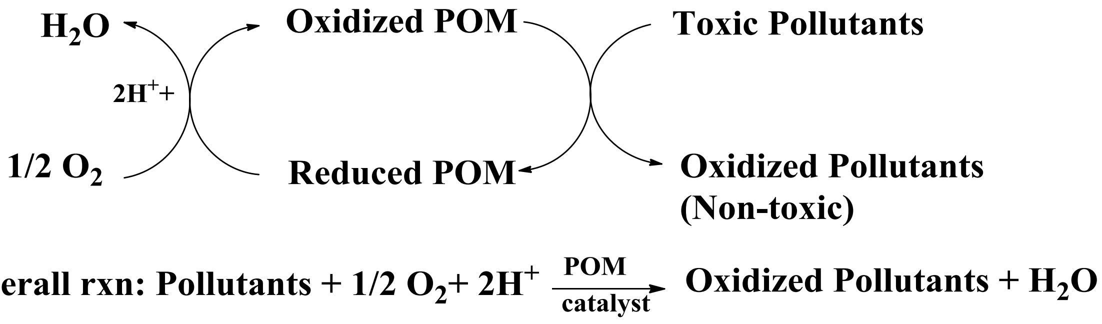

**Scheme 1.2** The general two-step mechanism for oxidations of organic compounds by $O_2$ catalyzed by POM.

## 1.3 Goals of this thesis and outline

The goal of chapter 2 to chapter 4 is to design and synthesize cobalt- or nickel-substituted POMs to catalyze water oxidation. The sodium or potassium salt of α-$[SiW_9O_{34}]^{10-}$ was used as the precursor. The stability of these TMSPs was evaluated and their WOC activity was also evaluated.

Chapter 5 addresses the synthesis of a POM with a hexa-zinc core, a molecular model for the useful semiconductor, zinc oxide.

Chapter 6 probes the catalytic activity of the WOC, $[Ru_4O_4(OH)_2(H_2O)_4(\gamma\text{-}SiW_{10}O_{36})_2]^{10-}$, for oxidation of organic compounds. I find that once the $Ru_4$-POM is reduced, it is very hard to re-oxidize it. Therefore, even though it is a good catalyst for water oxidation, it is a poor one for pollutant oxidation.

# *Chapter 2*

## Chapter 2 : Water Oxidation Catalyzed by a Tetracobalt-Substituted Polysilicotungstate: $[\{Co_4(\mu\text{-}OH)(H_2O)_3\}(Si_2W_{19}O_{70})]^{11-}$

with Yurii V. Geletii, Paul Kögerler, Helmut Schilder, Jie Song, Sheri Lense, Chongchao Zhao, Kenneth I. Hardcastle, Djamaladdin G. Musaev and Craig L. Hill

(Published partially in *Dalton Transactions*, 2012, **41**, 2084. - Reproduced by permission of The Royal Society of Chemistry)

**Abstract:** A new polysilicotungstate with earth abundant elements $[\{Co_4(\mu\text{-}OH)(H_2O)_3\}(Si_2W_{19}O_{70})]^{11-}$ (**2.1**) has been synthesized by reaction of $CoCl_2$ with $Na_{10}[\alpha\text{-}SiW_9O_{34}]$ at elevated temperature. The compound shows catalytic water oxidation activity. Although it is not stable and slowly hydrolyzes in aqueous solution, it is quite likely that the initial complex is the real catalyst, because the isolated hydrolysis products show lower WOC activity.

## 2.1 Introduction

Development of stable and efficient water oxidation catalysts (WOCs) is a central need in artificial photosynthesis. Various homogeneous and heterogeneous WOCs have been studied. Polyoxometalates (POMs) are attractive as all inorganic ligands for multi-electron-transfer catalysts, including WOCs, because they are oxidatively and hydrolytically resistant over wide pH ranges depending on alterable properties of the particular POM family.[40-46] In addition, many synthetically accessible structural families of POMs can bind two or more redox-active 3d or 4d metals in close proximity and release protons to facilitate multi-electron transfer events with redox leveling. Furthermore, additional features ranging from chirality to organic derivatization of metal-substituted POMs can be achieved by adjusting the pH, ionic strength, buffer, other metals or organic groups and POM counterions.[46-57] In addition, the heteroatom of the POM ligands, the chemical properties (such as redox potential or the $pK_a$s) of the whole molecule can be adjusted conveniently. For example, the $[Ru^{IV}{}_4O_4(OH)_2(OH_2)_4(\gamma\text{-}SiW_{10}O_{36})_2]^{12-}$ was synthesized and demonstrated to have WOC activity by our group and the Bonchio group simultaneously. The phosphorus analogue of the parent Si-heteroatom

POM, namely the polyanion $[Ru^{IV}{}_4O_6(OH_2)_4(\gamma\text{-}PW_{10}O_{36})_2]^{10-}$, was synthesized and also shown to be a water oxidation catalyst. About the same time, the Fukuzumi group compared the catalytic water oxidation activity of single-ruthenium-containing heteropolytungstates, $[Ru^{III}(H_2O)SiW_{11}O_{39}]^{5-}$ and $[Ru^{III}(H_2O)GeW_{11}O_{39}]^{5-}$.[58] In 2010, our group reported that the POM containing all earth-abundant elements, $[Co_4(H_2O)_2(PW_9O_{34})_2]^{10-}$, catalyzes water oxidation with the highest TOF (5 $s^{-1}$) documented for homogeneous WOCs at that time. It is very reasonable that its Si-analogue might also have WOC activity and comparable stability. We tried to prepare this tetra-cobalt POM by utilizing both the sodium and potassium salt of $[\alpha\text{-}SiW_9O_{34}]^{10-}$ or $Na_9[\beta\text{-}SiW_9O_{34}H]$, but never succeeded in making this target compound, either following the published procedure,[59] or using our own methods. However, we repeatedly obtained a new complex, $[\{Co_4(\mu\text{-}OH)(H_2O)_3\}(Si_2W_{19}O_{70})]^{11-}$ (**2.1**) by reaction of $CoCl_2$ with $Na_{10}[\alpha\text{-}SiW_9O_{34}]$ at elevated temperature. In this chapter, we report the structural and catalytic water oxidation activity of **2.1**, as well as it hydrolytic properties.

## 2.2 Experimental

### General methods and materials

$Na_{10}[\alpha\text{-}SiW_9O_{34}]$ was prepared by the literature procedure. The purity was checked by IR spectroscopy.[60] All reagents used were commercially available and were used as received. Elemental analyses for K, Na, Co, Si and W were performed by Galbraith Laboratories (Knoxville, Tennessee). IR spectra (2% sample in KBr pellet) were recorded on a NicoletTM 6700 FT-IR spectrometer. The electronic absorption spectra were taken on an Agilent 8453 UV-vis spectrometer. The thermogravimetric data were collected on an ISI TGA 1000 instrument.

Electrochemical data were obtained at room temperature using a BAS CV-50W electrochemical analyzer equipped with a glassy-carbon working electrode, a Pt-wire auxiliary electrode, and a Ag/AgCl (3 M NaCl) BAS reference electrode. All oxidation potentials are reported relative to this reference electrode. Temperature-dependent magnetic susceptibility measurements of the potassium, sodium salt of **2.1**, **$K_{10.2}Na_{0.8}$-2.1**, were performed on polycrystalline samples using a Quantum Design MPMS-XL5 SQUID magnetometer (2 – 290 K, 0.1 Tesla) and cylindrical PTFE sample holders. Susceptibility data were corrected for diamagnetic contributions ($\chi_{dia}$(**$K_{10.2}Na_{0.8}$-2.1**) = $-747.2 \times 10^{-6}$ $cm^3$ $mol^{-1}$). Comprehensive descriptions of computational details in the magnetochemical analysis of the $Co^{(II)}$-based systems have been published.[61,62]

**Syntheses**

**$K_{10.2}Na_{0.8}[\{Co_4(\mu\text{-}OH)(H_2O)_3\}(Si_2W_{19}O_{70})]\cdot 31H_2O$** (**$K_{10.2}Na_{0.8}$-2.1**). $Na_{10}[\alpha\text{-}SiW_9O_{34}]$ (0.8 g, 0.3 mmol) was dissolved in 15 mL of water. The pH was adjusted to 6.8 by 1 M HCl, then 190 mg (0.8 mmol) of $CoCl_2\cdot 6H_2O$ was added. The pH dropped to ~5. This solution was heated to 80 °C for 1 hr. Some precipitation became visible. After cooling the solution to room temperature, the pH was ~6.5. Subsequently the pH was adjusted to 5.8 by 0.5 M HCl. Addition of 2 mL of saturated KCl to the suspension and stirring for 10 min produced a precipitate which was filtered. Red block crystals were collected from the reaction solution after 24 h. Yield: 18% based on W. IR (KBr, ν / $cm^{-1}$): 992 (m), 946 (m), 888 (s), 786 (s), 703 (s), 668 (sh), 600 (m), 536 (sh), 523(m). Elemental analysis calculated (found) for $K_{10.2}Na_{0.8}[\{Co_4(\mu\text{-}OH)(H_2O)_3\}(Si_2W_{19}O_{70})]\cdot 31H_2O$: K: 6.70 (6.60); Na: 0.309

(0.296); Co: 3.96 (3.76); Si: 0.944 (0.938); W: 58.7 (58.4) %.

**$K_{10}Na[\{Co(H_2O)\}(\mu\text{-}H_2O)_2K\{Co(H_2O)_4\}(Si_2W_{18}O_{66})]\cdot 25H_2O$** (**$K_{10}$Na-2.2**). **$K_{10.2}Na_{0.8}$-2.1** (150 mg) was dissolved in 4 mL of water, then 1 mL of 1 M KOAc/HOAc buffer (pH 4.8) and 2 mL of 1 M NaOAc/HOAc buffer (pH 4.8) were added. Slow evaporation at room temperature results in crystals after one week. The geometrical structure of the polyanion in **$K_{10}$Na-2.2** is virtually identical to that of **1Co2-K(A)** in ref 54. IR (KBr, $\nu$ / cm$^{-1}$): 997 (m), 942 (m), 884 (s), 863 (m), 803 (m), 730 (s), 651 (m), 547 (w), 525 (w). Elemental analysis calculated (found): K: 7.55 (7.56); Na: 0.404 (0.653); Co: 2.07 (2.19); Si: 0.986 (0.901); W: 58.1 (57.6) %.

### X-Ray crystallography

Single crystals suitable for X-ray structure analysis were each coated with Paratone-N oil, suspended on a small fiber loop and placed in a cooled nitrogen gas stream at 173 K on a Bruker D8 APEX II CCD sealed tube diffractometer with graphite monochromator Mo K$\alpha$ ($\lambda$ = 0.71073 Å) radiation. Data were measured using a combination of $\varphi$ and $\omega$ scans with 10 s frame exposure and 0.3 ° frame widths. Data collection, indexing and initial cell refinements were all carried out using SMART.[63] Frame integration and final cell refinements were done using SAINT.[64] The molecular structure of each complex was determined using direct methods and Fourier techniques, and refined by the standard full-matrix least-squares procedure. A multiple absorption correction, including face indexing, was applied using the program SADABS.[65] The largest residual electron density for each structure was located close to (less than 1.0 Å from) the W atoms and was most likely due to imperfect absorption corrections frequently encountered in heavy-metal atom structures. Scattering factors and anomalous dispersion corrections are taken from the International Tables for X-ray Crystallography. Structure solution, refinement, graphic and generation of publication materials were performed by using SHELXTL, v 6.14 software.[66] The crystal data and structure refinement parameters are summarized in Table 2.1.

### Catalytic experiments

The water oxidation reactions were performed in a 10 mL Schlenk flask. The vessel was filled with 8 mL of a solution containing 1.0 mM $[Ru(bpy)_3]Cl_2$, 5 mM $Na_2S_2O_8$, 25 mM buffer solution and the desired concentration of catalyst. The solution was carefully deairated by bubbling argon. The reaction was initiated by exposing the reaction vessel to the light (the Xe-lamp filtered with a 420-520 nm band-pass filter). After the desired illumination time, the reaction was temporarily stopped by blocking the light, and the flask was vigorously shaken to allow equilibration of $O_2$ between the solution and the head-space. Analysis of the headspace gas was performed by withdrawing a 0.1 mL sample from the headspace and using a Agilent 7890A gas chromatograph equipped with thermal conductivity detector and a GC capillary column with 5Å molecular sieves to separate $O_2$ and $N_2$. Argon was used as the carrier gas. The reaction was complete after consumption of $Na_2S_2O_8$. The amount of $N_2$ detected allowed the correction for the air leaking in the reaction vessel. The detection limit for $O_2$ was 0.02 μmol.

**Table 2.1** Crystal data and structural refinement for the X-ray structure analyses of **$K_{10.2}Na_{0.8}$-2.1** and **$K_{10}Na$-2.2**

| | **$K_{10.2}Na_{0.8}$-2.1** | **$K_{10}Na$-2.2** |
|---|---|---|
| Molecular formula | $Co_4\ H_{69}K_{10.2}\ Na_{0.8}\ O_{105}\ Si_2\ W_{19}$ | $Co_2\ H_{64}K_{10}\ Na\ O_{98}\ Si_2\ W_{18}$ |
| Formula wt. / g mol$^{-1}$ | 5951.54 | 5529.58 |
| Temperature / K | 173(2) | 173(2) |
| Radiation (λ) / Å | 0.71073 | 0.71073 |
| Crystal system | Triclinic | Triclinic |
| Space group | *P*-1 | *P*-1 |
| *a* / Å | 13.049(7) | 14.632(4) |
| *b* / Å | 17.315 (9) | 18.179 (4) |
| *c* / Å | 22.642(12) | 18.284(4) |
| $\alpha$ / ° | 67.540(8) | 65.974(3) |
| $\beta$ / ° | 74.221(8) | 79.207(4) |
| $\gamma$ / ° | 84.294 (8) | 86.471 (4) |
| *V* / Å$^3$ | 4550(4) | 4362.8(18) |
| *Z* | 2 | 2 |
| $\rho_{calcd}$ / g cm$^{-3}$ | 4.111 | 3.987 |
| $\mu$ / mm$^{-1}$ | 25.223 | 24.607 |
| *F*(000) | 4918 | 4570 |
| Independent reflections | 20048 | 20765 |
| Goodness-of-fit on $\|F\|^2$ | 1.053 | 1.026 |
| Final *R* indices [$R > 2\sigma(I)$] | $R_1^a = 0.0554$, $wR_2^b = 0.1910$ | $R_1^a = 0.0449$, $wR_2^b = 0.1125$ |
| *R* indices (all data) | $R_1^a = 0.0667$, $wR_2^b = 0.2050$ | $R_1^a = 0.0581$, $wR_2^b = 0.1204$ |
| Largest diff. peak and hole / e Å$^{-3}$ | 3.555 and –8.785 | 7.293 and –6.896 |

$^a\ R_1 = \Sigma||F_0| - |F_c|| / \Sigma|F_0|$; $^b\ wR_2 = \Sigma[w(F_0^2 - F_c^2)^2] / \Sigma[w(F_0^2)^2]^{1/2}$

## 2.3 Results and discussion

### 2.3.1 Description of crystal structures $K_{10.2}Na_{0.8}[\{Co_4(\mu\text{-}OH)(H_2O)_3\}(Si_2W_{19}O_{70})] \cdot 31H_2O$ (**$K_{10.2}Na_{0.8}$-2.1**).

This polyanion has $C_1$ symmetry and is composed of a $Co_4$ cluster sandwiched by a $[A\text{-}\alpha\text{-}SiW_9O_{34}]^{10-}$ and a $[\alpha\text{-}SiW_{10}O_{37}]^{10-}$ unit. The Co1 and W8 moieties are disordered, resulting in two possible polyanion structures (**2.1a** and **2.1b** in Figure 2.1). The best refinement was obtained with occupation factors of 1/2 for each polyanion. Bond valence sum calculations reveal that the three terminal oxygens associated with the $Co_4$ cluster are all diprotonated; only the μ-oxo oxygen is monoprotonated. The connection motif of the central $Co_4$ cluster (Figures 2.1c and 2.1d) is rarely seen in polyanion chemistry. It contains three octahedrally coordinationed $Co^{2+}$ ions and one tetragonal pyramidally coordinated $Co^{2+}$ ion. The $Co2O_6$ and $Co4O_6$ units (octahedral Co centres) and $Co3O_5$ units (tetragonal pyramid is weakly bonded to $O_{27}W$) located at the trivacant sites of $[A\text{-}\alpha\text{-}SiW_9O_{34}]^{10-}$ complete the α-Keggin structure, $[\alpha\text{-}SiCo_3W_9O_{40}]^{16-}$. At the same time, $Co2O_6$ and $Co1O_6$ units (or $Co1AO_6$) replace two corner-sharing $WO_6$ octahedra from $[\alpha\text{-}SiW_{12}O_{40}]^{4-}$, resulting in the well-defined α-Keggin structure $[\alpha\text{-}SiCo_2W_{10}O_{40}]^{12-}$.

As in the synthesis of other TMSPs, factors such as pH, temperature and countercations, are all important in the synthesis of **$K_{10.2}Na_{0.8}$-2.1**. Under the slightly acidic synthetic conditions, two $[A\text{-}\alpha\text{-}SiW_9O_{34}]^{10-}$ link together with one of them gaining an extra tungsten atom. As we have discussed in Chapter 1, no isolated $[\alpha\text{-}SiW_{10}O_{37}]^{10-}$ has been obtained, but this structure can be stablized by incoporation of transition metal atoms, such as the $Co_4$ cluster here. Addition of high concentrations of potassium ions before the crystallization process is also crucial. No crystals are observed if the amount of potassium ion is insufficient.

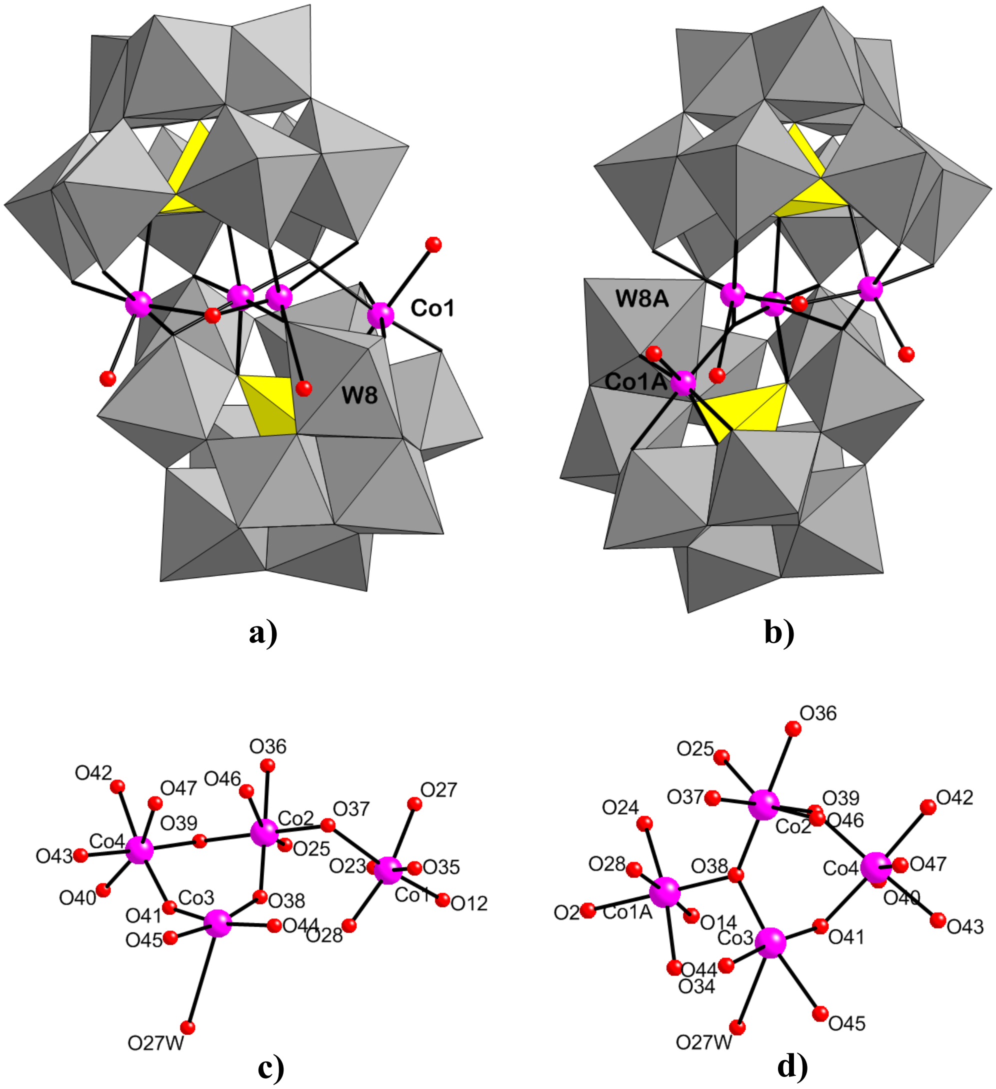

**Figure 2.1** The two isomers of $[\{Co_4(\mu\text{-}OH)(H_2O)_3\}(Si_2W_{19}O_{70})]^{11-}$ (**2.1a** and **2.1b**) coexisting in a 1:1 ratio in the single-crystal structure of **$K_{10.2}Na_{0.8}$-2.1**. The cobalt centers (purple) are shown in ball-and-stick notation, the polyoxometalate framework in polyhedral notation ($WO_6$ octahedra: gray, $SiO_4$ tetrahedra: yellow). Hydrogen atoms are omitted for clarity. Lower panels (c) and (d) show the μ-oxo connection motifs of the cobalt sites in **2.1a** and **2.1b**, respectively.

### 2.3.2 IR Characterization

Figure 2.2 shows a comparison of the IR spectra of compounds $K_{10.2}Na_{0.8}$-**2.1** and $K_{10}Na$-**2.2**. In the low-wavenumber region of the IR spectra ($\nu < 1000$ cm$^{-1}$), the two compounds show similar overall spectral shapes. However, the band positions are shifted, which makes it possible to differenciate the two compounds.

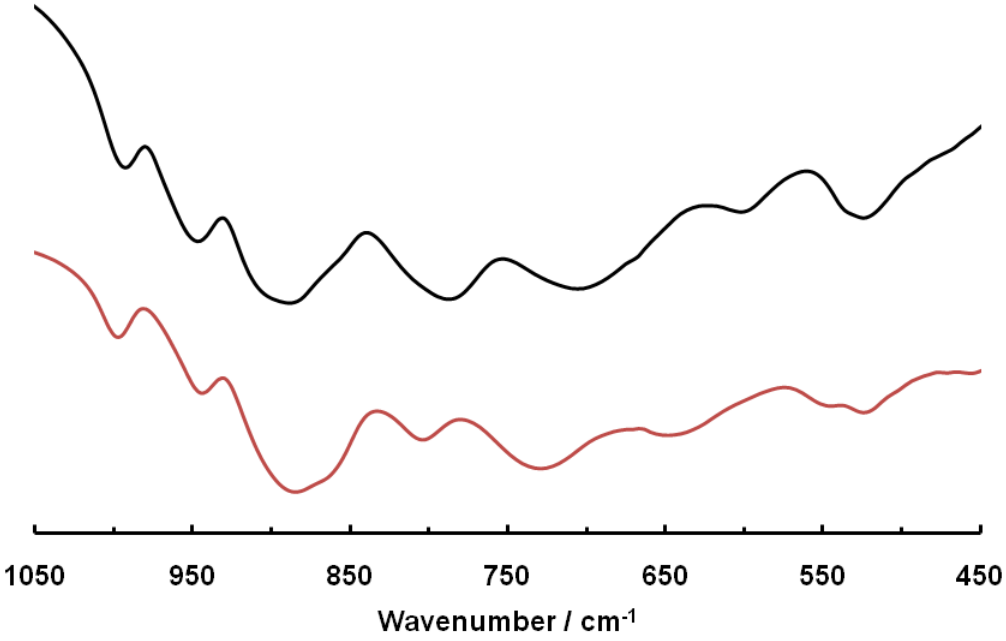

**Figure 2.2** IR spectra of $K_{10.2}Na_{0.8}$-**2.1** (black) and $K_{10}Na$-**2.2** (red).

### 2.3.3 Thermogravimetric Analysis (TGA)

From the TGA of $K_{10.2}Na_{0.8}$-**2.1** and $K_{10}Na$-**2.2** (Figure 2.3 and 2.4), we can calculate the weight percentage of the lattice water in these samples.

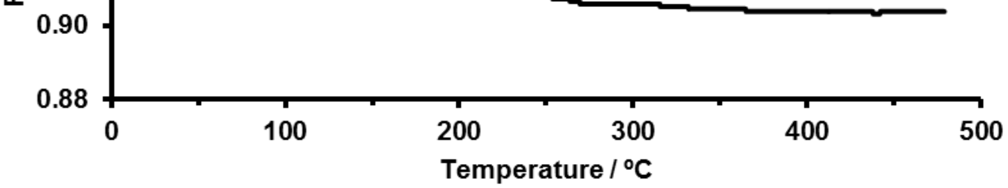

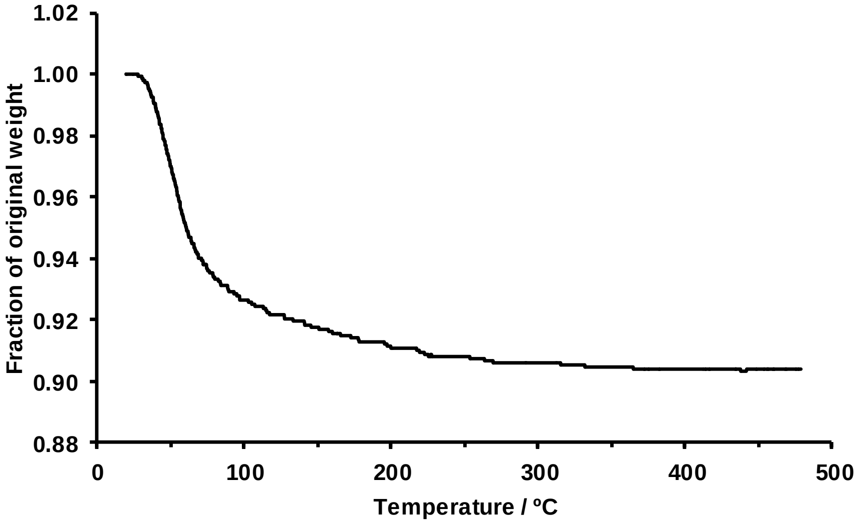

**Figure 2.3** TGA of crystalline $K_{10.2}Na_{0.8}$-**2.1**.

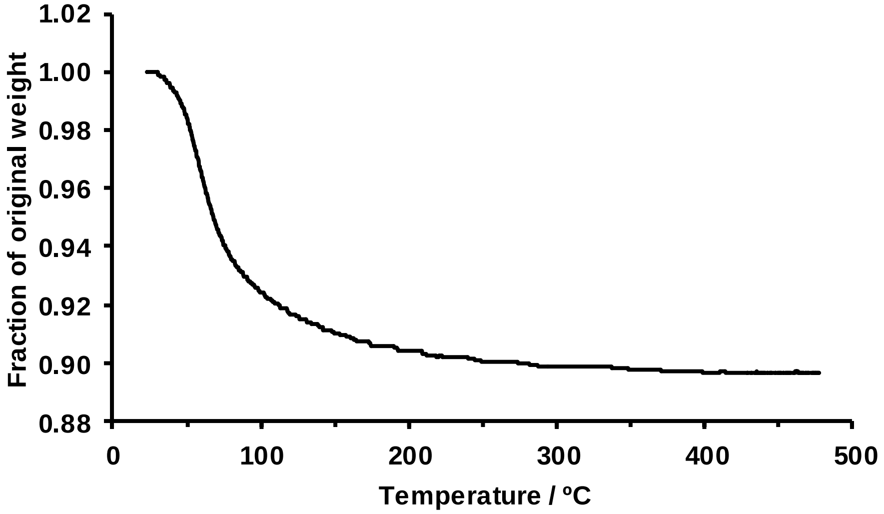

**Figure 2.4** TGA of crystalline $K_{10}Na$-**2.2**.

### 2.3.4 Magnetic properties of $[\{Co^{II}_4(\mu\text{-}OH)(H_2O)_3\}(Si_2W_{19}O_{70})]^{11-}$ (2.1)

In order to probe whether an equal mixture of the two possible structural scenarios involving the W8/Co1 distribution (**2.1a** and **2.1b)**, are compatible with magnetic characteristics, low-field susceptibility measurements (2–290 K, 0.1 and 1.0

Tesla) were performed and analyzed. Our computational framework CONDON, recently expanded to model polynuclear Co(II) clusters,[61,62]

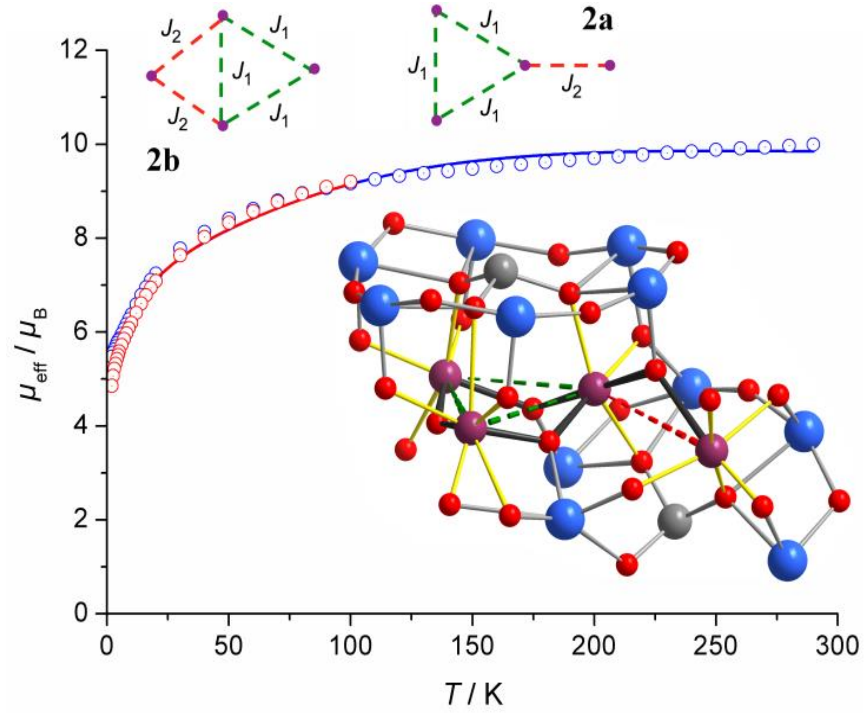

**Figure 2.5** Temperature dependence of $\mu_{eff}$ of **$K_{10.2}Na_{0.8}$-2.1** (circles: experimental data, graphs: best fits to Hamiltonian based on an equal ratio of scenarios **2.1a** and **2.1b**, with exchange patterns defined as in top panel) at 0.1 (blue) and 1.0 (red, < 100 K) Tesla. Inset: Binding modes of the $Co_4O_4$ fragment in **2.1a** between adjacent tungstate and silicate groups. The Co-O bonds forming the dominating magnetic exchange pathways are highlighted in dark grey; remaining Co-O bonds completing the Co coordination environments are shown in yellow. Exchange contacts: dashed green ($J_1$) / red ($J_2$) lines. W: blue, Si: grey, O: red, Co: purple spheres.

was used to simulate the two situations of a Co(II) spin tetrahedron with one (**2.1b**, Figure 2.1f) or two (**2.1a**, Figure 2.1c) missing edges between the basal $\{Co_3\}$ triangle and the apex, defined as either Co4 (**2.1a**) or Co1 (**2.1b**). In both cases, we assume uniform exchange coupling $J_1$ within the triangular $\{Co_3\}$ base, primarily mediated by three $\mu_2$-O bridges (**2.1a**) or by a single $\mu_3$-O center (**2.1b**). The exchange energy $J_2$ between the triangle and the outer (“apical”) Co site is also due to μ-O-mediated coupling (**2.1a**: O37; **2.1b**: O39,O41).

Generally, significant orbital contributions and the resulting strong magnetic anisotropy complicate the analysis of Co(II) species with octahedral ligand fields ($^4T_1$), and the canonical models are only applicable within narrow temperature limits. Thus, modeling the two scenarios **2.1a** and **2.1b** was based on a spin Hamiltonian accounting for not only exchange interactions and Zeeman splitting, but also spin-orbit coupling and ligand field effects. Ligand fields are approximated as cubic and uniform for all four Co environments (to avoid overparametrization). Within the constraints of this model, least-squares fitting to the 0.1 and 1.0 Tesla experimental data (Figure 2.5) yields the following parameter sets (SQ = 2.7%): For **2.1a**, ferromagnetic intra-triangle coupling $J_1 = +0.5\ \mathrm{cm}^{-1}$, and $J_2 = -1.91\ \mathrm{cm}^{-1}$; for **2.1b**, $J_1 = +2.0\ \mathrm{cm}^{-1}$, and $J_2 = -1.64\ \mathrm{cm}^{-1}$. These anti- and the ferromagnetic exchange energies are in line with the Co-O-Co angles of the respective exchange pathways. The ligand field parameters (in Wyborne notation) $B^4{}_0$ amount to 30900 $\mathrm{cm}^{-1}$ (**2.1a**) and 24350 $\mathrm{cm}^{-1}$ (**2.1b**), common values for slightly distorted $CoO_6$ environments. The fitting procedure employed fixed, standard values for the Racah parameter $B = 825\ \mathrm{cm}^{-1}$ and a spin-orbit coupling constant = 533 $\mathrm{cm}^{-1}$ for all $Co^{(II)}$ sites.

### 2.3.5 Catalytic properties

To probe the catalytic activity of **2.1** towards water oxidation at pH 5-9, we used $[Ru(bpy)_3]^{3+}$, generated *in situ*, as an oxidant.[16,38,39,67-69] It can be prepared either as solid material and then used as a stoichiometric oxidant, or photogenerated from

$[Ru(bpy)_3]^{2+}$ ($\lambda_{max}$ = 454 nm, $\varepsilon = 1.4\times10^4$ $M^{-1}cm^{-1}$) in the presence of $S_2O_8^{2-}$ as a sacrificial electron acceptor, eq 2.1.[38,67,69]

$$2\,[Ru(bpy)_3]^{2+} + S_2O_8^{2-} + h\nu \rightarrow 2\,[Ru(bpy)_3]^{3+} + 2\,SO_4^{2-} \qquad (2.1)$$

This light-driven process is well studied,[67] and proceeds via quenching of the excited state $[Ru(bpy)_3]^{2+*}$ by $S_2O_8^{2-}$, producing $[Ru(bpy)_3]^{3+}$ and $SO_4^{\bullet-}$.[70,71] The $SO_4^{\bullet-}$ produces a second molecule of $[Ru(bpy)_3]^{3+}$. Four equivalents of $[Ru(bpy)_3]^{3+}$ are required to oxidize two water molecules generating $O_2$ and four protons (eq 2.2):

$$2\,S_2O_8^{2-} + 2\,H_2O + 2\,h\nu \rightarrow 4\,SO_4^{2-} + O_2 + 4\,H^+ \qquad (2.2)$$

The exemplary kinetics of $O_2$ formation in eq 2.2 (expressed in turnover numbers, TON = $n(O_2)/n(cat)$) and the experimental conditions are given in Figure 2.6. The $O_2$ yield increases with pH and the TON approaches ~80. At present, the rate-limiting step of overall reaction in eq 2.2 is not established. Therefore only the initial apparent turnover frequency, defined as $TOF_{ap}$ = TON/time, is estimated, and this value is ~0.1 $s^{-1}$. The $O_2$ yield based on $S_2O_8^{2-}$, eq 2.2, is around 24 %. The reaction conditions were not optimized and only catalyst concentrations were varied. A decrease of catalyst concentration results in a decrease of both TON and $TOF_{ap}$.

### 2.3.6 Stability of 2.1

The stability of the catalyst under turnover conditions was a key point of interest. First, we evaluated the hydrolytic stability of **2.1**. In water, this complex has a very low absorbance in the range 450-700 nm. Therefore we measured the spectral changes of **2.1** at relatively high concentrations (4-6 mM) versus time at different pH values. In plain water (natural pH ~ 8) we observed a noticable absorbance increase (ca. 7%

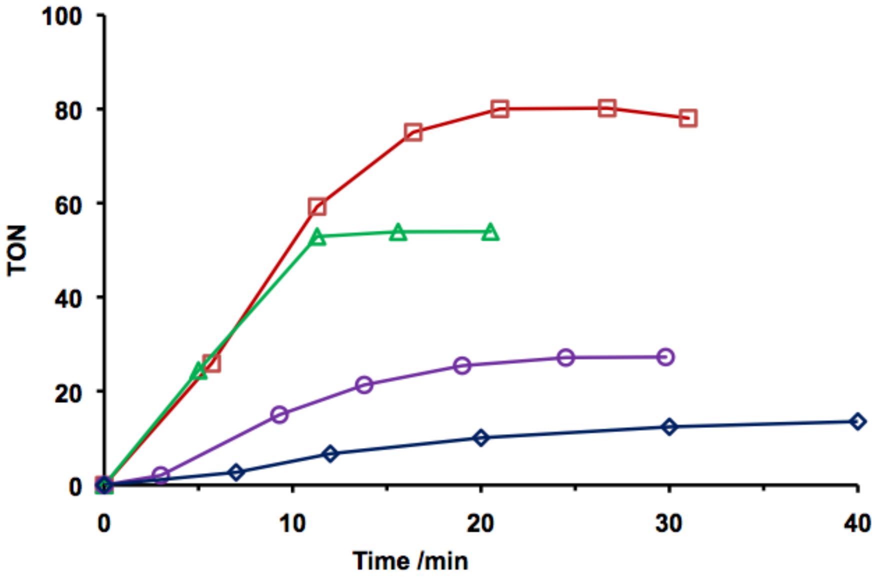

**Figure 2.6** Kinetics of catalytic light-induced $O_2$ formation from water by persulfate oxidation in different buffer solutions. Conditions: Xe lamp, 420-520 nm band-pass filter, 1.0 mM $[Ru(bpy)_3]Cl_2$, 5 mM $Na_2S_2O_8$, 25 mM buffer, 10.0 μM **2.1**, total solution volume 8 mL. Blue diamonds: sodium phosphate buffer, pH 7.2; open purple circles: 1:1 mixture of sodium phosphate and sodium borate buffers, pH 8; green triangles: sodium borate buffer, pH 8; red squares: sodium borate buffer, pH 9.

after 12 hrs) in the range 470-550 nm, prompting examination of the stability of **2.1** in 25 mM sodium acetate (pH 4.8), phosphate (pH 7.2) and borate (pH 9.0) buffer solutions. The initial changes in UV-Vis spectra in borate buffer at pH 9.0 are shown in Figure 2.7. A similar pattern was observed in sodium acetate and phosphate buffered solutions. At pH 9.0 the increase in absorbance was *ca.* 3 times faster than at pH 4.8. Longer aging leads to a notably different final spectrum (Figure 2.8). It takes about 40 days to complete the spectral evolution in water. We attempted to crystallize the product compound directly from the aged solutions by slow evaporation of water, but rather than crystals only a pink powder was obtained.

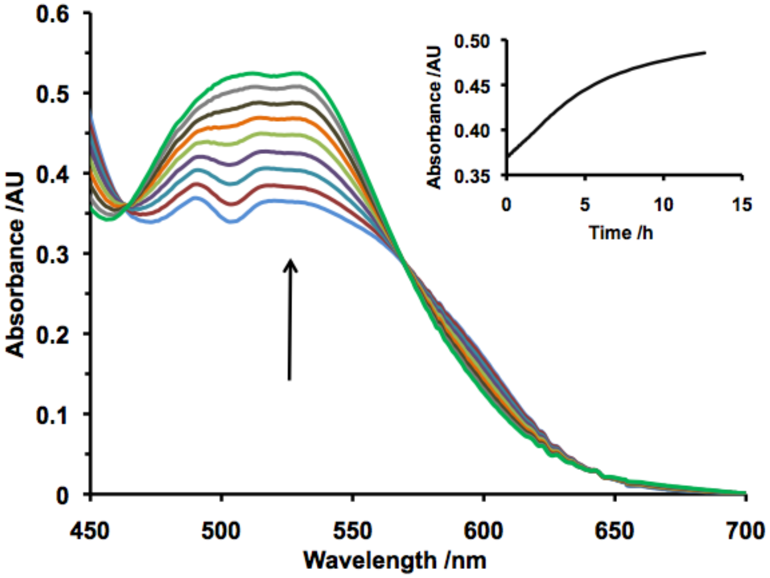

**Figure 2.7** Changes in UV-Vis spectra of 6.2 mM **2.1** in 25 mM sodium borate buffer at pH 9.0. The insert is an increase of absorbance at 489 nm with time.

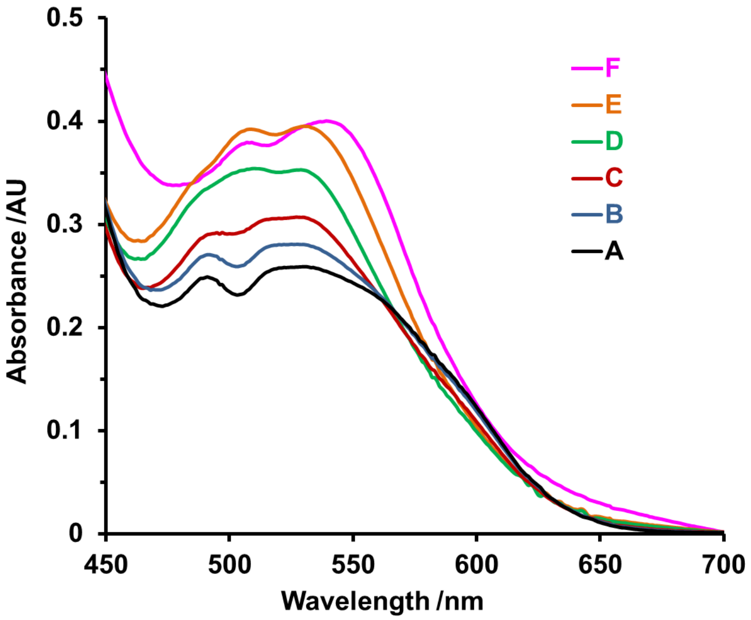

**Figure 2.8** Time profile of the electronic absorption spectra of **2.1 (**5.7 mM) in water after 0 h (A), 4.5 h (B), 22 h (C), 4 days (D), 10 days (E) and 40 days (F). Conditions: *l* = 1 cm, 25 ℃.

Therefore, we aged **2.1** in acetate buffer solution (pH 4.8) for about one week, and X-ray quality crystals of the resulting K$_{10}$Na-**2.2** were obtained by slow evaporation of water. After collection of the complex K$_{10}$Na-**2.2**, the solution was left to evaporate more water, and dark red crystals of a salt of $[Co(H_2O)SiW_{11}O_{39}]^{6-}$ (**2.3**)[72] were obtained (the counter cation(s) were not identified).

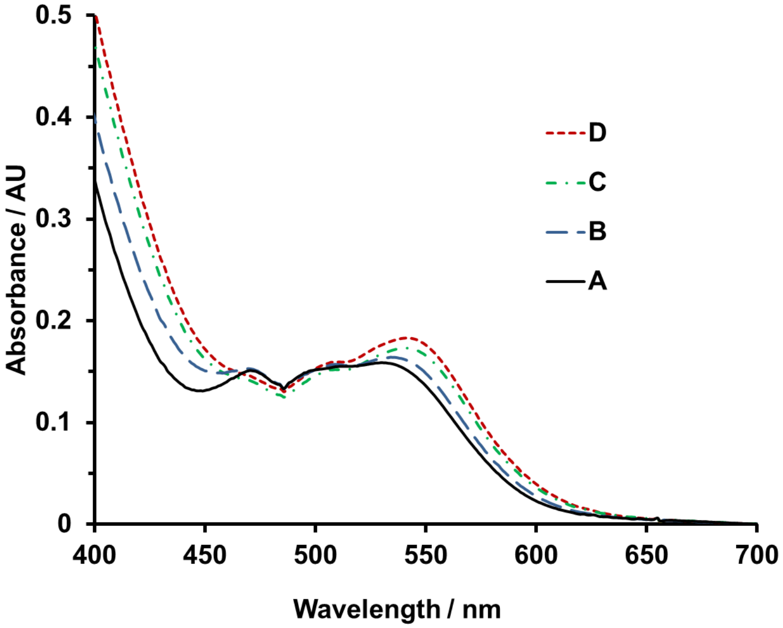

**Figure 2.9** Time profile of the electronic absorption spectra of K$_{10}$Na-**2.2** (4.7 mM) in water after 0 day (A), 5 days (B), 23 days (C) and 30 days (D). Conditions: *l* = 1 cm, 25 ℃.

Based on literature studies,[29,73] the $[\alpha\text{-}Si_2W_{18}O_{66}]^{16-}$ framework in **2.2** is an intermediate between the monomer $[A\text{-}\alpha\text{-}SiW_9O_{34}]^{10-}$ and the hypothetical $[\alpha\text{-}Si_2W_{18}O_{62}]^{8-}$ Wells-Dawson anion. The $K^+$ ion in the central pocket plays a key role in the stabilizing **2.2** in solution. It bridges the two half-anions and provides rigidity to the metal-oxide framework. In **2.1**, a {Co$_4$} unit links $[A\text{-}\alpha\text{-}SiW_9O_{34}]^{10-}$ and [α-

$SiW_{10}O_{37}]^{10-}$, therefore the tungstosilicate framework in **2.1** could be an unstable intermediate on the way to production of the monomer $[A\text{-}\alpha\text{-}SiW_9O_{34}]^{10-}$ and an open Wells-Dawson unit, $[\alpha\text{-}Si_2W_{18}O_{66}]^{16-}$. Complex **2.2** is a quite kinetically stable compound, but it further converts to the thermodynamically more stable mono-substituted Keggin derivative, **2.3**, after aging for 1 month (Figure 2.9). UV-vis spectra also indicate this stable compound is **2.3** (Figure 2.10).

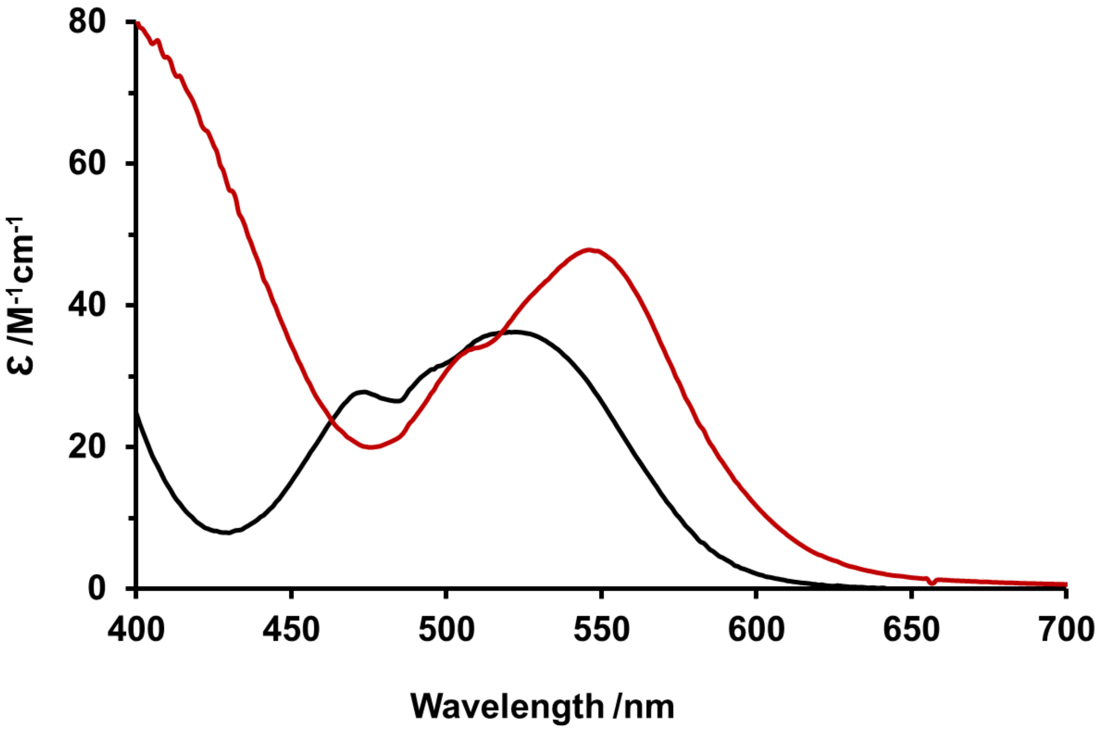

**Figure 2.10** UV-vis spectra of **$K_{10}$Na-2.2** (black line) and **2.3** (red line).

We attempted to simulate the UV-vis spectrum of aged solution of **2.1** (after 40 days) by combining UV-vis spectra of $K_{10}$Na-**2.2**, **2.3**, and $Co_{aq}^{2+}$ (as $CoCl_2$). A reasonably good simulation was achieved by combining the spectra of **2.3** and $Co_{aq}^{2+}$ with 1:5.5 ratio (Figure 2.11). The remaining difference might be assigned to the presence of small amounts of $K_{10}$Na-**2.2** and other unidentified compounds. Thus

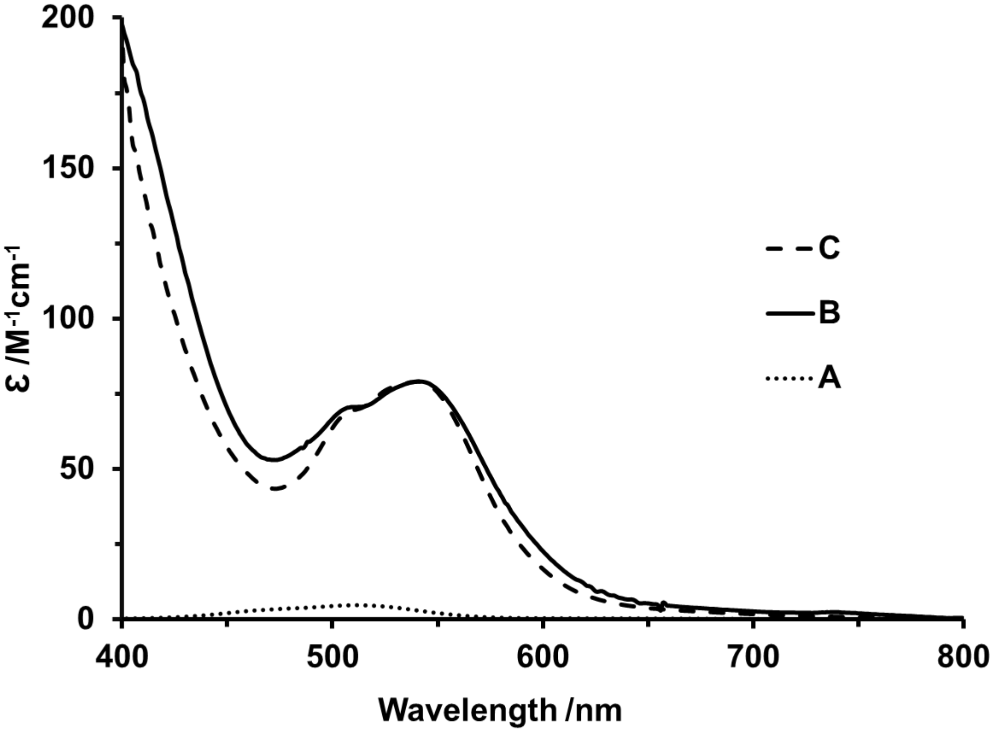

**Figure 2.11** Simulation of the spectrum of aged solution of **2.1**: **[**Co($H_2O$)$_6$]$^{2+}$ (as $CoCl_2$) (A), aged solution of **2.1** after 40 days (B) and simulation (C).

$K_{10}Na$-**2.2** is thermodynamically unstable to hydrolysis and is consequently absent in the 40-day aged solution. As a consequence, at least three compounds form during aging of aqueous solutions of **2.1**.

As a result, the most likely decomposition of **2.1** can be roughly described by the following equations ($pK_a$ of [Co($H_2O$)]$^{2+}$ is around 10):[74,75]

$[\{Co_4(\mu\text{-}OH)(H_2O)_3\}(Si_2W_{19}O_{70})]^{11-} + K^+ + 9\ H_2O + H^+ \rightarrow [\{Co(H_2O)\}(\mu\text{-}H_2O)_2K\{Co(H_2O)_4\}(Si_2W_{18}O_{66})]^{11-} + 2\ [Co(H_2O)_6]^{2+} + WO_4^{2-}$ (2.3)

$[\{Co(H_2O)\}(\mu\text{-}H_2O)_2K\{Co(H_2O)_4\}(Si_2W_{18}O_{66})]^{11-} + 4\ WO_4^{2-} + 8\ H^+ \rightarrow 2\ [Co(H_2O)SiW_{11}O_{39}]^{6-} + K^+ + 10\ H_2O$ (2.4)

The overall reaction is eq 2.5:

$4[\{Co_4(\mu\text{-}OH)(H_2O)_3\}(Si_2W_{19}O_{70})]^{11-} + 3\ K^+ + 12\ H^+ + 50H_2O \rightarrow 3[\{Co(H_2O)\}(\mu\text{-}H_2O)_2K\{Co(H_2O)_4\}(Si_2W_{18}O_{66})]^{11-} + 2\ [Co(H_2O)SiW_{11}O_{39}]^{6-} + 8\ [Co(H_2O)_6]^{2+}$ (2.5)

### 2.3.7 Catalytic activity of aged solution of 2.1

Since **2.1** decomposes slowly in aqueous solution, the question arises: is it the actual water oxidation catalyst? In our previous paper we used 2,2'-bipyridine (bpy) as a poisoning agent to selectively inhibit the activity of $[Co(H_2O)_6]^{2+}$.[39] Addition of bpy to $[Co(H_2O)_6]^{2+}$ results in rapid formation of $[Co(bpy)_3]^{2+}$ which is catalytically inactive for water oxidation. However, addition of three equivalents of bpy per cobalt to a freshly prepared solution of **2.1** in water results in immediate precipitation. Slow evaporation of the filtrate in a vessel open to air results in formation of crystals. Preliminary X-ray studies show that these crystals contain $[Co(H_2O)SiW_{11}O_{39}]^{6-}$ with $[Co(bpy)_3]^{2+}$ as counterion(s). In contrast to $[Co_4(H_2O)_2(PW_9O_{34})_2]^{10-}$, bpy quickly removes Co centers from **2.1**, consistent with **2.1** being significantly less stable than $[Co_4(H_2O)_2(PW_9O_{34})_2]^{10-}$.

We meticulously studied the activity of aged stock solutions of **2.1** prepared in plain water, comparing with the activity of freshly prepared solutions of complexes **2.2** and **2.3**. After 3-4 weeks of aging, the TON is 20-30% lower than of freshly prepared solutions of **2.1**. Freshly prepared solutions of complex **2.2** are ca. 3 times less active and slower (Figure 2.12 A, $TOF_{ap}$ ~0.025 $s^{-1}$) than freshly prepared solutions of **2.1**. Complex **2.3** is inactive (Figure 2.12D).[39] Therefore, the overall decrease of catalytic activity of stock solutions of **2.1** with aging may be caused by the transformation to **2.2** and **2.3**. The generation of $[Co(H_2O)_6]^{2+}$ during the decomposition in aged stock solutions is also likely to contribute to the final observed catalytic activity. We can also observe from Figure 2.12B and C that the pure potassium salf of **2.2** ($K_{11}$-**2.2**) has a lower WOC activity than the mixed potassium and sodium salt $K_{10}Na$-**2.2**. A similar effect of alkali metal cation has also been shown in the kinetics of water oxidation catalyzed by $[Ru^{IV}{}_4O_4(OH)_2(OH_2)_4(\gamma\text{-}SiW_{10}O_{36})_2]^{12-}$, using $[Ru(bpy)_3]^{3+}$ as the oxidant (addtion of $K^+$ results in larger drop of $O_2$ yield than $Na^+$ or $Li^+$).[68]

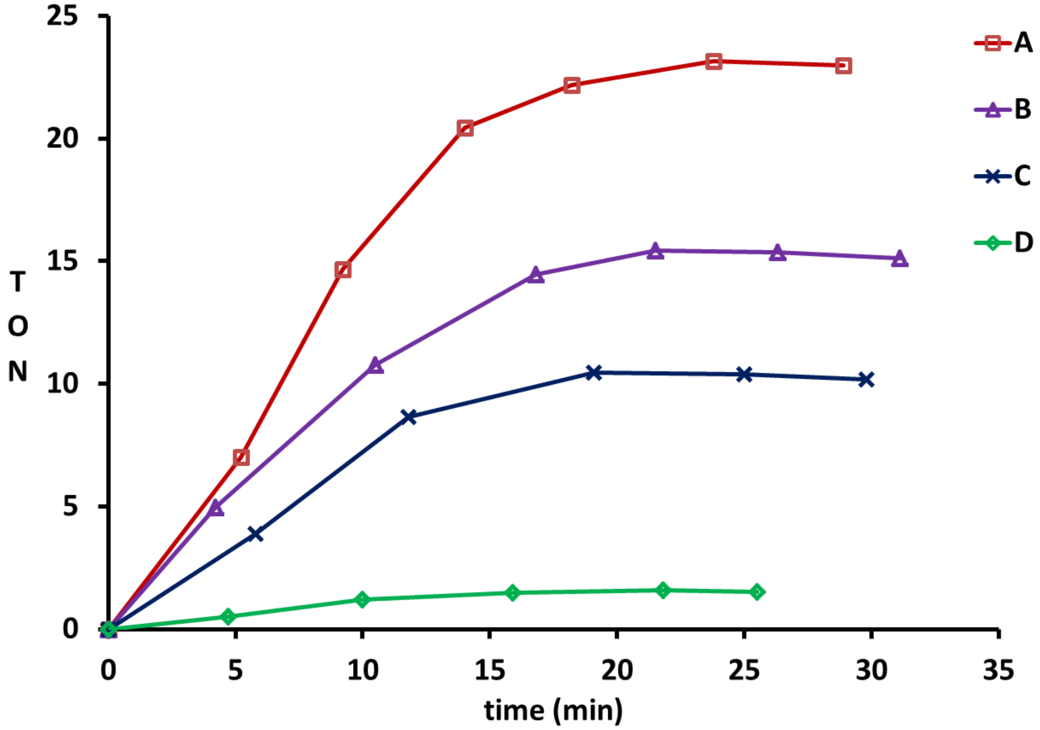

**Figure 2.12** Kinetics of catalytic light-induced $O_2$ formation from water by persulfate oxidation catalyzed by $K_{10}Na$-**2.2** (A), $K_{10}Na$-**2.2** + 17 mM of KCl (B), $K_{11}$-**2.2** (C) and **2.3** (D). Conditions: Xe lamp, 420-520 nm band-pass filter, 1.0 mM $[Ru(bpy)_3]Cl_2$, 5 mM $Na_2S_2O_8$, 25 mM buffer, 10.0 μM catalyst, total solution volume 8 mL.

Hence, the intact **2.1** could well be a water oxidation catalyst. This is indicated by the following findings: (i) the oxidation of water in the presence of **2.1** proceeds much faster than in the presence of its decomposition products (**2.2** and **2.3**); (ii) the overall activity of stock solutions of **2.1** decreases very slowly with aging time; (iii) **2.1** is stable on the time-scale of the light-driven water oxidation process (~ 30 min).

Under turnover conditions the cobalt(s) centres in **2.1** are briefly in a higher oxidation state(s) than 2+. The oxidized form of **2.1** might both be less stable and decompose faster than **2.1** (all Co(II) centres) itself. We cannot assign the catalytic activity to a specific isomer (**2.1a** or **2.1b**).

## 2.4 Conclusions

We have synthesized and characterized a new tetracobalt-substituted polyoxometalate which co-crystallizes as a 1:1 mixture of two isomers. While thermodynamically unstable, this POM is likely to catalyze water oxidation in a light-driven system with $[Ru(bpy)_3]^{2+}$ and $S_2O_8^{2-}$ as the photosensitizer and sacrificial electron acceptor, respectively. Several decomposition products of **2.1** in solution were isolated and characterized. Their catalytic activity towards water oxidation is lower than for **2.1**.

# *Chapter 3*

## Chapter 3 : Synthesis and Characterization of Di- and Tri-Cobalt Polyoxometalates and Their Application in Photocatalytic Water Oxidation

with Yurii V. Geletii, Jie Song, Chongchao Zhao, Elliot N. Glass, John Bacsa, and Craig L. Hill

(Reproduced in part with permission from *Inorganic Chemistry* 2013, **52,** 1018−1024.

**Abstract:** Di- and tri-cobalt silicotungstate complexes, $K_5Na_4H_4[\{Na_3(\mu\text{-}OH_2)_2Co_2(\mu\text{-}OH)_4\}(Si_2W_{18}O_{66})]\cdot 37H_2O$ (**3.1**) and $K_6Na_3[Na(H_2O)\{Co(H_2O)_3\}_2\{Co(H_2O)_2\}(Si_2W_{18}O_{66})]\cdot 22H_2O$ (**3.2**) have been synthesized through reaction of cobalt chloride and $[A\text{-}\alpha\text{-}SiW_9O_{34}]^{10-}$ in acidic buffer solution. They have been characterized by X-ray crystallography, elemental analysis, cyclic voltammetry, infrared, and UV-vis spectroscopy. In **3.1**, two cobalt atoms as well as three sodium atoms are incorporated in the central pocket of the $[Si_2W_{18}O_{66}]^{16-}$ polyanion. In **3.2**, one cobalt atom and one sodium atom are incorporated in the pocket of $[Si_2W_{18}O_{66}]^{16-}$; two other cobalt atoms in this complex protrude outside the pocket and connect with $WO_6$ units of other $[Si_2W_{18}O_{66}]^{16-}$ polyanions to form a one-dimensional polymeric structure. The crucial parameters in the synthesis of these two compounds are discussed. Both **3.1** and **3.2** can effectively catalyze water oxidation under the investigated conditions. Four lines of evidence show that neither complex forms measurable quantities of metal oxide decomposition products under the catalytic conditions. However, both **3.1** and **3.2** aren't stable in potassium acetate buffer (pH 4.8, 1 M) at elevated temperature, and decompose to $K_{11}[\{Co_2(H_2O)_8\}K(Si_2W_{18}O_{66})]\cdot 17H_2O$ (**3.3**) based on spectroscopic studies and an X-ray crystal structure.

## 3.1 Introduction

Transition-metal-substituted polyoxometalates (TMSPs) are a promising class of homogeneous WOCs because of their stability under oxidative conditions in certain pH ranges. The earth-abundant-element-containing TMSPs are especially important because of their low cost. Since the 2010 *Science* paper which reported that $[Co_4(H_2O)_2(\alpha\text{-}PW_9O_{34})_2]^{10-}$ (**$Co_4P_2$**)is a highly active WOC with turnover frequencies of 5 mol $s^{-1}$,[39] Several cobalt-POM WOCs have been developed, whose structural features are very different. These WOCs include two cobalt-containing polymolybdates, $[CoMo_6O_{24}H_6]^{3-}$,[76] $[Co_2Mo_{10}O_{38}H_4]^{6-}$,[76] the silicon analogue of **$Co_4P_2$**, $[Co_4(H_2O)_2(SiW_9O_{34})_2]^{12-}$,[2] $\{Co_9(H_2O)_6(OH)_3(HPO_4)_2(PW_9O_{34})_3\}^{16-}$,[77,78] and $[Co^{III}Co^{II}(H_2O)W_{11}O_{39}]^{7-}$. Theoretically, if the metal center contains multiple cobalt atoms, which could be helpful in the four-electron transfer process. However, some multi-cobalt-containing POMs show no WOC activity, such as the $Co_4$-Wells-Dawson analogue of **$Co_4P_2$**.[39] Therefore, exploring more cobalt-POMs with different structures and building up the structure-activity correlations are now important. This chapter reports two new cobalt-containing POM WOCs that involve the POM ligand, $[Si_2W_{18}O_{66}]^{16-}$. The latter forms from the dimerization of $[A\text{-}\alpha\text{-}SiW_9O_{34}]^{10-}$ under acidic conditions.

As we have discussed in Chapter 1, $[Si_2W_{18}O_{66}]^{16-}$ can accommodate multiple d-electron metal centers in the lacunary cavity, such as penta-copper and tetra-iron.[30,32] However, only mono-cobalt or di-cobalt atoms connected with potassium atoms have been successfully incorporated in its cavity.[5,79] In this chapter, we report the synthesis and structural characterization of novel di-cobalt and tri-cobalt POMs connected with sodium atoms based on the $[Si_2W_{18}O_{66}]^{16-}$ multi-defect unit, as well as their WOC activity.

## 3.2 Experimental

### General Methods and Materials

$K_{10}A$-α-$[SiW_9O_{34}]\cdot 13H_2O$ was prepared by the literature procedure,[5] and its purity was checked by IR spectroscopy. Except for tris(2,2'-bipyridyl) dichlororuthenium(II) hexahydrate, which was recrystallized using the literature procedure,[69] all other reagents were the highest quality available from commercial sources and used as received. Elemental analyses for K, Na, Co, Si, and W were performed by Galbraith Laboratories (Knoxville, Tennessee). IR spectra (2% samples in KBr pellet) were collected on a Nicolet™ 6700 FT-IR spectrometer. The electronic absorption spectra were obtained on an Agilent 8453 UV-vis spectrometer. Electrochemical data were obtained using a BAS CV-50W electrochemical analyzer at room temperature equipped with a glassy-carbon working, a Pt-wire auxiliary, and a Ag/AgCl (3 M NaCl) BAS reference electrodes. All redox potentials are reported relative to this reference electrode. Dynamic light scattering (DLS) measurements were made on a Zetasizer Nano ZS 90 instrument (Malvern Instruments Ltd., UK), which can measure particle sizes from 0.3 to 5000 nm (diameter).

## Syntheses

**$K_5Na_4H_4[\{Na_3(\mu\text{-}OH_2)_2Co_2(\mu\text{-}OH)_4\}(Si_2W_{18}O_{66})]\cdot 37H_2O$ (3.1).** $K_{10}[A$-α-$SiW_9O_{34}]\cdot 13H_2O$ (1 g, 0.32 mmol) was dissolved in 40 mL of 1 M sodium acetate (NaOAc) buffer (pH 4.8). To this solution, 210 mg (0.88 mmol) of $CoCl_2\cdot 6H_2O$ was added. The solution was heated to 85 °C for 1 h, cooled to room temperature, and then filtered through a fine frit. The filtrate afforded red needle crystals after 1 week of evaporation in air. Yield: 22% (based on W). IR (2 % in KBr, ν/cm$^{-1}$): 997 (m), 941 (m), 878 (s), 804 (m), 726 (s), 630 (m), 548 (w), 525 (w) cm$^{-1}$. Elemental analysis calcd (%) for **1**: K, 3.45; Na, 2.84; Co, 2.08; Si, 0.99; W, 58.4. Found (%): K, 3.44; Na, 2.94; Co, 1.64; Si, 1.16; W, 57.8.

**$K_6Na_3[Na(H_2O)\{Co(H_2O)_3\}_2\{Co(H_2O)_2\}(Si_2W_{18}O_{66})]\cdot 22H_2O$** (**3.2**): $K_{10}$[A-α-$SiW_9O_{34}$] ·$13H_2O$ (0.5 g, 0.16 mmol) was dissolved in 10 mL of 1 M NaOAc buffer (pH 4.8). To this solution, 105 mg (0.44 mmol) of $CoCl_2$ $6H_2O$ was added. The solution was heated to 85 ℃ for 1 h, cooled to room temperature, and then filtered through a fine frit. Pink needle crystals appeared after several hours of evaporation in air, and were collected after 24 h. Yield: 20 % (based on W). IR (2% in KBr, $\nu/cm^{-1}$): 996 (m), 944 (m), 887 (s), 835 (w), 802 (w), 730 (s), 615 (m), 554 (w), and 533(w) $cm^{-1}$. Elemental analysis calcd (%) for **3.2**: K, 4.28; Na, 1.68; Co, 3.22; Si, 1.02; W, 60.4. Found (%): K, 3.84; Na, 1.61; Co, 3.29; Si, 0.97; W, 58.1.

**$K_{11}[\{Co_2(H_2O)_8\}K(Si_2W_{18}O_{66})]\cdot 17H_2O$** (**3.3**): Complex **3.1** or **3.2** (300 mg) was dissolved in 12 mL of pH 4.8 KOAc/HOAc buffer (1 M) by heating. The solution was stirred for 1 hr at 80°C, cooled down to room temperature, and then filtered through a fine frit. Pink needle crystals can be obtained in a 20 mL beaker after one day or several days of slow evaporation, depending on the starting material used. Yield: 35 % (based on W). IR (2% in KBr, $\nu/cm^{-1}$): 996 (m), 943 (m), 884 (s), 862 (sh), 804 (m), 730 (s), 667 (m), 650 (m), 547 (w), and 525 (w) $cm^{-1}$. Elemental analysis calcd (%) for **3**: K, 8.60; Co, 2.16; Si, 1.03; W, 60.6. Found (%): K, 7.85; Co, 1.70; Si, 1.07; W, 58.0.

**X-ray Crystallography.** Single crystals of **3.1, 3.2** and **3.3** suitable for X-ray analysis were investigated using a Bruker D8 SMART APEX CCD sealed tube diffractometer. Diffraction intensities were measured using graphite monochromated Mo Kα radiation (λ = 0.71073 Å) at 173(2) K. Data collection, indexing and initial cell refinements were obtained by SMART.[63] Frame integration and final cell refinements were done using SAINT.[80] The molecular structure of each complex was determined using direct methods and refined by the standard full-matrix least-squares procedures. Face-indexing absorption correction was applied using the program SADABS.[65] Structure solution, refinement, graphic and generation of publication materials were performed by using SHELXTL-97/ Olex2.[81,82] Crystal data collection and refinement parameters are given in Table 3.1.

The purity of each sample was checked using powder diffraction (PXRD). PXRD experiments were performed using a Bruker D8 DIFFRAC powder diffractometer (Co K-alpha radiation) with a VANTECH detector in theta-theta mode. We found that grinding the samples resulted in poor diffraction, and that the microcrystalline material gave better diffraction. Theta-theta scans were performed in the 2θ ranges 8-90 degrees with a step width of 0.01 degrees and scan time of 1 s/step.

**Catalytic Experiments.** Water oxidation was performed in a cylindrical cuvette (NSG, 32G10) with OD = 2 cm and *l* = 1 cm with a total volume of ~ 2.8 mL. The cuvette was sealed with a rubber septum, filled with 2 mL of a solution containing 1.0 mM $[Ru(bpy)_3]Cl_2$, 5 mM $Na_2S_2O_8$, 80 mM sodium borate buffer solution and 6 μM catalyst. The vessel was carefully deaerated by purging with argon. A magnetically-coupled stirring system (SYS 114, SPECTROCELL) was placed on the back side of the cell, and the reaction solution was stirred during the entire process. The process was started by exposing the reaction vessel to a 455-nm LED light source (17 W) from Sandhouse Design. Two lenses were used to focus the light beam on the front window of the cuvette with OD ≈ 0.4-0.5 cm. The reaction was temporarily stopped by blocking the light to carry out the headspace gas analysis. A 0.10 mL sample was withdrawn from the headspace, and then 0.05 mL was injected into a gas chromatograph Agilent 7890A equipped with thermal conductivity detector and a GC capillary column with 5Å molecular sieves. Argon was used as the carrier gas. The amount of $N_2$ detected was used to correct for small air leaks over the course of the catalytic reactions.

**Kinetics of catalytic $[Ru(bpy)_3]^{3+}$ reduction.** A Hi-Tech Stopped Flow SF-61SX2 instrument equipped with a diode array detector operating in wavelength range 400-700 nm was used to study the kinetics of $[Ru(bpy)_3]^{3+}$ reduction catalyzed by **3.1, 3.2** and $Co(NO_3)_2$. $[Ru(bpy)_3](ClO_4)_3$ stock solution was placed in one of the feeding syringes, and a buffered solution of **3.1, 3.2** or $Co(NO_3)_2$ was in the second syringe. The consumption of $[Ru(bpy)_3]^{3+}$ was monitored by a decrease in absorbance at 670 nm ($\varepsilon_{670} = 4.2 \times 10^2$ $M^{-1}$ $cm^{-1}$) (optical path length $l$ = 10 mm). Each data set included 200 spectra collected with different timescales: from 0-0.4 s up to 0-20 s. The data were acquired using KinetAsyst™ 3.0 software and treated with Microsoft Excel.

## 3.3 Results and discussion

### 3.3.1 Structures

The polyanion units in both **3.1** and **3.2** consist of a $[Si_2W_{18}O_{66}]^{16-}$ framework which can be viewed as a fusion of two A-α-$[SiW_9O_{34}]^{10-}$ units through two W-O-W corner-shared junctions. This structure type was first described by Hervé et al.[79,83] Compound **3.1** has $C_2$ symmetry (Figure 3.1a). The two $Co^{2+}$ cations in **3.1** are localized in the central pocket. Each cobalt cation is coordinated to one half of the polyanion through a central oxygen atom shared with the $SiO_4$ tetrahedron and two oxygen atoms that bridge to tungsten. Three $Na^+$ cations are also incorporated in the central pocket. Two of the $Na^+$ cations (Na1 and Na3) are coordinated to each half of the polyanion in the same manner as the cobalt atoms, while Na2 sits in the center of the polyanion, connecting

**Table 3.1** Crystal Data and Structure Refinement for **3.1**, **3.2** and **3.3**).

| | **3.1** | **3.2** | **3.3** |
|---|---|---|---|
| Molecular formula | $Co_2H_{86}K_5$ $Na_4O_{109}$ $Si_2$ $W_{18}$ | $Co_3$ $H_{62}K_6$ $Na_4$ $O_{97}$ $Si_2$ $W_{18}$ | $Co_2H_{50}K_{12}O_{91}Si_2$ $W_{18}$ |
| Formula wt. / g mol$^{-1}$ | 5670.37 | 5483.25 | 5458.94 |
| Temperature / K | 173(2) | 173 (2) | 110(2) |
| Radiation (λ) / Å | 0.71073 | 0.71073 | 0.71073 |
| Crystal system | Triclinic | Monoclinic | Monoclinic |
| Space group | $P\bar{1}$ | $P2_1$/m | $P2_1/n$ |
| $a$ / Å | 12.846(5) | 13.3935(12) | 12.2891(3) |
| $b$ / Å | 18.671(7) | 16.1715(15) | 23.5596(5) |
| $c$ / Å | 20.889(7) | 20.3596(18) | 30.7185(7) |
| $\alpha$ / ° | 69.166(5) | 90.00 | 90.00 |
| $\beta$ / ° | 87.147(6) | 106.3640(10) | 95.8800(10) |
| $\gamma$ / ° | 81.561(6) | 90.00 | 90.00 |
| $V$ / Å$^3$ | 4632(3) | 4231.1(7) | 8847.0(4) |
| $Z$ | 2 | 2 | 4 |
| $\rho_{calcd}$ / g cm$^{-3}$ | 4.111 | 4.164 | 4.098 |
| $\mu$ / mm$^{-1}$ | 22.988 | 25.390 | 24.371 |
| $F$(000) | 4576 | 4635 | 9680.0 |
| Crystal size / mm$^3$ | 0.17 × 0.15 × 0.12 | 0.10 × 0.02 × 0.02 | 0.22 × 0.13 × 0.11 |
| Reflections collected | 94080 | 82692 | 160685 |
| Independent reflections | 28073 | 13265 | 28156 |
| Absorption correction | Numerical | Numerical | Numerical |
| Refinement method | Full-matrix least-squares on $F^2$ | Full-matrix least-squares on $F^2$ | Full-matrix least-squares on $F^2$ |
| Goodness-of-fit on $\|F\|^2$ | 1.043 | 1.016 | 1.085 |
| Final $R$ indices [$R > 2\sigma(I)$] | $R_1{}^a = 0.0524$, $wR_2{}^b = 0.1430$ | $R_1{}^a = 0.0487$, $wR_2{}^b = 0.1025$ | $R_1{}^a = 0.0482$, $wR_2{}^b = 0.1104$ |
| $R$ indices (all data) | $R_1{}^a = 0.0681$, $wR_2{}^b = 0.1520$ | $R_1{}^a = 0.0952$, $wR_2{}^b = 0.1212$ | $R_1{}^a = 0.0592$, $wR_2{}^b = 0.1154$ |
| Largest diff. peak and hole / e Å$^{-3}$ | 12.199 and –7.053 | 4.860 and –3.256 | 6.09 and –3.30 |

$^a R_1 = \Sigma||F_0| - |F_c|| / \Sigma|F_0|$; w$R_2 = \Sigma[w(F_0{}^2 - F_c{}^2)^2]/ \Sigma[w(F_0{}^2)^2]]^{1/2}$

other Na atoms, Co atoms and $[Si_2W_{18}O_{66}]^{16-}$ unit through bridging oxygens. Bond valence sum (BVS) calculations indicate that O38 and O39 are diprotonated, whereas other bridging oxo groups between cobalt atoms are all monoprotonated. In contrast to **3.1**, the complex $[Cu_5(OH)_4(H_2O)_2(A\text{-}\alpha\text{-}SiW_9O_{33})_2]^{10-}$ (Figure 1.9c) has a similar cluster fragment,[30] with $\{Cu_5(OH)_4(H_2O)_2\}^{6+}$ moiety instead of $\{Na_3(\mu\text{-}OH_2)_2Co_2(\mu\text{-}OH)_4\}^{3+}$ in the open Wells-Dawson framework.

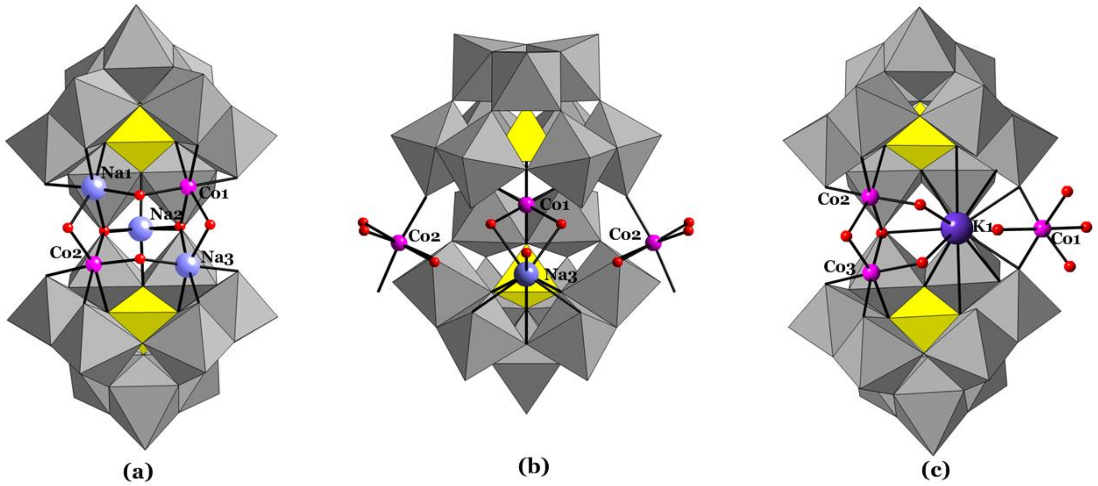

**Figure 3.1** Combined polyhedral/ball-and-stick representations of the polyanion units in **3.1** (a), **3.2** (b) and **3.3** (c). $WO_6$ units: grey polyhedra; $SiO_4$ units: yellow tetrahedra; Na: light blue spheres; Co: magenta spheres; O: red spheres.

In compound **3.2**, three Co(II) centers reside in the cavity of $[Si_2W_{18}O_{66}]^{16-}$ (Figure 3.1b). The W-O-W corner junction angles between the two $\{SiW_9\}$ units in **3.2** (142.6°) is larger than that in **3.1** (139.2°) (smaller dihedral angle defined by the two $\{SiW_9\}$ subunits). Na3 is located inside the pocket, bound to only one half of $[Si_2W_{18}O_{66}]^{16-}$ though five bridging oxygen atoms. It is also bound to the central cobalt through two oxygen atoms and to one terminal water ligand. All three cobalt atoms have at least two bonds to the $[Si_2W_{18}O_{66}]^{16-}$ framework. The central cobalt atom Co1 is bound to the two bridging oxygen atoms at the two {$SiW_9$} junctions and two central oxygen atoms of the central $SiO_4$ tetrahedron. The other two cobalt atoms (two Co2 atoms) are located outside the central pocket of $[Si_2W_{18}O_{66}]^{16-}$; they are bonded to one oxygen atom on each {$SiW_9$} subunit. A third Co-O-W' bond connects with another $[Si_2W_{18}O_{66}]^{16-}$ unit of **3.2** forming a zigzag-shaped one-dimensional chain (Figure 3.2a and 3.2b). A tricobalt POM in the literature, $[\{Co(H_2O)_2\}_3(SiW_9O_{34})_2]^{14-}$ (Figure 1.2d), has three Co(II) centers sandwiched between two separate {$SiW_9$} subunits.[5] The complex $[\{Mn(H_2O)\}K(\mu\text{-}H_2O)_2K\{Mn(H_2O)_4\}(Ge_2W_{18}O_{66})]^{10-}$ also has a chain structure, but with germanotungstate as the framework, and the chains are linked by potassium and manganese cations. [84]

Compound **3.3** (Figure 3.1c) has an almost identical structure to a literature compound $K_{11}[\{Co(H_2O)\}(\mu\text{-}H_2O)_2K\{M(H_2O)_4\}(Si_2W_{18}O_{66})]\cdot 36H_2O$ (**1Co2-K(B)**) but with better refinement of the X-ray crystal parameters.[79] It contains one potassium ion and two Co(II) in the cavity. Co1 is fully occupied, linking the two {$SiW_9$} units, while Co2 and Co3 are disordered (with a best refinement of 30% and 70% occupancies, respectively), leaning towards either {$SiW_9$} unit. Interestingly, the disorder of the two kinds of crystals is quite similar (the other study fixed the occupancies as 0.33 and 0.67).

Complexes **3.1**, **3.2 and 3.3** have been characterized by their IR spectra (Figure 3.3). The strong similarities between these compounds and $K_{16}\alpha\text{-}[Si_2W_{18}O_{66}]\cdot 25H_2O$ in the low-frequency IR region ($\nu < 1100$ $cm^{-1}$) strongly suggest that all of them contain the $[Si_2W_{18}O_{66}]^{16-}$ structural unit. Each complex displays subtle differences in the absorption frequencies of these bands.

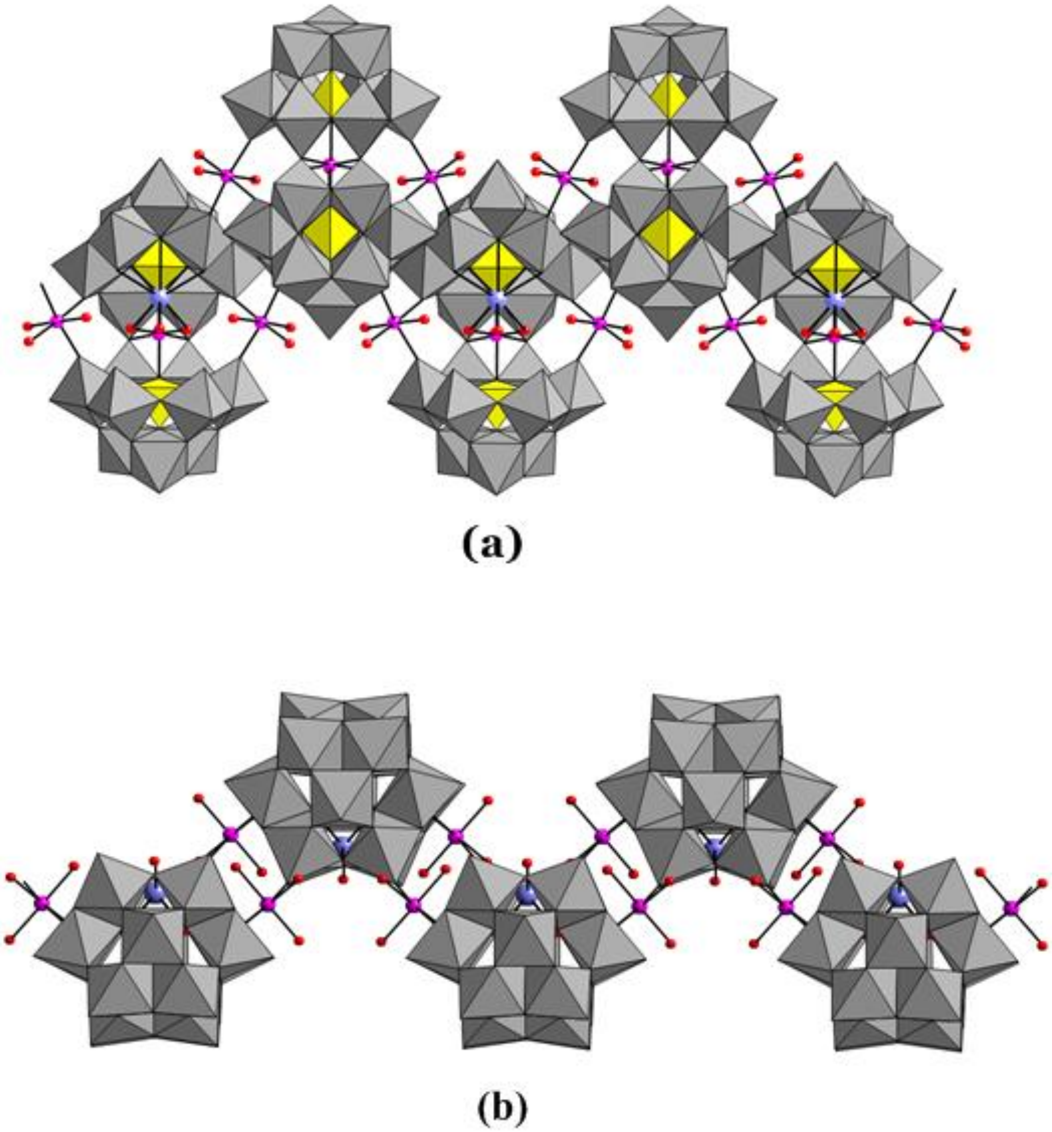

**Figure 3.2** Combined polyhedral/ball-and-stick representations of the one-dimensional chains of **3.2**; side view (a), top view (b). $WO_6$ units: grey polyhedra; $SiO_4$ units: yellow tetrahedra; Na: light blue spheres; Co: magenta spheres; O: red spheres.

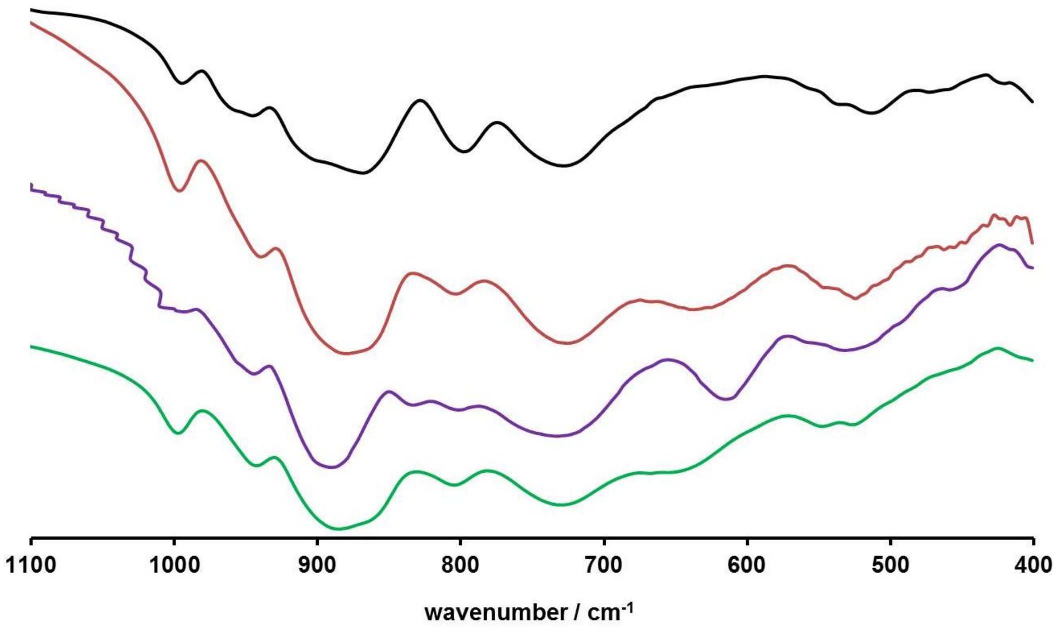

**Figure 3.3** IR spectra of $K_{16}\alpha$-$[Si_2W_{18}O_{66}]\cdot25H_2O$ (black), **3.1** (red), **3.2** (purple) and **3.3** (green).

### 3.3.2 Synthesis

The synthesis of these new multi-cobalt polytungstates, **3.1** and **3.2**, like other d-electron-metal-substituted POMs, depends on many factors, including pH, the counterions of the POMs, the temperature and the nature of the substituted metal center. We now address the latter three factors.

Factor 1: counterions. Complexes **3.1** and **3.2** were obtained using the same molar ratio of $CoCl_2\cdot6H_2O$ to $K_{10}A$-α-$[SiW_9O_{34}]$, but the reactant solutions had different initial concentrations. Different $K^+$ concentrations (from the POM precursor) dictate the formation of different products. The higher concentration of $K^+$ in the synthesis of **3.2** leads to its rapid crystallization (several hours), while a lower concentration of $K^+$ in the synthesis of **3.1** leads to slow crystallization (several days). The proper $K^+$ concentration is needed to keep both the open-mouthed $[Si_2W_{18}O_{66}]^{16-}$ structure present and control the specific location of cobalt atoms in both **3.1** and **3.2**. The ratio of $K^+$ to $Na^+$ is also important to the formation of different structures. In the literature study, it was concluded that the central $K^+$ bridging the two $\{SiW_9\}$ units defined the angle of the cavity and the locations of the transition metal cations in compounds $K_{13}[\{Co(H_2O)\}(\mu\text{-}H_2O)_2K(Si_2W_{18}O_{66})] \cdot 40H_2O$ and $K_{11}[\{Co(H_2O)\}(\mu\text{-}H_2O)_2K\{Co(H_2O)_4\}(Si_2W_{18}O_{66})] \cdot 36 H_2O$;[79] however, in **3.1** and **3.2**, the involvement of $Na^+$ leads to different arrangement of cobalt cations.

**Table 3.2** Summary of Synthetic Conditions for Cobalt Substituted Silicotungstates.

| Entry | Molar ratio of the TM cation to the precursor | T (℃) | Reaction system | Product | Ref |
|---|---|---|---|---|---|
| 1 | $Co^{2+}/K_{10}A\text{-}\alpha\text{-}[SiW_9O_{34}] = 2.8/1$ | 85 | HOAc/NaOAc buffer | **3.1 or 3.2** | This chapter |
| 2 | $Co^{2+}/K_{10}A\text{-}\alpha\text{-}[SiW_9O_{34}] = 1/1$ | R.T. | Aqueous solution | $K_{11}[\{Co(H_2O)\}(\mu\text{-}H_2O)_2K\{Co(H_2O)_4\}(Si_2W_{18}O_{66})] \cdot 25H_2O$ | [83,79] |
| 3 | $Co^{2+}/K_{10}A\text{-}\alpha\text{-}[SiW_9O_{34}] = 0.5/1$ | R.T. | Aqueous solution | $K_{13}[\{Co(H_2O)\}(\mu\text{-}H_2O)_2K(Si_2W_{18}O_{66})] \cdot 40H_2O$ | [79] |
| 4 | $Co^{2+}/Na_{10}A\text{-}\alpha\text{-}[SiW_9O_{34}] = 4.1/1$ | 40 | 1 M KOAc aqueous solution | $K_5Na_3[(A\text{-}\alpha\text{-}SiW_9O_{34})Co_4(OH)_3(CH_3COO)_3] \cdot 18H_2O$ | [85] |
| 5 | $Co^{2+}/Na_{10}A\text{-}\alpha\text{-}[SiW_9O_{34}] = 4.1/1$ | 40 | 1 M KOAc aqueous solution+sodium azide | $K_5Na_3[(A\text{-}\alpha\text{-}SiW_9O_{34})Co_4(OH)(N_3)_2(CH_3COO)_3] \cdot 18H_2O$ | [85] |
| 6 | $Co^{2+}/Na_{10}A\text{-}\alpha\text{-}[SiW_9O_{34}] = 4.1/1$ | R.T. | 0.5 M NaOAc aqueous solution, $CO_3^{2-}$ | $K_8Na_8[(A\text{-}\alpha\text{-}SiW_9O_{34})_2Co_8(OH)_6(H_2O)_2(CO_3)_3] \cdot 52H_2O$ | [85] |
| 7 | $Co^{2+}/Na_{10}A\text{-}\alpha\text{-}[SiW_9O_{34}] = 4.1/1$ | 80 | Aqueous solution | $K_{10.2}Na_{0.8}[\{Co_4(\mu\text{-}OH)(H_2O)_3\}(Si_2W_{19}O_{70})] \cdot 31H_2O$ | [86] |
| 8 | $Co^{2+}/K_{10}A\text{-}\alpha\text{-}[SiW_9O_{34}] = 1.5/1$ | R.T. | Aqueous solution | $K_{10.75}[Co(H_2O)_6]_{0.5}[Co(H_2O)_4Cl]_{0.25}A\text{-}\alpha\text{-}[K_2\{Co(H_2O)_2\}_3(SiW_9O_{34})_2] \cdot 32H_2O$ | [5] |
| 9 | $Co^{2+}/Na_9[\beta\text{-}SiW_9O_{34}H] =$ | 80 | HOAc/KAc buffer | $K_{10}[Co_4(H_2O)_2(B\text{-}\alpha\text{-}SiW_9O_{34}H)_2] \cdot 21H_2O$ | [59] |

| | | | | | |
|---|---|---|---|---|---|
| | 2.0/1 | | | | |
| 10 | $Co^{2+}$/α-$Na_{10}[SiW_9O_{34}] \cdot 15H_2O$ = 3.0/1 | 70 to 80 | Aqueous solution | $K_{11}Na_1[Co_4(H_2O)_2(SiW_9O_{34})_2] \cdot nH_2O$ | [2] |
| 11 | $Co^{2+}/K_8$[γ-$SiW_{10}O_{36}$] = 0.9/1 | 20 | pH 8.0, 1 M NaCl,bhep | $K_9Na_3[Co_3(H_2O)$(B-β-$SiW_9O_{34}$)(B-β-$SiW_8O_{29}(OH)_2)] \cdot 18H_2O$ | [22] |
| 12 | $Co^{2+}/K_8$[γ-$SiW_{10}O_{36}$] = 0.9/1 | 20 | pH 8.8, 1 M NaCl, bhep | $K_2Na_{12}$ $[Co_3(H_2O)$(B-α-$SiW_9O_{34}$)(B-β-$SiW_8O_{31})] \cdot 26H_2O$ | [22] |
| 13 | $Co^{2+}/K_8$[γ-$SiW_{10}O_{36}$] = 0.9/1 | 50 | pH 8.0, 1 M NaCl, bhep | $K_{15}Na_2[Co_9Cl_2(OH)_3(H_2O)_9$(B-β-$SiW_8O_{31})_3] \cdot 29H_2O$ | [22] |
| 14 | $Co^{2+}/K_8$[γ-$SiW_{10}O_{36}$] = 13.2/1 | 50 | NaCl aqueous solution | $Na_5[Co_6(H_2O)_{30}\{Co_9Cl_2(OH)_3(H_2O)_9$(β-$SiW_8O_{31})\}] \cdot 37H_2O$ | [25] |
| 15 | $Co^{2+}/K_8$[γ-$SiW_{10}O_{36}$] = 2.2/1 | 50 | HOAc/NaOAc buffer | $K_{10}Na_{12}[\{Co_3$(B-β-$SiW_9O_{33}(OH)$(B-β-$SiW_8O_{29}(OH)_2)\}_2] \cdot 49H_2O$ | [21] |
| 16 | $Co^{2+}/K_8$[γ-$SiW_{10}O_{36}$] = 2.1/1 | R.T. | $AcO^-$ | $K_{20}[\{$B-β-$SiW_9O_{33}(OH)$)(β-$SiW_8O_{29}(OH)_2)Co_3(H_2O)\}_2Co(H_2O)_2] \cdot 47 H_2O$ | [85] |
| 17 | $Co^{2+}/K_8$[γ-$SiW_{10}O_{36}$] = 2.1/1 | R.T. | Cyanate | $K_7[Co_{1.5}(H_2O)_7)]$[(γ-$SiW_{10}O_{36}$)(β-$SiW_8O_{30}(OH))Co_4(OH)(H_2O)_7] \cdot 36H_2O$ | [85] |
| 18 | $Co^{2+}/(K_8$[β-$SiW_{11}O_{39}$]+ $K_8$[γ-$SiW_{10}O_{36}$]) = 5.7/1 | boil | Aqueous solution, $NaN_3$ | $K_4Na_6Co_2(H_2O)_{12}\{Co(H_2O)_4[Co_2(H_2O)_{10}$ $Co_4(H_2O)_2$(B-α-$SiW_9O_{34})_2]_2\} \cdot 40H_2O$ | [87] |
| 19 | $Co^{2+}/K_8$[γ-$SiW_{10}O_{36}$] = 1.1/1 | 50 | Aqueous solution | $K_{10}[Co(H_2O)_2$(γ-$SiW_{10}O_{35})_2] \cdot 8.25H_2O$ | [20] |
| 20 | $Co^{2+}/K_8$[γ-$SiW_{10}O_{36}$] = 2.7/1 | 45 | Imidazole, pH 3.6 | $(HIm)_8[\{K(H_2O)\}_2\{(\mu_3$-$H_2O)Co(H_2O)\}(Si_2W_{20}O_{70})] \cdot 9H_2O$[a] | [19] |
| 21 | $Co^{2+}/H_3SiW_{12}O_{40} \cdot nH_2O$ = 1.1/1 | boil | Aqueous solution | $K_6[Co(H_2O)SiW_{11}O_{39}]$ | [72] |
| 22 | $Co^{2+}/H_3SiW_{12}O_{40} \cdot nH_2O$ = 1.1/1 | 80 or R.T. | Oxidizing $K_6[Co(H_2O)SiW_{11}O_{39}]$ by $Na_2S_2O_8$ at high temperature or electrolysis at R.T. | $Cs_5[Co(H_2O)SiW_{11}O_{39}]$ / $(CN_8H_6)_5[Co(H_2O)SiW_{11}O_{39}]$ | [72] |

Factor 2: temperature. Lowering the temperature of the reaction medium from 85 ℃ to 80 ℃ leads to the formation of **3.2** under either set of synthetic conditions.

Factor 3: the nature of the transition metal. The number of transition metal(s) incorporated into the framework is highly dependent on the nature of the transition metal. When replacing the $Co^{(II)}$ centers in **3.1** and **3.2** with $Ni^{(II)}$, only powders were obtained. When $Cu^{(II)}$ is used as the starting material, the $C_{2v}$ symmetry penta-copper polytungstate, $[Cu_5(OH)_4(H_2O)_2(A\text{-}\alpha\text{-}SiW_9O_{33})_2]^{10-}$ in Figure 1.9c is obtained. In this paper, slight variations in reaction conditions, and with $Co^{(II)}$ precursor in excess, lead to two or three cobalt atoms (**3.1** or **3.2**) being incorporated into the framework. Table 3.2 summarizes the synthetic conditions, related products, and transformations between different cobalt-substituted silicotungstates in literature studies as well as this work. As evident from the table, the fused dimeric lacunary $[Si_2W_{18}O_{66}]^{16-}$ structures are more easily maintained by using the potassium salt of $[SiW_9O_{34}]^{10-}$ or excess KCl added before the crystallization process under acidic conditions (entries 1-3),[79] while the reconstituted (substituted plenary) Keggin structures and sandwich structures are more often obtained by using the sodium salt of $\alpha\text{-}[SiW_9O_{34}]^{10-}$ or $\beta\text{-}[SiW_9O_{34}]^{10-}$ (entries 4-10).[2,5,59,85,86] Using $K_8[\gamma\text{-}SiW_{10}O_{36}]$ as a precursor can produce a variety of cobalt-substituted lacunary silicotungstates, which are formed by losing one or two tungsten atoms from $K_8[\gamma\text{-}SiW_{10}O_{36}]$ in acidic or basic conditions (entries 11-18).[21,22,25,87] These structures are minimally predictable using this synthetic protocol. Interestingly, $K_8[\gamma\text{-}SiW_{10}O_{36}]$ can also form a dimeric structure via two W-O-W bridges under acidic conditions (entries 19 and 20).[19,20] The presence of carboxylato, azido, carbonato, cyanato ligands[85] and the buffer bhep[*N*,*N*'-bis(2-hydroxylethyl)piperazine][22] can facilitate the isolation of some unusual POM structures (entries 5-7, 11-13). Mono-cobalt substituted silicotungstates are synthesized by using plenary (parent structure) 12-tungstosilicic acid (entry 21, 22).[72]

### 3.3.3 Electrochemistry

The cyclic voltammetry (CV) of **3.1** and **3.2** was recorded in sodium acetate buffer solutions (0.02 M NaOAc/HOAc with 0.38 M $NaNO_3$, or in 0.4 M NaOAc/HOAc, pH 4.8). No oxidation /reduction processes at the metal Co centers are observed at the glassy carbon electrode in either positive or negative potential domains, but the reduction of W centers is readily seen and is well defined (Figure 3.4). In 0.02 M NaOAc/HOAc buffer solution, the cathodic peak potentials of **3.1** are at - 0.73, - 0.93 V vs Ag/AgCl (3 M NaCl), and those of **3.2** are at - 0.72 and - 0.86 V (Figure 3.4 top). The CVs are more reversible in 0.02 M NaOAc/HOAc with 0.38 M $NaNO_3$ than in 0.4 M NaOAc/HOAc buffer (Figure 3.4 bottom).

The CVs of 1 mM **3.1** and **3.2** were also recorded in pH 9 sodium borate buffer. When the applied potential is higher than 1.0 V, a film (with uncharacterized structure) is formed on the glassy carbon anode. This film is catalytically active in water oxidation at E > 1.0V, in the same manner as the cobalt oxide film generated *in situ* from $[Co_4(H_2O)_2(PW_9O_{34})_2]^{10-}$ (**$Co_4P_2$**) studied by Stracke & Finke.[88]

### 3.3.4 Catalytic Activity in Water Oxidation

The ability of **3.1** and **3.2** to catalyze water oxidation was studied using the photo-driven system comprising $S_2O_8^{2-}$ as a sacrificial electron acceptor, and $[Ru(bpy)_3]^{2+}$ as a photosensitizer, which is the same system as used in Chapter 2.[38,67-70,86,89] Oxygen quickly forms under visible light illumination (455 nm) at pH 9 in borate buffer in the presence of **3.1** or **3.2**, with yields comparable with that of the **$Co_4P_2$** (Figure 3.5). The total turnover number, TON = $n(O_2)/n(cat)$ is up to 50 for 6 μM of **3.1** and 110 for 6 μM

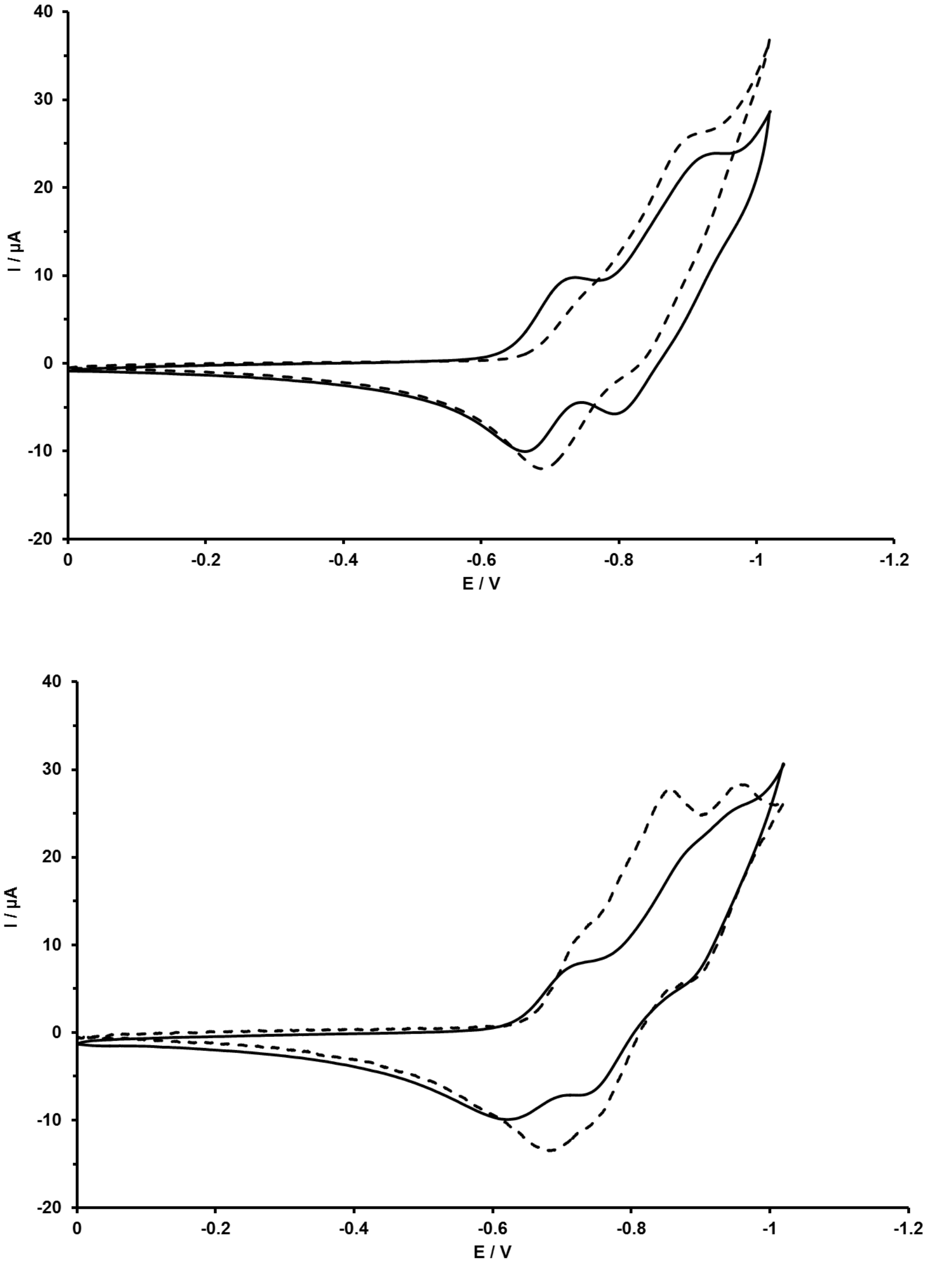

**Figure 3.4** Top: CV of 1 mM **3.1** (solid line) and **3.2** (dashed line) obtained in the solution of 0.02 M pH 4.8 NaOAc / HOAc buffer with 0.38 M $NaNO_3$, scan rate 25 mV

$s^{-1}$. Bottom: CV of 1 mM **3.1** (solid line) and **3.2** (dashed line) obtained in 0.4 M NaOAc/HOAc buffer at pH 4.8, scan rate 25 mV $s^{-1}$.

of **3.2** (corrected for control), compared to the TON = 170 for **$Co_4P_2$**. The oxygen yield based on $S_2O_8^{2-}$ (eq 2.2), is *ca.* 10% for **3.1** and 25% for **3.2** compared to 40% for **$Co_4P_2$**. The data for 4 µM catalysts are also shown in Figure 3.5. Chemical yield decreases at lower catalyst concentrations. The photodegradation of $[Ru(bpy)_3]^{2+}$ was inhibited in the presence of **3.1** or **3.2** (Figure 3.6), similar to other WOC POMs.[76]

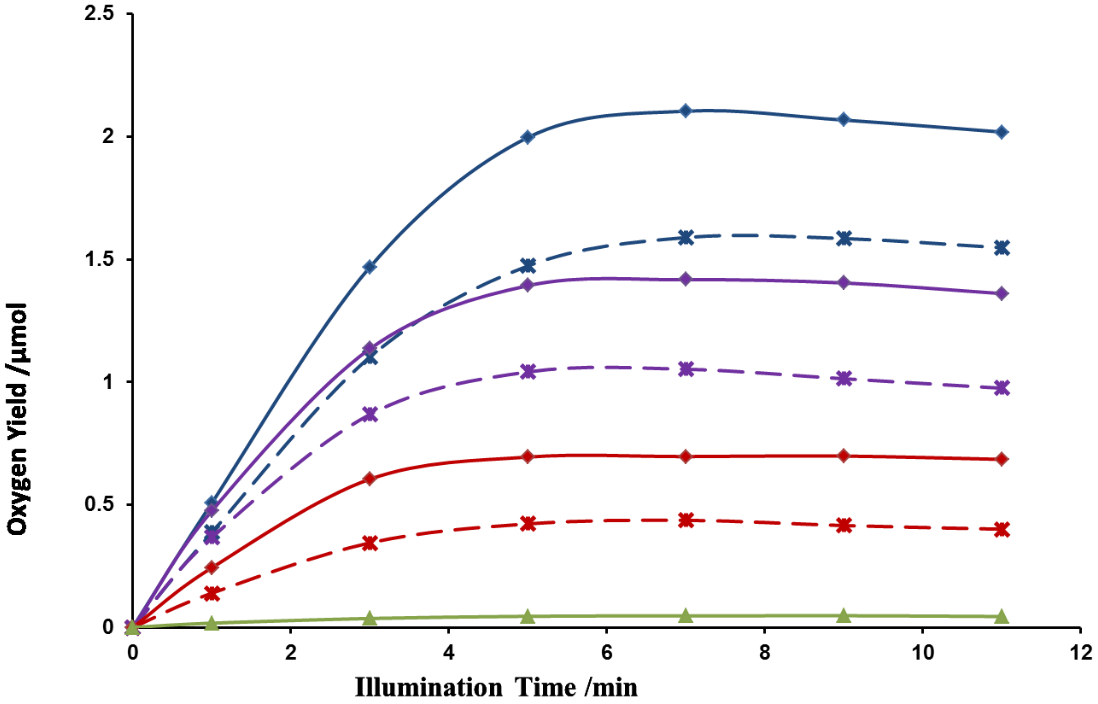

**Figure 3.5** Oxygen yield in the light-driven reaction catalyzed by 6 µM **3.1** ((solid red curve), 6 µM **3.2** (solid purple curve), 6 µM **$Co_4P_2$** (solid blue curve), 4 µM **3.1** ((dashed red curve), 4 µM **3.2** (dashed purple curve), 4 µM **$Co_4P_2$** (dashed blue curve), and without catalyst (solid green curve) as a function of illumination time. LED light source

(455 nm, 17mW), 80 mM sodium borate buffer with initial pH 9, 1.0 mM $[Ru(bpy)_3]Cl_2$, 5 mM $Na_2S_2O_8$, total volume 2.0 mL, reaction solution volume 2 mL, 25 ℃.

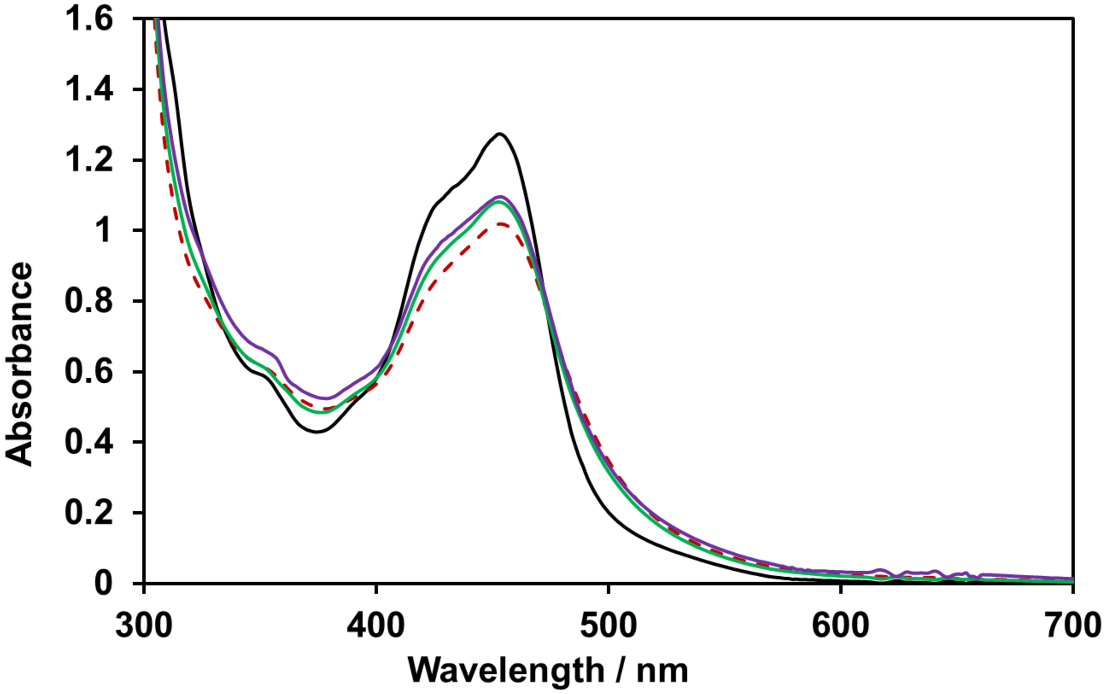

**Figure 3.6** UV-vis spectra of 10-fold diluted solution of 1 mM $[Ru(bpy)_3]^{2+}$ and 5.0 mM $Na_2S_2O_8$ in 80 mM borate buffer before the photodriven catalytic water oxidation reaction (black line), after this reaction (after irradiation) in the absence (red dotted line) and presence of 6 μM **3.1** (purple line) or in the presence of 6 μM **3.2** (green line). $l = 1$ cm.

### 3.3.5 Stability Studies

The concern about whether an initial soluble complex is the actual catalyst (or immediate catalyst precursor, i.e. the system involves homogeneous catalysts), or this initial complex is solely a precursor for an insoluble material (particles or film) that is the actual catalyst is an issue that has been addressed by Crabtree and others for many years.[88,90-93] Also given the fact that under some conditions POM WOCs do indeed convert to metal oxides but under other conditions the opposite happens (metal oxide converts to POMs), this catalyst versus catalyst precursor issue is relevant to water oxidation catalyzed by **3.1** and **3.2**. Here we study the stability of **3.1** and **3.2** both in simple aqueous solution and under catalytic water oxidation conditions.

### 3.3.5.1 Stability in water or buffer solutions

The natural pH of 3 mM **3.1** in water is 8.3, while the natural pH of 3 mM **3.2** is 6.3. In water, these complexes have a very low absorbance in the range 450-700 nm. Acid/base titration shows reversible behavior (based on several successive titrations in both pH directions) involving 6 protons/(hydroxyl anions) in the pH region of 3.0 ~ 8.9 for both **3.1** and **3.2** (Figure 3.7). As a consequence of having this many $pK_a$ values in close proximity, the titration curves are nearly featureless (no marked inflection points). The UV-vis spectra of both **3.1** and **3.2** obtained during acid/base titration show significant but also reversible changes in accordance with the pH changes in the region of 3.0 ~ 8.9 (Figures 3.8, 3.9, 3.10 and 3.11). The changes in spectral shape are significant at pH values around their natural pH, which likely reflects protonation/deprotonation of oxygens in the cobalt cores.[94] Both compounds are also relatively stable in NaOAc/HOAc buffer (80 mM, pH 4.8) and in pH 9 sodium borate buffer. The overnight changes in absorbance are less than 9% for **3.1** (7 mM), less than 2% for **3.2** (7.5 mM) in sodium acetate buffer (Figure 3.12 & 3.13), and less than 2% for both **3.1** and **3.2** in pH 9 borate buffer (Figure 3.14 & 3.15). No particle formation is observed after aging µM level solutions of **3.1** and **3.2** in 80 mM borate buffer at pH 9 for one month by Dynamic Light Scattering (DLS).

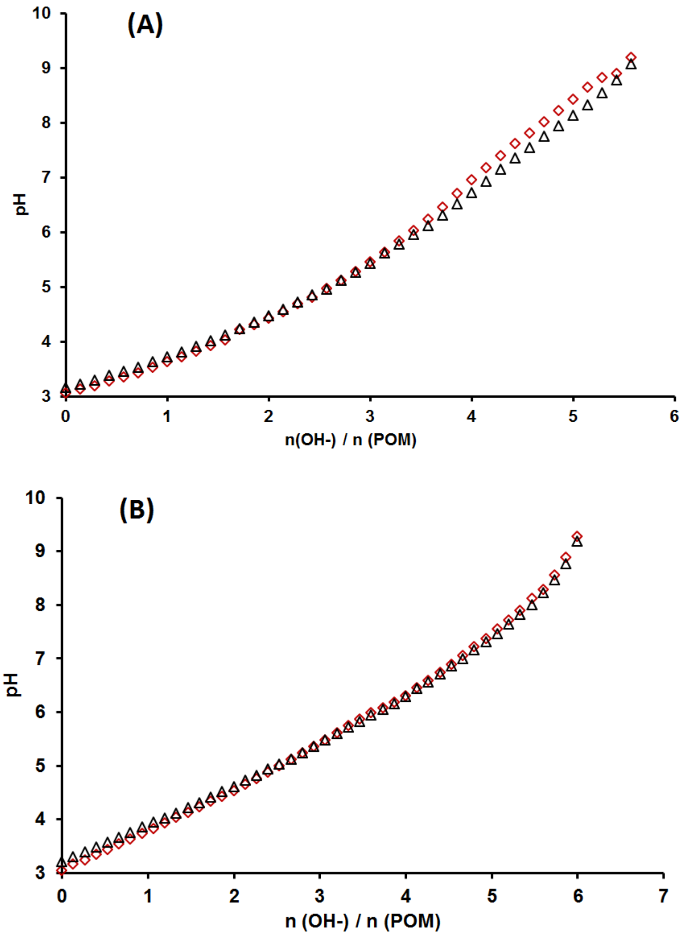

**Figure 3.7** Acid/base titration of an acidified 3 mM solution of **3.1** (A) and **3.2** (B) with 0.1 M NaOH solution (red squares) and 0.1 M HCl solution (black triangles). Five equivalents of 0.1 M HCl were added to acidify aqueous solution of **3.1** from the natural pH 8.3 to pH 3, and 4 equivalents of 0.1 M HCl were added to acidify aqueous solution of **3.2** from the natural pH 6.3 to pH 3. Titrations of both complexes were done repeatedly in both directions establishing that the protonation/deprotonation processes were reversible (only one reversible titration is shown here). No irreversible reactions were seen. Data have been corrected for dilution factor.

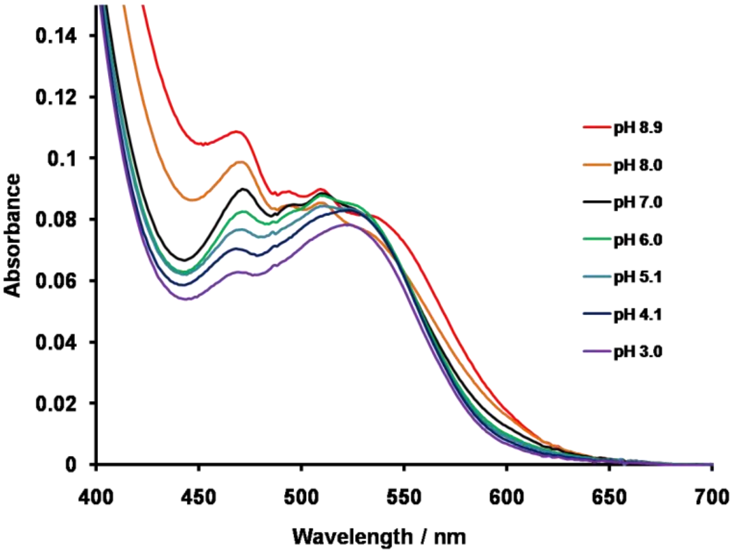

**Figure 3.8** Electronic absorption spectra obtained during acid/base titration of 3 mM **3.1** (dilution-corrected). *l* = 1 cm.

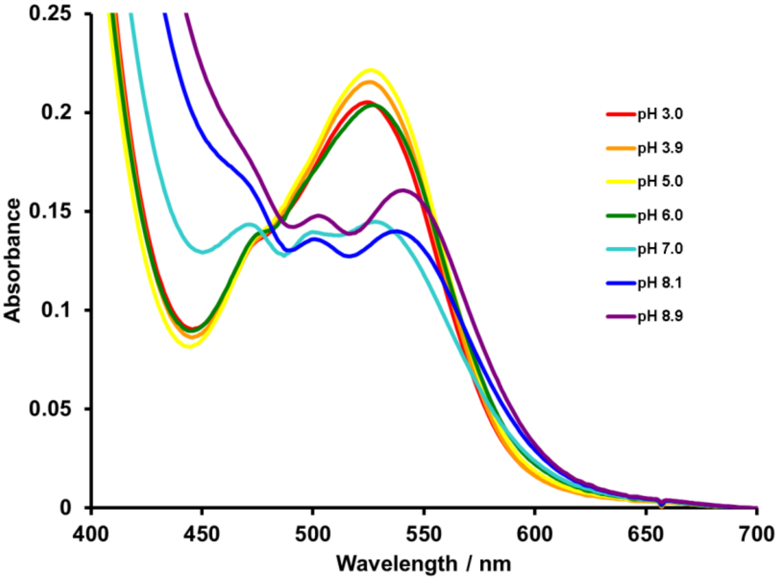

**Figure 3.9** Electronic absorption spectra obtained during acid/base titration of 3 mM **3.2** (dilution-corrected). *l* = 1 cm.

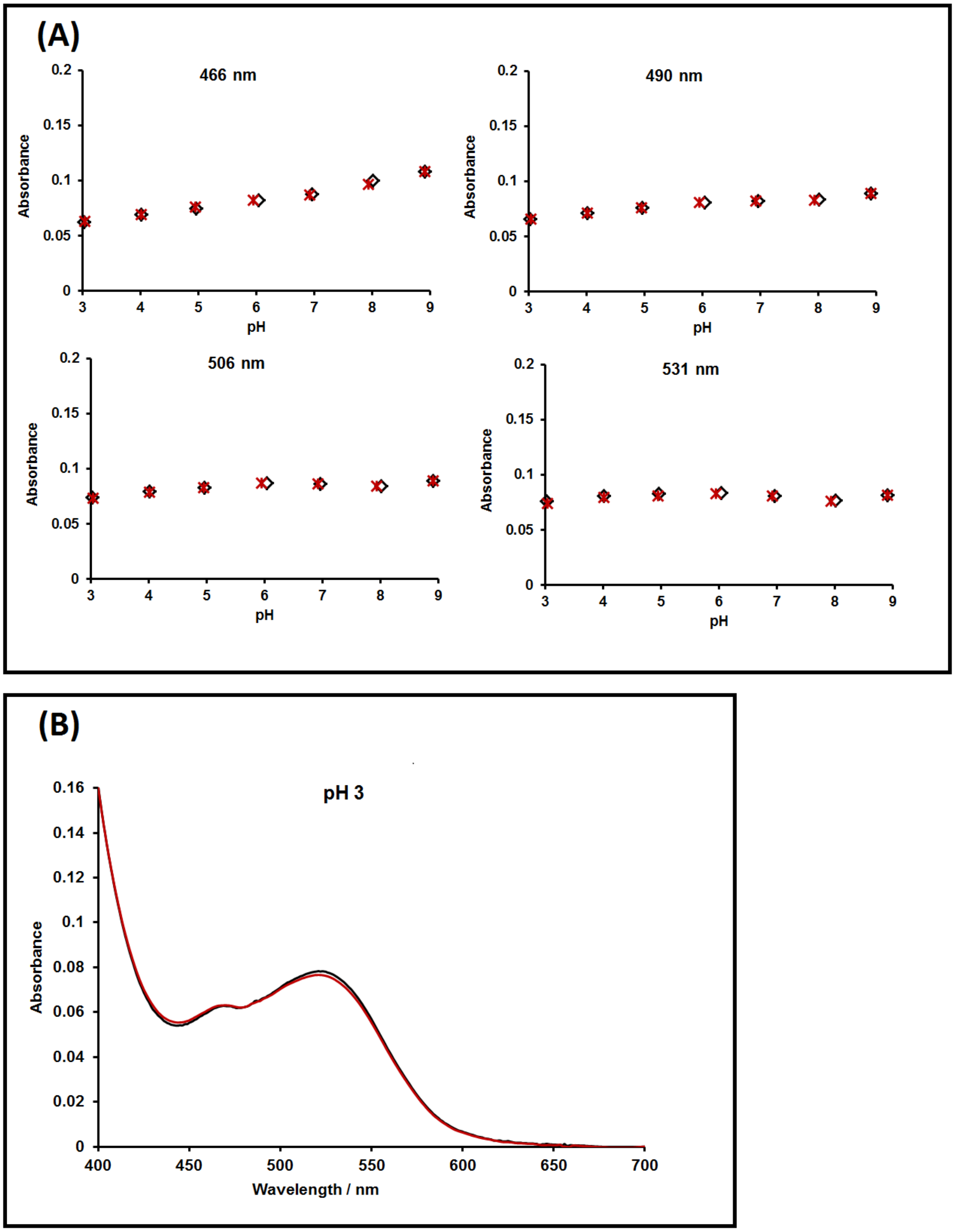

**Figure 3.10** (A) Absorbance changes at four different wavelengths during the acid/base titration of an acidified 3 mM solution of **3.1** with 0.1 M NaOH solution (black diamond) and 0.1 M HCl solution (red star), showing almost no change in the spectrum during the acid/base titration at the same pH values. (B) An example of overlay of the UV-vis spectra before (black curve) and after (red curve) acid/base titration at pH 3. *l* = 1 cm.

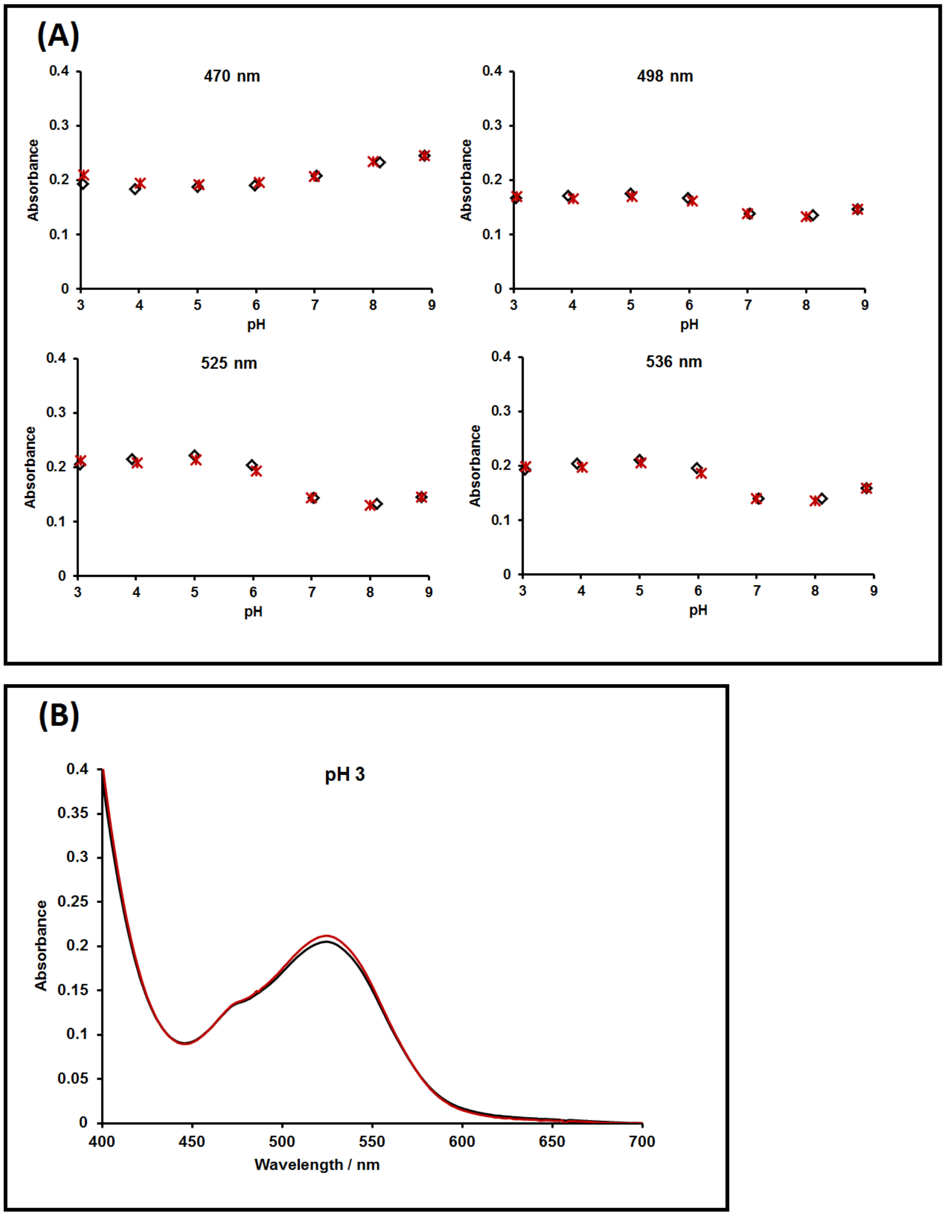

**Figure 3.11** (A) Absorbance changes at four different wavelengths during the acid/base titration of an acidified 3 mM solution of **3.2** with 0.1 M NaOH solution (black diamond) and 0.1 M HCl solution (red star), showing almost no change in the spectrum during the acid/base titration at the same pH values. (B) An example of overlay of the UV-vis spectra before (black curve) and after (red curve) acid/base titration at pH 3. $l = 1$ cm.

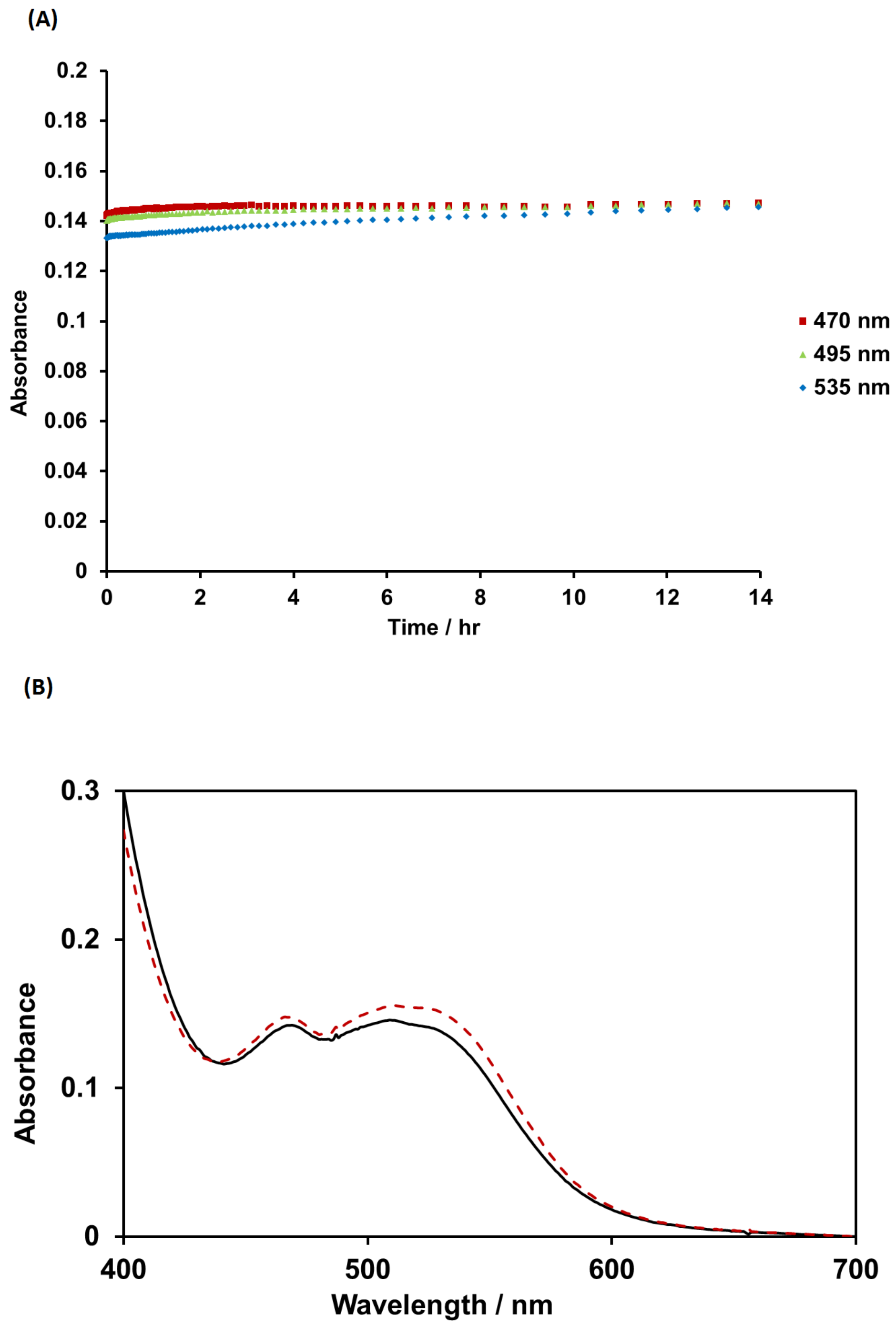

**Figure 3.12** Kinetic traces of local maxima in the UV-vis spectrum of 7 mM **3.1** in 80 mM pH 4.8 sodium acetate buffer, and (B) UV-vis spectrum of this solution at 0 hr (black solid line) and 14 hr (red dotted line). *l* = 1 cm.

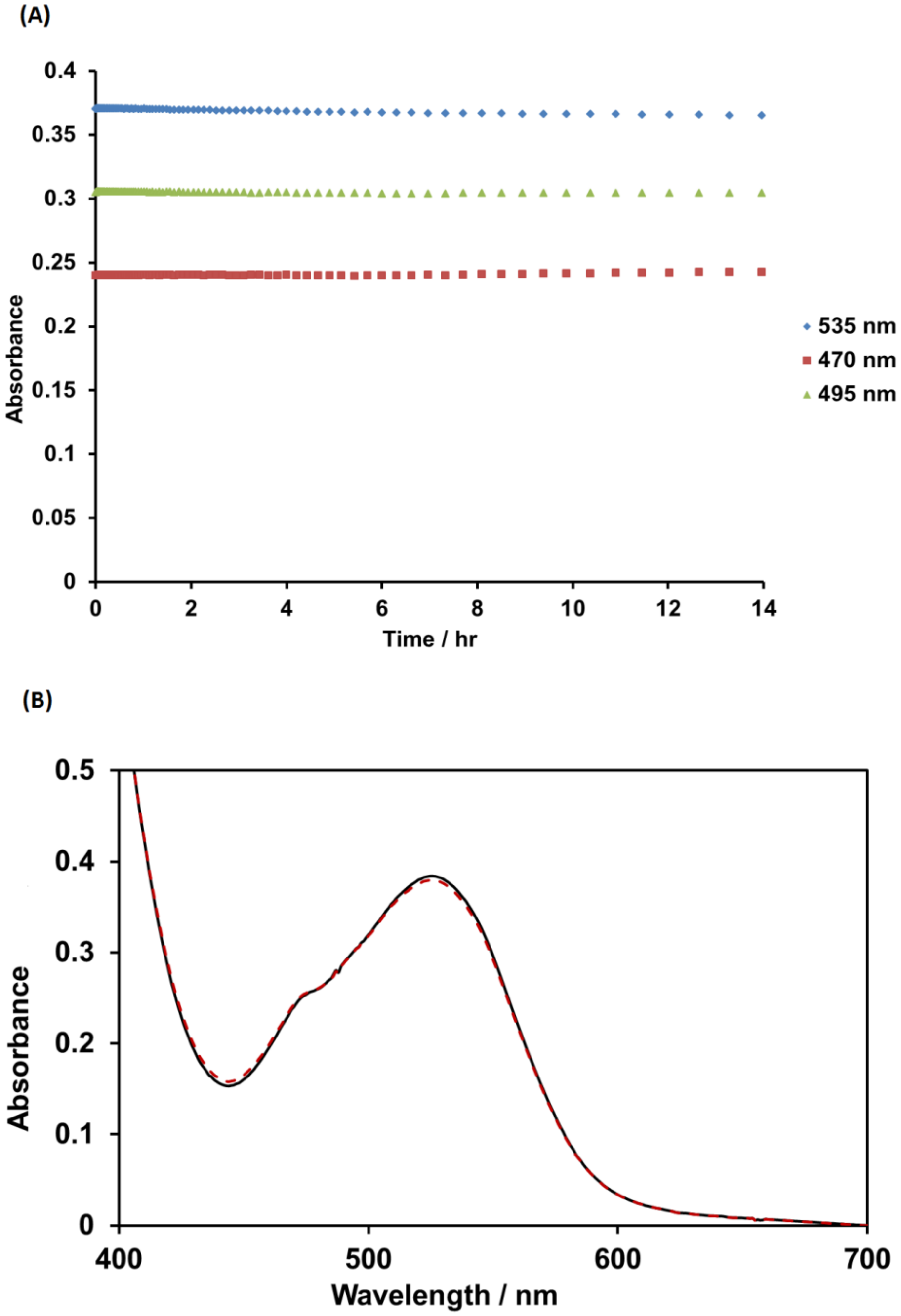

**Figure 3.13** (A) Kinetic traces of local maxima in the UV-vis spectrum of 7.5 mM **3.2** in 80 mM pH 4.8 sodium acetate buffer, and (B) UV-vis spectrum of this solution at 0 hr (black solid line) and 14 hr (red dotted line). *l* = 1 cm.

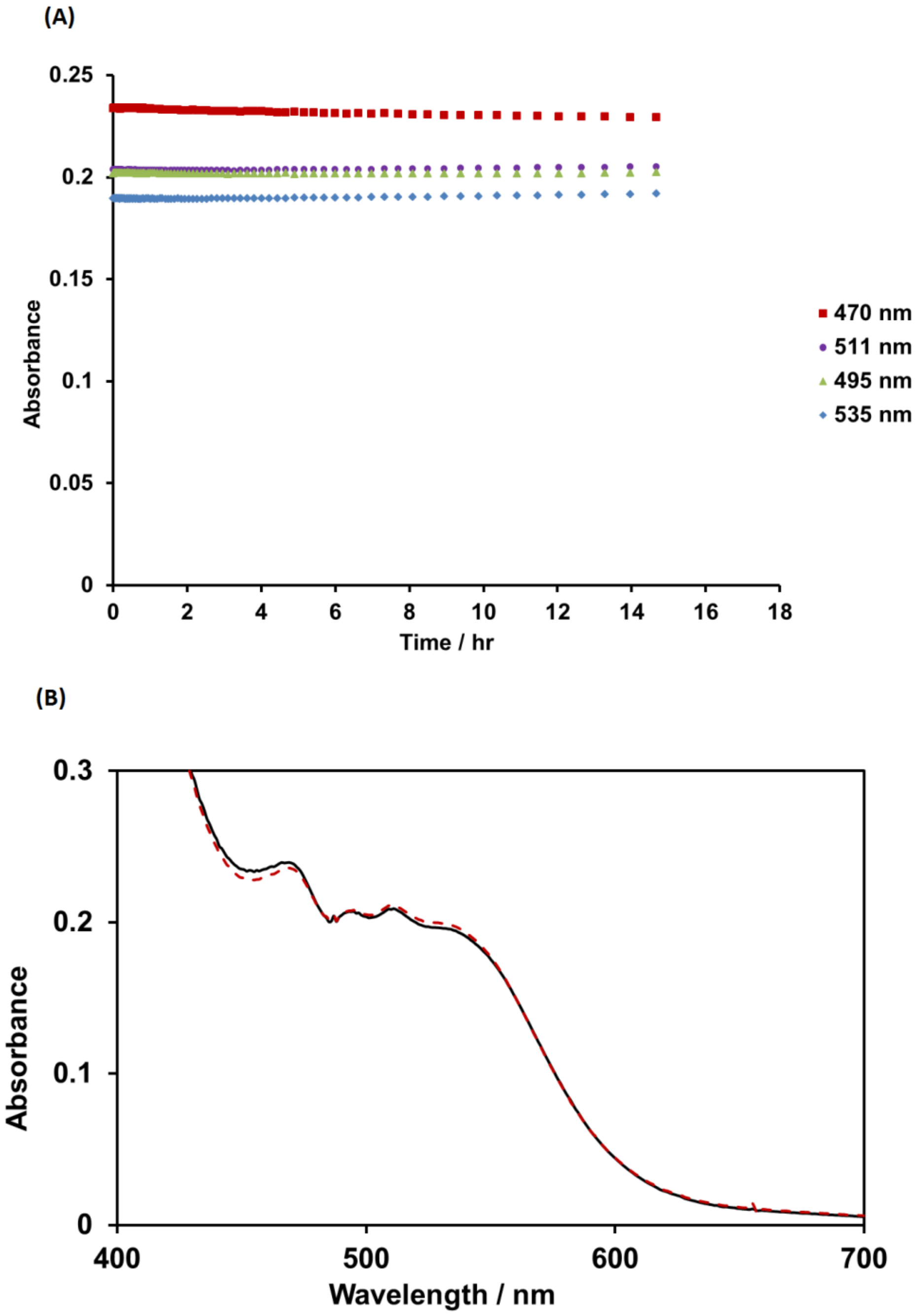

**Figure 3.14** (A) Kinetic traces of local maxima of UV-vis spectrum of 7 mM **3.1** in 80 mM pH 9 sodium borate buffer, and (B) UV-vis spectrum of this solution at 0 hr (black solid line) and 16 hr (red dotted line). $l$ = 1 cm.

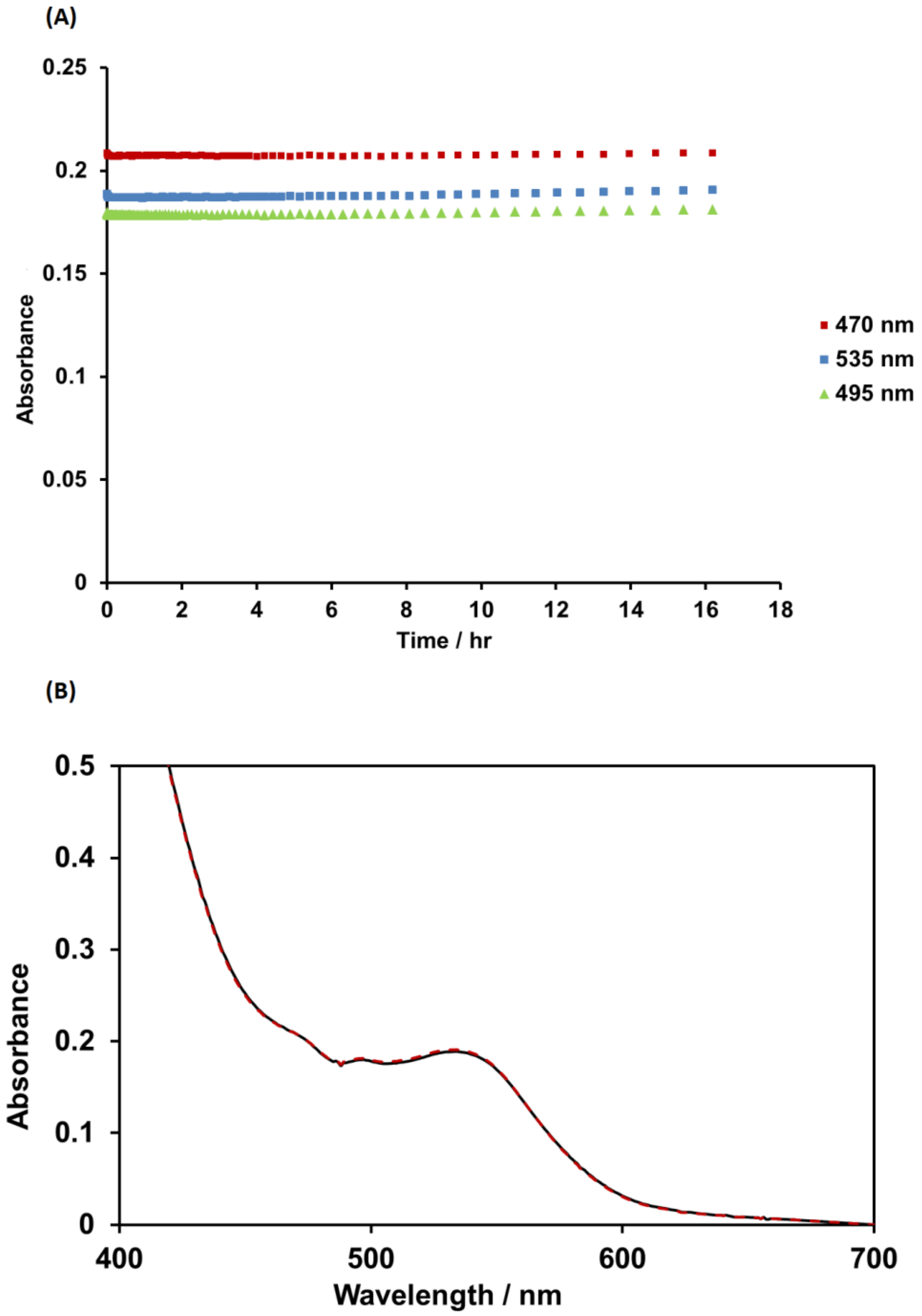

**Figure 3.15** (A) Kinetic traces of local maxima in the UV-vis spectrum of 4.5 mM **3.2** in 80 mM pH 9 sodium borate buffer, and (B) UV-vis spectrum of this solution at 0 hr (black solid line) and 16 hr (red dotted line). *l* = 1 cm.

The stability of **3.1**, **3.2** and the literature compounds $K_{13}[\{Co(H_2O)\}(\mu\text{-}H_2O)_2K(Si_2W_{18}O_{66})] \cdot 40H_2O$,[79] $K_{11}[\{Co(H_2O)\}(\mu\text{-}H_2O)_2K\{M(H_2O)_4\}(Si_2W_{18}O_{66})] \cdot 36 H_2O$ [79] and $K_{10.2}Na_{0.8}[\{Co_4(\mu\text{-}OH)(H_2O)_3\}(Si_2W_{19}O_{70})] \cdot 31H_2O$ [86] at high temperature (80 $^oC$) conditions were investigated. Heating 5 mM solutions of each of these five compounds in deionized water, pH 4.8 NaOAc buffer (1 M), NaCl (1 M) or KCl (1 M) lead, in all cases, to powders after slow evaporation of water. However, needle-like pink crystals were obtained from all five compounds when pH 4.8 KOAc buffer was used as the solvent (1 M). Interestingly, X-ray crystallographic analysis and IR spectra indicate that the resulting pink crystals from all 5 compounds have only one structure, that of compound **3.3**. These results indicate again that in particular pH ranges and at high $K^+$ concentrations, compound **3.3** is the most stable POM.

#### 3.3.5.2 Stability under catalytic water oxidation conditions

Three lines of evidence showing **3.1** and **3.2** are stable under catalytic water oxidation conditions.

First, the reproducible initial kinetics (no induction periods) of oxygen generation (Figure 3.5) argue that the complexes themselves, and not subsequently-formed "$Co^{2+}$ (aq)", are the active catalysts. Significantly, when $Co^{2+}$ (aq) (in the form of $Co(NO_3)_2$) is used as the catalyst in the same system, induction periods are always observed.[96]

Second, no induction period was observed in the $[Ru(bpy)_3]^{3+}$ reduction stopped-flow experiment (eqs 3.1 & 3.2), consistent with no formation of $Co^{2+}$(aq) during the catalytic process. Figure 3.16 shows that the addition of catalyst (**3.1**or **3.2**) or $Co(NO_3)_2$, significantly increases the rate of $[Ru(bpy)_3]^{3+}$ reduction. The comparison of kinetic curves shows that at least a leaching of 0.6 μM of $Co^{2+}$ (aq) would afford the same rate of

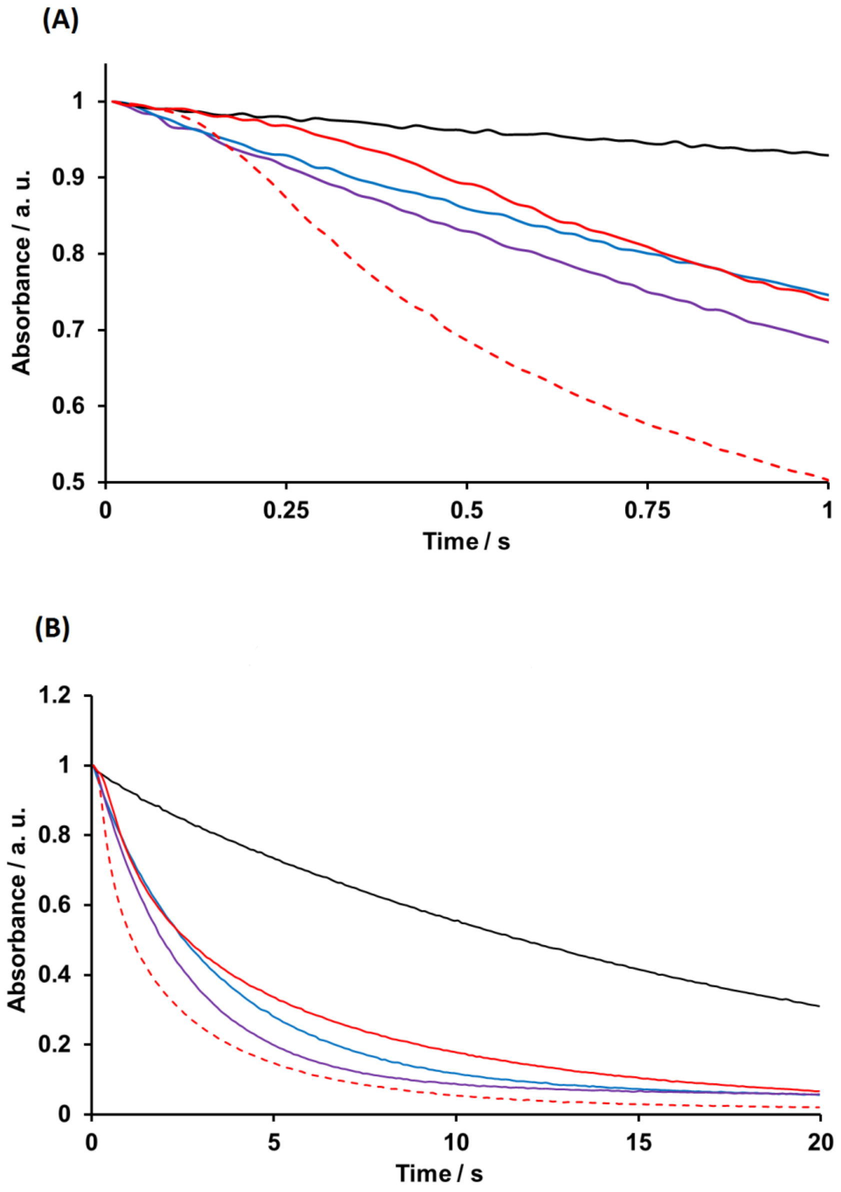

**Figure 3.16** Kinetics of $[Ru(bpy)_3]^{3+}$ self-decomposition (black) and catalytic reduction with 6 μM **1** (blue line), 6 μM **2** (purple line)**,** 0.6 μM $Co(NO_3)_2$ (red solid line) and 1 μM $Co(NO_3)_2$ (red dotted line) collected in 1 s (A) and 20 s (B). Conditions: 1.0 mM $[Ru(bpy)_3]^{3+}$, 80 mM sodium borate buffer with initial pH 9.0. The initial concentration of $[Ru(bpy)_3]^{3+}$ varied in the range 0.93-1.07 mM. Therefore, the initial values of absorbance at 670 nm also varied in the range 0.39-0.45. In order to visualize the difference in reaction kinetics, the curves are normalized per initial absorption.

$[Ru(bpy)_3]^{3+}$ reduction as 6 μM **3.1** or **3.2**. Note that 0.6 μM $Co^{2+}$(aq) is the equivalent of 5 % of the cobalt atoms of 6 μM **3.1** and 3 % of those in 6 μM **3.2**. Significantly, the characteristic induction periods were observed when 0.6 μM of $Co^{2+}$(aq) is used as the catalyst, while no induction periods were detected for **3.1** or **3.2**. This indicates that $Co^{2+}$(aq) is very likely not the catalytic species in this process. However, it must be noted that eq 3.1 is also catalyzed by **3.1** and/or **3.2** which results in low $O_2$ yields.

$$[Ru(bpy)_3]^{3+} \rightarrow \text{decomposition products} \qquad (3.1)$$

$$4[Ru(bpy)_3]^{3+} + 2H_2O \rightarrow 4[Ru(bpy)_3]^{2+} + O_2 + 4H^+ \qquad (3.2)$$

Third, almost identical FTIR spectra were observed for both **3.1** and **3.2** before and after the illumination (Figure 3.17 & 3.18), indicating that the structures of **3.1** and **3.2** remain intact during the catalytic processes. FTIR spectra were recorded for the products formed from a more concentrated (16 μM) reaction solution compared to Figure 3.5 to achieve a reasonable signal-to-noise ratio.

Dynamic light scattering (DLS) was used to check the formation of cobalt oxide nanoparticles in the catalytic reaction system (mixture of photosensitizer, oxidant and catalysts). Particles with diameters of 300 nm – 4000 nm are detected by DLS both before and after the photoirradiation (Figure 3.19 & 3.20). Due to the low solubility of highly negatively charged POM (-13 charge for **3.1** and -9 charge for **3.2**) in the presence of excess $[Ru(bpy)_3]^{2+}$ and the low solubility of any cobalt oxide potentially generated, DLS data is not informative in proving the true nature of the particles. Attempts to avoid the formation of nanoparticles by decreasing the concentration of catalyst or that of the photosensitizer all led to oxygen yields that were too low to be satisfactorily quantified. As stated in two previous papers from our group, the solubility of highly charged POM

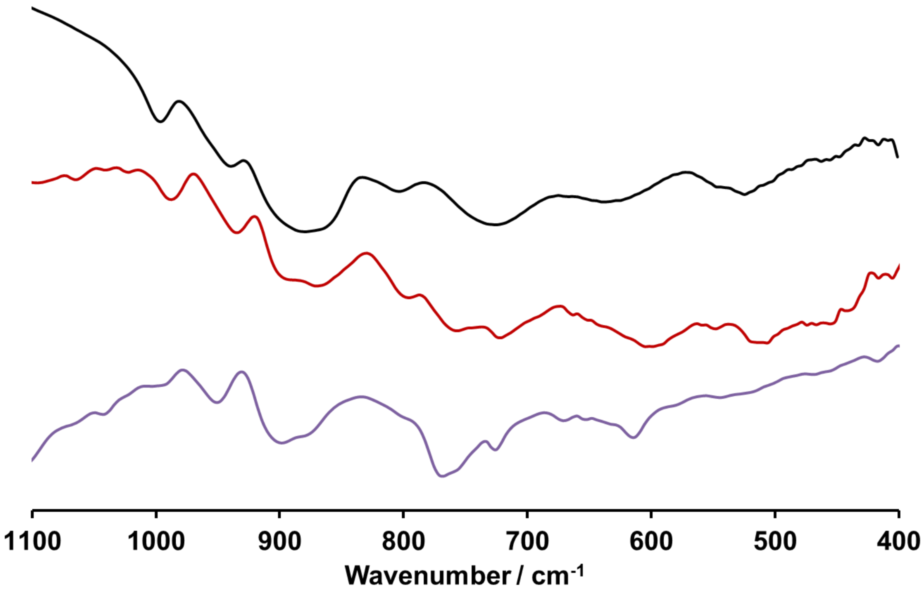

**Figure 3.17** FT-Infrared spectrum of **3.1** (black), precipitate obtained from mixing $[Ru(bpy)_3]^{2+}$ and **3.1** solutions (red), and precipitate isolated from a post reaction solution with **3.1** as the catalyst (purple).

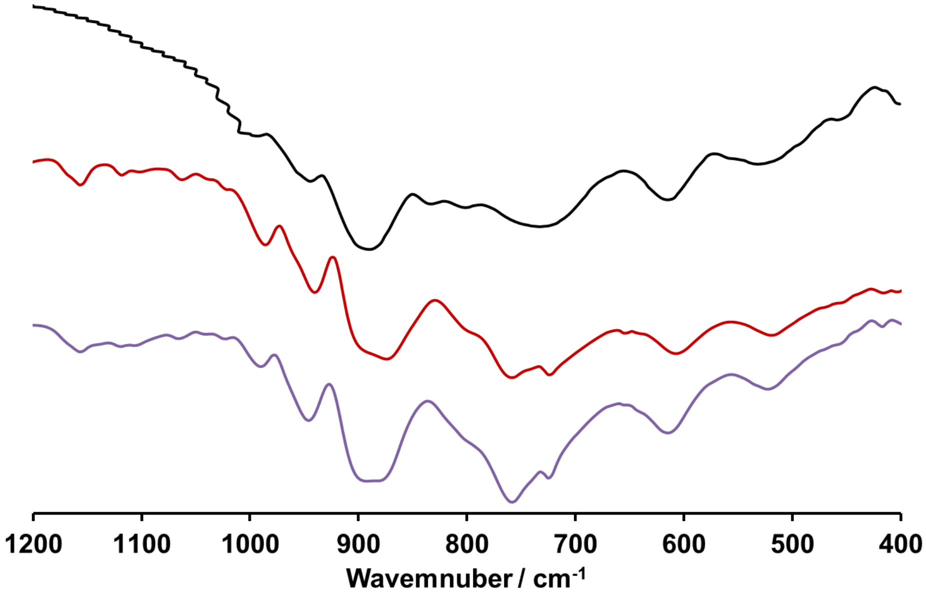

**Figure 3.18** FT-Infrared spectrum of **3.2** (black), precipitate obtained from mixing $[Ru(bpy)_3]^{2+}$ and **3.2** solutions (red), and precipitate isolated from a post reaction solution with **3.2** as the catalyst (purple).

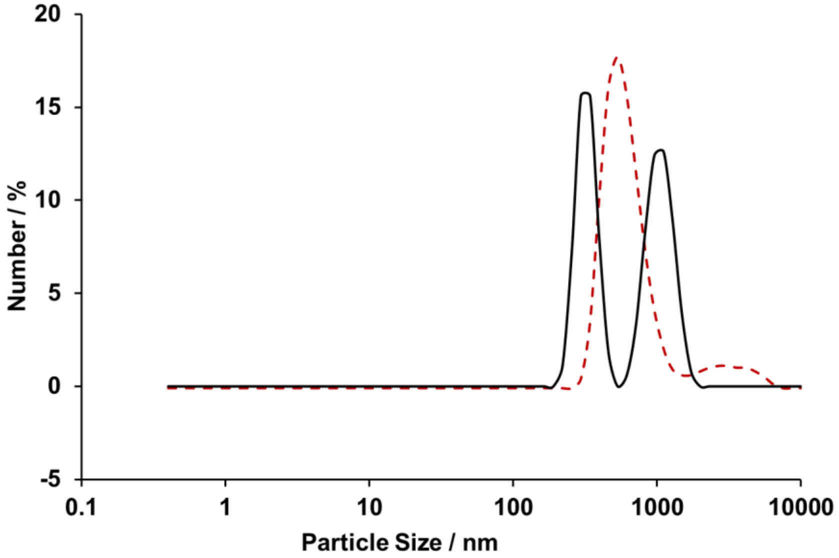

**Figure 3.19** Particle size distribution measured by DLS in a solution of 6 µM **3.1**, 1 mM $[Ru(bpy)_3]Cl_2$ and 5 mM $Na_2S_2O_8$ in 80 mM pH 8.0 sodium borate buffer before (black solid line) and after (red dotted line) photo-irradiation for 11 min (455 nm LED light, 17 mW).

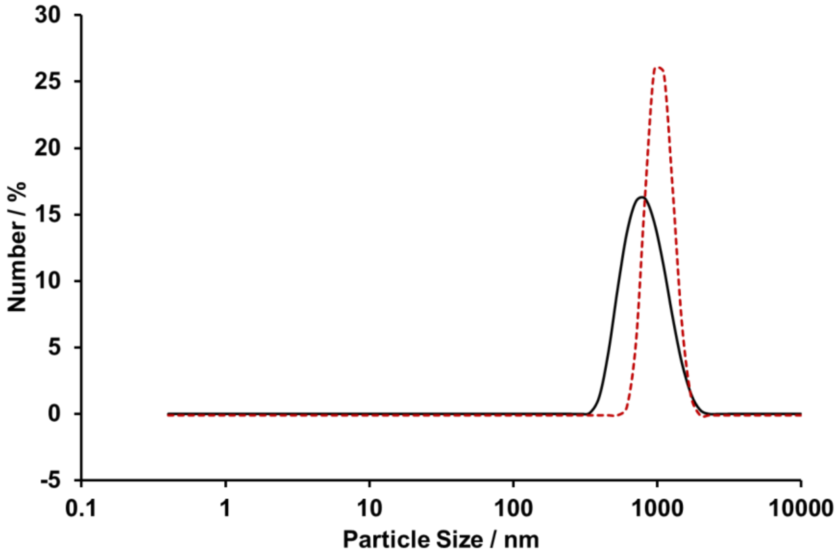

**Figure 3.20** Particle size distribution measured by DLS in a solution of 6 µM **3.2**, 1 mM $[Ru(bpy)_3]Cl_2$ and 5 mM $Na_2S_2O_8$ in 80 mM pH 8.0 sodium borate buffer before (black solid line) and after (red dotted line) photo-irradiation for 11 min (455 nm LED light, 17 mW).

catalysts in the presence of the photosensitizer $[Ru(bpy)_3]^{2+}$ is very low.[39] The minimally soluble $[Ru(bpy)_3]^{2+}$-POM salts (with **3.1** and **3.2**) form nanoparticles. Importantly however, the FTIR spectra of the $[Ru(bpy)_3]^{2+}$-POM salts are unchanged by catalytic water oxidation implying there is no change in the geometrical structures of the polyanion units in **3.1** and **3.2**. Thus these POM catalysts remain molecular and homotopic[2,90] (only a single type of active site is present) during and after catalysis.

## 3.4 Conclusions

Two new $Co^{II}$-silicotungstate complexes have been synthesized using $K_{10}A$-α-$[SiW_9O_{34}]\cdot 13H_2O$ as the precursor. Both compounds comprise two or three cobalt atoms in a central multi-oxygen ligation pocket afforded by the polyanion framework. Both **3.1** and **3.2** have been characterized by X-ray crystallography and several spectroscopic methods. They are fairly stable over a range of pH values, but convert to **3.3** in pH 4.8 potassium acetate buffer at elevated temperature. Both complexes show moderate catalytic activities in water oxidation. FTIR, stopped-flow and water oxidation kinetics data suggest these compounds remain homotopic during catalysis.

# *Chapter 4*

## Chapter 4 : A nickel-containing polyoxo-metalate water oxidation catalyst

with Elliot N. Glass, Chongchao Zhao, Hongjin Lv, James W. Vickers,

Yurii V. Geletii, Djamaladdin G. Musaev, Jie Song and Craig L. Hill

(Published partially in *Dalton Transactions*, 2012, **41**, 13043 -13049. -

Reproduced by permission of The Royal Society of Chemistry)

**Abstract**: A new penta-nickel silicotungstate complex $K_{10}H_2[Ni_5(OH)_6(OH_2)_3(Si_2W_{18}O_{66})]\cdot 34H_2O$ (KH-**4.1**) has been identified to be a water oxidation catalyst in a photo-driven system with $[Ru(bpy)_3]^{2+}$ as photosensitizer and $Na_2S_2O_8$ as sacrificial electron acceptor. The low solubility of highly negatively charged KH-**4.1** in the presence of $[Ru(bpy)_3]^{n+}$ lead to the suspension formation; however, several lines of evidence indicate that **4.1** is stable and retains its molecular structure under catalytic turnover conditions.

## 4.1 Introduction

Nickel oxides / nickel hydroxides have been used as efficient, robust, earth-abundant element-based water oxidation catalysts (WOCs). They have been used mostly in alkaline solutions (pH>11), until recently, when electrodeposited $NiO_x$-borate films were found to catalyze water oxidation at near neutral pH (pH 9.2). [97,98] Prior to the research in this chapter, there were no known molecular nickel-based WOCs.

Classical homogeneous catalysts are distinguished from heterogeneous catalysts by involvement of only one phase instead of multiple phases. However, sometimes there is no distinct boundary between different phases. The size of a metal cluster could be very small, but still considered to be a heterogeneous catalyst due to its multiple reactive sites. Therefore, in this chapter, we adopt the terminology popularized by Crabtree of “homotopic”/”heterotopic”.[90] A heterotopic catalyst has multiple types of catalytically active sites, while a homotopic catalyst has a single type of active site or limited number of active sites (if the molecular catalyst has more than one active site). Therefore, the catalytic properties of an insoluble homotopic catalyst remain the same as its soluble form, even though it may exist in a different phase than its reaction solution.

In the photo-driven system for catalytic water oxidation, $[Ru(bpy)_3]^{2+}$ are often used as the photo-sensitizer. However, for a highly-negatively-charged POM catalyst, the solubility of the $[Ru(bpy)_3]^{n+}$-POM salt is usually low and depends on the charge, the size and the shape of the POM, etc. Therefore, suspensions may be formed before the reaction starts. Another souce of suspension formation may come from the decomposition of molecular POM WOCs into metal oxide nanoparticles, which are well known to be good water oxidation catalysts. As a result, the stability of new POM WOCs must be evaluated, especially when a suspension is present in the reaction system. Identifying the nature of the suspension species is a difficult but important task.

Besides cobalt complexes, organometallic mangnese complexes, copper complexes, iron complexes have also been shown to have WOC activity.[99] Our group has been focusing on studying the WOC activity by Co-POMs, but other transition-metal-substituted POMs also have the potential to be catalytically active as well. Mn-POMs have been studied by our group, and shown to have higher catalytic activity for decomposition of $[Ru(bpy)_3]^{2+}$ than for water oxidation. The Fe-POMs we evaluated didn't show any WOC activity. Patzke's group has shown that $\alpha$-$K_{11}Na_1[Ni_4(H_2O)_2(SiW_9O_{34})_2]\cdot 27H_2O$ has no WOC activity (no crystal structure is provided for this compound), but the buffer used was acidic ($Na_2SiF_6$ buffer pH 5.8).[2] We report here the first nickel-containing POM WOC, $K_{10}H_2[Ni_5(OH)_6(OH_2)_3(Si_2W_{18}O_{66})]\cdot 34H_2O$ (KH-**4.1**). We provide several arguments that this new POM, **4.1**, in the presence of $[Ru(bpy)_3]^{n+}$ (n = 2 or 3) exists as an equilibrium between **4.1** in solution and the low-solubility $[Ru(bpy)_3]^{n+}$-**4.1** complex, and that during catalytic water oxidation, **4.1** remains molecular, i.e. it does not decompose to Ni hydroxide / oxide particles or films.

## 4.2 Experimental

### Materials and Methods

$Na_{10}[\alpha\text{-}SiW_9O_{34}]$[60] was prepared and purified by the literature procedure. Tris(2,2'-bipyridyl)dichlororuthenium(II) hexahydrate ($[Ru(bpy)_3]^{2+}$), sodium persulfate, and all other chemicals and salts were of the highest purity available from commercial sources. $[Ru(bpy)_3]^{2+}$ was recrystallized before use as previously reported.[69] $[Ru(bpy)_3]^{3+}$ was prepared as previously reported.[68] Nickel hydroxide was freshly prepared as follows: 5 mL of a 1.0 M aqueous $NiCl_2$ solution was added to 5 mL of 4.0 M aqueous KOH dropwise with vigorous stirring. The precipitate was collected by filtration through a medium sized frit, washed thoroughly with DI water, ethanol and diethyl ether, and air dried. Infrared spectra (2% sample in KBr pellet) were recorded on a Nicolet 6700 FT-IR spectrometer. Elemental analyses for K, Na, Ni, Si and W were performed by Galbraith Laboratories (Knoxville, Tennessee). Thermogravimetric data were collected on an ISI TGA 1000 instrument. Electronic absorption spectra were acquired using an Agilent 8453 spectrophotometer equipped with a diode-array detector and Agilent 89090A cell temperature controller unit. A Zetasizer Nano ZS 90 instrument (Malvern Instruments Ltd., UK) was used for dynamic light scattering (DLS) measurements. The particle sizes suitable for measurement by this instrument range from 0.3 to 5000 nm (diameter).

Isolation of the post-reaction catalyst: The photo-driven reaction was scaled up by using 50 mL of solution, containing 1 mM $[Ru(bpy)_3]Cl_2$, 5 mM $Na_2S_2O_8$, 8 μM $Ni_5Si_2W_{18}$ and 80 mM pH 8 sodium borate buffer. The solution was kept under the LED light for 100 min. The volume of the reacted solution was decreased to 20 mL via rotary evaporation. The precipitate was collected by centrifugation, dried in air and characterized using FTIR spectroscopy.

The reaction of KH-**4.1** and $Ni(NO_3)_2$ with $Ru(bpy)_3^{3+}$ under equivalent conditions to the light-driven reaction was studied using a Hi-Tech KinetAsyst Stopped Flow SF-61SX2 instrument equipped with a diode array detector operating in wavelength range 400-700 nm. One of the syringes was filled with a 2 mM $Ru(bpy)_3^{3+}$ solution, and the other with a buffered solution of KH-**4.1** or $Ni(NO_3)_2$. The consumption of $Ru(bpy)_3^{3+}$ was followed by a decrease in absorbance at 670 nm ($\varepsilon_{670}$ = 4.2 x $10^2$ $M^{-1}$ $cm^{-1}$) with optical path length *l* = 10 mm. Detailed analysis of kinetic data was performed using both Copasi 4.7 (Build 34) [Hoops, S., Sahle, S., Gauges, R., Lee, C., Pahle, J., Simus, N., Singhal, M., Xu, L., Mendes, P., and Kummer, U. (2006). COPASI - a COmplex PAthway SImulator. Bioinformatics 22, 3067-74.] and the Solver subprogram in Microsoft Excel.

Quantification of $O_2$ produced under identical conditions as above was performed using A Hi-Tech Scientific SF-61SX2 mixing apparatus for consistent fast-mixing. Solutions were deaerted with Ar in round bottom flasks before being injected into the mixer with 1010 TLL Gastight Hamilton syringes. One of the feeding syringes was filled with 2.0 mM $[Ru(bpy)_3]^{3+}$ solution and the other with a freshly prepared solution of KH-**4.1** in 160 mM sodium borate buffer at pH 8.0. The mixing apparatus was connected with PEEK tubing to an Ocean Optics FOXY-FLOW-CELL fitted with an oxygen probe. All joints were sealed with Teflon tape and DAP Blue Stik adhesive putty. Oxygen measurements were made using an Ocean Optics Neofox Phase Measurement System with a FOXY-R probe and FOXY-AF-MG coating. The probe was calibrated using a two point curve (0 and 20.9%). Repeated shots were performed until the oxygen reading was constant for three consecutive shots.

### $K_{10}H_2[Ni_5(OH)_6(OH_2)_3(Si_2W_{18}O_{66})]\cdot 34H_2O$ (KH-4.1)

$Na_{10}[\alpha\text{-}SiW_9O_{34}]$ (1.5 grams, 0.54 mmol) were added with stirring to 30 mL of deionized water, forming a turbid white suspension. The pH was adjusted to 6.8 with the dropwise addition of 1 M HCl, causing the suspension to dissolve into a solution. $NiCl_2\cdot 6H_2O$ (320 mg, 1.35 mmol) was added to the stirring solution. The pH was 5.2 after addition and was adjusted using 1 M HCl if necessary. The solution was stirred, refluxed for two hours, cooled to room temperature, filtered, and then 20 mL of saturated KCl was added. The resulting solution was placed in an ice bath with stirring for an hour and the pale green precipitate that slowly formed over this time was collected via filtration. The crude product was recrystallized twice from minimal hot water. Slow evaporation over two days produced 0.258 g (16.3% yield based on W) of green needle crystals. An unidentified yellow crystalline byproduct and other impurities crystallized shortly after the product. IR (KBr pellet; 2%): 998 (w), 987 (w), 947 (m), 894 (s), 843 (sh), 799 (s), 709 (m), 634 (m), 525 (w) $cm^{-1}$. Anal. Calcd (Found) for $K_{10}H_2[Ni_5(OH)_6(OH_2)_3(A\text{-}\alpha\text{-}SiW_9O_{33})_2]\bullet 34H_2O$ (KH-**4.1**): K, 6.65 (6.29); Ni, 4.99 (4.68); Si, 0.95 (0.93); W, 56.3 (56.4).

### $K_{10}H_2[Ni_{3.5}(OH)_4(OH_2)_2Si_2W_{18.5}O_{67})]\cdot 19H_2O$ (KH-4.2)

Na-$SiW_9$ (0.533 g) was added with stirring to 10 mL of deionized water, forming a turbid white suspension. $NiCl_2\bullet 5H_2O$ (74 mg) was added to the stirring suspension, and the pH was 7.3. The pH was adjusted to 5.2 with 0.5 M HCl. The solution, covered with a glass slip, was heated at 80 °C and stirred for 1 hr. The resulting solution was cooled to room temperature and the pH was 5.9. Then 2 mL of saturated KCl was added, and the suspension was filtered with fine filter paper. Green needle crystals were produced overnight. IR (KBr pellet; 2%): 987 (w), 941 (m), 891 (s), 799 (s), 708 (m), 667 (sh), 637 (m), 525 (w) $cm^{-1}$.

## X-ray crystallography

Representative diffraction-quality single crystals of KH-**4.1** and KH-**4.2** were coated with Paratone-N oil, suspended on a small fiber loop and placed in a cooled nitrogen gas stream at 173 K on a Bruker D8 APEX II CCD sealed tube diffractometer. Graphite monochromatic Mo Kα (λ = 0.71073 Å) radiation was used. Data were obtained using a combination of φ and ω scans with 10 s frame exposure and 0.3° frame widths. The data were collected, indexed and initial cell refined using SMART.[63] Frame integration and final cell refinements were done using SAINT.[80] The molecular structure was determined using direct methods and Fourier techniques; the standard full-matrix least-squares procedure was used in the refinement. Absorption correction was also conducting by face indexing using the program SADABS.[100] The greatest residual electron density was located near the W atoms (less than 1.0 Å) and was most likely due to imperfect absorption corrections. The latter are frequently encountered in heavy-metal atom structures such as polyoxotungstates. Anomalous dispersion corrections and scattering factors were taken from the International Tables for X-ray Crystallography, and SHELXTL, v 6.14 software was used in the structure solution, refinement, graphic and generation of publication materials.[81] The crystal data and structure refinement parameters are summarized in Table 4.1.

**Table 4.1** Crystal Data and Structure refinement for KH-**4.1** and KH-**4.2.**

| | KH-**4.1** | KH-**4.2** |
|---|---|---|
| Empirical formula | $K_{10}Ni_5Si_2W_{18}O_{109}H_{88}$ | $K_{10}Ni_{3.5}Si_2W_{18.5}O_{92}H_{40}$ |
| Formula wt. / g $mol^{-1}$ | 5882.37 | 5445.34 |
| Temperature / K | 173(2) | 173(2) |
| Radiation (λ) / Å | 0.71073 | 0.71073 |
| Crystal system | Triclinic | Triclinic |
| Space group | $P\bar{1}$ | $P\bar{1}$ |
| $a$ / Å | 13.320(2) | 13.0076(1) |
| $b$ / Å | 15.860(3) | 17.2224(2) |
| $c$ / Å | 23.521(4) | 22.572(2) |
| $\alpha$ / ° | 74.624(3) ° | 112.137(0) |
| $\beta$ / ° | 76.583(3) ° | 100.975(2) |
| $\gamma$ / ° | 75.041(2) ° | 96.5360(1) |
| $V$ / $Å^3$ | 4557.0(14) | 4501.4(7) |
| $Z$ | 2 | 2 |
| $\rho_{calcd}$ / g $cm^{-3}$ | 3.978 | 4.018 |
| $\mu$ / $mm^{-1}$ | 24.210 | 24.638 |
| $F(000)$ | 4788 | 4762 |
| Crystal size / $mm^3$ | 0.34 x 0.17 x 0.07 | 0.29 x 0.09 x 0.08 |
| Reflections collected | 69370 | 82714 |
| Independent reflections | 19331 [R(int) = | 24078 [R(int) = 0.0838] |
| Absorption correction | Numerical | Numerical |
| Refinement method | Full-matrix least- | Full-matrix least-squares |
| Goodness-of-fit on $\|F\|^2$ | 1.042 | 1.061 |
| Final $R$ indices [$R > 2\sigma(I)$] | $R_1^a = 0.0517$, $wR_2^b =$ | $R_1^a = 0.0517$, $wR_2^b = 0.1889$ |
| $R$ indices (all data) | $R_1^a = 0.0926$, $wR_2^b =$ | $R_1^a = 0.1091$, $wR_2^b = 0.2192$ |
| Largest diff. peak and hole / e | 3.676 and -2.993 | 4.735 and -7.513 |

$^a R_1 = \Sigma||F_0| - |F_c|| / \Sigma|F_0|$; $wR_2 = \Sigma[w(F_0^2 - F_c^2)^2] / \Sigma[w(F_0^2)^2]^{1/2}$

## Photodriven catalytic water oxidation

Light-induced water oxidation was performed in the quartz cylindrical optical cell (NSG, 32G10) with a 1-cm optical path length, OD = 22 mm, and total volume ~ 2.8 mL equipped with standard taper joint. In a typical reaction, the vessel was filled with 2 mL of a solution with the desired concentrations of $Ru(bpy)_3Cl_2$, $Na_2S_2O_8$, catalyst, and sodium borate buffer. The vessel was then sealed with a rubber septum and carefully purged with Ar. The headspace was checked by gas chromatography (GC) to confirm the absence of $O_2$ before the experiment. All procedures were performed with a minimum exposure to ambient light. The reaction was initiated by turning on the Sandhouse Design LED light source (LLS) equipped with a 455-nm LED. A light beam with OD = 0.4-0.5 cm and 17 mW power was focused on the flat front of the reaction vessel using two lenses. The solution was agitated by a magnetic stirring bar spinning vertically on the back side of the cell. After the desired illumination time, the reaction was temporarily stopped by blocking the light. The $O_2$-yield was quantified by GC as described earlier.[69]

## Computational procedures

All calculations were performed using the Gaussian 09 program.[101] The geometries of all species were optimized without any symmetry constraint at the B3LYP[102-104] level of theory. In these calculations we used Hay-Wadt effective core potentials (ECPs) with the associated Lanl2dz basis set for transition metals[105-107] and the standard 6-31G* split-valence-polarization basis set for all other atoms. The solvent effects were estimated by using the self-consistent reaction field IEF-PCM method[108] with water as a solvent (dielectric constant = 78.39).

## 4.3 Results and discussion

### 4.3.1 Syntheis and structure

Two new pentanickel POMs were prepared in acidic aqueous solution from $Na_{10}[\alpha\text{-}SiW_9O_{34}]$ and $NiCl_2$. They are readily purified by recrystallization of the potassium salt from water. The sequence of adding reactants is very important. If $NiCl_2$ is added after the pH of $Na_{10}[\alpha\text{-}SiW_9O_{34}]$ solution is adjusted to 4.2, KH-**4.1** is formed; if $NiCl_2$ is added directly into $Na_{10}[\alpha\text{-}SiW_9O_{34}]$ solution before the pH ajustment, KH-**4.2** is formed.

The molecular structure of the polyanion, **4.1**, is composed of a large $[Ni_5(OH)_6(OH_2)_3]^{4+}$ assembly supported in the central cavity of the clamshell-shaped isopolytungstate $[Si_2W_{18}O_{66}]^{16-}$ (Figure 4.1). The $[Si_2W_{18}O_{66}]^{16-}$ polytungstate framework present in **4.1** is formed by reaction of $[A\text{-}\alpha\text{-}SiW_9O_{34}]^{10-}$ under acidic conditions and high concentrations of $K^+$.[79] The pentanickel unit in **4.1** has multiple bridging oxo groups. A pentacopper derivative of the same polyanion present in KH-4.1 has been characterized by Kortz and co-workers (Figure 4.2).[30] However, their overall polyanion has a significantly different structure than 4.1. In our pentanickel POM, a nickel atom is positioned outside the framework; it is not bound to any of the tungsten octahedra. Furthermore, KH-**4.1** does not contain a central axis due to the position of the nickel atom. This reduces the molecular symmetry from $C_{2v}$ to $C_s$. In the Kortz's pentacopper polyanion, there is no equivalent atom. Instead, a copper atom is nestled in the center and bound to both halves of $[Si_2W_{18}O_{66}]^{16-}$. Bond valence sum (BVS) calculations on the Kortz polyanion and on **4.1** indicate that in both complexes all bridging oxo groups linking adjacent copper or nickel atoms are either mono- or diprotonated.

The **4.2** polyanion of has $C_1$ symmetry (Figure 4.3). The $Ni_4$ atom is disordered with a $W_{19}$ atom, and the best refinement was achieved with occupation factors of about ½ and ½, respectively. That is, half of the polyanions have structures like $Ni_4Si_2W_{18}$ (Figure 4.3a), and the other half of the polyanions have structures as $Ni_3Si_2W_{19}$ (Figure 4.3b). For $Ni_4Si_2W_{18}$ structure (Figure 4.3 a), two $[A\text{-}\alpha\text{-}SiW_9O_{34}]^{10-}$ units are linked by sharing one terminal oxygen atom, and a tetra-nickel cluster is located in between. The $Ni2O_6$, $Ni3O_6$, and $Ni4O_6$ units located at the trivacant sites of one $[A\text{-}\alpha\text{-}SiW_9O_{34}]^{10-}$ completing the α-Keggin structure $[\alpha\text{-}SiNi_3W_9O_{40}]^{16-}$. At the same time, $Ni1O_6$, $Ni2O_6$ and $K5O_6$ units complete the other $[A\text{-}\alpha\text{-}SiW_9O_{34}]^{10-}$. Bond valence sum calculations reveal that the two terminal oxygens associated with the $Ni_4$ cluster are both deprotonated; the μ-oxo oxygen is monoprotonated. For $Ni_3Si_2W_{19}$ structure (Figure 4.3b), the $Ni_3$ cluster is located in between a $[A\text{-}\alpha\text{-}SiW_9O_{34}]^{10-}$ unit and a $[\alpha\text{-}SiW_{10}O_{37}]^{10-}$ unit. The structure is very similar with **2.1a**, except that one of the cobalt atoms is changed to $K^+$, and the other cobalt atoms are changed to $Ni^{2+}$. No further catalytic study was undertaken on this complex, because it will be hard to interpret mechanistic experiments based on this disordered POM. The IR spectra of KH-**4.1** and **4.2** are very similar (Figure 4.4).

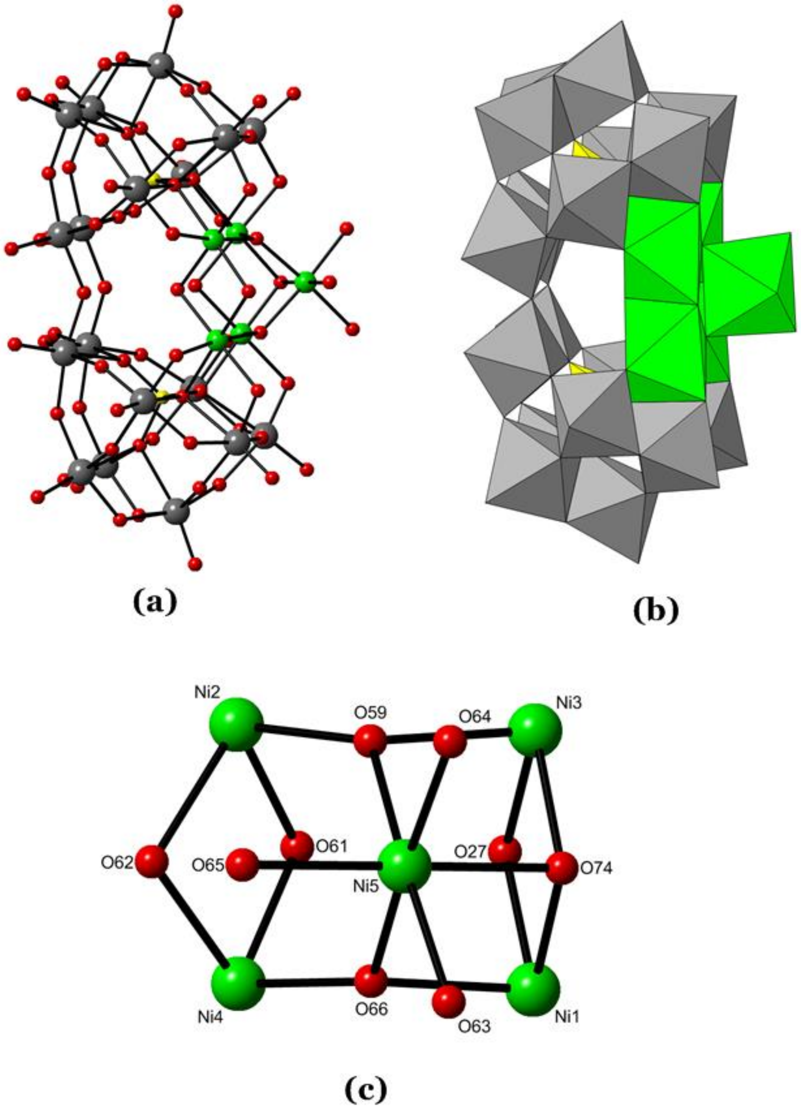

**Figure 4.1** Ball and stick (a) and polyhedral (b) representations of **4.1**, Ball and stick representation of the central $[Ni_5(OH)_6(OH_2)_3(Si_2W_{18}O_{66})]^{12-}$ fragment of **4.1**(c). The color code is as follows: nickel (green), tungsten (grey), silicon (yellow), and oxygen (red).

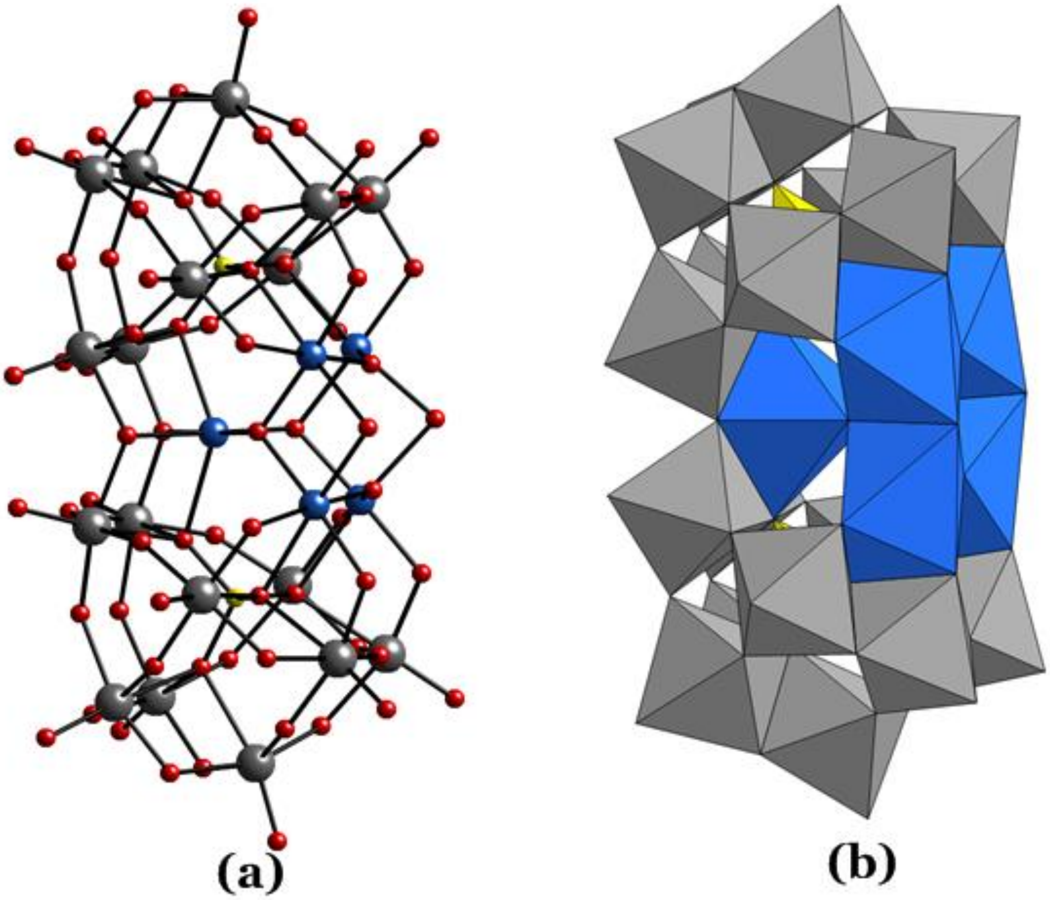

**Figure 4.2** Ball and stick (a) and polyhedral (b) representations of $[Cu_5(OH)_4(H_2O)_2(A\text{-}\alpha\text{-}SiW_9O_{33})_2]^{10-}$. Color code: copper (blue), tungsten (grey), silicon (yellow), and oxygen (red).

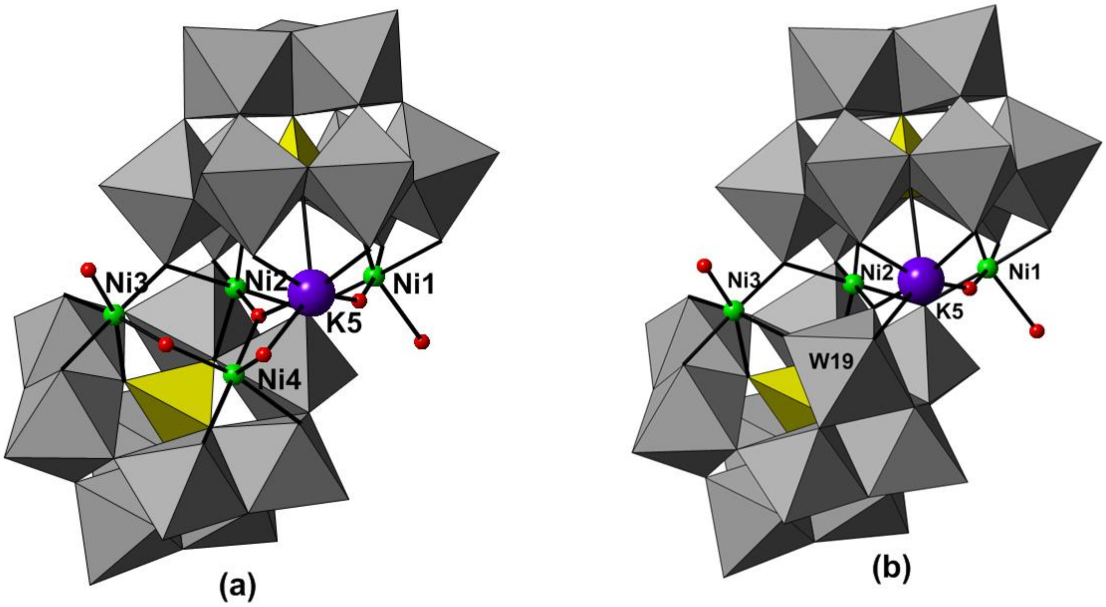

**Figure 4.3** Combined polyhedral/ball-and-stick representations of the polyanion units in **4.2**. $WO_6$ units: grey polyhedra; $SiO_4$ units: yellow tetrahedra; Ni: green spheres; K: pureple spheres; O: red spheres.

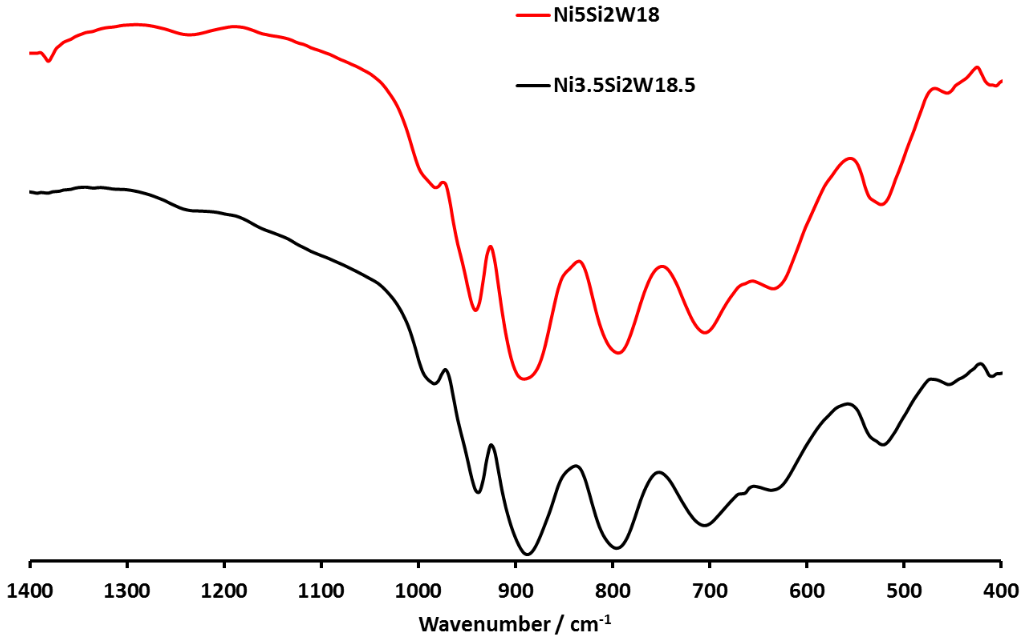

**Figure 4.4** IR spectra of KH-**4.1**(red) and 4**.2** (black).

### 4.3.2 $[Ru(bpy)_3]^{n+}$-4.1 formation

In the catalytic experiments below, when KH-**4.1** is added to either of the catalytic reactions (dark reactions using $[Ru(bpy)_3]^{3+}$ as oxidant or light driven reactions using $[Ru(bpy)_3]^{2+}$ as a photosensitizer and $Na_2S_2O_8$ as a sacrificial electron acceptor), a $[Ru(bpy)_3]^{n+}$ salt of **4.1** forms. This $[Ru(bpy)_3]^{n+}$-**4.1** complex has a very low solubility in the buffered water used in all these reactions, thus the catalyst is present in solution and in the form of nanoparticles. The solubility of the $[Ru(bpy)_3]^{2+}$ salt of **4.1** is lower than the $[Ru(bpy)_3]^{3+}$ salt of **4.1** thus in the dark water oxidation reactions as $[Ru(bpy)_3]^{3+}$ is converted to $[Ru(bpy)_3]^{2+}$, the amount of **4.1** present as insoluble particles increases with time. This increase in the quantity of precipitate with time is directly observed in all the dark water oxidation reactions catalyzed by **4.1**. The precipitation of two POM WOCs as $[Ru(bpy)_3]^{n+}$ salts was noted very recently by Patzke and co-workers,[2] and ion pairing in POMs is well documented to affect solubility and other properties of the polyanion.[109,110] In both our studies here and in those by Patzke, several methods were used to confirm that the POM WOC in the $[Ru(bpy)_3]^{n+}$-POM complex is stable and does not decompose to produce metal hydroxide / oxide particles.

The following specific studies confirm the formation of low-solubility $[Ru(bpy)_3]^{n+}$-**4.1** particles in this study. Dynamic light scattering (DLS) measurements show the formation of 700-1300 nm diameter nanoparticles immediately after mixing the photosensitizer and 2 μM KH-**4.1** solutions in the dark. The same is true even if 0.5 μM solutions of KH-**4.1** are used. However, DLS does not address the stability of the catalyst

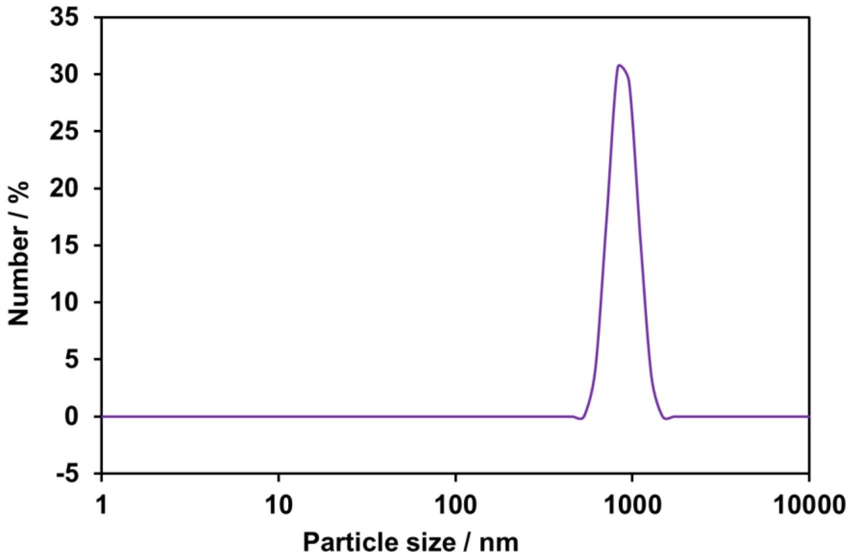

**Figure 4.5** Particle size distribution measured by DLS in a solution of 0.5 μM KH-**4.1**, 1 mM [Ru(bpy)$_3$]Cl$_2$ and 5 mM $Na_2S_2O_8$ in 80 mM pH 8.0 sodium borate buffer.

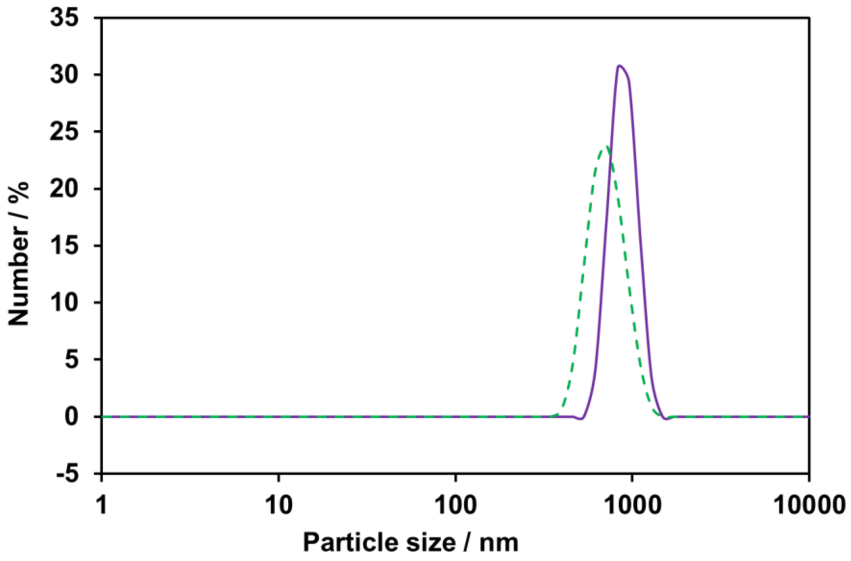

**Figure 4.6** Particle size distribution measured by DLS in a solution of 2 μM KH-**4.1**, 1 mM [Ru(bpy)$_3$]Cl$_2$ and 5 mM $Na_2S_2O_8$ in 80 mM pH 8.0 sodium borate buffer before (purple solid line) and after (green dotted line) photoirradiation for 11 min (455 nm LED light, 17 mW).

under turnover conditions because this technique cannot distinguish between an intact catalyst that is minimally soluble and the most likely product of decomposition, nickel hydroxide, which is completely insoluble. If the system is filtered before the photo-illumination, no $O_2$ is generated from the supernatant solution and no nanoparticles are formed confirming a very low solubility of the $[Ru(bpy)_3]^{n+}$-**4.1** complex. The lack of $O_2$ generation in **4.1** after filtration indicates that the photosensitizer-POM complex is the active species. The same behavior was found for $[Ru(bpy)_3]^{n+}$-POM WOC complexes examined by Patzke and co-workers.[2] Importantly, when the same experiment is performed by replacing **4.1** with 1 μM $Ni(NO_3)_2$, the supernatant after filtration still generates oxygen, supporting the argument that $Ni^{2+}$ is not leached from **4.1** prior to formation of the $[Ru(bpy)_3]^{n+}$-POM complex. In the dark water oxidation reactions (stopped-flow experiments described below) the kinetics follow the same trend as the kinetics of light-driven catalytic $O_2$ generation (Figure 4.7) provided the concentration of **4.1** is equal or below 4 μM. The rising baseline in the visible spectra when the concentration of **4.1** reaches 5 μM is clear evidence of precipitation. Experiments to overcome the solubility limit of the photosensitizer-POM salt, $[Ru(bpy)_3]^{2+}$-**4.1**, by decreasing the concentrations of photosensitizer and catalyst failed to achieve satisfactory oxygen evolution kinetics (minimal error and maximal reproducibility of the full catalyst runs).

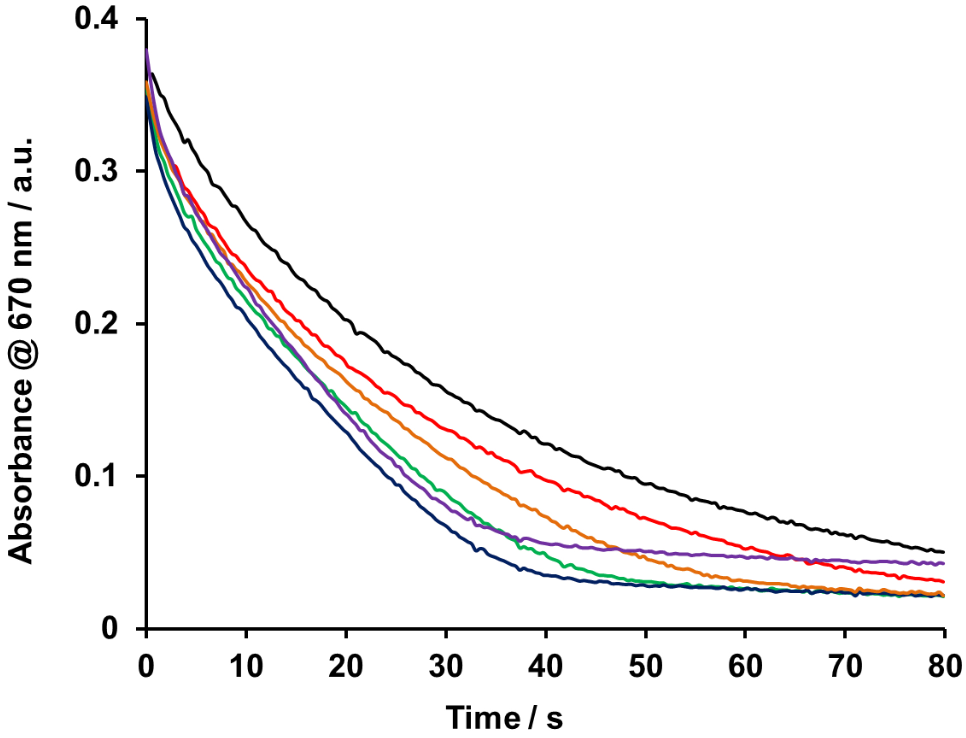

**Figure 4.7** Kinetics of $[Ru(bpy)_3]^{3+}$ self-decomposition (black) and catalytic reduction with 1 µM (red), 2 µM (orange), 3 µM (green), 4 µM (blue), 5 µM (purple) KH-**4.1.** Conditions: 1.0 mM $[Ru(bpy)_3]^{3+}$, 80 mM sodium borate buffer with initial pH 8.0.

### 4.3.3 Catalytic properties

The ability of **4.1** to catalyze water oxidation was studied under photo-driven conditions (Figure 4.8). To probe this activity, the net oxidant, $[Ru(bpy)_3]^{3+}$, was photogenerated *in situ* by reaction with $S_2O_8^{2-}$, the sacrificial electron acceptor. The overall net reaction is:

$$2\ S_2O_8^{2-} + 2\ H_2O + 2\ h\nu \rightarrow 4\ SO_4^{2-} + O_2 + 4\ H^+ \qquad (4.1)$$

A small amount of $O_2$ is generated in the absence of any catalyst probably due to the decomposition of $[Ru(bpy)_3]^{3+}$ to $RuO_2$, a well-known and active WOC. In the figure below, the $O_2$ yield in the reaction catalyzed by **4.1** is taken as a difference between yields in catalyzed and non-catalyzed reactions. The yield of $O_2$ per persulfate, 2 x $O_2$/(persulfate), is ca. 5% in the presence of 2.0 μM **4.1**. The $O_2$ yield and turnover number (TON) depend on catalyst concentration. The overall turnover number, TON = n ($O_2$)/n (cat) with 2 μM **4.1** is *ca*. 60. The quantum yield, (initial $O_2$ formation rate) / (photon flux), is calculated as $\Phi_{QY}(0) = N(O_2)/[N(h\nu)/2] = 2\,(\Delta[O_2]/\Delta(h\nu))_0$, (the number of $O_2$ molecules formed per two photons absorbed) is *ca*. 3.8 % at 2.0 μM **4.1**. The low value of Φ is consistent with low chemical yield.[69]

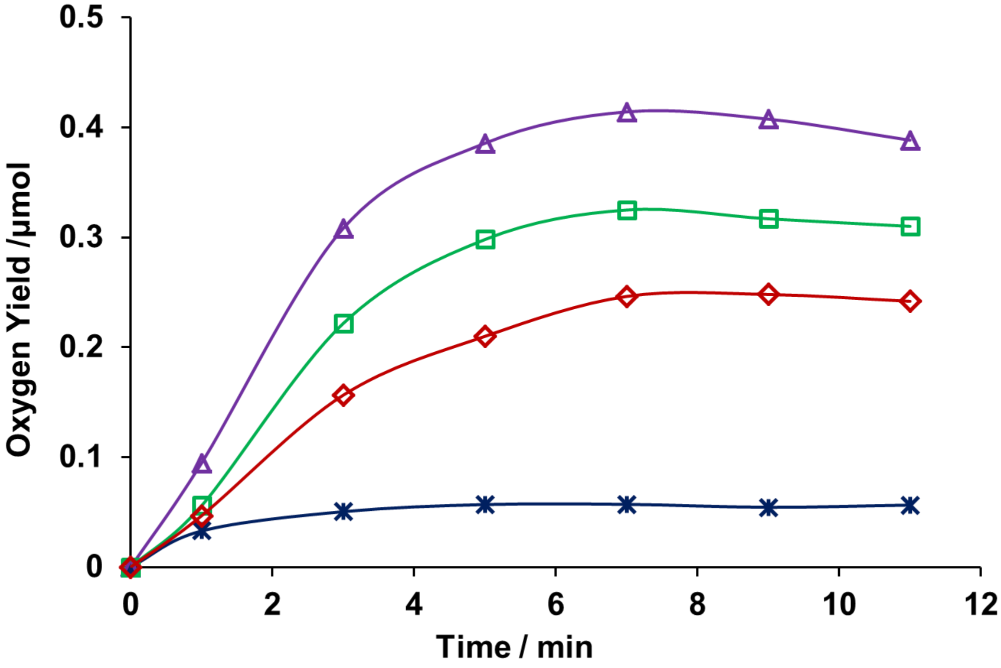

**Figure 4.8** Kinetics of light-driven catalytic $O_2$ evolution from water oxidation. The purple, green and red curves are for 4.0 μM**,** 3 μM and 2 μM KH-**4.1**, respectively, and the dark blue curve is a control (no catalyst). Conditions: 455 nm LED light (17 mW, beam diameter ~0.5 cm), 1.0 mM $[Ru(bpy)_3]Cl_2$, 5.0 mM $Na_2S_2O_8$, 80 mM sodium borate buffer with initial pH 8.0, total volume 2.0 mL.

In addition, we used the stopped flow technique to follow the rate of $[Ru(bpy)_3]^{3+}$ reduction by water oxidation (eq 4.2). Under turnover conditions $[Ru(bpy)_3]^{3+}$ also decomposes exponentially with $k_2 = 0.012\ s^{-1}$ (eq 4.3).

$$4[Ru(bpy)_3]^{3+} + 2H_2O \rightarrow 4[Ru(bpy)_3]^{2+} + O_2 + 4H^+ \qquad (4.2)$$

$$[Ru(bpy)_3]^{3+} \rightarrow \text{ decomposition products} \qquad (4.3)$$

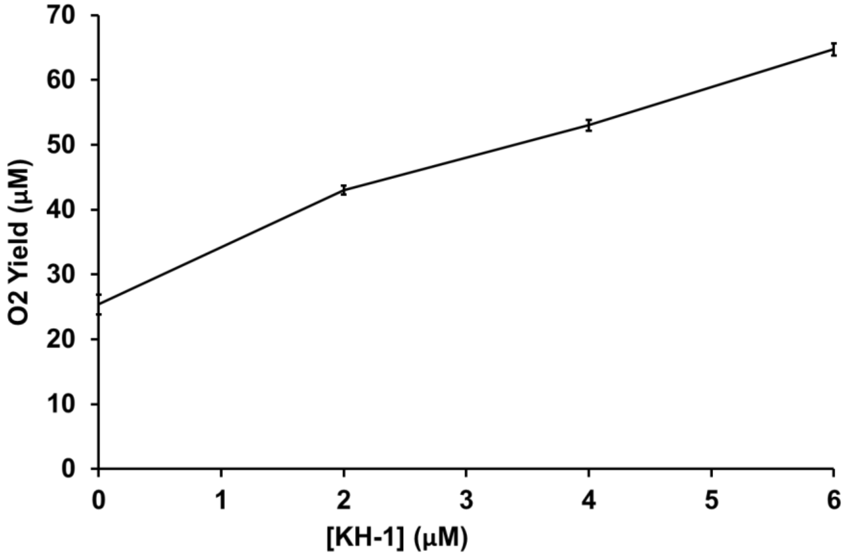

**Figure 4.9** Fast-mixing $O_2$ yield vs. KH-**4.1** concentration measured with a FOXY-R probe using sacrificial oxidant $[Ru(bpy)_3]^{3+}$. Each point represents the average of three consecutive shots, with error bars showing the range of measured values. Conditions: 1 mM $[Ru(bpy)_3]^{3+}$, 80 mM sodium borate buffer at pH 8.0.

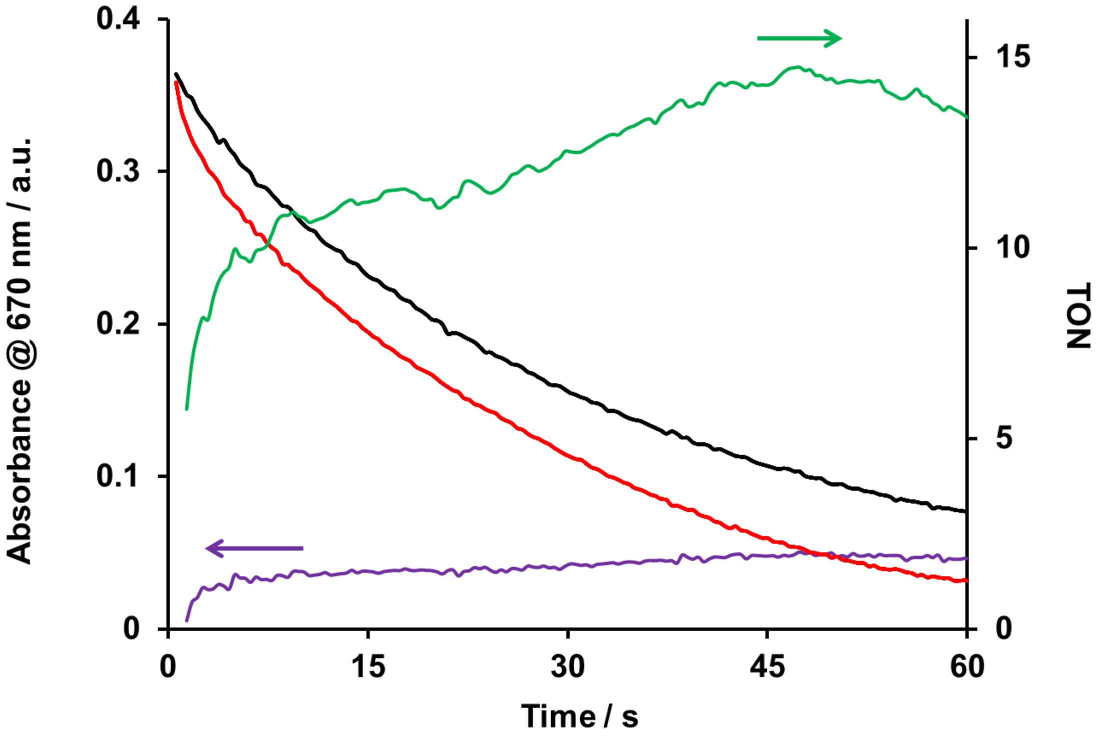

**Figure 4.10** Kinetics of $[Ru(bpy)_3]^{3+}$ self-decomposition (black) and catalytic reduction with 2 μM KH-**4.1** (red line). The purple line is the difference between the two kinetic curves. Turnover number (green line) is calculated as TON = (purple lines/420) / (4 x [KH-**4.1**]), where 420 is the extinction coefficient of $[Ru(bpy)_3]^{3+}$ at 670 nm, and 4 is the stoichiometric coefficient in eq. 4.2. Conditions: 1.0 mM $[Ru(bpy)_3]^{3+}$, 80 mM sodium borate buffer with initial pH 8.0.

The addition of KH-**4.1** (leading to formation of $[Ru(bpy)_3]^{n+}$-**4.1** particles) results in an acceleration of the reaction at the beginning followed by rate decreases due to inhibition of the reaction by the accumulating $[Ru(bpy)_3]^{2+}$.[68] The TON quickly grows to ~10 during the first 15-20 s (the TOF during the first 10 seconds is ~1 $s^{-1}$) and then slowly reaches a plateau. These data are in good agreement with results obtained in the light driven reaction. Importantly, $O_2$ was quantified under similar conditions confirming that $[Ru(bpy)_3]^{3+}$ reduction corresponds to production of $O_2$ (Figure 4.9). The catalyst is efficient only at a high ratio of $[Ru(bpy)_3]^{3+}$/$[Ru(bpy)_3]^{2+}$. In the light-driven system, the rather high ratio is maintained by continuous photogeneration of $[Ru(bpy)_3]^{3+}$. Consequently, the TON in Fig. 4.8 is higher than estimated in Fig. 4.10. The presence of a fast and selective WOC minimizes organic ligand oxidation.[67,68,76] However, if no KH-**4.1** solution is added, the spectral change of $[Ru(bpy)_3]^{2+}$ is close to that in the presence of KH-**4.1** (Figure 4.11), indicating that the decomposition of $[Ru(bpy)_3]^{3+}$, eq 4.3, competes to some extent with catalytic water oxidation, eq 4.2. As a result, the chemical and quantum yields of $O_2$ formation are relatively low.

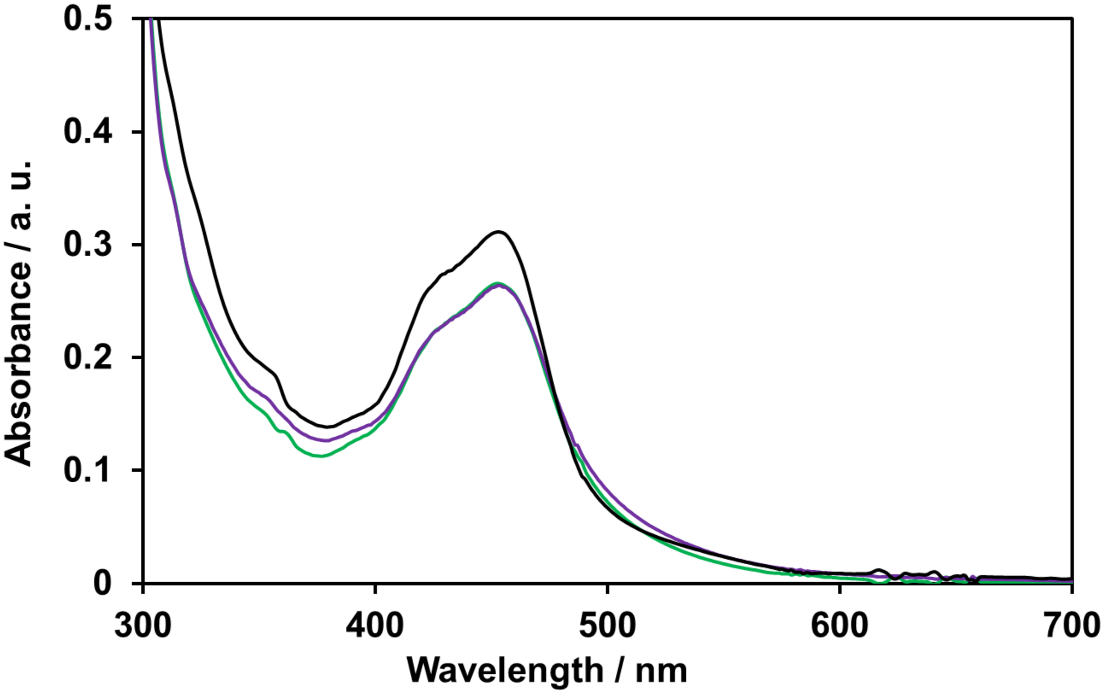

**Figure 4.11** UV-vis spectra of 40-fold diluted solution of 1 mM $[Ru(bpy)_3]^{2+}$ and 5.0 mM $Na_2S_2O_8$ in 80 mM borate buffer before the photodriven catalytic water oxidation reaction (black curve), after this reaction (after irradiation) in the absence (green curve) and presence (purple curve) of 2 μM KH-**4.1**.

### 4.3.4 Stability Studies.

Three experiments indicate that **4.1** is stable in the catalytic medium (pH 8 sodium borate buffer) prior to addition of $[Ru(bpy)_3]^{n+}$. First, the UV-vis spectrum remains unchanged overnight (Figure 4.12 and Figure 4.13). In addition, the IR spectrum of crystals obtained by slow evaporation of the same buffered solution after aging for two years is identical to that of the recently synthesized samples. Also, DLS measurements show that no precipitate forms after KH-**4.1** is aged one month in 80 mM pH 8 borate buffer. A nickel-borate film forms on electrode surfaces by electrodeposition of $Ni^{2+}$ at pH 8 in borate buffer above +1.1 V (consistent with the literature report),[97,98] but no decomposition is observed under non-electrochemical conditions. Thus, UV-vis, IR and DLS all show that KH-**4.1** is stable in buffered aqueous solutions in the absence of photosensitizer, $[Ru(bpy)_3]^{2+}$, and oxidant, persulfate.

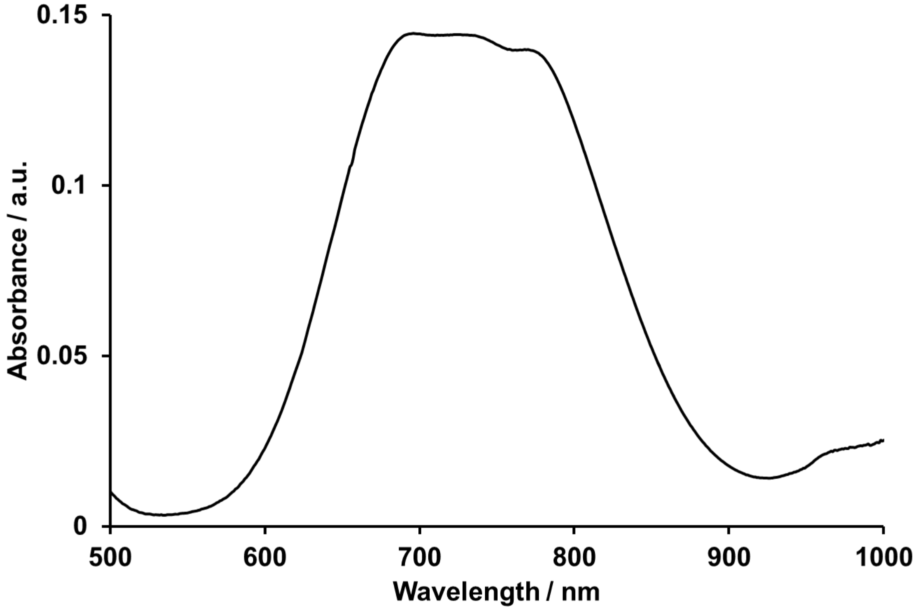

**Figure 4.12** UV-visible spectrum of 6 mM KH-**4.1** in 80 mM pH 8 sodium borate buffer.

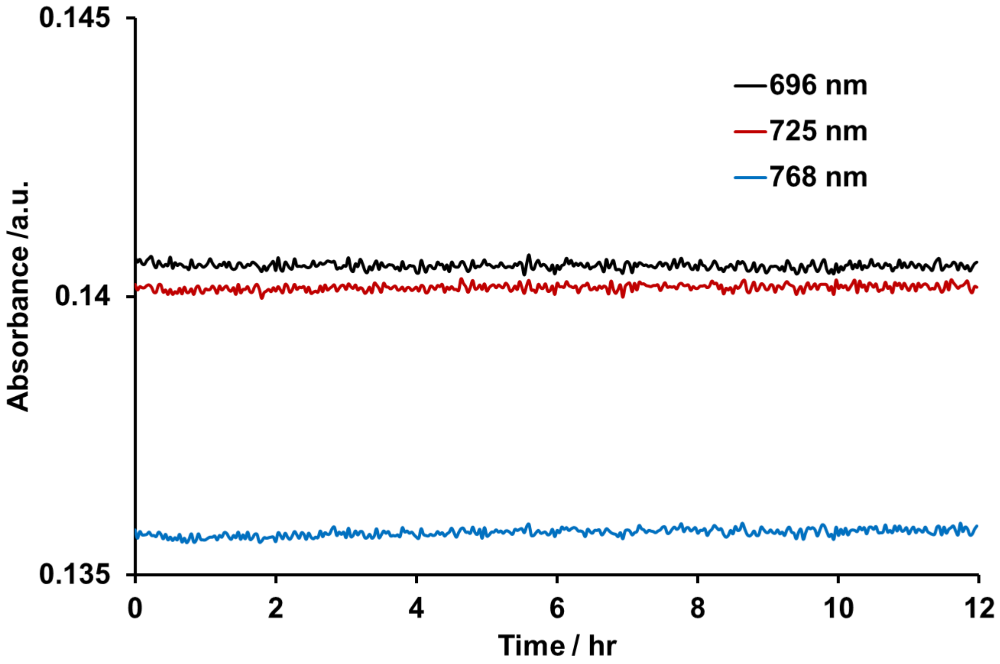

**Figure 4.13** Kinetic traces of the local maxima of KH-**4.1** in the UV-visible spectrum of 6 mM KH-**4.1** in 80 mM pH 8 sodium borate buffer, showing no change in the spectrum upon aging the solution overnight.

More interestingly, four lines of evidence indicate that the **4.1** in the **4.1** (solution) ⇌ $[Ru(bpy)_3]^{n+}$-**4.1** equilibrium is stable and does not form catalytically important nickel hydroxide particles during catalytic water oxidation. First, the FTIR spectra of the full catalyst system before and after irradiation (100 min and 40 turnovers) are almost identical (Figure 4.14). Only slight shifts are observed**,** which is consistent with previous ion pairing studies of POMs,[110] and with the $[Ru(bpy)_3]^{n+}$-**4.1** complexes of Car et al., where similar shifts in the POM unit stretching frequencies are seen. Second, the FTIR spectra show no evidence of additional peaks that would indicate **4.1** decomposes to an active metal hydroxide / oxide catalyst. The FTIR spectra of pure nickel hydroxide and artificially doped KH-**4.1** have characteristic peaks at 525 $cm^{-1}$ and 3640 $cm^{-1}$ (Figure

4.15). The nickel hydroxide peak at 525 cm$^{-1}$ overlaps with one of the metal-oxo stretches of KH-**4.1**, but changes in the ratio of this peak relative to other POM peaks, if visible, would be indicative of the presence of nickel hydroxide. Furthermore, the sharp peak at 3640 cm$^{-1}$ is free of interfering species. No evidence of either of the two nickel hydroxide peaks can be seen in the FTIR spectra after irradiation (after catalytic water oxidation).

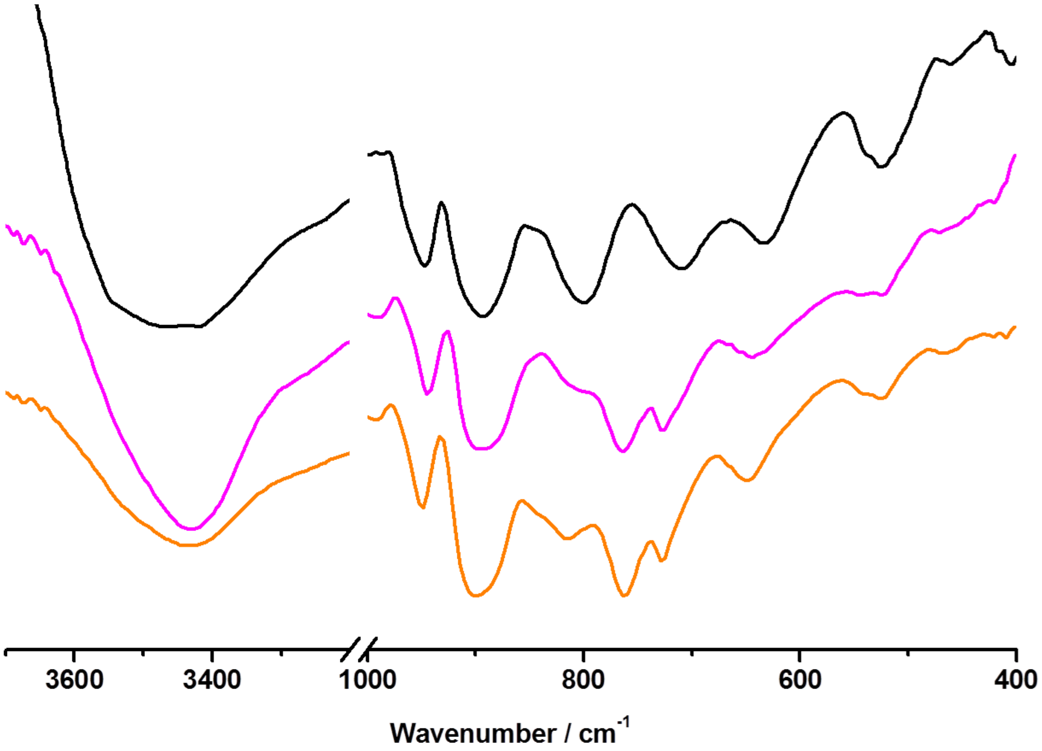

**Figure 4.14** Infrared spectra of KH-**4.1**. Black: spectrum of the freshly prepared and purified KH-**4.1**. Magenta: precipitate obtained from mixing $[Ru(bpy)_3]^{2+}$ and KH-**4.1** solutions (the peaks are a simple superposition of the spectra of each compound). Orange: precipitate isolated from a post reaction solution. The spectra before and after water oxidation (irradiation for 100 minutes, TON ca. 40) show no changes indicative of structural rearrangement or metal oxide formation.

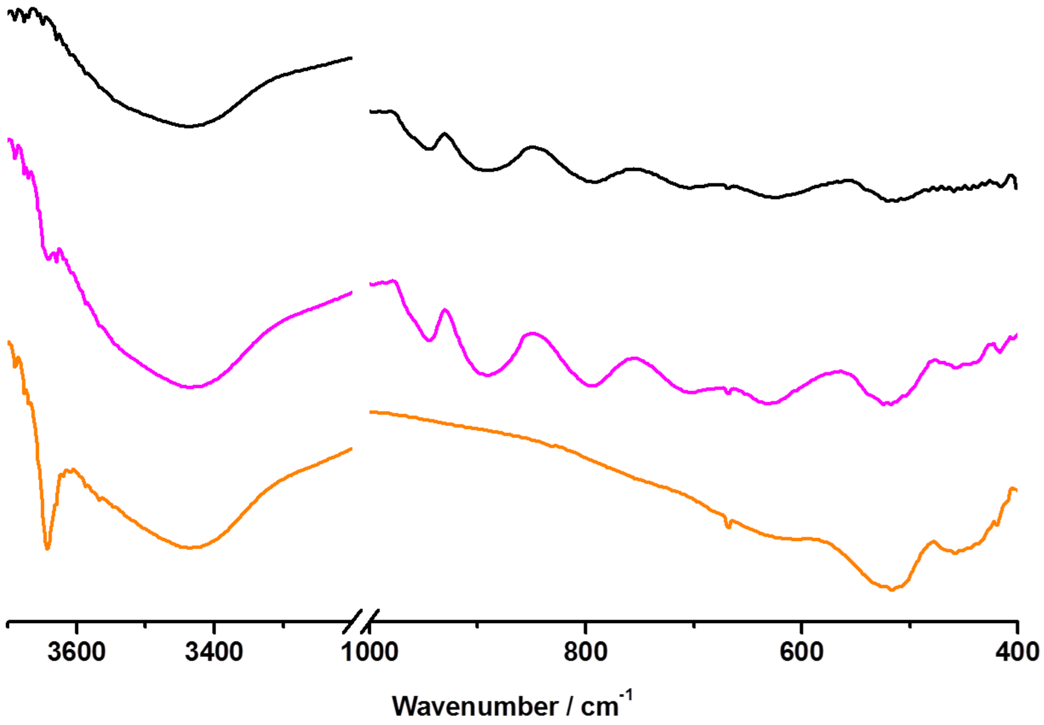

**Figure 4.15** Infrared spectra of KH-**4.1** and nickel hydroxide. Black: spectrum of KH-**4.1**. Magenta: KH-**4.1** doped with ~10% nickel hydroxide. Orange: nickel hydroxide, highlighting the characteristic peaks at 525 cm$^{-1}$ and 3640 cm$^{-1}$ that would be visible if KH-**4.1** decomposes to nickel hydroxide particles under catalytic conditions.

A third argument that **4.1** remains a molecular WOC and is not simply a precursor for catalytic nickel hydroxide particles is the kinetic traces for the catalytic water oxidation in the dark and in the light. They are very similar (Figure 4.8 vs. Figure 4.7), and this would be quite unlikely if **4.1** is merely transforming into catalytic nickel hydroxide *in situ*. A fourth argument that **4.1** is the actual catalyst and not nickel hydroxide or a mixture of the two is that the dependence of the $O_2$ evolution rate on the concentration of **4.1** is similar in both dark and light-driven reactions (Figure 4.8 vs. Figure 4.9).

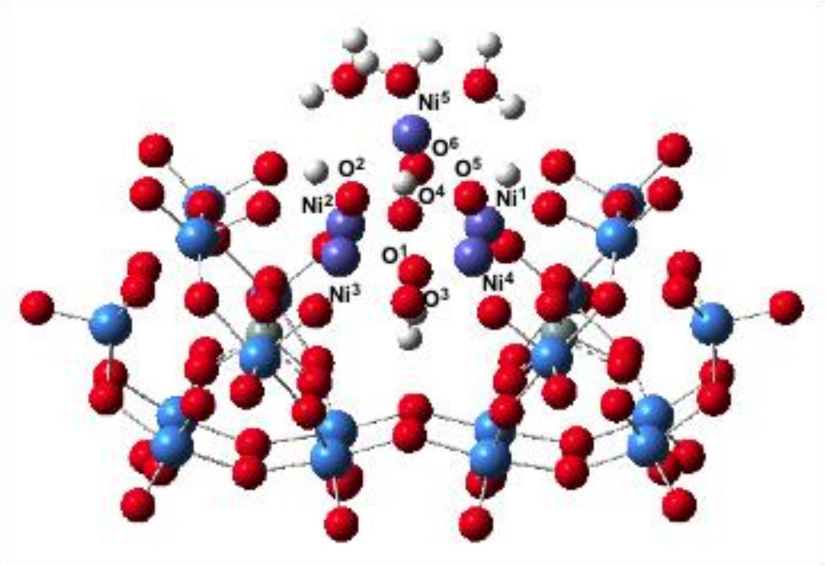

**Figure 4.16** Notation of atoms in the calculated structure of KH-**4.1**.

### 4.3.5 Computational studies

Computational studies of the electronic structure of KH-**4.1** provide additional support for the nature of Ni centers and oxidative stability of the polytungstate ligands (Figure 4.16). It was shown that KH-**4.1** has several lower-lying electronic states among which high-spin ferromagnetically coupled $^{11}$A and antiferromagnetically coupled $^{3}$A states are the lowest in energy: $^{3}$A state is only 1.7 kcal/mol higher in energy than $^{11}$A state. Spin density analyses show that Ni5 and other Ni-atoms (i.e. Ni1, Ni2, Ni3 and Ni4) are very different. In the $^{11}$A state, Ni1-Ni4 centers are the high-spin Ni(II) centers with 1.85, 1.72, 1.76 and 1.71 α-spins, respectively, while Ni5 has only 0.46 α-spins. The rest of 10 unpaired α-spins are located on bridging (between Ni-centers) O-centers. Larger unpaired spins (0.52 and 0.60) are on $O^3$ and $O^1$. In the $^{3}$A state, the Ni1-Ni4 centers are antiferromagnetically coupled, while Ni5 has only 0.45 unpaired α-spin. The fully antiferromagnetically coupled $^{1}$A state is only 0.6 kcal/mol higher than $^{3}$A state. The frontier orbital analysis (HOMOs and LUMOs) is consistent with the above presented electronic state analyses. The several top singly-occupied MOs of a high-spin ground state KH-**4.1** are mostly Ni core orbitals, and there is almost no involvement of tungstate orbitals. The findings indicate that the polytungstate ligands are unlikely to participate in the water oxidation reaction and should be effectively inert under catalytic conditions.

## 4.4 Conclusions

We report a nickel-containing water oxidation catalyst comprising a $[Ni_5(OH)_6(OH_2)_3]^{4+}$ assembly cradled in the central cavity of the clamshell-shaped polytungstate, $[Si_2W_{18}O_{66}]^{16-}$. This polyanion, $[Ni_5(OH)_6(OH_2)_3(Si_2W_{18}O_{66})]^{12-}$, **4.1**, forms a minimially soluble complex in both dark and light-driven reactions with $[Ru(bpy)_3]^{n+}$. Several lines of spectroscopic, kinetic, and other evidence confirm that this polyoxometalate-based WOC remains molecular throughout and does not form apprecible or kinetically significant nickel hydroxide under the catalytic water oxidation reaction conditions.

# *Chapter 5*

## Chapter 5 : A Dodecanuclear Zn Cluster Sandwiched by Polyoxometalate Ligands

with Yurii V. Geletii, Chongchao Zhao, Djamaladdin G. Musaev, Jie Song

and Craig L. Hill

(Published partially in *Dalton Transactions*, 2012, **41**, 9908. - Reproduced

by permission of The Royal Society of Chemistry )

**Abstract**: A dodecazinc silicotungstate $K_{20}Na_2[Zn_6(OH)_7(H_2O)(Si_2W_{18}O_{66})]_2$ $34H_2O$ (**5.1**) has been synthesized and characterized by X-ray crystallography, elemental analysis, infrared, UV-vis spectroscopy, cyclic voltammetry, acid/base titration, and DFT calculations. The twelve zinc atoms between the two $[Si_2W_{18}O_{66}]^{16-}$ frameworks makes this complex more stable hydrolytically than the heteropolytungstate ligands, $[Si_2W_{18}O_{66}]^{16-}$, themselves. The structurally unique central $Zn_{12}$ core is formed by the fusion of two $[Zn_6(OH)_7(H_2O)]^{5+}$ units through two edge-sharing $Zn_6$ atoms. DFT B3LYP calculations give HOMO–LUMO and (HOMO-1)–LUMO energy gaps of ~3.65 and 3.91 eV, respectively as compared to the band gap in ZnO of 3.35 eV.

## 5.1 Introduction

In the past two decades, transition-metal-based high-nuclear complexes (ten or more metals) have attracted interest based on their electronic, magnetic, optical and biological properties. Polyoxometalates (POMs) are one category of metal oxide clusters that can function as all-inorganic ligands with high hydrolytic and oxidative robustness.[41,111-114] To date several high-nuclearity paramagnetic all-inorganic 3d-metal-oxo-containing POMs have been reported,[11,52,115-117] but no high-nuclearity diamagnetic metal-substituted POMs. POMs with two to six Zn centers have been reported but none with a higher nuclearity. POMs have been reported with the following number of Zn ions in the polyanion unit: two ($[(Zn^{II}OH_2)_2(Fe^{III})_2(X_2W_{15}O_{56})_2]^{14-}$ (X = P, As),[118] $[Zn_2(H_2O)_6(WO_2)_2(SbW_9O_{33})_2]^{10-}$,[119] $[Zn_2M_2(PW_9O_{34})_2]^{12-}$ (M = Na, Li),[120] $[(\alpha\text{-}AsW_9O_{33})_2WO(H_2O)Zn_2(H_2O)_2]^{10-}$,[121] three

$[Zn_3(H_2O)_3(\alpha\text{-}XW_9O_{33})_2]^{12-}$ (X = As$^{III}$, Sb$^{III}$),[121] four $[Zn_2Bi_2(\beta\text{-B-}ZnW_9O_{34})_2]^{14-}$,[122] $[Zn_4(H_2O)_2(\text{B-}\alpha\text{-}XW_9O_{34})_2]^{12-}$ (X = Si, Ge),[1,123] $[Zn_4(H_2O)_2(XW_9O_{34})_2]^{10-}$ (X = P, As),[124,125] $[Zn_4(H_2O)_2(X_2W_{15}O_{56})_2]^{16-}$ (X = P, As),[124,126] $[Zn_4(H_2O)_2(H_4AsW_{15}O_{56})_2]^{18-}$,[127] $[\{Zn_4(OH)_2(H_2O)_2\}\{\text{B-}\alpha\text{-}AsW_9O_{34}\}\{\text{B-}\beta\text{-}AsW_8O_{31}\}\{(RuC_6H_6)_3\}]^{6-}$,[128] $[Zn_4(H_2O)_2(GaW_9O_{34})_2]^{14-}$,[129] $[\{Zn_2W(O)O_3\}_2H_4\{\alpha\text{-}SiW_9O_{33}\}_2]^{8-}$,[130] $[\{Zn_2W(O)O_3\}_2H_4\{\beta\text{-}SiW_9O_{33}\}_2]^{8-}$,[130] $[\{Zn(OH_2)(\mu_3\text{-}OH)\}_2\{Zn(OH_2)_2\}_2\{\gamma\text{-}HSiW_{10}O_{36}\}_2]^{8-}$,[130,131] five $[WZn_3(H_2O)_2(ZnW_9O_{34})_2]^{12-}$,[132] and six $[(Zn\ Cl)_6(BiW_9O_{33})_2]^{12-}$,[133] $[Zn_6(phen)_2(AsW_9O_{33})_2]^{4-}$ (phen = phenanthroline),[134] $[(ZnCl)_6(AsW_9O_{33})_2]^{14-}$,[134] $[Zn(C_2N_2H_8)_2\}_2\{(GeW_9O_{34})_2Zn_4(C_2N_2H_9)_2\}^{4-}$,[135] $[Zn_6(imi)_6(\text{B-}\alpha\text{-}HAsW_9O_{33})_2]$ (imi = imidazole),[136] $[Zn(Hen)]_6[\text{B-}\alpha\text{-}HAsW_9O_{33}]_2$ [137] (en = ethylenediamine). These multi-zinc nuclear compounds were studied as catalysts[130,131] and molecular materials with interesting optical properties.[137]

We report here a POM containing a dodecanuclear Zn$^{II}$-oxo cluster: $K_{20}Na_2[Zn_6(OH)_7(H_2O)(Si_2W_{18}O_{66})]_2\cdot 34H_2O$ (**5.1**).

## 5.2 Experimental

### Materials and Methods

$Na_{10}[\alpha\text{-}SiW_9O_{34}]$ was prepared following the literature procedure.[60] All reagents used were from the commercially available sources and of the highest purity. IR spectra (2% sample in KBr pellet) were taken on a NicoletTM 6700 FT-IR spectrometer. Elemental analyses (K, Na, Zn, Si and W) were done by Galbraith Laboratories (Knoxville, Tennessee). UV-vis spectra were taken using an Agilent 8453 UV-vis spectrometer. Cyclic voltammograms were obtained at room temperature using a BAS CV-50W voltammetric analyzer, a Pt-wire auxiliary electrode, a glassy-carbon working electrode, and a Ag/AgCl (3 M NaCl) BAS reference electrode. All redox potentials are reported relative to this reference electrode.

### Synthesis of $K_{20}Na_2[Zn_6(OH)_7(H_2O)(Si_2W_{18}O_{66})]_2 \cdot 34H_2O$ (5.1)

$Na_{10}[\alpha\text{-}SiW_9O_{34}]$ (1.6 g, 0.65 mmol) was dissolved in 30 mL of water. The pH was adjusted to 6.8 by 1 M HCl, then $ZnCl_2$ (130 mg, 0.95 mmol) was added. The pH dropped to ~5.4. This solution was heated to 85 ℃ for 1 hr. Some precipitation became visible. After cooling the solution to room temperature, the pH was ~6.8. Subsequently the pH was adjusted to 5.8 by 0.5 M HCl. Addition of 4 mL of saturated KCl to the suspension and stirring for 10 min produced a precipitate which was separated by filteration. Colorless needle-shaped crystals were collected from the reaction solution after one week. Yield: 6 % based on W. IR (KBr, / $cm^{-1}$): 994(m), 946 (m), 887 (s), 854 (sh), 817 (sh), 790 (s), 711 (s), 660 (w), 610 (m), 532 (m), 462 (w). Elemental analysis calcd for **5.1** (%): K, 6.89; Na, 0.405; Zn, 6.92; Si, 0.990; W, 58.4. Found (%): K, 7.53; Na, 0.465; Zn, 6.49; Si, 1.35; W, 59.2.

### X-Ray crystallography of $K_{20}Na_2[Zn_6(OH)_7(H_2O)(Si_2W_{18}O_{66})]_2 \cdot 34H_2O$ (5.1)

Single crystals suitable for X-ray structure analysis were each coated with Paratone-N oil, suspended on a small fiber loop and placed in a cooled nitrogen gas stream at 173 K on a Bruker D8 APEX II CCD sealed tube diffractometer with graphite monochromator Mo K$\alpha$ ($\lambda$ = 0.71073 Å) radiation. Data collection, indexing and initial cell refinements were all carried out using SMART[63]. Frame integration and final cell refinements were done using SAINT.[64] The molecular structure of each complex was determined using direct methods and Fourier techniques and refined by the standard full-matrix least-squares procedure. A multiple absorption correction, including face indexing, was applied using the program SADABS.[65] Structure solution, refinement, graphics and generation of publication materials were performed using SHELXTL, v 6.14 software.[66] SQUEEZE command of the PLATON software was used to remove the scattering from the highly disordered counterions and water molecules. The resulting new HKL file was applied to further refine the structure.

### Computational procedures

Since calculations of full complex, **5.1**, at a reasonable computational level are not possible, we studied the electronic structure of the monomer, **5.1_m**. In **5.1_m**, the $[Zn_6(H_2O)(OH)_7]^{5+}$ cluster is incorporated into the $[Si_2W_{18}O_{66}]^{16-}$ fragment.

All reported calculations were performed using the Gaussian 09 program.[101] The geometries of all species were optimized without any symmetry constraint at the B3LYP[102,103,138] level of theory. In these calculations we used Hay-Wadt effective core potentials (ECPs) with the associated Lanl2dz basis set for transition metals[105-107] and the standard 6-31G* split-valence-polarization basis set for all other atoms. The solvent effects were estimated by using the self-consistent reaction field IEF-PCM method[108] with water as a solvent (dielectric constant $\varepsilon = 78.39$).

**Table 5.1** Crystal Data and Structure refinement for **5.1.**

| | $H_{86}K_{20}Na_2O_{182}Si_4W_{36}Zn_{12}$ |
|---|---|
| Temperature / K | 173(2) |
| Radiation (λ) / Å | 0.71073 |
| Crystal system | Triclinic |
| Space group | $P\bar{1}$ |
| $a$ / Å | 16.5333(12) |
| $b$ / Å | 17.6488(13) |
| $c$ / Å | 19.2093(14) |
| $\alpha$ / ° | 70.2990(10) ° |
| $\beta$ / ° | 77.5210(10) ° |
| $\gamma$ / ° | 63.8060(10) ° |
| $V$ / Å$^3$ | 4720.1(6) |
| $Z$ | 1 |
| $\rho_{calcd}$ / g cm$^{-3}$ | 3.990 |
| $\mu$ / mm$^{-1}$ | 23.906 |
| $F$(000) | 5024 |
| Crystal size / mm$^3$ | 0.44 x 0.35 x 0.12 |
| Reflections collected | 79742 |
| Independent reflections | 22478[R(int) = 0.0725] |
| Absorption correction | Numerical |
| Refinement method | Full-matrix least-squares on $F^2$ |
| Goodness-of-fit on $\|F\|^2$ | 1.053 |
| Final $R$ indices [$R > 2\sigma(I)$] | $R_1^a = 0.0469$, $wR_2^b = 0.1310$ |
| $R$ indices (all data) | $R_1^a = 0.0574$, $wR_2^b = 0.1372$ |
| Largest diff. peak and hole / e Å$^{-3}$ | 3.468 and -2.926 |

$^a R_1 = \Sigma||F_0| - |F_c|| / \Sigma|F_0|$; $^b wR_2 = \Sigma[w(F_0^2 - F_c^2)^2]/ \Sigma[w(F_0^2)^2]^{1/2}$

## 5.3 Results and Discussion

### 5.3.1 Synthesis and structure of $K_{20}Na_2[Zn_6(OH)_7(H_2O)(Si_2W_{18}O_{66})]_2{\bullet}34H_2O$ (5.1).

The reaction of $ZnCl_2$ and $Na_{10}[A\text{-}\alpha\text{-}SiW_9O_{34}]$ (molar ratio = 1.5 : 1) in aqueous solution leads to a solution which upon slow evaporation at room temperature for 7 days gives colorless needle-like crystals of **5.1** with 6% yield based on tungsten. The ratio between $Zn^{2+}$ and $[\alpha\text{-}SiW_9O_{34}]^{10-}$ is vital for synthesis of the target polyanion. If the synthesis is conducted at higher molar ratio between $Zn^{2+}$ and $SiW_9$, only powders are obtained.

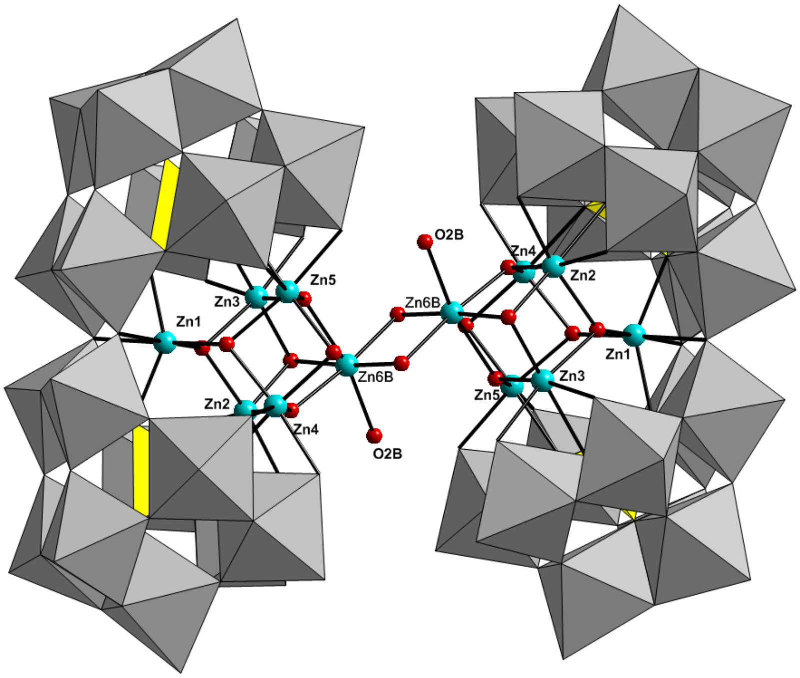

**Figure 5.1** Combined polyhedral/ball-and-stick representations of the polyanion units in **5.1** $WO_6$ units: grey polyhedra; $SiO_4$ units: yellow tetrahedra; Zn: Cyan spheres; O: red spheres.

The $C_{2h}$ polyanion in **5.1** is composed of a large $\{[Zn_6(OH)_7(H_2O)]_2\}^{10+}$ moiety sandwiched between two $[Si_2W_{18}O_{66}]^{16-}$ fragments (Figure 5.1). The polyanion

$[Si_2W_{18}O_{66}]^{16-}$ is constituted by fusion of two $[\alpha\text{-}SiW_9O_{34}]^{10-}$ units, which was reported previously to form under acidic conditions and at high concentrations of $K^+$.[79,83] The central $Zn_{12}$ core is formed by the fusion of two $[Zn_6(OH)_7(H_2O)]^{5+}$ units through two edge sharing Zn6 atoms. In each $Zn_6$ unit, five zinc atoms (Zn1, Zn2, Zn3, Zn4 and Zn5) are located inside the POM framework pocket, and Zn6 is located outside the pocket. Zn1 is connected to two silicon tetrahedra; Zn3 and Zn5 are connected to one silicon, and Zn2 and Zn4 are connected to the other silicon. Zn6 connects with Zn2 and Zn3 via edge sharing oxygen atoms and with Zn4 and Zn5 via corner sharing oxygen atoms. There is a repartition disorder of the Zn6 atom on the Zn6A and Zn6B positions; the best refinement was obtained with occupation factors of about 0.65 and 0.35 (Figure 5.1 shows the polyanion structure taking Zn6B as an example). Figure 5.2 shows the positions of Zn6A compared to Zn6B (only half of the $\{[Zn_6(OH)_7(H_2O)]_2\}^{10+}$ fragment is shown for clarity). The distance between Zn6A and Zn6B is 1.105 Å, and they are located either closer to O39 or to O71, shifting to one side of the pocket. Bond valence sum (BVS) calculations indicate that all bridging oxo groups linking adjacent zinc atoms are either mono- or diprotonated. Specifically, oxygen atoms O1B, O34, O36, O37, O39, O72, and O71 are monoprotonated whereas oxygen atom O2B (O1A for Zn6A) are diprotonated. The Zn-O distances are in the range from 1.978 to 2.261 Å. The overall metal topology of **5.1** resembles two connected octahedra (Figure 5.3). The shortest distance of neighboring Zn ···Zn is 2.977 Å. $K^+$ appears to have a structural directing role, as

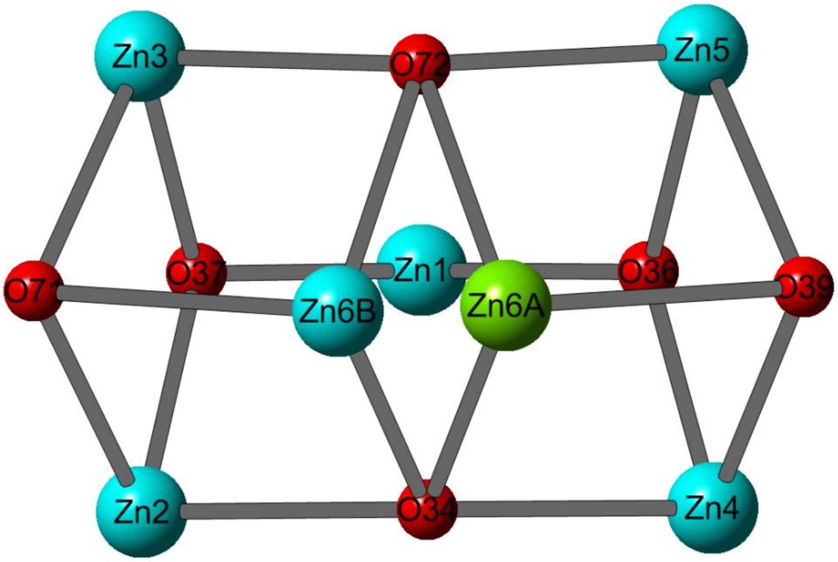

**Figure 5.2** Ball and stick representation of half of the central fragment of **5.1**, showing the positions of the disordered Zn6B and Zn6A.

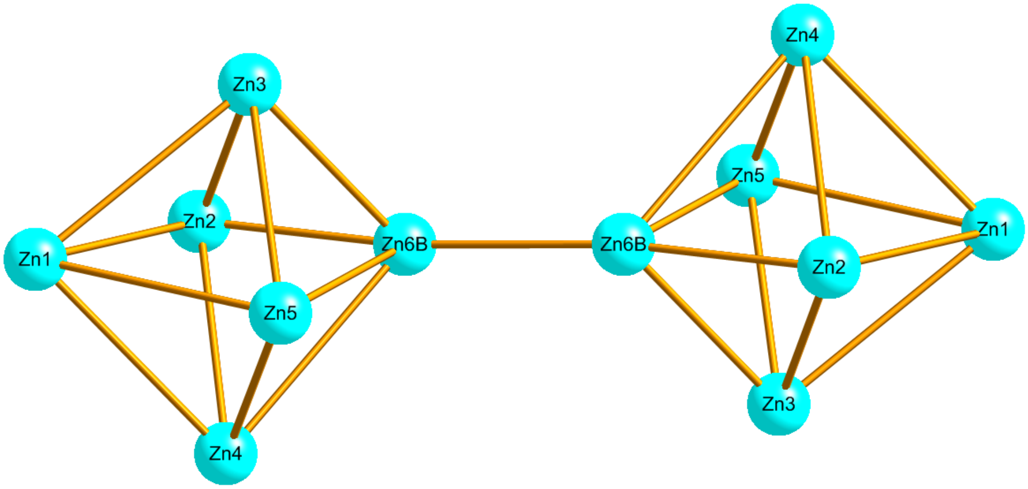

**Figure 5.3** The zinc-only skeleton of **5.1**.

can be seen from the crystal structure (Figure 5.4). In the crystal, two $[Si_2W_{18}O_{66}]^{16-}$ frameworks are linked not only by $Zn_{12}$ fragment, but also by $K_4$ and $K_{10}$ through the linking of terminal oxygens. $K_4$ also associates two $\{[Zn_6(OH)_7(H_2O)(Si_2W_{18}O_{66})]_2\}^{22-}$ anions to form chains. We have made considerable attempts to acquire $^{29}Si$ and $^{183}W$ NMR on the title complex. Unfortunately all efforts to obtain these NMR spectra have failed because this $Zn_{12}$ POM is simply too insoluble. We conducted cation exchange experiments to increase the solubility of the complex but these exchange reactions lead to some decomposition and are thus not informative.

Other oxygen-bridged transition metal centers ($Cu_5$[30], $Fe_4$[36], $V_2$[36]) incorporated into the $[Si_2W_{18}O_{66}]^{16-}$ POM framework have been reported, but high nuclearity clusters like this $Zn_{12}$ core have never been obtained. The $Zn_{12}$ core in **5.1** is the first $Zn_{12}$ cluster in a totally inorganic environment. Up to now, only two kinds of dodecanuclear POM structures have been described, a $Fe_{12}/Ti_{12}$ core and a $Ni_{12}$ core[115,116] (Figure 5.5). The $Fe_{12}O_{46}/Ti_{12}O_{46}$ core (Figure 5.5a ) is composed of four groups of three edge-shared, corner-linked $FeO_6/TiO_6$ octahedra, and outside the metal cluster are four $\{P_2W_{15}\}$ units. The $Ni_{12}$ (Figure 5.5b) is formed by the connection of three distorted $[Ni_4O(OH)_3]$ units, and outside the $Ni_{12}$ cluster are three $\{PW_9\}$ units, a $WO_4$ tetrahedron and a $[W_7O_{26}(OH)]^{11-}$ unit. The $Fe_3O_6$ and $Ti_3O_6$ moieties cap $\{P_2W_{15}\}$ units and complete Wells-Dawson structures, while the $Ni_4O(OH)_3$ moieties cap $\{PW_9\}$ units to complete Keggin structures. For the “open Wells-Dawson” POM, $[Si_2W_{18}O_{66}]^{16-}$, both the pentazinc (as the pentacopper structure in Figure 1.9c) or hexazinc clusters can form a cap to complete the structure.

However, the dimerized hexazinc (i.e. dodecazinc) cluster in **5.1** is the only polyzinc unit obtained to date.

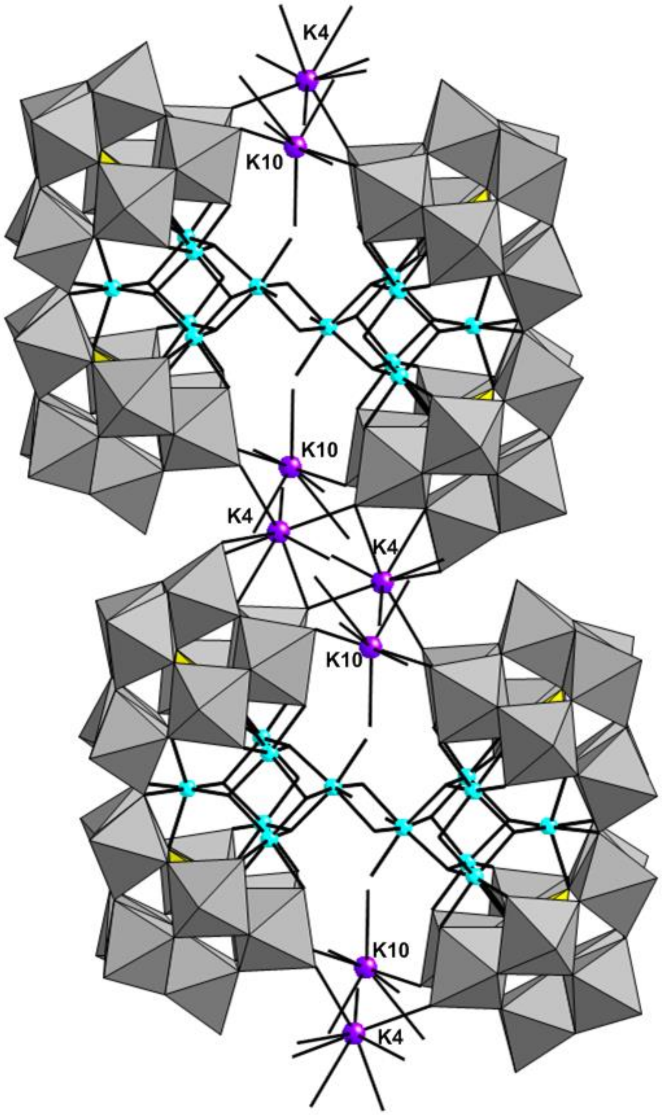

**Figure 5.4** Combined polyhedral/ball-and-stick representation of **5.1** in the lattice. The color code is as follows: zinc (cyan), tungsten (grey), silicon (yellow), and K (purple).

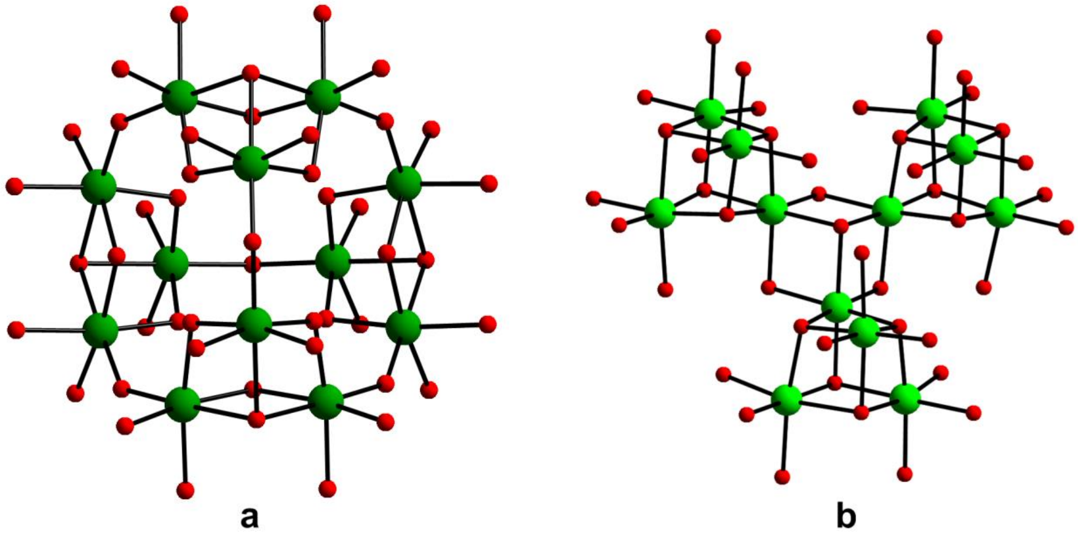

**Figure 5.5** Polyhedral views of the dodecanuclear-transition metal clusters in the reported sandwich-type POMs: $Fe_{12}/Ti_{12}$ cluster (a) and $Ni_{12}$ cluster (b) The color code is as follows: Fe/Ti (dark green), Ni (light green) and oxygen (red).

### 5.3.2 Electronic absorption spectra

Figure 5.6 shows the UV spectra of **5.1** and the POM fragment $[Si_2W_{18}O_{66}]^{16-}$. The extinction coefficient of **5.1** in aqueous solution at 250 nm is ca. $1.2 \times 10^5\ M^{-1}cm^{-1}$, and that of $[Si_2W_{18}O_{66}]^{16-}$ is ca. $0.46 \times 10^5\ M^{-1}cm^{-1}$. The latter number is about twice lower than that of **5.1**, which is consistent with number of $[Si_2W_{18}O_{66}]^{16-}$ units in the two compounds. The UV spectra of **5.1** and the POM fragment $[Si_2W_{18}O_{66}]^{16-}$ in aqueous solution both display an absorption peak at 192 nm. The principal absorption ($O_{b,c} \rightarrow W$) band in $[Si_2W_{18}O_{66}]^{16-}$ and **5.1** is at 250 nm and 255 nm, respectively. The shift in this band reflects the incorporation of the zinc metal into the framework. The shoulder at 279 nm in spectra of **5.1** (identified by fitting the spectra with multiple Gaussian peaks using "Origin" data analysis and graphing software) likely derives from increased oxygen-to-metal transitions in the dodecazinc cluster. The UV spectra of 9 μM **5.1** in water are not changed after 15 hours (less than 1 %, which is within the instrument variability) (Figure 5.7). This indicates that the $[Si_2W_{18}O_{66}]^{16-}$ structure remains essentially intact in **5.1**. In contrast, $[Si_2W_{18}O_{66}]^{16-}$ alone is hydrolytically unstable and converts to $[\alpha\text{-}SiW_{11}O_{39}]^{8-}$.[79] This dodecazinc POM is non-luminescent in aqueous solution.

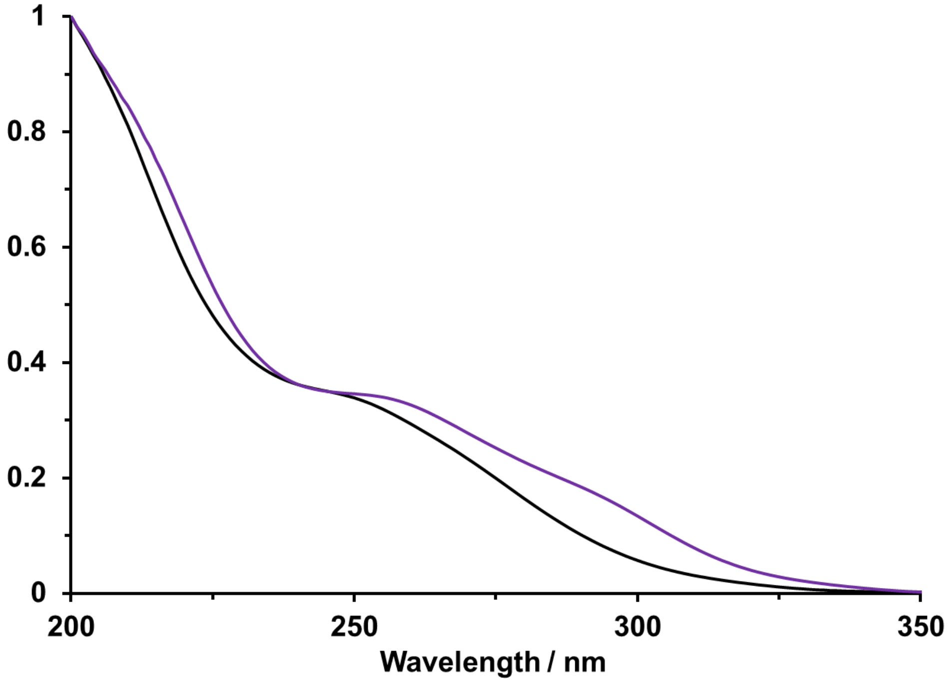

**Figure 5.6** Normalized UV-vis spectra of **5.1** (purple curve) and $K_{16}\alpha\text{-}[Si_2W_{18}O_{66}]$ (black curve) in aqueous solution at 25 ℃.

### 5.3.3 Acid-base titration

The titration of 1.6 mM of **5.1** by 0.1 M HCl from pH 8.9 (pH after dissolution of **5.1** in water) to pH 2.5 shows the consumption of 16 protons per one molecule of **5.1** (Figure 5.8). Multiple successive $pK_a$ values are undistinguishable in this pH range. This aqueous solution was aged for 2 hrs before it was back titrated with NaOH solution. The pH increased only by 0.1 unit during the aging, which accounts for consumption of 0.6

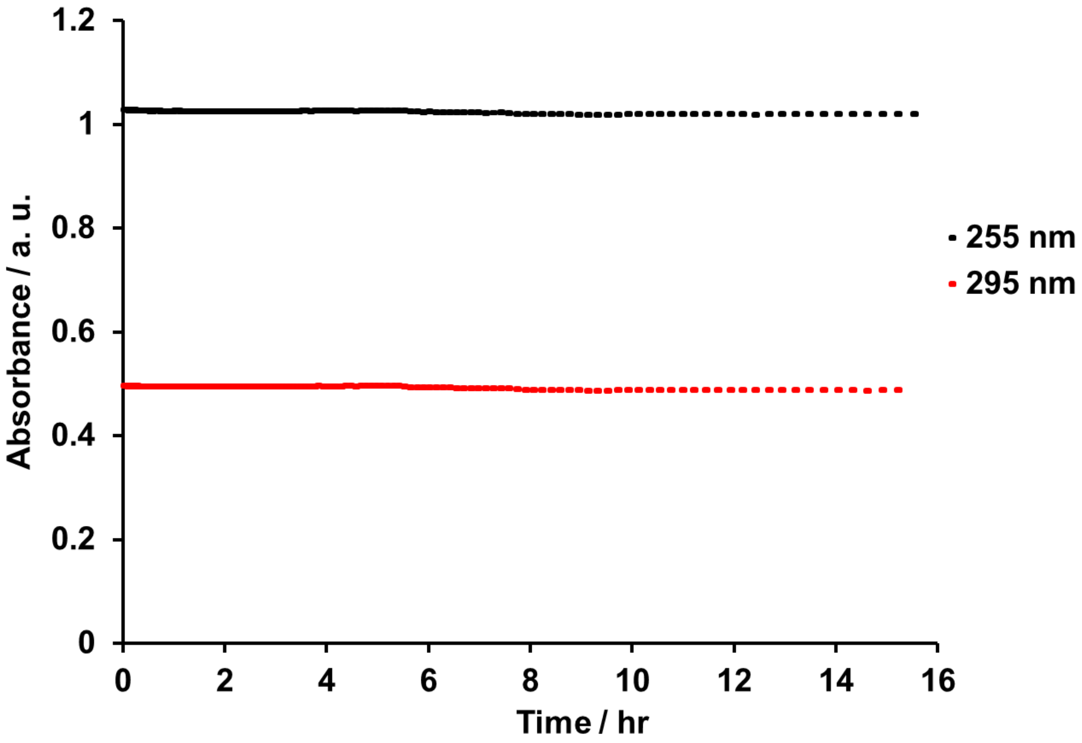

**Figure 5.7** Changes in absorbance at 255 nm and 295 nm of 9 µM **5.1** in water with time.

proton per POM. The back titration curve is slightly different indicating a slow decomposition and/or isomerization of **5.1** at pH 2.5. In contrast, the titration of 3.3 mM of $[Si_2W_{18}O_{66}]^{16-}$ between the natural pH 8.2 and pH 2.5 is completely irreversible even without aging (Figure 5.8, insert), indicating the instability of this isopolyanion under acidic conditions.

### 5.3.4 Electrochemistry

The redox properties of **5.1** and $[Si_2W_{18}O_{66}]^{16-}$ were studied at pH 4.8 in 0.4 M sodium acetate buffer (Figure 5.9). The cyclic voltammograms (CVs) of **5.1** and

$[Si_2W_{18}O_{66}]^{16-}$ are similar, but W(VI)-reductions in **5.1** take place at slightly more negative potentials,

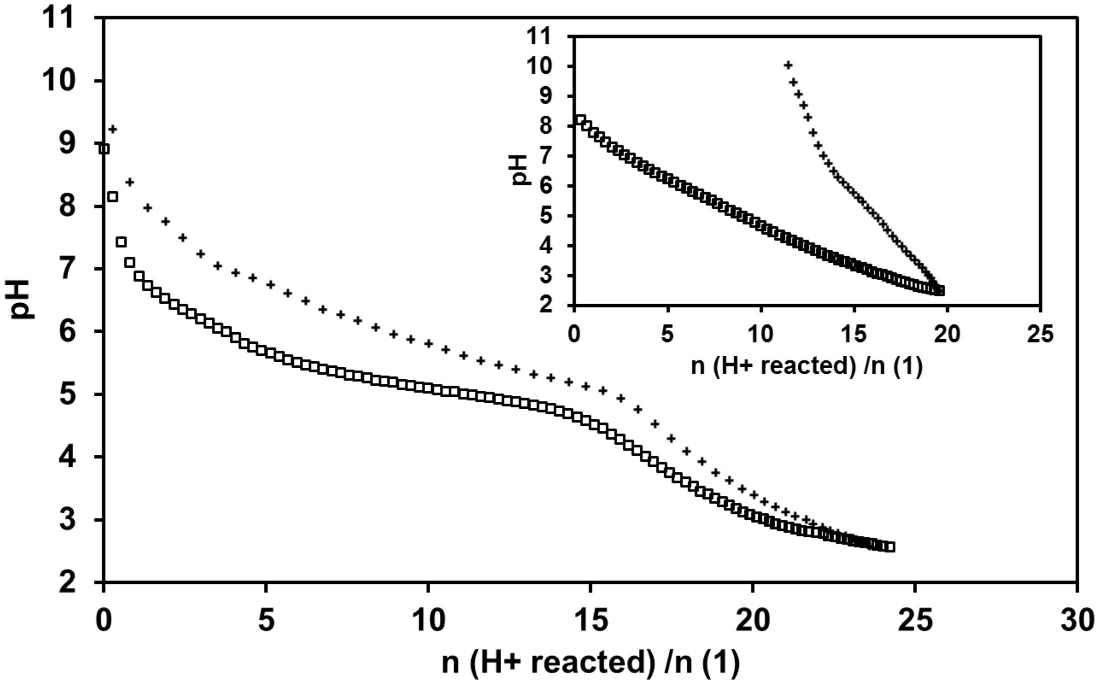

**Figure 5.8** The acid/base titration of 7.4 μmol (83.8 mg) of **5.1** and 15 μmol (82.6 mg) of $K_{16}\alpha$-$[Si_2W_{18}O_{66}]$ (insert) between pH ca. 9 and ca. 2.5 with 0.1 M HCl (squares) and between pH ca. 2.5 and ca. 9 with 0.2 M NaOH (crosses). Initial volume = 4.5 mL, initial pH values are the natural pH values (8.92 for **5.1** and 8.47 for $K_{16}\alpha$-$[Si_2W_{18}O_{66}]$). The measured pH is plotted versus n ($H^+$ reacted ) / n (**5.1**). n ($H^+$ reacted) = n (HCl added) – n ($H^+$ in the solution). Solutions were deaerated with Ar prior to use. The back titration of **5.1** with aqueous NaOH solution was done after aging the solution at pH 2.5 for 2 hrs, and the back titration of $K_{16}\alpha$-$[Si_2W_{18}O_{66}]$ was done immediately after the pH of the solution lowered to 2.5.

which is consistent with the more negative charge of the entire polyanion. Based on the value of the current, the second reduction peak is likely to be two-electron process. In order to compare the stability of **5.1** and $[Si_2W_{18}O_{66}]^{16-}$ in this buffer, the time profiles of the CVs of each were also recorded. The CVs of **5.1** in 0.4 M sodium acetate buffer solution change very slowly with a storage time. Some changes in the CVs are observed after 3 days, which becomes evident after 11 days (Figure 5.10). In contrast, the CV of $[Si_2W_{18}O_{66}]^{16-}$ becomes noticably different after 3 days of storage and is completely altered after 11 days (Figure 5.11). As pointed out previously, $[Si_2W_{18}O_{66}]^{16-}$ decomposes into $[\alpha\text{-}SiW_{11}O_{39}]^{8-}$,[79] which is stable between pH 4.5 to 7.[60]

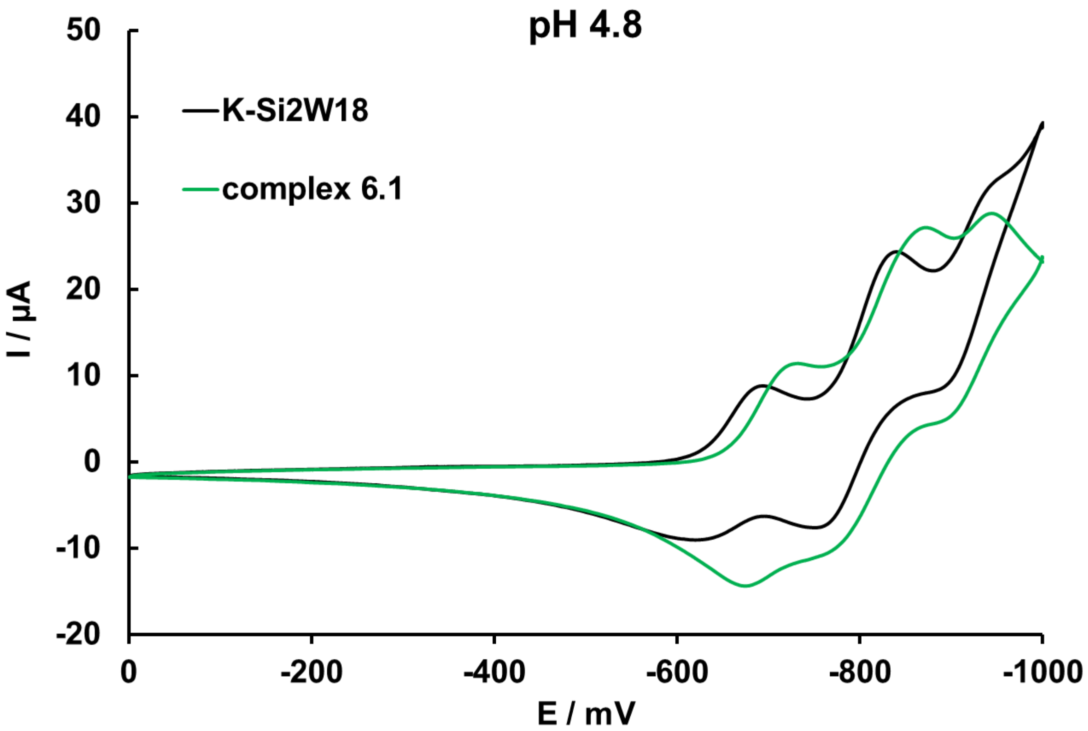

**Figure 5.9** Cyclic voltammograms (CVs) of 0.5 mM **5.1** and 1 mM $K_{16}\alpha\text{-}[Si_2W_{18}O_{66}]$ in 0.5 M sodium acetate buffer, pH 4.8, scan rate 25 mV $s^{-1}$, at ambient temperature.

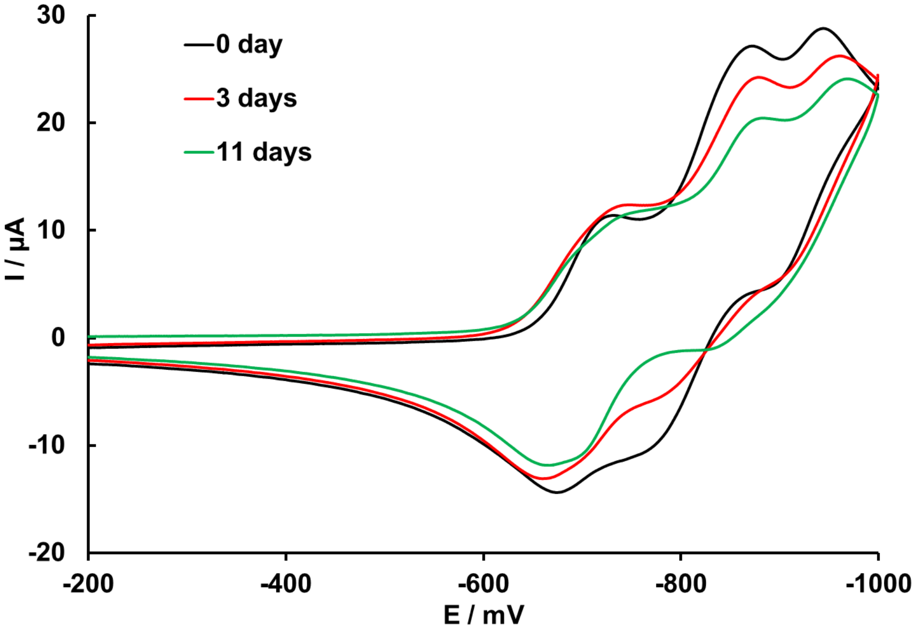

**Figure 5.10** Changes in cyclic voltammograms with storage time of 0.5 mM **5.1** in 0.5 M sodium acetate buffer, pH 4.8, scan rate 25 mV s$^{-1}$, at ambient temperature.

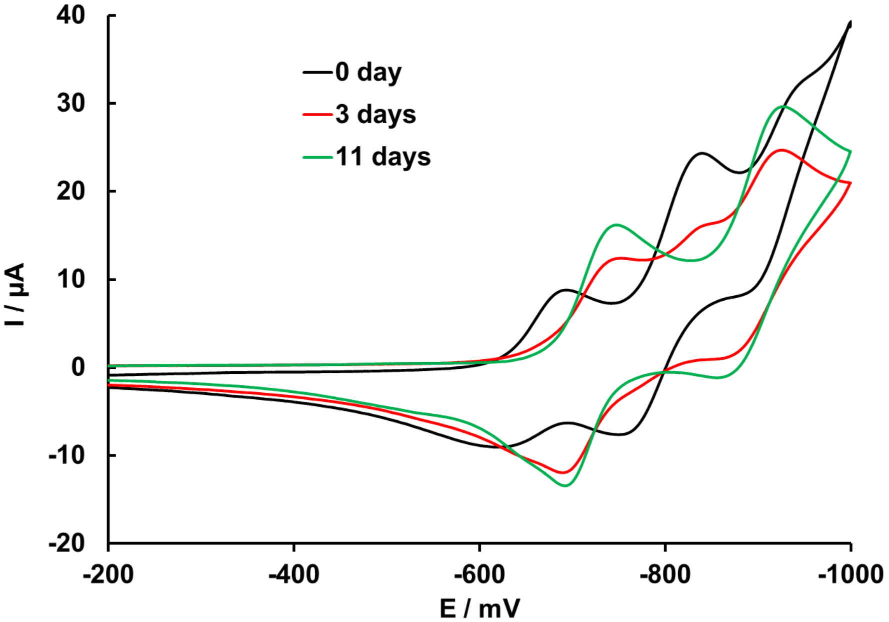

**Figure 5.11** Changes in cyclic voltammograms with storage time of 1 mM $K_{16}[Si_2W_{18}O_{66}]$ in 0.5 M sodium acetate buffer, pH 4.8, scan rate 25 mV s$^{-1}$, at ambient temperature.

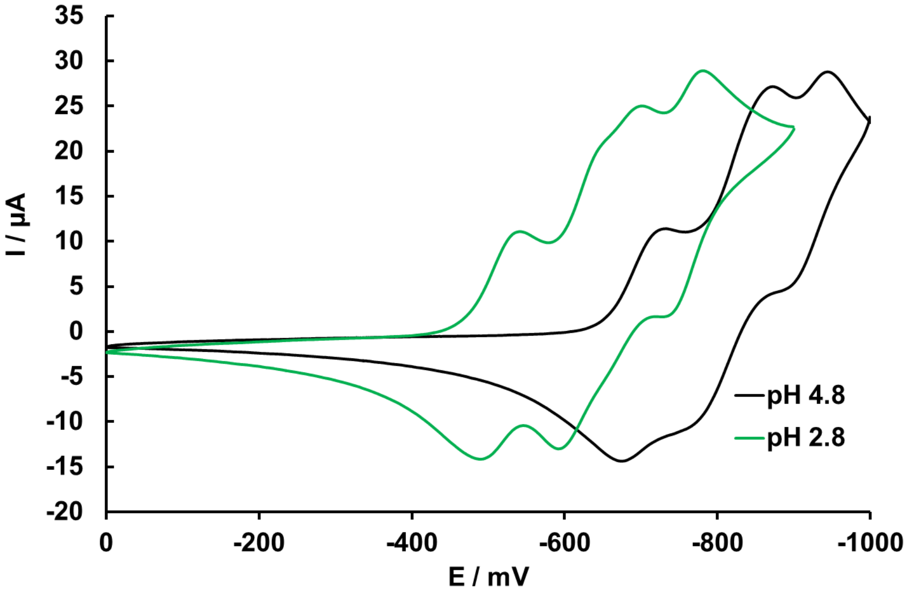

**Figure 5.12** CVs of 0.5 mM **5.1** in 0.5 M sodium acetate (pH 4.8, black curve) and sodium chloroacetate buffer (pH 2.8, green curve), scan rate 25 mV $s^{-1}$, at ambient temperature.

A 0.4 M sodium chloroacetate buffer solution at pH 2.8 was used to assess the effect of pH on the redox behavior of **5.1** (Figure 5.12). At lower pH the reduction **5.1** proceeds at potential by ~200 mV more positive, consistent with a decrease of the negative charge of **5.1** due to protonation. The second cathodic peak splits into two one-electron processes, probably due to the larger difference in $pK_a$s of reduced and oxidized states at this pH.

### 5.3.5 Computational studies.

Computational studies of $[Zn_6(OH)_7(H_2O)(Si_2W_{18}O_{66})]^{11-}$, **5.1_m** (the monomeric half of **5.1**; see Figure 5.13) show, as expected, that **5.1_m** (and **5.1**) has a diamagnetic $^1A$ state. Its highest occupied MO (HOMO) is a lone-pair of the $O^1H$ ligand, which is almost surely involved in the bond formation upon dimerization of **5.1_m** to form **5.1**.

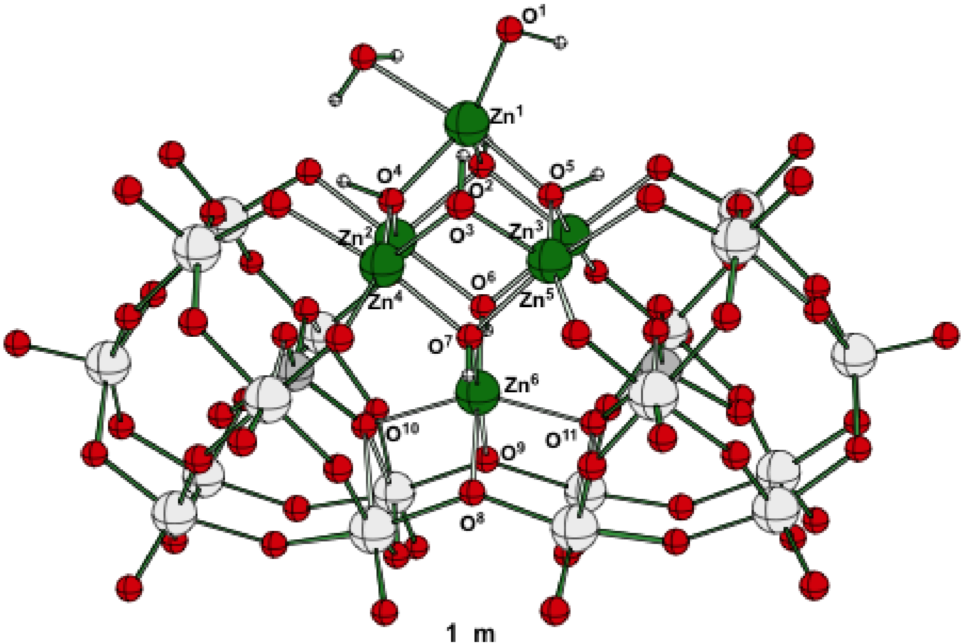

1_m

Zn$^{1}$-O$^{1}$ = 1.976 (2.068)
Zn$^{1}$-O$^{2}$ = 2.155 (2.240)
Zn$^{1}$-O$^{4}$ = 2.068 (2.117)
Zn$^{1}$-O$^{5}$ = 2.158 (2.170)

Zn$^{2}$-O$^{2}$ = 2.098 (2.061)
Zn$^{2}$-O$^{4}$ = 2.138 (2.064)
Zn$^{2}$-O$^{6}$ = 2.113 (2.052)

Zn$^{3}$-O$^{2}$ = 2.115 (2.049)
Zn$^{3}$-O$^{5}$ = 2.104 (2.039)
Zn$^{3}$-O$^{6}$ = 2.160 (2.094)

Zn$^{4}$-O$^{4}$ = 2.106 (2.022)
Zn$^{4}$-O$^{7}$ = 2.133 (2.087)
Zn$^{4}$-O$^{3}$ = 2.099 (2.057)

Zn$^{5}$-O$^{5}$ = 2.089 (2.020)
Zn$^{5}$-O$^{3}$ = 2.097 (2.056)
Zn$^{5}$-O$^{7}$ = 2.138 (2.069)

Zn$^{6}$-O$^{6}$ = 2.057 (1.979)
Zn$^{6}$-O$^{7}$ = 2.067 (1.978)
Zn$^{6}$-O$^{8}$ = 2.213 (2.131)
Zn$^{6}$-O$^{9}$ = 2.226 (2.163)
Zn$^{6}$-O$^{10}$ = 2.261 (2.238)
Zn$^{6}$-O$^{11}$ = 2.283 (2.241)

**Figure 5.13** Notation of atoms and comparison of the calculated important bond distances (in Å) of **5.1_m** with their experimental values (in parenthesis) in **5.1**. The calculated important geometry parameters of **5.1_m** are in good agreement with their experimental values reported for the dimer complex **5.1**. These findings justify the use of model **5.1_m** to study electronic properties of **5.1**.

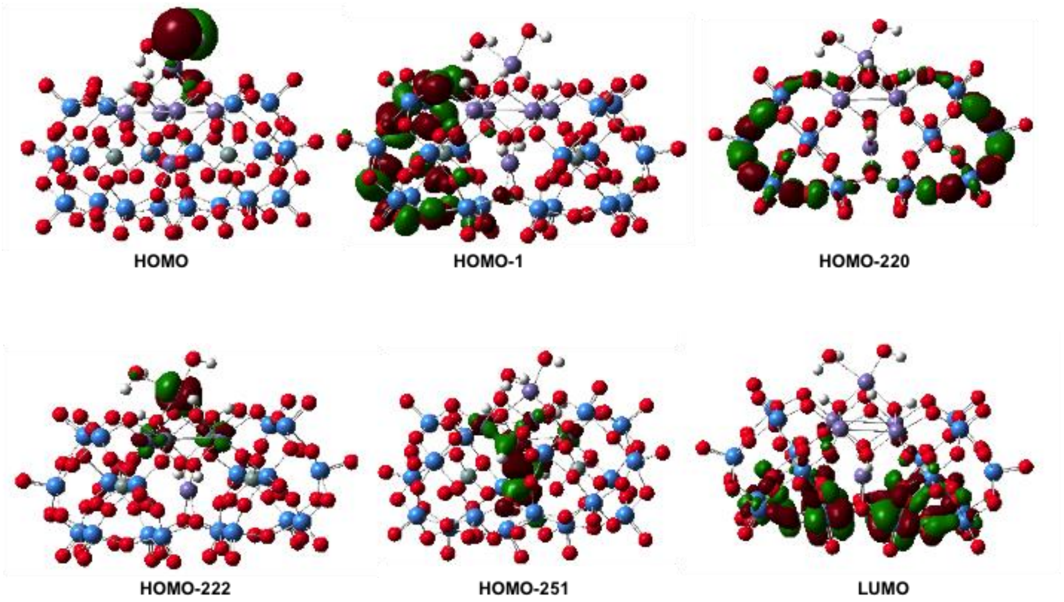

HOMO HOMO-1 HOMO-220

HOMO-222 HOMO-251 LUMO

**Figure 5.14** Representative HOMO and LUMO orbitals of **5.1_m** calculated at the B3LYP/[Lanl2dz + 6-31G(d)] level of theory.

The lower-lying 220 highest occupied orbitals of **5.1_m** (or 440 HOMOs of **5.1**) are W-O bonding orbitals with large contributions from the O ligands and Si-O bonding orbitals. These frontier orbital analyses indicate that the polytungstate ligands are likely to participate in the oxidation/reduction processes (see Figure 5.14). Doubly occupied d orbitals of Zn centers are clustered within 0.7 eV and located 8.6-9.3 eV below the highest HOMO. These data indicate that the Zn centers most likely will not be available for redox processes, consistent with the effectively non-existent redox chemistry of isolated Zn sites. Among the Zn orbitals the highest MOs are the $Zn^1$ orbitals and the lowest MOs are associated with the $Zn^6$ center, which are involved in bonding with six (H)O-ligands. The lowest several LUMOs are the d-orbitals of the W centers. The calculated HOMO-LUMO and (HOMO-1)-LUMO energy gaps are ~3.65 and 3.91 eV, respectively. This compares to the band gap in ZnO of 3.35 eV.

## 5.4 Conclusions

A dodecanuclear zinc POM with an open Wells-Dawson structure has been synthesized and characterized. UV-vis, acid/base titration and cyclic voltammetry data for this new POM, **5.1**, and the lacunary polysilicotungstate ligand, $[Si_2W_{18}O_{66}]^{16-}$, are similar but systematically shifted slightly. The twelve zinc centres incorportated between two open Wells-Dawson multidentate ligands makes this compound more hydrolytically stable than the parent $[Si_2W_{18}O_{66}]^{16-}$. Structurally analogous complexes with multi-d-electron centers of potential interest in catalysis are being sought using a similar synthetic strategy. DFT B3LYP calculations give a HOMO–LUMO gap for **5.1** of ~3.65 eV which is slightly larger than that in ZnO (band gap = 3.35 eV).

# *Chapter 6*

## Chapter 6 : Oxidation of Alcohols and Phenols in Acetonitrile by a Tetraruthenium Polyoxometalate Complex: Kinetics and Mechanism

**Abstract:** We have synthesized and characterized a derivative of $Rb_8K_2[Ru^{IV}{}_4O_4(OH)_2(H_2O)_4(\gamma\text{-}SiW_{10}O_{36})_2]\bullet 25H_2O$ (RbK-**$Ru_4$POM**) which is soluble in acetonitrile: $[(CH_3(CH_2)_3N]_6H_4[\{Ru^{IV}{}_4O_4(OH)_2(H_2O)_4\}(\gamma\text{-}SiW_{10}O_{36})_2]\cdot 10H_2O$ (TBA-**$Ru_4$POM**). The catalytic activity of this compound for oxidation of 3,5,3',5'-tetra-*t*-butyl-biphenyl-4,4'-diol ($BPH_2$) by dioxygen was explored. This complex with small amount of strong acids stoichiometrically oxidizes alcohols in acetonitrile under Ar to aldehydes/ketones, forming the 2-electron-reduced form of TBA-**$Ru_4$POM**. The reaction kinetics and stoichiometry were studied by GC, NMR and UV-vis spectrometries. The reactivities of TBA-**$Ru_4$POM** towards *para*-substituted benzyl alcohols, $X\text{-}C_6H_4CH_2OH$ (X = $CH_3O$, $CH_3$, H, F, Cl, Br, $CF_3$) do not obey the Hammett law. The kinetic isotope effect, $C_6H_5CH_2OH$ versus $C_6D_5CD_2OH$, is about 2~3. The addition of water slightly accelerates the reaction. There is no significant difference in reaction kinetics if $H_2O$ is replaced with $D_2O$. The reaction rate reaches a plateau with increase in alcohol concentration, which may indicate an intermediate complex formation between TBA-**$Ru_4$POM** and alcohol. All experimental attempts to observe such an intermediate failed. Several reaction mechanisms were analyzed by fitting of the reaction kinetic curves obtained from changes of UV-Vis spectra versus time.

## 6.1 Introduction

Selective oxidation of alcohols to ketones/aldehydes is one of the central reactions in both biological and industrial process. Ruthenium oxo and dioxo complexes in their high valent oxidation state (IV, V, and VI) have been widely studied as both stoichiometric oxidants and catalysts for alcohol oxidation. Meyer et al. investigated systematically the redox reactions of ruthenium oxo polypyridyl complexes.[139-142] It has been demonstrated that $Ru^{(IV)}$ is versatile as both one- and two-electron oxidants in aqueous media at pH 7. Mechanistic studies on *cis*-$[Ru^{IV}(bpy)_2(py)(O)]^{2+}$ reactions with alcohols and hydroquinone showed they proceed via hydride[140,141] and proton coupled electron-transfer pathways,[143] respectively. Importantly, both reactions are characterized by large kinetic isotopic effects. For the alcohol oxidation, it has been speculated that alcohol binds to the complex to give a seven-coordinated $Ru^{(IV)}$ intermediate followed by intermolecular oxidation.[141] On the other hand, there were numerous reports that $[Ru(bpy)_3]^{3+}$ and related polypyridyl complex could oxidize water to oxygen. However, the real reactions are actually the oxidations of the organic ligands.[139,144] Initially, Meyer et al designed related complexes containing two chemically linked $Ru\text{-}OH_2^{2+}$ sites,[139,145] such as *cis,cis*-$[(bpy)_2(H_2O)Ru^{III}\text{-}O\text{-}Ru^{III}(H_2O)(bpy)_2]^{4+}$, which appeared to be catalytically active in water oxidation by the strong oxidant $Ce^{(IV)}$.[146] This complex is well known as the “blue dimer” with the reactive form formulated as $[(bpy)_2(O)Ru^{V}\text{-}O\text{-}Ru^{V}(O)(bpy)_2]^{4+}$. Chloride anion, if present in the system, is quickly oxidized to chlorine, $Cl_2$.[139] Comparison of the relative reactivities of the monomer, $[Ru^{IV}(bpy)_2(py)(O)]^{2+}$, and the dimers ($[(bpy)_2(O)Ru^{V}\text{-}O\text{-}Ru^{V}(O)(bpy)_2]^{4+}$ and $[(bpy)_2(O)Ru^{V}\text{-}O\text{-}Ru^{III}(py)(bpy)_2]^{4+}$ (μ-oxo complexes)), for oxidation of organic molecules, such as alcohols or hydroquinone, have been determined.[147] In general, the reactions of these dimers appear to be very pH-dependent and more reactive towards organics than water.

Inspired by studies of di-ruthenium catalysts for water oxidation by Meyer and other researchers, our group initially synthesized an all-inorganic and therefore oxidatively stable di-Ru-substituted polyxometalate complex, $[\{Ru^{III}(OH)_2(H_2O)_2\}(\gamma\text{-}SiW_{10}O_{34})]^{4-}$,[148] which showed substantial catalytic activity for water oxidation by $[Ru(bpy)_3]^{3+}$ at neutral pH (unpublished data). However, this POM proved to be unstable in water, and we consequently failed to fully characterize it despite considerable efforts.[16,68] While attempting to isolate this complex, we synthesized and fully characterized a tetraruthenium POM, $R_bK_2[\{Ru_4O_4(OH)_2(H_2O)_4\}((\gamma\text{-}SiW_{10}O_{34})_2]$ (RbK-**$Ru_4$POM**), with a central $\{Ru^{IV}_4(\mu\text{-}O)_4(\mu\text{-}OH)_2(H_2O)_4\}^{6+}$ core.[16,68] This complex can be viewed as a dimer and likely forms from oxidative dimerization of $[\{Ru^{III}(OH)_2(H_2O)_2\}(\gamma\text{-}SiW_{10}O_{34})]^{4-}$.[149] It shows a high catalytic activity in water oxidation by $[Ru(bpy)_3]^{3+}$ at pH 7.2.[16,67,68] Simultaneously, Bonchio et al synthesized the same tetraruthenium complex with different countercations $Cs_{10}[Ru_4(\mu\text{-}O)_4(\mu\text{-}OH)_2(H_2O)_4(\gamma\text{-}SiW_{10}O_{36})_2]$ (Cs-**$Ru_4$POM**) via a different method and also demonstrated its high catalytic activity in water oxidation by $Ce^{(IV)}$ under very acidic conditions[17,150] or in a light-induced process at neutral pH.[151] All our data led to a mechanism for water oxidation by $[Ru(bpy)_3]^{3+}$ catalyzed by RbK-**$Ru_4$POM** as follows:[68]

**$Ru_4$POM (0)** + $[Ru(bpy)_3]^{3+} \rightarrow$ **$Ru_4$POM (+1)** + $[Ru(bpy)_3]^{2+}$ fast (6.1)

**$Ru_4$POM (+1)** + $[Ru(bpy)_3]^{3+} \rightarrow$ **$Ru_4$POM (+2)** + $[Ru(bpy)_3]^{2+}$ fast (6.2)

**$Ru_4$POM (+2)** + $[Ru(bpy)_3]^{3+} \rightarrow$ **$Ru_4$POM (+3)** + $[Ru(bpy)_3]^{2+}$ fast (6.3)

**$Ru_4$POM (+3)** + $[Ru(bpy)_3]^{3+} \rightarrow$ **$Ru_4$POM (+4)** + $[Ru(bpy)_3]^{2+}$ rate limiting step (6.4)

**$Ru_4$POM (+4)** $\rightarrow$ **$Ru_4$POM (0)** + $O_2$ (6.5)

The parent polyanion, $[Ru^{IV}_4(\mu\text{-}O)_4(\mu\text{-}OH)_2(H_2O)_4(\gamma\text{-}SiW_{10}O_{36})_2]^{10-}$ with all four ruthenium centers in the +4 oxidation state, is designated as **$Ru_4$POM (0)**. Its one-electron- and two-electron-oxidized polyanions, are **$Ru_4$POM (+1)** and **$Ru_4$POM (+2)**, respectively. While equations 6.1-6.5 all involve the oxidized form of **$Ru_4$POM (0)**, we are also interested the reduced forms of **$Ru_4$POM (0)**. As we can see from the general mechanism for oxidations of organic compounds (Scheme 1.2), the properties of the reduced forms of **$Ru_4$POM (0)** can be studied through this kind of process. Therefore, organic-soluble form of **$Ru_4$POM**, $[(CH_3(CH_2)_3N]_6H_4[\{Ru^{IV}{}_4O_4(OH)_2(H_2O)_4\}(\gamma\text{-}SiW_{10}O_{36})_2]\cdot 10H_2O$ (TBA-**$Ru_4$POM**) was prepared. The study in this chapter shows that TBA-**$Ru_4$POM** has no catalytic oxygenation activity toward many organic substrates except 3,5,3’,5’-tetra-tert-butyl-biphenyl-4,4’-diol (henceforth $BPH_2$). The kinetics of stoichiometric alcohol oxidations by TBA-**$Ru_4$POM** is studied in detail, and the mechanism is proposed.

## 6.2 Experimental

**Materials.** $Rb_8K_2[Ru^{IV}{}_4O_4(OH)_2(H_2O)_4(\gamma\text{-}SiW_{10}O_{36})_2]\bullet 25H_2O$ (RbK-**$Ru_4$POM**) was prepared according to the literature method.[16] Elemental analyses were performed by Columbia Analytical Services (Tucson, AZ) and Atlantic Microlab Inc. (Norcross, GA). Water for the preparation of solutions was obtained from a Barnstead Nanopure® water-purification system. Deuterium oxide, 99.9 atom % (Aldrich), acetonitrile (EMD, Ominisolv®, High purity solvent), benzyl alcohol (Sigma-Aldrich, puriss), and benzaldehyde was distilled before use. All other materials were reagent grade and were used without additional purifications.

**General method.** Infrared spectra (2% sample in KBr) were recorded on a Nicolet 510 FTIR spectrometer. UV-vis spectra were acquired using an Agilent 8453 spectrophotometer equipped with a diode-array detector and with a magnetic stirrer and temperature controller (Agilent 89090A). The spectra were recorded in a 10 mm two-neck quartz cell with a stopper and a stopcock under Ar, air, or $O_2$. Thermal gravimetric analyses (TGA) were performed on an ISI TGA 1000 under $N_2$ flow from 25 to 400 ℃ at a rate of 10 ℃/min. Products of benzyl alcohol oxidation were identified and quantified a gas chromatography using Hewlett Packard 6890 instrument equipped with a flame ionization detector and 5% phenyl methyl silicone capillary column. Cyclooctane was used as an internal standard.

**Synthesis of $[(n\text{-}C_4H_9)_4N]_6H_4[Ru^{IV}{}_4O_4(OH)_2(H_2O_4](\gamma\text{-}SiW_{10}O_{36})_2]$ (TBA-$Ru_4$POM).** After dissolving 1 g of $Rb_8K_2[Ru^{IV}{}_4O_4(OH)_2(H_2O)_4(\gamma\text{-}SiW_{10}O_{36})_2]\bullet 25H_2O$ (0.14 mmole) in 50 mL $H_2O$, the pH was adjusted to 1.6 by adding 4 M HCl. Then, 0.45 g of tetra-*n*-butylammonium bromide was added by small portion under stirring. After stirring for another 10 minutes, the suspension was centrifuged and washed with acidic water (pH 1.6, water acidified by hydrochloric acid). The precipitate was re-dissolved in a minimal amount of acetonitrile. This solution was filtered through a fine frit, then the filtrate was poured into to 20 mL of acidic water (pH 1.6, water acidified by HCl), and stirred for an additional 10 minutes. The suspension was centrifuged to obtain the solid material. This material was once again re-dissolved in a minimal amount of acetonitrile. After filtration through a fine frit the solution was added to 20 mL of diethyl ether, stirred for 10 minutes. The suspension was collected on a fine frit and dried overnight under low pressure (c.a. 100 mm Hg). The yield of TBA-**$Ru_4$POM** was ca. 0.68 g (~ 70 % based on W). UV-vis spectrum in acidified $CH_3CN$ (~ 20 μM of 70% $HClO_4$ in water) shows a characteristic peak at 453 nm with $\varepsilon = 5.0\text{x}10^4\ M^{-1}cm^{-1}$. Elemental analysis calcd (%) for TBA-**$Ru_4$POM**: C, 16.7; H, 3.4; N, 1.2; Ru, 5.8; Si, 0.8; W, 53.2. Found (%): C, 16.8; H, 3.5; N, 1.2; Ru, 5.9; Si, 0.5; W, 49.3.

**Characterization of alcohol oxidation products.** Benzyl alcohol oxidation was carried out under Ar at ambient temperature in a vessel wrapped in alumina foil. Acetonitrile containing 20 μM $HClO_4$ was used as a solvent. The initial concentration of benzyl alcohol was 50 mM, while 20 mM of TBA-**Ru$_4$POM** was used, and the reactions were completed within 5 min. The product was characterized by GC and $^1$H NMR.

**Kinetic measurements.** The UV-vis spectra of RbK-**Ru$_4$POM** in water at pH 2.0 and TBA-**Ru$_4$POM** in acidified $CH_3CN$ (70% $HClO_4$ as a source of protons) are almost the same. The peak in $CH_3CN$ is shifted to longer wavelengths by 5-6 nm, while the extinction coefficients are the same, $5.0x10^4$ $M^{-1}cm^{-1}$. The reduction of two $Ru^{(IV)}$ to two $Ru^{(III)}$ in RbK-**Ru$_4$POM** in acidic water results in an almost complete disappearance of a characteristic peak at 445 nm.[68] The same phenomenon is observed for TBA-**Ru$_4$POM** in acidified acetonitrile upon addition of such strong reducing agents as ascorbic acid or $SnCl_2$. Therefore, the reduction of TBA-**Ru$_4$POM** in acidified acetonitrile by alcohols was followed by a decrease in absorbance at 453 nm. In a typical experiment a solution of 20 μM TBA-**Ru$_4$POM** in acetonitrile containing 20 μM $HClO_4$ was prepared in the two-neck quartz cell. The solution is degassed by vacuum pump, followed by purging by Ar under ambient pressure. Stock solutions of alcohols were prepared in $CH_3CN$ and stored under Ar. A required amount of alcohol was quickly injected through a rubber septum and mixed well before collecting the data. The reaction appeared to be UV-light-sensitive, therefore a filter blocking the UV-light at $\lambda < 400$ nm was used. Additionally the whole cell compartment was covered with a black cloth. The reaction was very slow and carried out in a thermostated cell holder.

## 6.3 Results and discussion

### 6.3.1 Synthesis of TBA-$Ru_4$POM

Metathesis of cation in RbK-**$Ru_4$POM** with $Bu_4N^+$ in acidic, aqueous solution followed by purification of the product from acetonitrile / diethyl ether yields a dark brown powder. The success of $Rb^+$, $K^+$ / $Bu_4N^+$ metathesis depends on maintaining the solution at low pH. The TBA salt does not precipitate at high pH, likely because of the strong repulsions among the largely charged polyanions. Numerous attempts to grow X-ray-quality crystals from diffusion of low solubility solvents into high solubility solvents were unsuccessful. By changing the cation to $TPP^+$ or $PPN^+$, the solubility of the $Ru_4$POMs in organic solvents decreases, therefore they readily precipitate by using diffusion methods without providing high quality crystals.

Crystals of organic soluble **$Ru_4$POM** were grown by slow diffusion of reactants together using three liquid layers: a POM solution at the bottom, a mixed solvent [$H_2O$/ethylene glycol (EG) = 2:1] separation layer in the middle, and a solution of the organic soluble counterion at the top (layered over the mixed solvent layer). Use of dense and viscous EG further facilitates slow diffusion of the reactants. The crystallization conditions were optimized by varying the density of the layers and the height of the central separating solvent layer. We attempted to grow crystals of $Ru_4$POM using $(CH_4)_4NCl$, $(C_2H_5)_4NCl \cdot xH_2O$, $(CH_3)_3(C_6H_5)NCl$ (TMPACl), $(CH_3CH_2CH_2)_4NBr$ (TPABr), TPPBr and PPNCl. However, no crystals or powder formed using $(CH_4)_4N^+$, $(C_2H_5)_4N^+$ or $TMPA^+$ because of the high solubility of these salts. Some precipitates were formed using $TPP^+$ and $PPN^+$. The $TPA^+$ and $TBA^+$ salt of the POM readily formed crystals, but they did not diffract adequately.

## 6.3.2 Characterization of TBA-$Ru_4$POM

### 6.3.2.1 Electronic Absorption Spectroscopy

The UV-Visible spectra of TBA-**$Ru_4$POM** in acetonitrile was pH dependent; a maximum absorbance at 456 nm, observed in acidic medium (by adding $HClO_4$), was assigned to ruthenium d-d transitions, while at neutral pH this peak was not obvious. The electronic absorption spectrum of TBA-**$Ru_4$POM** (which has a peak at 445 nm) is slightly red shifted compared to that of RbK-**$Ru_4$POM** due to the solvent effect (Figure 6.1). The extinction coefficient of the two compounds is both about $5 \times 10^4$ $M^{-1}cm^{-1}$ in acetonitrile and water. It has been proven that the oxidation state of the Ru centers in RbK-**$Ru_4$POM** are (IV, IV, IV, IV), therefore it is reasonable to consider that all Ru atoms are in the + 4 oxidation states in TBA-**$Ru_4$POM**.

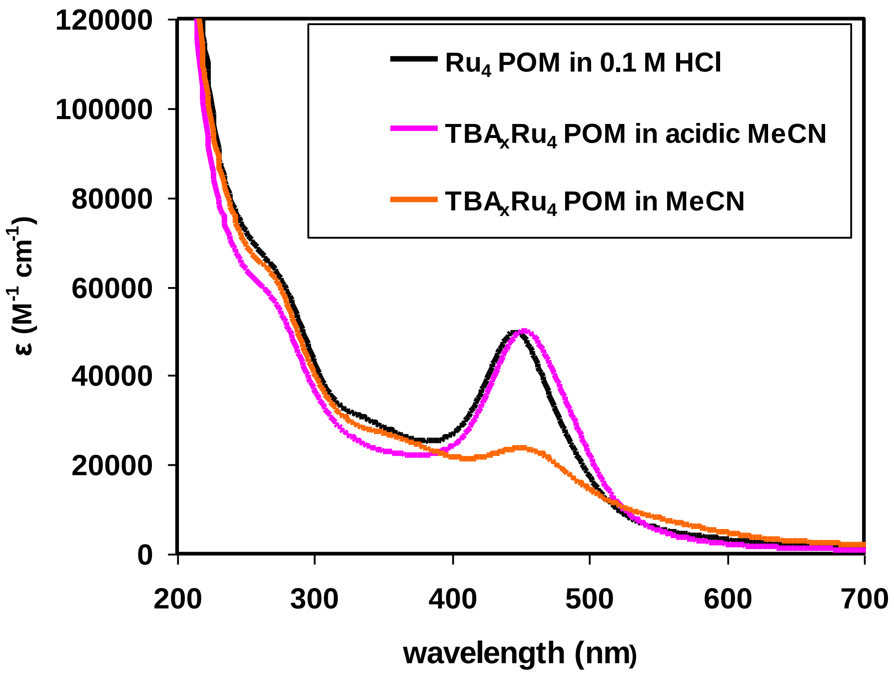

**Figure 6.1** Electronic absorption spectra of RbK-**$Ru_4$POM** in 0.1 M HCl, TBA-**$Ru_4$POM** in MeCN and in acidic MeCN with 0.1 M $HClO_4$.

### *6.3.2.2 IR spectroscopy*

The characteristic peaks for the organic part of compound TBA-**$Ru_4$POM** are evident in the IR spectra, and the characteristic peaks for the POM structure are mostly retained after the cation metathesis (Figure 6.2). However, in RbK-**$Ru_4$POM**, there is a very broad peak in the 830 ~ 700 $cm^{-1}$ region; whereas, in TBA-**$Ru_4$POM**, there are two separate peaks, 813 $cm^{-1}$ and 756 $cm^{-1}$, respectively. The lacunary POM, potassium decatungstosilicate ($K_8[\gamma\text{-}SiW_{10}O_{36}]\cdot 12H_2O$) has two peaks in this region. Normally the two peaks merging into one strongly suggests that the lacunary sites in $\gamma$-$SiW_{10}O_{36}$ have become occupied by metal atoms. Why the merged peaks separate again in the TBA salt is not clear. To assess whether the **$Ru_4$POM** polyanion structure remains intact, we compared the IR spectrum of **$Ru_4$POM** with the cesium salt of **$Ru_4$POM** made by Bonchio's group.[17] The Cs salt also has two peaks in this region (Figure 6.3) indicating that peaks in this region are affected by the cations. The TBA cations probably induce a structural distortion of the POM subunits.

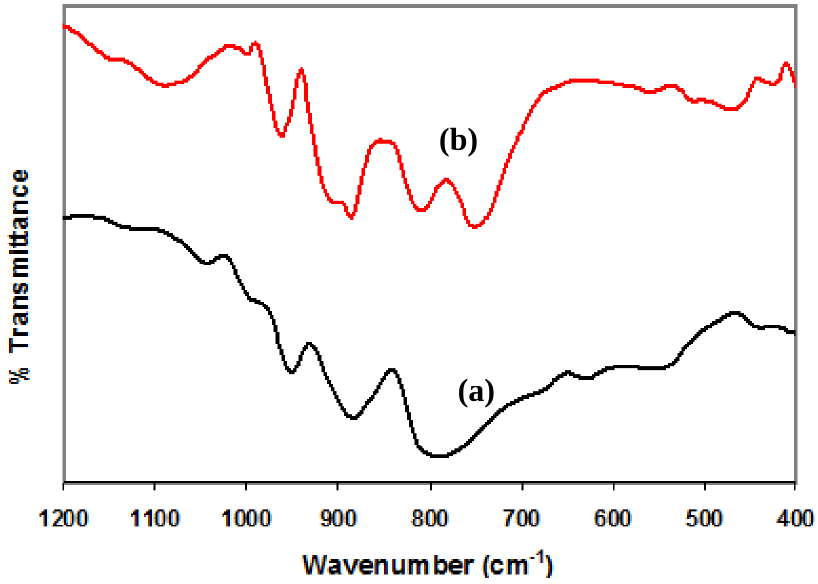

**Figure 6.2** IR spectra of (a) RbK-**$Ru_4$POM**, (b) TBA-**$Ru_4$POM**.

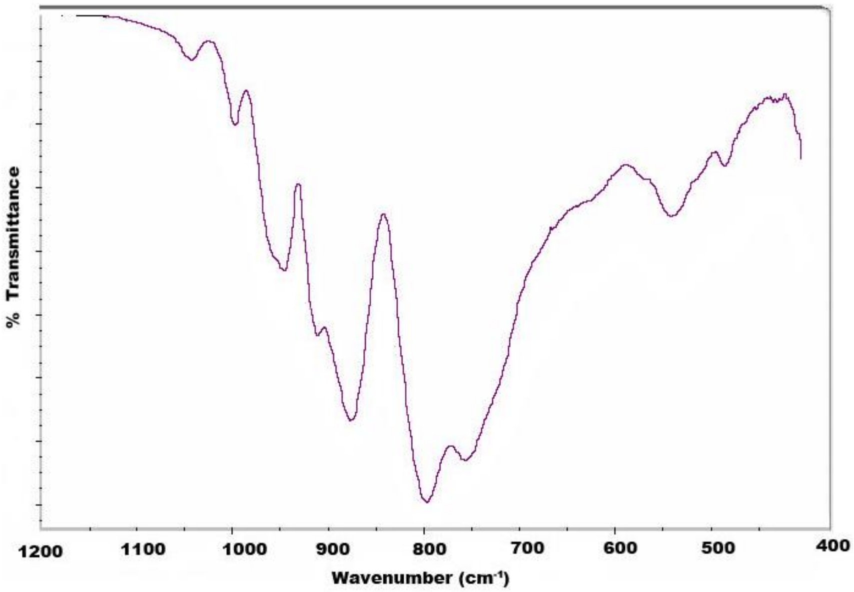

**Figure 6.3** IR spectrum of $Cs_{10}[\{Ru_4O_4(OH)_2(H_2O)_4\}(\gamma\text{-}SiW_{10}O_{36})_2]\cdot 25H_2O$.[17]

## 6.3.3 TBA-$Ru_4$POM catalysis of organic substrate oxidations.

### *6.3.3.1 Preliminary screening of substrates and oxidants*

The strong acidity and oxidizing power of POMs have led to many studies on homogeneous and heterogeneous catalysis. The oxidation of thioethers and the epoxidation of alkenes catalyzed by POMs with various oxidation donors or molecular oxygen have been investigated thoroughly.[152,153] Therefore, several thioethers and cyclohexene were selected as substrates, and several oxygen donors were selected as oxidants, as summarized in Table 6.1. TBA-**$Ru_4$POM** showed no catalytic oxygenation activity towards tetrahydrothiophene (THT), 2-chloroethyl ethyl sulfide (CEES) or cyclohexene. Of the organic substrates screened, only the quinone, 3,5,3’,5’-tetra-*tert*-butyl-biphenyl-4,4’-diol (henceforth $BPH_2$), was oxidized by $O_2$ in the presence of this POM. Its stoichiometric and catalytic reaction mechanisms were studied subsequently.

**Table 6.1** Oxidation of organic substrates catalyzed by TBA-**$Ru_4$POM**.

| Substrate | Oxidant | Temperature ( °C) | Reaction Time | Detection Instrument | Reactivity |
|---|---|---|---|---|---|
| THT | $O_2$ | 80 | 24 h | GC | N |
| | $(NH_4)_2Ce(NO_3)_6$ | R.T. | 0.5 h | GC | N |
| CEES | $(NH_4)_2Ce(NO_3)_6$ | R. T. | 0.5 h | GC | N |
| cyclohexene | $TBAIO_4$ | 50 | 2 h | GC | N |
| | $F_5PhI(TFAc)_2$ | 50 | 2h | GC | N |
| $BPH_2$ | $O_2$ | R. T. | 1h | UV-vis | Y |

*6.3.3.2 Stoichiometry and Reaction Mechanism*

The phenolic substrate is suitable for study of the reaction stoichiometry, because it produces only a single oxidation product, 3,5,3',5'-tetra-*t*-butyl-diphenoquinone (DPQ). As a prerequisite to address the reaction mechanism for $BPH_2$ oxidation by $O_2$ catalyzed by TBA-**$Ru_4$POM**, it was essential to look at the kinetics of the stoichiometric reaction under Ar, eq 6.6.

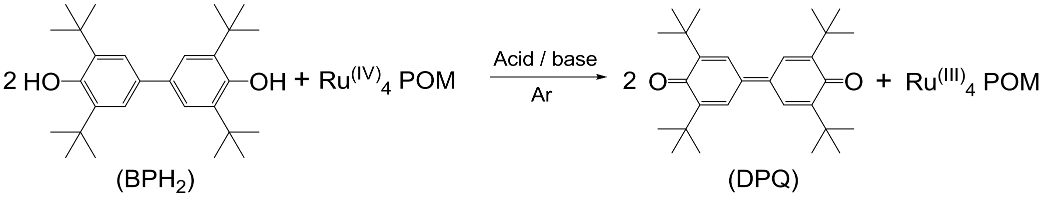

(6.6)

As we can see from this stoichiometric reaction between $BPH_2$ and $Ru^{(IV)}{}_4$ POM, the ratio of DPQ formed per POM is 2:1. The four ruthenium centers are reduced from (IV, IV, IV, IV) to (III, III, III, III), and each $BPH_2$ loses two electrons in oxidation to DPQ. The overall reaction can be separated into four successive reactions (eqs 6.7-6.10). Since the redox potential of **$Ru^{(IV)}{}_4$POM** is affected by the acidity/basicity of the reaction system, certain amounts of $HClO_4$ or triethylamine were added to see if the reaction stoichiometry would change.

$$BPH_2 + Ru^{(IV)}{}_4POM \rightarrow BPH_2\bullet^+ + Ru^{(IV)}{}_3{}^{(III)}POM \qquad (6.7)$$

$$BPH_2\bullet^+ + Ru^{(IV)}{}_3{}^{(III)}POM \rightarrow DPQ + Ru^{(IV)}{}_2{}^{(III)}{}_2POM \qquad (6.8)$$

$$BPH_2 + Ru^{(IV)}{}_2{}^{(III)}{}_2POM \rightarrow BPH_2\bullet^+ + Ru^{(IV)(III)}{}_3POM \qquad (6.9)$$

$$BPH_2\bullet^+ + Ru^{(IV)\,(III)}{}_3POM \rightarrow DPQ + Ru^{(III)}{}_4POM \qquad (6.10)$$

The stoichiometry of the reaction was quantified by UV-vis spectroscopic measurements of the amount of DPQ formed. We chose the wavelength 390 nm (not the $\lambda_{max}$) to study the reaction kinetics and stoichiometry for the following reasons: (a) The extinction coefficient of DPQ is high at 390 nm ($3.6\times10^4$ $M^{-1}cm^{-1}$) (Figure 6.4); (b) the electronic absorption isosbestic point of TBA-**$Ru_4$POM** in acetonitrile with and without $HClO_4$ is at 390 nm, with the extinction coefficient $2.2\times10^4$ $M^{-1}cm^{-1}$ (Figure 6.1); (c) the electronic absorption spectra of TBA-**$Ru_4$POM** in acetonitrile is comparable with RbK-**$Ru_4$POM** in water with Ru in different oxidation states, which also has an isosbestic point at 390 nm (Figure 6.5).

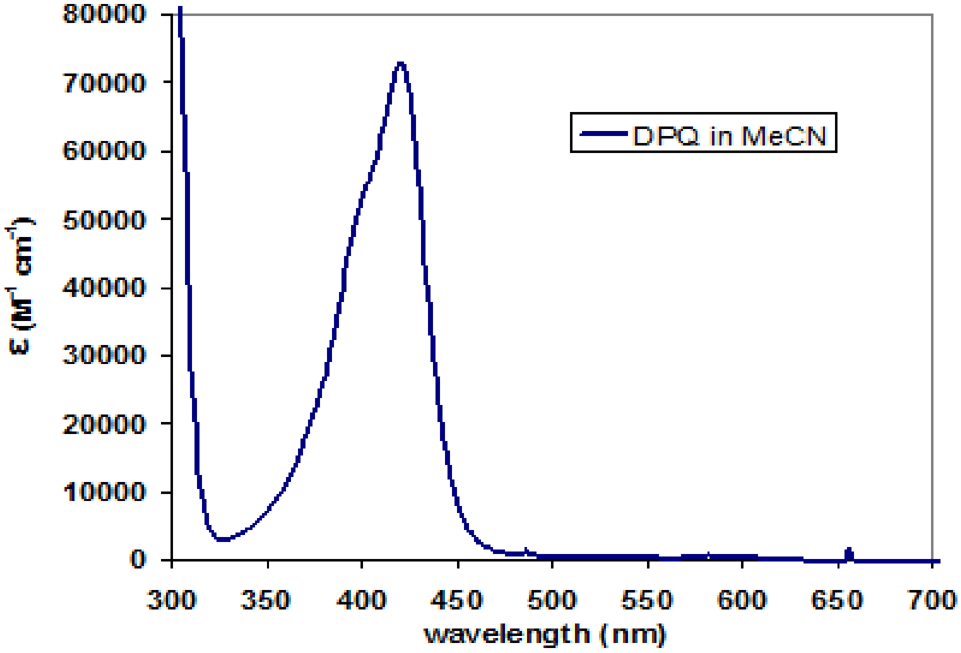

**Figure 6.4** UV-vis spectrum of DPQ in acetonitrile.

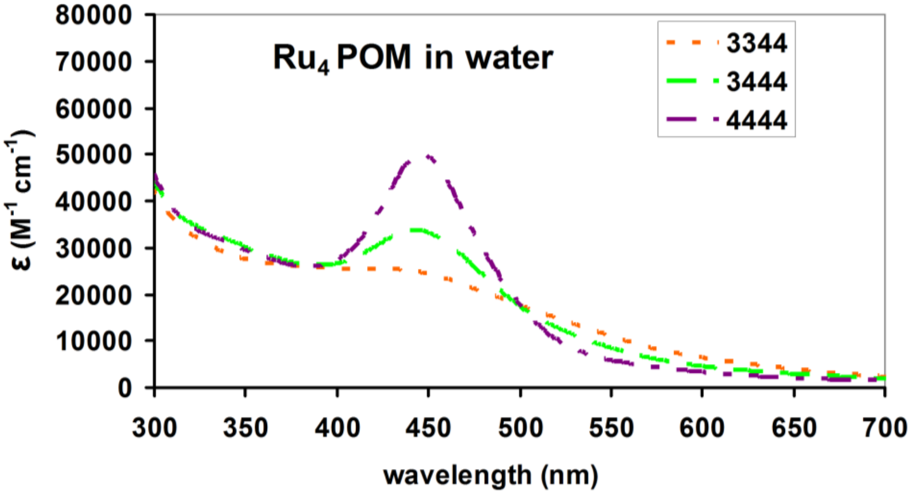

**Figure 6.5** Electronic absorption spectra of TBA-**Ru$_4$POM** with Ru in different oxidation states (0.1 M HCl solution).

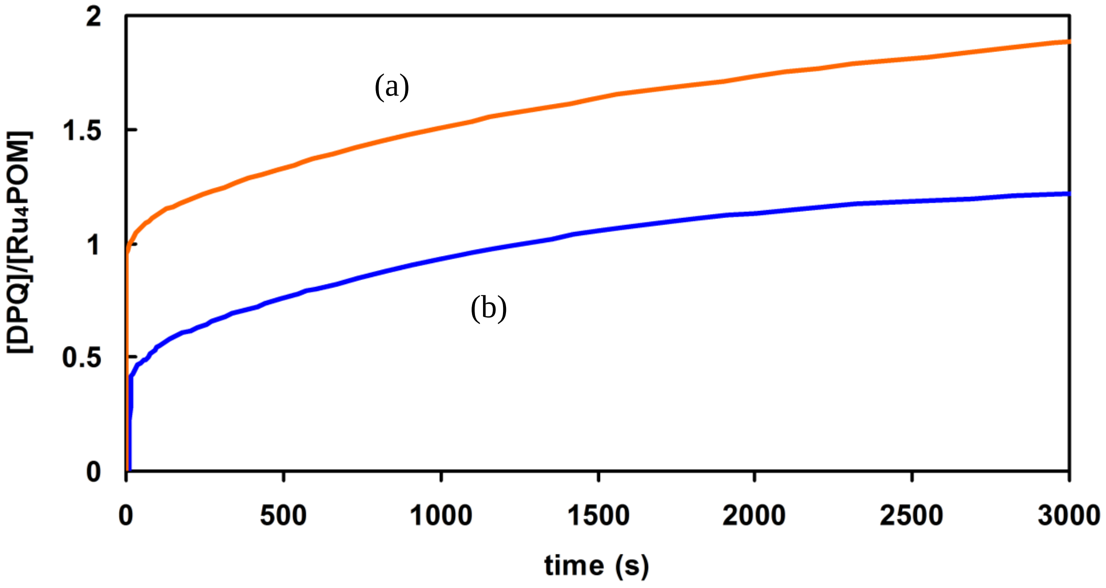

**Figure 6.6** Stoichiometry of $BPH_2$ oxidation by $Ru^{(IV)}_4$ POM. (a) 1 mM $BPH_2$ + 10 μM TBA-**$Ru_4$POM** + 100 μM $HClO_4$ (b) 1 mM $BPH_2$ + 10 μM TBA-**$Ru_4$POM** + 3 mM triethylamine.

As shown in Figure 6.6, under acidic conditions, the first equivalent of DPQ is generated very quickly, and the final concentration is twice higher than the concentration of **$Ru_4$POM**. However, in basic conditions, the first half equivalent of DPQ is generated very quickly, and at the final concentration only about one equivalent of $Ru_4$POM is produced. That is, in acidic conditions, eq 6.7 and eq 6.8 proceed quickly, and eq 6.9 and eq 6.10 proceed slowly. In basic conditions, eq 6.7 proceeds quickly, eq 6.8 proceeds slowly. Eqs 6.9 and 6.10 do not proceed under basic conditions. Therefore, we conclude that the acidified **$Ru^{(IV)}_4$-POM** is a much stronger oxidant, and that it can be reduced to **$Ru^{(III)}_4$POM**. In the presence of base, **$Ru^{(IV)}_4$-POM** is a much weaker oxidant and can only be reduced to **$Ru^{(IV)}_2Ru^{(III)}_2$POM**.

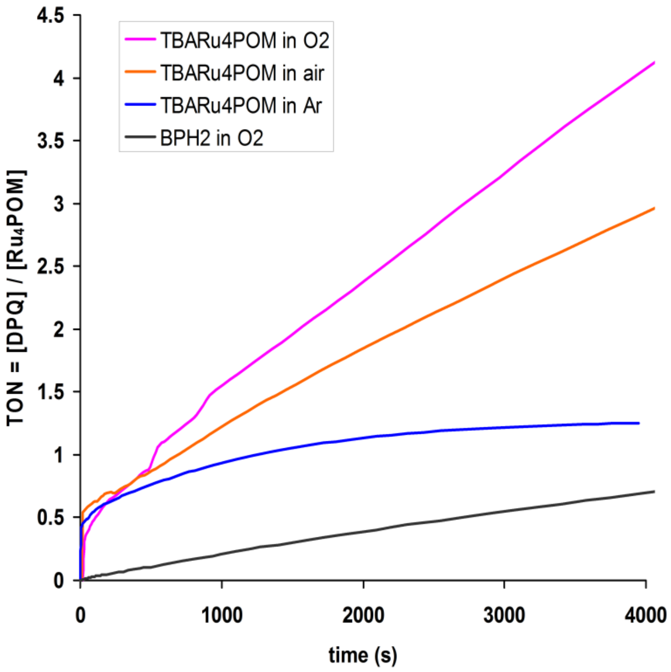

**Figure 6.7** Catalytic activity of TBA-**Ru$_4$POM** in BPH$_2$ oxidation by dioxygen and by air, compared with the stoichiometric reaction under Ar and the control experiment under O$_2$ but without catalyst.

### *6.3.3.3 Catalytic activity study*

The catalytic activities for BPH$_2$ oxidation by dioxygen were investigated under acidic and basic conditions by adding HClO$_4$, 2,6-di-*t*-butylpyridine (DBP) or triethylamine (TEA) to the reactions. Under HClO$_4$ and DBP, BPH$_2$ is oxidized to DPQ by TBA-**Ru$_4$POM** as a stoichiometric oxidant. However, in the presence of a base, TEA, the **Ru$_4$POM** catalyzes this reaction with a TON = 3.75 (turnover number, TON = [quinone] / [**Ru$_4$ POM**]) after 1h (Figure 6.7).

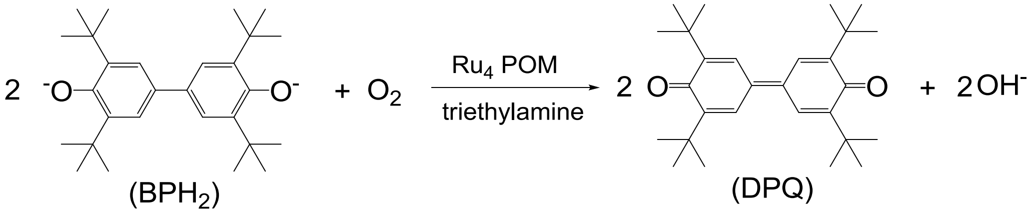

(6.11)

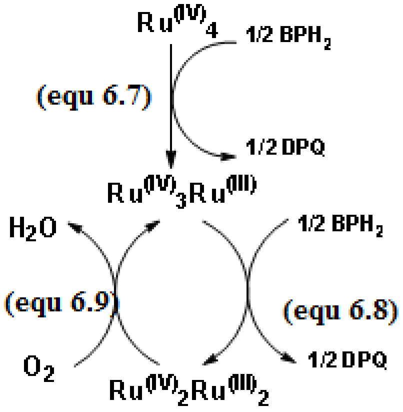

**Scheme 6.1** Catalytic cycle for the oxidation of $BPH_2$ to DPQ by TBA-**$Ru_4$POM**.

**Table 6.2** p*K*$_a$ values of different substances.

| | $HClO_4$ | DBP[154] | TEA | $BPH_2$ | TBA-**$Ru_4$POM** |
|---|---|---|---|---|---|
| p*Ka* | -10 | 3.58 | 10.78 | ~ 10 | 3.5 ~ 4.5 |

The overall catalytic reaction is given in eq 6.11. The control involving the reaction under the same conditions and under $O_2$ but without POM was conducted. The rate of quinone formation is about 5 times faster with POM than without POM. It can also be seen from Figure 6.7 that the reaction rate for the formation of the first half equivalent of DPQ under $O_2$ is the same as under Ar. However, the subsequent reaction rate was much faster under $O_2$ than under Ar. Scheme 6.1 describes the proposed catalytic cycle. The p$K_a$ values of the substances are listed in Table 6.2. The p$K_a$ value of DBP is abnormally low compared with other pyridine because of the steric effect.[154] The p$K_a$ value of 4,4'-biphenyldiol is 9.4,[155] therefore the p$K_a$ value of $BPH_2$ is estimated to be about 10. We suppose TBA-**$Ru_4$POM** has similar p$K_a$ values to RbK-**1**: they are both prepared in pH = 1.6 aqueous media. RbK-**$Ru_4$POM** has two p$K_a$ values in the pH range 3.5 – 4.5.[16] The successful formation of a catalytic cycle in presence of TEA can be attributed to its basicity. It deprotonates both TBA-**$Ru_4$POM** and $BPH_2$. The deprotonated form of phenol, phenolate, has a much stronger electron density than phenol and is thus much easier to oxidize. Therefore, the reaction rate of eq 6.8 (the reduction from $Ru^{(IV)}{}_3Ru^{(III)}$ to $Ru^{(IV)}{}_2Ru^{(III)}{}_2$) in this system is much faster than systems with $HClO_4$ or DBP. At the same time, deprotonated POM has a much lower redox potential, facilitating $Ru^{(IV)}{}_2Ru^{(III)}{}_2$ reoxidation to $Ru^{(IV)}{}_3Ru^{(III)}$ by $O_2$ (eq 6.9). In comparison, DBP might be able to deprotonate TBA-**$Ru_4$POM**, but it cannot deprotonate phenol, and thus cannot accelerate the rate of eq 6.8. $HClO_4$ increases the redox potential of TBA-**$Ru_4$POM,** and thus slows down the reoxidation of **$Ru^{(IV)}{}_2Ru^{(III)}{}_2$POM** to **$Ru^{(IV)}{}_2Ru^{(III)}{}_2$POM**.

To determine if the reoxidation step is rate limiting, pure $O_2$ was replaced by air. The rate in air was slower than in $O_2$, but not by a factor of 1/5 (Figure 6.7). This suggests the reaction of reduced **$Ru_4$POM** with $O_2$ partly controls the overall rate.

### *6.3.3.4 Reoxidation of RbK-$Ru_4$POM under $O_2$ ($O_2$ activation)*

$$Rb_8K_2Ru^{(IV)}{}_4POM + CH_3CH_2OH \rightarrow Rb_5K_{3.5}Ru^{(IV,IV,III,III)}{}_4POM + CH_3CHO \quad (6.12)$$

Single crystals of RbK-**$Ru_4$POM (-2)** (RbK-**$Ru^{(IV)}{}_2Ru^{(III)}{}_2$POM**) was obtained by reacting RbK-**$Ru_4$POM** with ethanol (reactions conducted by Claire Besson). The reoxidation of **$Ru^{(IV)}{}_2Ru^{(III)}{}_2$POM** in 0.1 M HCl by pure $O_2$ is a very slow process. Around 16% of **$Ru^{(IV)}{}_2Ru^{(III)}{}_2$POM** is oxidized to **$Ru^{(IV)}{}_3Ru^{(III)}$ POM** overnight (Figure 6.8).

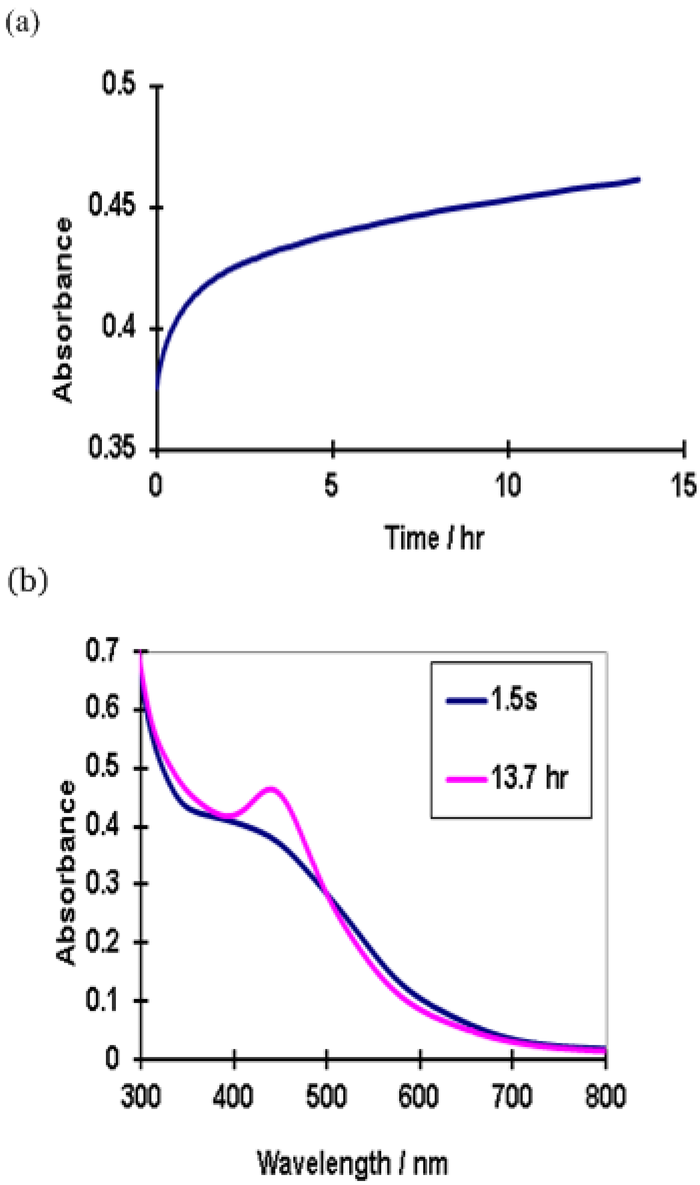

**Figure 6.8** (a) Kinetic traces of local maxima (λ = 445 nm) in the UV-vis spectrum of the reoxidation of RbK-$\mathbf{Ru^{(IV)}{}_2Ru^{(III)}{}_2}$**POM** by pure $O_2$, and (B) UV-vis spectrum of this solution at 1.5 s (blue line) and 13.7 hr (magneta line). $l$ = 1 cm.

### *6.3.3.5 Alcohol oxidations by TBA-**Ru$_4$POM***

**Table 6.3** Alcohol oxidations with TBA-**Ru$_4$POM** as oxidant in acetonitrile.

| Substrate | concentration | Temperature | Reaction Time | Detection Instrument | Reactivity |
|---|---|---|---|---|---|
| PhCH(OH)CH$_3$ | [POM]=10 mM<br>POM:PhCH(OH)CH$_3$ =1: 5 | R.T. | 13 min | GC | Finished |
| PhCH$_2$OH | [POM]=20 mM<br>POM : PhCH$_2$OH =1:5 | R.T. | 10 min | GC, UV-vis,NMR | Finished |
| *Cyclohexanol* | *[POM]=20 mM*<br>*POM : cyclohexanol =1:5* | *60 ºC* | *24 hr* | *GC* | *7%* |
| CH$_3$CH$_2$OH | [POM]=20 μM<br>POM:CH$_3$CH$_2$OH =1: 10000 | R.T. | 6 days | UV-vis, X-ray | Finished |
| 1-propanol | [POM]=20 μM<br>POM:CH$_3$CH$_2$OH =1: 10000 | R.T. | 7 days | UV-vis | Finished |
| *2-propanol* | *[POM]=20 μM*<br>*POM:CH$_3$CH$_2$OH =1: 10000* | *R.T.* | *8 hrs/ 5 days* | *UV-vis* | *No reaction/ 50 %* |

#### 6.3.3.5.1 UV-vis spectra

Figure 6.9 are the spectral changes that accompany the oxidation of benzyl alcohol by TBA-**Ru$_4$POM** in acetonitrile. A light filter is used to block the light under 400 nm because of the light sensitivity of the reaction. There is an isosbestic point at 529 nm, which is attributed to reduction of TBA-**Ru$_4$POM** from **Ru$^{(IV)}_4$POM** to **Ru$^{(IV)}_3$Ru$^{(III)}$ POM**, and finally **Ru$^{(IV)}_2$Ru$^{(III)}_2$ POM**. By monitoring the reaction at 453 nm (Figure 6.12, dotted line), we can see the reaction kinetics obey a bi-exponential rate law for the consumption of **Ru$_4$POM**.

#### 6.3.3.5.2 GC and NMR

The conversion of benzyl alcohol to benzyladehyde was detected by GC and $^1$H NMR (Figure 6.10 & Figure 6.11). The stoichiometry is 1 molecule of benzyladehyde generated per POM molecule. The reaction is complete in 2 hrs.

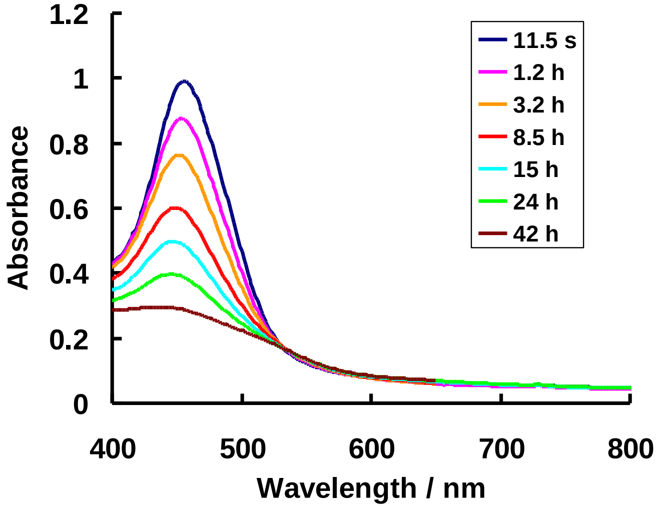

**Figure 6.9** Successive spectral scans during the oxidation of benzyl alcohol by TBA-**$Ru_4$POM** in 20 μM $HClO_4$, [TBA-**$Ru_4$POM**]=20 μM, [$PhCH_2OH$] = 80 mM.

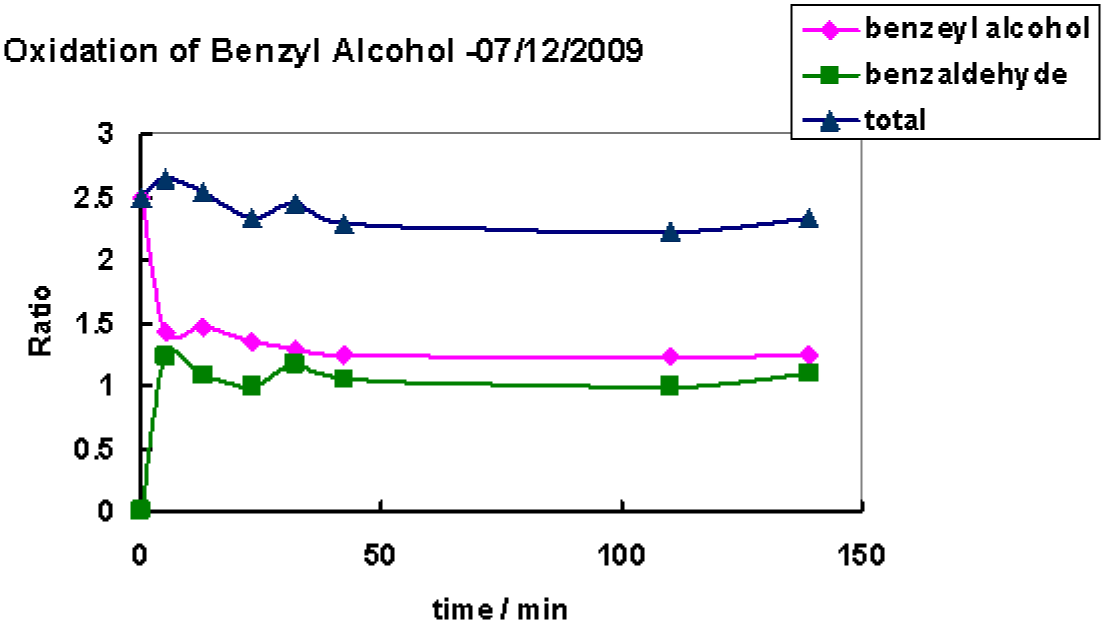

**Figure 6.10** The products of benzyl alcohol oxidized by TBA-**$Ru_4$POM** detected by GC. [benzyl alcohol]=50 mM, [TBA-**$Ru_4$POM**]= 20 mM, internal standard is cyclooctane .

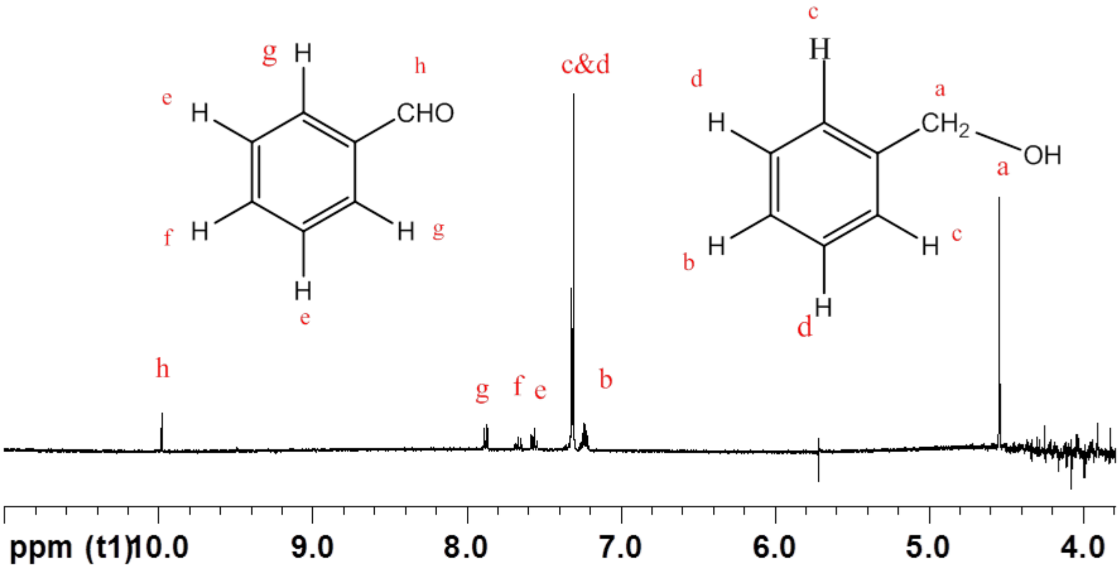

**Figure 6.1** The products of benzyl alcohol oxidized by TBA-**Ru$_4$POM** detected by $^1$H NMR with the same reaction solution as in Figure 6.12.

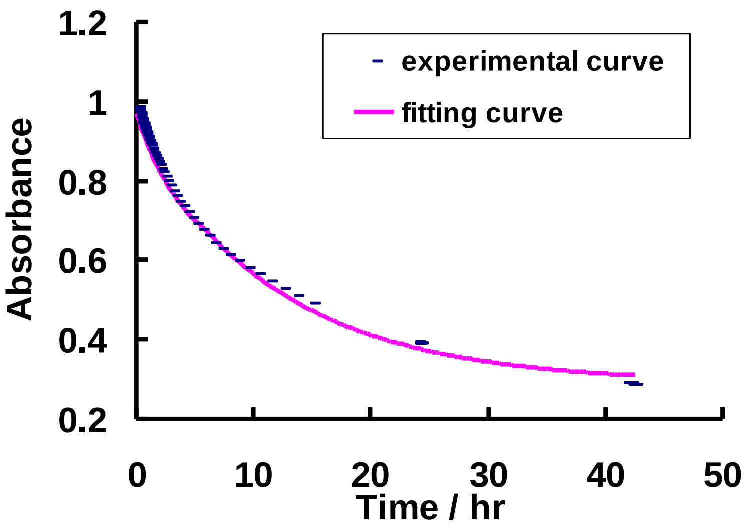

**Figure 6.2** Absorbance trace at 453 nm versus time plot and the fitting curve using Gepasi for the oxidation of benzyl alcohol by TBA-**Ru$_4$POM** in 20 μM $HClO_4$, [POM]=20 μM, [$PhCH_2OH$] = 80 mM.

6.3.3.5.3 Kinetic fittings

The kinetic curves can be fitted using the following equations by Gepasi:

A - > C $k_{(R1)}$

A + C = B + B $k_1/k_{-1}$=1000/1

B - > D $k_{(R3)}$

B + D = C + C $k_1/k_{-1}$=1000/1

That is:

$$\mathrm{Ru_4(IV, IV, IV, IV) + R_1R_2CHOH \xrightarrow{k(R1)} Ru_4\ (IV, IV, III, III) + R_1R_2C = O}$$

$$\mathrm{Ru_4(IV, IV, IV, IV) + Ru_4(IV, IV, III, III) \xleftrightarrow{k1/k\text{-}1=1000} 2\,Ru_4(IV, IV, IV, III)}$$

$$\mathrm{Ru_4(IV, IV, IV, III) + R_1R_2CHOH \xrightarrow{k(R1)} Ru_4(IV, III, III, III) + R_1R_2C = O}$$

$$\mathrm{Ru_4(IV, IV, IV, III) + Ru_4(IV, III, III, III) \xleftrightarrow{k1/k\text{-}1=1000} 2\,Ru_4(IV, IV, III, III)}$$

---

$$\mathrm{2Ru_4(IV, IV, IV, III) + 2Ru_4(IV, III, III, III) \rightarrow 2\,Ru_4(IV, IV, III, III) + 2\,R_1R_2C = O} \qquad \text{net}$$

The fitting results are shown in Figure 6.12. Values of the rate constants of the R1 derived from the Gepasi fitting for the oxidation of several alcohols are given in Table 6.4. Interestingly, the oxidation of 2-propanol and cyclohexanol is very slow. In the process of fitting, if the reaction takes an extremely long time, further two reactions are applied to get the best fitting:

$$\mathrm{Ru_4(IV, IV, III, III) + alcohol \xrightarrow{k(R1)} Ru_4(III, III, III, III) + aldehyde}$$

$$\mathrm{Ru_4(IV, IV, III, III) + (III, III, III, III) \xleftrightarrow{k1/k\text{-}1=1000} Ru_4(IV, III, III, III)}$$

6.3.3.5.4 Solvent Effects

Data in Table 6.4 show that with ethanol oxidation rate constant is much greater in water than in $CH_3CN$. By adding a small amount of $H_2O$ or $D_2O$ to the benzyl alcohol

**Table 6.4** Rate Constants of $R_1$ for the alcohol oxidations by TBA-**$Ru_4$POM** at 25 $^0$C.

| Substrate | Medium | $k_{(R1)}$ ($\times 10^{-5}$ mM $s^{-1}$) |
|---|---|---|
| Methanol | 20 uM $HClO_4$,$CH_3CN$ | 0.59 |
| Ethanol | 20 uM $HClO_4$,$CH_3CN$ | 1.1 |
| 1-propanol | 20 uM $HClO_4$,$CH_3CN$ | 1.7 |
| 4-brominebenzyl alcohol | 20 uM $HClO_4$,$CH_3CN$ | 2.0 |
| Benzyl alcohol | 20 uM $HClO_4$,$CH_3CN$ | 3.6 |
| 4-fluorobenzyl alcohol | 20 uM $HClO_4$,$CH_3CN$ | 4.6 |
| 4-methylbenzyl alcohol | 20 uM $HClO_4$,$CH_3CN$ | 5.8 |
| 4-trifluromethylbenzyl alcohol | 20 uM $HClO_4$,$CH_3CN$ | 8.1 |
| 4-chlorobenzyl alcohol | 20 uM $HClO_4$,$CH_3CN$ | 9.4 |
| 4-nitrobenzyl alcohol | 20 uM $HClO_4$,$CH_3CN$ | 19 |
| Ethanol | 0.1 M HCl, water | 25 |
| 4-methoxylbenzyl alcohol | 20 uM $HClO_4$,$CH_3CN$ | 87 |

oxidation reactions, the rate constants also increase with increasing percentage (volume percentage) of water (Figure 6.13). However, if the water content exceeds 1%, the kinetic curves can't be fitted by the same mechanism (large deviations will be generated). This may be caused by either the UV-vis spectral change of reduced TBA-**$Ru_4$POM** in water/acetonitrile mixed solvent, or a change of reaction mechanism. $D_2O$ has smaller influence to the rate constants than $H_2O$. Acetone was also assessed as a solvent, but the characteristic peak at 453 nm decreased greatly even without added alcohol.

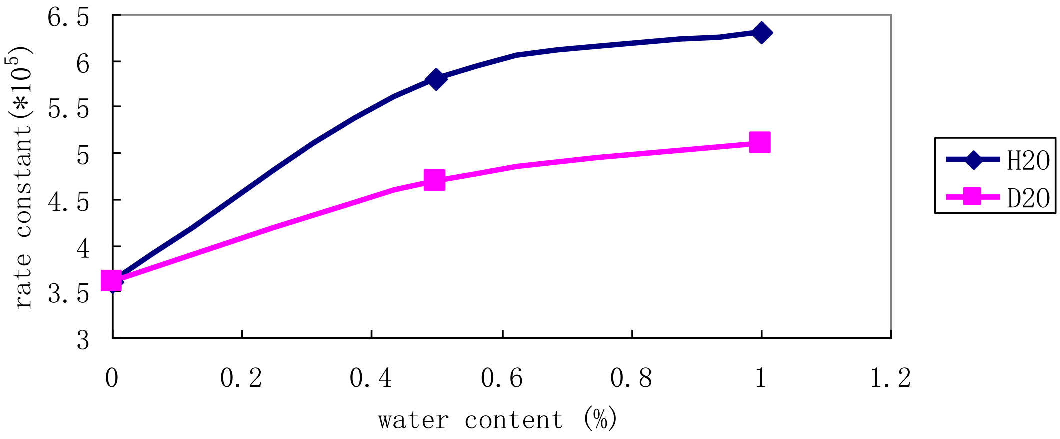

**Figure 6.3** Plots of $k_{(R1)}$ vs. water content in acetonitrile for benzyl alcohol oxidation by TBA-$\mathbf{Ru_4POM}$.

### 6.3.3.5.5 Acidity

From Table 6.5, we can see that within a certain range, the concentration of $HClO_4$ does not change the rate constant.

**Table 6.5** Rate constants versus [$HClO_4$] in acetonitrile for benzyl alcohol oxidation by TBA-$\mathbf{Ru_4POM}$.

| | 20 uM $HClO_4$ | 40 uM $HClO_4$ | 80 uM $HClO_4$ |
|---|---|---|---|
| $k_{(R1)}(*10^5)$ | 3.6 | 3.5 | 2.8 |

### 6.3.3.5.6 Substituent Effect & Selectivity

The rate of oxidation of alcohols by TBA-$\mathbf{Ru_4POM}$ is sensitive to changes in the alcohol structure. Under the same conditions as the reactants in Table 6.3, 2-propanol shows no reactions after 10 hrs. Normally, the rate constants for alcohol oxidation by ruthenium compounds follow the trend: methyl < primary < secondary < benzyl; however for $Ru_4POM$ the following order is seen: secondary < methyl < primary < benzyl.

For the series of benzylic alcohols, $k_{(R1)}$ varies randomly with variations in the para substituents as shown by the attempted Hammett plot in Figure 6.14.

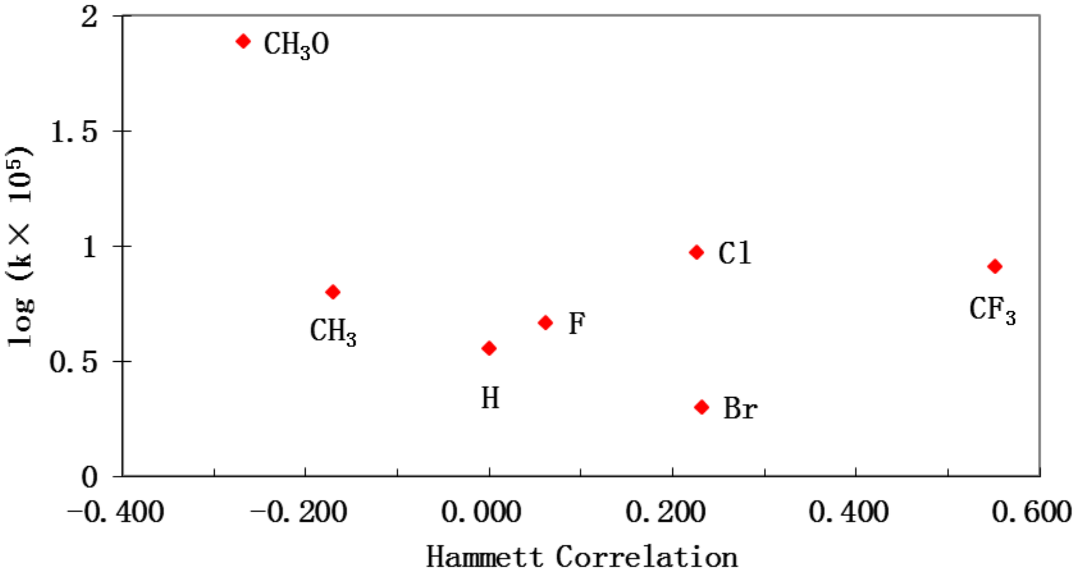

**Figure 6.14** Hammett plot for the oxidation of *para*-substituted benzyl alcohols by TBA-**Ru$_4$POM** in acetonitrile wth 20 µM $HClO_4$, [TBA-**Ru$_4$POM**] = 20 µM, [alcohol] = 80 mM.

6.3.3.5.7 Isotope effect

Figure 6.15 and Table 6.6 shows the substrate isotope effect. Plots of $k_{(R1)}$ vs. [alcohol] were nonlinear with benzyl alcohols as substrate. A reasonable assumption to explain this behavior is that a pre-association occurs between reactants. At high substrate concentrations, the concentration of the association complex becomes appreciable. Therefore, the rate constant reaches a plateau when the concentration of benzyl alcohol is high.

$$A + B \underset{k_{-1}}{\overset{k_1}{\rightleftharpoons}} A,B \longrightarrow D$$

$$\mathrm{Ru_4(IV,IV,IV,IV) + C_6H_5CH_2OH} \underset{k_{-1}(R_1)}{\overset{k_1(R_1)}{=}} \mathrm{Ru_4(IV,IV,IV,IV)\ {-}{-}{-}\ OCH_2C_6H_5 + H_2O}$$

$$\mathrm{Ru4(IV,IV,IV,IV){-}{-}{-}OCH_2C_6H_5 + H_2O} \xrightarrow{k_2(R_2)} \mathrm{Ru_4(IV,IV,III,III) + C_6H_5CHO}$$

$$\mathrm{Ru_4(IV,IV,IV,IV) + Ru_4(IV,IV,III,III)} \underset{k_{-3}(R_3)}{\overset{k_3(R_3)}{=}} \mathrm{2\ Ru_4(IV,IV,IV,III)} \qquad \text{(fast)}$$

A proposed detailed mechanism is shown in Scheme 6.2. Although good fitting can be achieved by this mechanism using Gepasi (Figure 6.16), the deviation of $k_{1(\mathrm{R1})}$, $k_{-1(\mathrm{R1})}$ or $k_{2(\mathrm{R2})}$ is above 200 %. Efforts have been made to isolate the intermediate by using $CH_3OH$, $(CH_3)_3COH$ and $C_6H_5CH_2OH$ as the substrates, but with no success thus far.

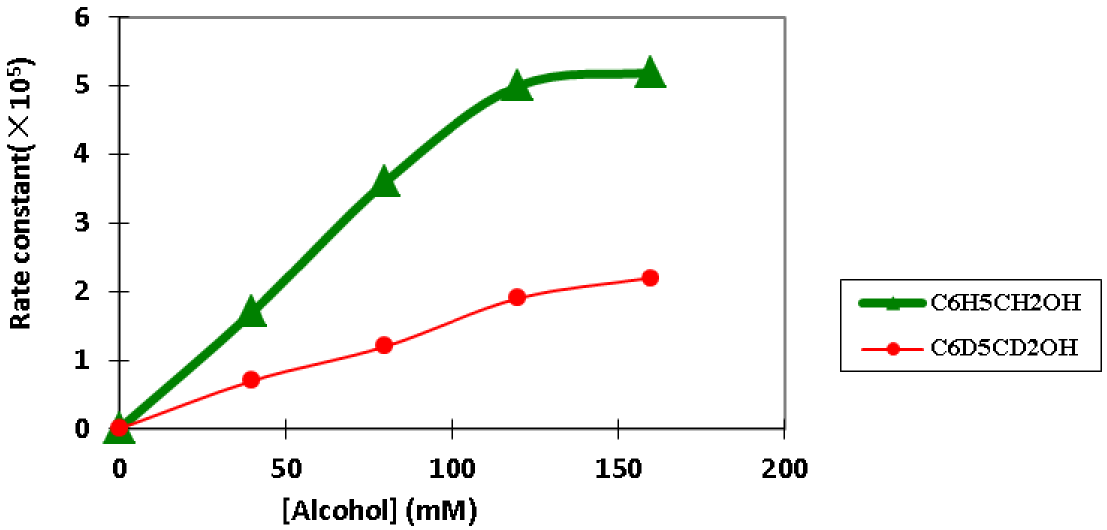

**Figure 6.4** Plots of $k_{(\mathrm{R1})}$ vs. [$C_6H_5CH_2OH$] and [$C_6D_5CD_2OH$] in acetonitrile for alcohol oxidation by TBA-**$Ru_4$POM**.

**Table 6.6** Rate constants for the isotope effect of benzyl alcohol by TBA-**$Ru_4$POM** fitting no-intermediate mechanism.

| $[C_6H_5CH_2OH]$ or $[C_6D_6CD_2OH]$ (mM) | $k_H(R_1)$ (× $10^5$) | $k_D(R_1)$ (× $10^5$) | $k_H/k_D$ |
|---|---|---|---|
| 40 | 1.7 ±0.010 | 0.76 ±0.044 | 2.4 |
| 80 | 3.6 ±0.016 | 1.2 ±0.011 | 3.0 |
| 120 | 5.0 ±0.059 | 1.9 ±0.016 | 2.6 |
| 160 | 5.2 ±0.061 | 2.2 ±0.019 | 2.4 |

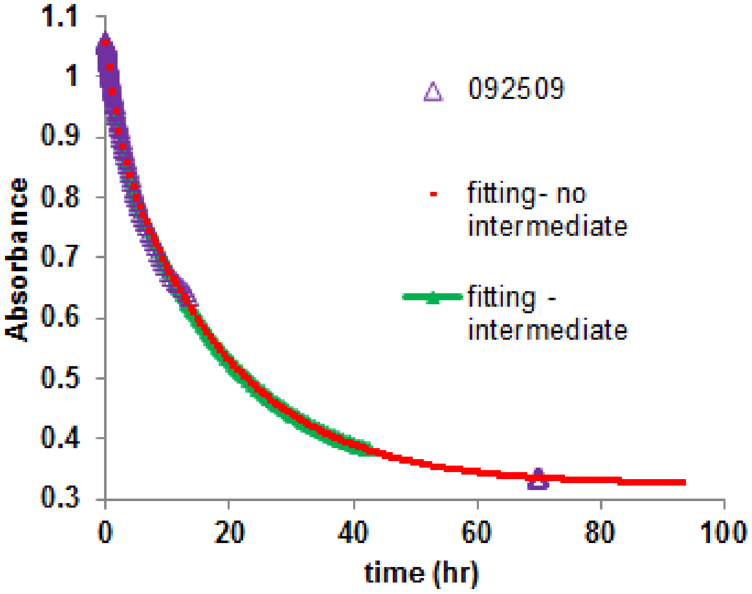

**Figure 6.5** Absorbance trace at 453 nm vs. time plot and the fitting curve using Gepasi for the oxidation of benzyl alcohol by TBA-**$Ru_4$POM** in 20 µM $HClO_4$, [POM] = 20 µM, $[PhCH_2OH]$ = 80 mM.

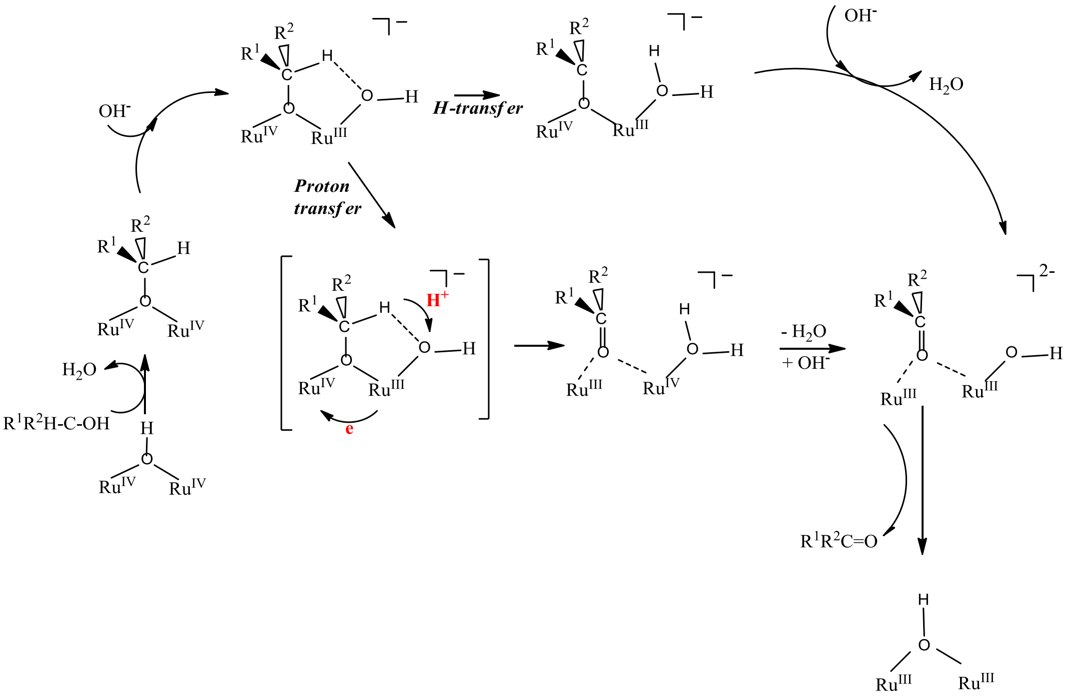

**Scheme 6.2** Proposed alcohol oxidation mechanism by TBA-**Ru$_4$POM** with intermediates.

## 6.4 Conclusions

TBA-**Ru$_4$POM** was synthesized and characterized. The catalytic oxidation activities of TBA-**Ru$_4$POM** towards several organic substrates (THT, CEES, cyclohexene and $BPH_2$) were studied in acetonitrile. TBA-**Ru$_4$POM** only catalyzes oxidations of $BPH_2$. The reaction kinetics and products for a series of alcohol oxidations by TBA-**Ru$_4$POM** were also studied in acetonitrile. Benzyl alcohols are oxidized to benzaldehydes. The reactions are slower in acetonitrile than in water/acetonitrile mixtures. In the series of *para*-substituted benzyl alcohols, X-$C_6H_4CH_2OH$ (X = $CH_3O$, H, Cl, and $NO_2$), the reaction rate doesn't follow any trend. The kinetic isotope effect, $C_6H_5CH_2OH$ versus $C_6D_5CD_2OH$, is $k_H/k_D \approx 2$. Based on the available experimental data, two mechanisms (one with intermediate and one without intermediate) are proposed. Further studies are needed to find the right mechanism.

## References

(1) Kortz, U.; Isber, S.; Dickman, M. H.; Ravot, D. *Inorg. Chem.* **2000**, *39*, 2915.

(2) Car, P.-E.; Guttentag, M.; Baldridge, K. K.; Albertoa, R.; Patzke, G. R. *Green Chem.* **2012**, *14*, 1680.

(3) Anderson, T. M.; Neiwert, W. A.; Hardcastle, K. I.; Hill, C. L. *Inorg. Chem.* **2004**, *43*, 7353.

(4) Leclerc-Laronze, N.; Marrot, J.; Haouas, M.; Taulelle, F.; Cadot, E. *Eur J Inorg Chem* **2008**, 4920.

(5) Laronze, N.; Marrot, J.; Hervé, G. *Inorg. Chem.* **2003**, *42*, 5857.

(6) Wassermann, K.; Lunk, H. J.; Palm, R.; Fuchs, J. *Acta Crystallogr., Sect. C: Cryst. Struct. Commun.* **1994**, *50*, 348.

(7) Liu, J. G.; Ortega, F.; Sethuraman, P.; Katsoulis, D. E.; Costello, C. E.; Pope, M. T. *J. Chem. Soc., Dalton Trans.* **1992**, 1901.

(8) Gamelas, J. A. F.; Carapuça, H. M.; Balula, M. S.; Evtuguin, D. V.; Schlindwein, W.; Figueiras, F. G.; Amaral, V. S.; Cavaleiro, A. M. V. *Polyhedron* **2010**, *29*, 3066.

(9) Tézé, A.; Vaissermann, J. *Comptes Rendus de l'Académie des Sciences - Series IIC - Chemistry* **2000**, *3*, 101.

(10) Car, P.-E.; Spingler, B.; Weyeneth, S.; Patscheider, J.; Patzke, G. R. *Polyhedron* **2013**, *52*, 151.

(11) Bassil, B. S.; Ibrahim, M.; Al-Oweini, R.; Asano, M.; Wang, Z.; Tol, J. v.; Dalal, N. S.; Choi, K.-Y.; Biboum, R. N.; Keita, B.; Nadjo, L.; Kortz, U. *Angew. Chem. Int. Ed.* **2011**, *50*, 5961.

(12) Tan, R.; Pang, X.; Wang, H.; Cui, S.; Jiang, Y.; Wang, C.; Wang, X.; Song, W. *Inorganic Chemistry Communications* **2012**, *25*, 70.

(13) Kortz, U.; Jeannin, Y. P.; Tézé, A.; Hervé, G.; Isber, S. *Inorganic Chemistry* **1999**, *38*, 3670.

(14) Zhang, Z. M.; Li, Y. G.; Yao, S.; Wang, E. B. *Dalton Trans* **2011**, *40*, 6475.

(15) Botar, B.; Geletii, Y. V.; Kögerler, P.; Musaev, D. G.; Morokuma, K.; Weinstock, I. A.; Hill, C. L. *J. Am. Chem. Soc.* **2006**, *128*, 11268.

(16) Geletii, Y. V.; Botar, B.; Kögerler, P.; Hillesheim, D. A.; Musaev, D. G.; Hill, C. L. *Angew. Chem. Int. Ed.* **2008**, *47*, 3896.

(17) Sartorel, A.; Carraro, M.; Scorrano, G.; Zorzi, R. D.; Geremia, S.; McDaniel, N. D.; Bernhard, S.; Bonchio, M. *J. Am. Chem. Soc.* **2008**, *130*, 5006.

(18) Compain, J. D.; Mialane, P.; Dolbecq, A.; Mbomekalle, I. M.; Marrot, J.; Secheresse, F.; Duboc, C.; Riviere, E. *Inorganic Chemistry* **2010**, *49*, 2851.

(19) Liu, H.; Peng, J.; Su, Z.; Chen, Y.; Dong, B.; Tian, A.; Han, Z.; Wang, E. *Eur. J. Inorg. Chem.* **2006**, 4827.

(20) Bassil, B. S.; Dickman, M. H.; Reicke, M.; Kortz, U.; Keita, B.; Nadjo, L. *Dalton Trans.* **2006**, 4253.

(21) Bassil, B. S.; Kortz, U.; Tigan, A. S.; Clemente-Juan, J. M.; Keita, B.; Oliveira, P. d.; Nadjo, L. *Inorg. Chem.* **2005**, *44*, 9360.

(22) Mitchell, S. G.; Ritchie, C.; Long, D.-L.; Cronin, L. *Dalton Trans.* **2008**, 1415.

(23) Ritchie, C.; Ferguson, A.; Nojiri, H.; Miras, H. N.; Song, Y.-F.; Long, D.-L.; Burkholder, E.; Murrie, M.; Kögerler, P.; Brechin, E. K.; Cronin, L. *Angew. Chem. Int. Ed.* **2008**, *47*, 5609.

(24) Zhang, Z. M.; Li, Y. G.; Wang, E. B.; Wang, X. L.; Qin, C.; An, H. Y. *Inorganic Chemistry* **2006**, *45*, 4313.

(25) Bassil, B. S.; Nellutla, S.; Kortz, U.; Stowe, A. C.; Tol, J. v.; Dalal, N. S.; Keita, B.; Nadjo, L. *Inorg. Chem.* **2005**, *44*, 2659.

(26) Liu, H. S.; Gomez-Garcia, C. J.; Peng, J.; Feng, Y. H.; Su, Z. M.; Sha, J. Q.; Wang, L. X. *Inorganic Chemistry* **2007**, *46*, 10041.

(27) Luo, Z.; Kögerler, P.; Cao, R.; Hakim, I.; Hill, C. L. *Dalton Trans.* **2008**, 54.

(28) Kortz, U.; Matta, S. *Inorg. Chem.* **2001**, *40*, 815.

(29) Leclerc-Laronze, N.; Marrot, J.; Hervé, G. *Inorg. Chem.* **2005**, *44*, 1275.

(30) Bi, L.-H.; Kortz, U. *Inorg. Chem.* **2004**, *43*, 7961.

(31) Nellutla, S.; Tol, J. v.; Dalal, N. S.; Bi, L.-H.; Kortz, U.; Keita, B.; Nadjo, L.; Khitrov, G. A.; Marshall, A. G. *Inorg. Chem.* **2005**, *44*, 9795.

(32) Leclerc-Laronze, N.; Marrot, J.; Hervé, G. *C. R. Chimie* **2006**, *9*, 1467.

(33) Ni, L.; Spingler, B.; Weyeneth, S.; Patzke, G. R. *Eur J Inorg Chem* **2013**, *2013*, 1681.

(34) Ni, L. B.; Hussain, F.; Spingler, B.; Weyeneth, S.; Patzke, G. R. *Inorganic Chemistry* **2011**, *50*, 4944.

(35) Chen, Y. G.; Meng, F. X.; Pang, H. J.; Shi, D. M.; Sun, Y. *J Clust Sci* **2007**, *18*, 396.

(36) Leclerc-Laronze, N.; Haouas, M.; Marrot, J.; Taulelle, F.; Hervé, G. *Angew. Chem. Int. Ed.* **2006**, *4*, 139.

(37) Lv, H.; Geletii, Y. V.; Zhao, C.; Vickers, J. W.; Zhu, G.; Luo, Z.; Song, J.; Lian, T.; Musaev, D. G.; Hill, C. L. *Chem. Soc. Rev.* **2012**, *41*, 7572.

(38) Besson, C.; Huang, Z.; Geletii, Y. V.; Lense, S.; Hardcastle, K. I.; Musaev, D. G.; Lian, T.; Proust, A.; Hill, C. L. *Chem. Commun.* **2010**, 2784.

(39) Yin, Q.; Tan, J. M.; Besson, C.; Geletii, Y. V.; Musaev, D. G.; Kuznetsov, A. E.; Luo, Z.; Hardcastle, K. I.; Hill, C. L. *Science* **2010**, *328*, 342.

(40) Pope, M. T.; Müller, A. *Angew. Chem. Int. Ed.* **1991**, *30*, 34.

(41) Borrás-Almenar, J. J.; Coronado, E.; Müller, A.; Pope, M. T. *Polyoxometalate Molecular Science. Proceedings of the NATO Advanced Study Institute, Tenerife, Spain from 25 August to 4 September 2001*; Kluwer Academic Publishers: Dordrecht, 2003; Vol. 98.

(42) Pope, M. T. In *Comprehensive Coordination Chemistry II: From Biology to Nanotechnology*; Wedd, A. G., Ed.; Elsevier Ltd.: Oxford, UK, 2004; Vol. 4, p 635.

(43) Long, D.-L.; Burkholder, E.; Cronin, L. *Chem. Soc. Rev.* **2007**, *36*, 105.

(44) Proust, A.; Thouvenot, R.; Gouzerh, P. *Chem. Commun.* **2008**, 1837.

(45) Kortz, U.; Müller, A. *J. Cluster Sci.* **2006**, *17*, 139.

(46) Putaj, P.; Lefebvre, F. *Coord. Chem. Rev.* **2011**, *255*, 1642.

(47) Kim, G. S.; Hagen, K. S.; Hill, C. L. *Inorg. Chem.* **1992**, *31*, 5316.

(48) Gouzerh, P.; Proust, A. *Chem. Rev.* **1998**, *98*, 77.

(49) Müller, A.; Serain, C. *Acc. Chem. Res.* **2000**, *33*, 2.

(50) Anderson, T. M.; Hardcastle, K. I.; Okun, N.; Hill, C. L. *Inorg. Chem.* **2001**, *40*, 6418.

(51) Müller, A.; Beckmann, E.; Bögge, H.; Schmidtmann, M.; Dress, A. *Angew. Chem.* **2002**, *114*, 1210.

(52) Mal, S. S.; Kortz, U. *Angew. Chem. Int. Ed.* **2005**, *44*, 3777.

(53) Fang, X.; Anderson, T. M.; Benelli, C.; Hill, C. L. *Chem. Eur. J.* **2005**, *11*, 712.

(54) Hasenknopf, B.; Micoine, K.; Lacôte, E.; Thorimbert, S.; Malacria, M.; Thouvenot, R. *Eur. J. Inorg. Chem.* **2008**, 5001.

(55) Bi, L.-H.; Hou, G.-F.; Li, B.; Wu, L.-X.; Kortz, U. *Dalton Trans.* **2009**, 6345.

(56) Mitchell, S. G.; Streb, C.; Miras, H. N.; Boyd, T.; Long, D.-L.; Cronin, L. *Nature Chem.* **2010**, *2*, 308.

(57) Miras, H. N.; Cooper, G. J. T.; Long, D.-L.; Bögge, H.; Müller, A.; Streb, C.; Cronin, L. *Science* **2010**, *327*, 72.

(58) Murakami, M.; Hong, D.; Suenobu, T.; Yamaguchi, S.; Ogura, T.; Fukuzumi, S. *J. Am. Chem. Soc.* **2011**, *133*, 11605.

(59) Zhang, L.-Z.; Gu, W.; Liu, X.; Dong, Z.; Yang, Y.-S.; Li, B.; Liao, D.-Z. *Inorg. Chem. Commun.* **2007**, *10*, 1378.

(60) Tézé, A.; Hervé, G. In *Inorg. Synth.*; Ginsberg, A. P., Ed.; John Wiley and Sons: New York, 1990; Vol. 27, p 85.

(61) Zheng, Y.-Z.; Speldrich, M.; Schilder, H.; Chen, X.-M.; Kögerler, P. *Dalton Trans.* **2010**, *39*, 10827.

(62) Malaestean, I. L.; Speldrich, M.; Baca, S. G.; Ellern, A.; Schilder, H.; Kögerler, P. *Eur. J. Inorg. Chem.* **2009**, 1011.

(63) Bruker AXS, I.; Analytical X-ray Sysems: Madison, WI, 2003.

(64) Bruker AXS, I.; Analytical X-Ray Sytems: Madison, WI, 2003.

(65) Sheldrick, G. In *SADABS*; ver. 2.10 ed. 2003.

(66) Bruker AXS, I. Madison, WI, 2003.

(67) Geletii, Y. V.; Huang, Z.; Hou, Y.; Musaev, D. G.; Lian, T.; Hill, C. L. *J. Am. Chem. Soc.* **2009**, *131*, 7522.

(68) Geletii, Y. V.; Besson, C.; Hou, Y.; Yin, Q.; Musaev, D. G.; Quinonero, D.; Cao, R.; Hardcastle, K. I.; Proust, A.; Kögerler, P.; Hill, C. L. *J. Am. Chem. Soc.* **2009**, *131*, 17360.

(69) Huang, Z.; Luo, Z.; Geletii, Y. V.; Vickers, J.; Yin, Q.; Wu, D.; Hou, Y.; Ding, Y.; Song, J.; Musaev, D. G.; Hill, C. L.; Lian, T. *J. Am. Chem. Soc.* **2011**, *133*, 2068.

(70) Kaledin, A. L.; Huang, Z.; Geletii, Y. V.; Lian, T.; Hill, C. L.; Musaev, D. G. *J. Phys. Chem. A* **2010**, *114*, 73.

(71) Kaledin, A. L.; Huang, Z.; Yin, Q.; Dunphy, E. L.; Constable, E. C.; Housecroft, C. E.; Geletii, Y. V.; Lian, T.; Hill, C. L.; Musaev, D. G. *J. Phys. Chem. A* **2010**, *114*, 6284.

(72) Weakley, T. J. R.; Malik, S. A. *J. Inorg. Nucl. Chem.* **1967**, *29*, 2935.

(73) Laronze, N.; Marrot, J.; Herve, G. *Chem. Commun. (Cambridge, U. K.)* **2003**, 2360.

(74) Coates, J. H.; Gentle, G. J.; Lincoln, S. F. *Nature* **1974**, *249*, 773.

(75) Baes, J., Charles F.; Mesmer, R. E. *The Hydrolysis of Cations*; John Wiley & Sons: New York, 1976.

(76) Tanaka, S.; Annaka, M.; Sakai, K. *Chem. Commun.* **2012**, *48*, 1653.

(77) Goberna-Ferrón, S.; Vigara, L.; Soriano-López, J.; Galán-Mascarós, J. R. *Inorg. Chem.* **2012**, *51*, 11707.

(78) Soriano-López, J.; Goberna-Ferrón, S.; Vigara, L.; Carbó, J. J.; Poblet, J. M.; Galán-Mascarós, J. R. *Inorg. Chem.* **2013**, *52*, 4753.

(79) Leclerc-Laronze, N.; Marrot, J.; Hervé, G. *Inorg. Chem.* **2005**, *44*, 1275.

(80) Bruker AXS, I.; Analytical X-ray Systems: Madison, WI, 2003.

(81) Sheldrick, G. M. *SHELXL-97; Program for the Refinement of Crystal Structure*; University of Göttingen: Göttingen, 1993.

(82) Sheldrick, G. M. *Acta Crystallogr., Sect. A* **1990**, *46*, 467.

(83) Laronze, N.; Marrot, J.; Hervé, G. *Chem. Commun.* **2003**, 2360.

(84) Wang, C.-L.; Liu, S.-X.; Sun, C.-Y.; Xie, L.-H.; Ren, Y.-H.; Liang, D.-D.; Cheng, H.-Y. *J. Mol. Struct.* **2007**, *841*, 88.

(85) Lisnard, L.; Mialane, P.; Dolbecq, A.; Marrot, J.; Clemente-Juan, J.-M.; Coronado, E.; Keita, B.; Oliveira, P. D.; Nadjo, L.; Secheresse, F. *Chem. Eur. J.* **2007**, *13*, 3525.

(86) Zhu, G.; Geletii, Y. V.; Kögerler, P.; Schilder, H.; Song, J.; Lense, S.; Zhao, C.; Hardcastle, K. I.; Musaev, D. G.; Hill, C. L. *Dalton Trans.* **2012**, *41*, 2084.

(87) Zhang, Z.; Wang, E.; Li, Y.; An, H.; Qi, Y.; Xu, L. *J. Mol. Struct.* **2008**, *872*, 176.

(88) Stracke, J. J.; Finke, R. G. *J. Am. Chem. Soc.* **2011**, *133*, 14872.

(89) Geletii, Y. V.; Yin, Q.; Hou, Y.; Huang, Z.; Ma, H.; Song, J.; Besson, C.; Luo, Z.; Cao, R.; O'Halloran, K. P.; Zhu, G.; Zhao, C.; Vickers, J. W.; Ding, Y.; Mohebbi, S.; Kuznetsov, A. E.; Musaev, D. G.; Lian, T.; Hill, C. L. *Isr. J. Chem.* **2011**, *51*, 238.

(90) Crabtree, R. H. *Chem. Rev.* **2012**, *112*, 1536.

(91) Limburg, B.; Bouwman, E.; Bonnet, S. *Coord. Chem. Rev.* **2012**, *256*, 1451.

(92) Du, P.; Eisenberg, R. *Energy Environ. Sci.* **2012**, *5*, 6012.

(93) Schley, N. D.; Blakemore, J. D.; Subbaiyan, N. K.; Incarvito, C. D.; D’Souza, F.; Crabtree, R. H.; Brudvig, G. W. *J. Am. Chem. Soc.* **2011**, *133*, 10473.

(94) Ohlin, C. A.; Harley, S. J.; McAlpin, J. G.; Hocking, R. K.; Mercado, B. Q.; Johnson, R. L.; Villa, E. M.; Fidler, M. K.; Olmstead, M. M.; Spiccia, L.; Britt, R. D.; Casey, W. H. *Chem. Eur. J.* **2011**, *17*, 4408.

(95) Zhu, G.; Geletii, Y. V.; Zhao, C.; Musaev, D. G.; Song, J.; Hill, C. L. *Dalton Trans.* **2012**, *41*, 9908.

(96) Vickers, J.; Lv, H.; Zhuk, P. F.; Geletii, Y. V.; Hill, C. L. In *2011 MRS Fall Meeting, Symposium E - Advanced Materials for Solar-Fuel Generation* Boston, MA., 2012; Vol. 1387, p 9.

(97) Bediako, D. K.; Lassalle-Kaiser, B.; Surendranath, Y.; Yano, J.; Yachandra, V. K.; Nocera, D. G. *J. Am. Chem. Soc.* **2012**, *134*, 6801.

(98) Dincă, M.; Surendranath, Y.; Nocera, D. G. *Proc. Natl. Acad. Sci.* **2010**, *107(23)*, 10337.

(99) Singh, A.; Spiccia, L. *Coord. Chem. Rev.* **2013**, *257*, 2607.

(100) Sheldrick, G.; 4th edition ed. 2007.

(101) Frisch, M. J.; Trucks, G. W.; Schlegel, H. B.; Scuseria, G. E.; Robb, M. A.; Cheeseman, J. R.; Scalmani, G.; Barone, V.; Mennucci, B.; Petersson, G. A.; Nakatsuji, H.; Caricato, M.; Li, X.; Hratchian, H. P.; Izmaylov, A. F.; Bloino, J.; Zheng, G.; Sonnenberg, J. L.; Hada, M.; Ehara, M.; Toyota, K.; Fukuda, R.; Hasegawa, J.; Ishida, M.; Nakajima, T.; Honda, Y.; Kitao, O.; Nakai, H.; Vreven, T.; J. A. Montgomery, J.; Peralta, J. E.; Ogliaro, F.; Bearpark, M.; Heyd, J. J.; Brothers, E.; Kudin, K. N.; Staroverov, V. N.; Kobayashi, R.; Normand, J.; Raghavachari, K.; Rendell, A.; Burant, J. C.; Iyengar, S. S.; Tomasi, J.; Cossi, M.; N. Rega, J. M. M.; Klene, M.; Knox, J. E.; Cross, J. B.; Bakken, V.; Adamo, C.; Jaramillo, J.; Gomperts, R.; Stratmann, R. E.; Yazyev, O.; Austin, A. J.; Cammi, R.; Pomelli, C.; Ochterski, J. W.; Martin, R. L.; K. Morokuma, V. G. Z.; Voth, G. A.; Salvador, P.; Dannenberg, J. J.; Dapprich, S.; Daniels, A. D.; Ö. Farkas, J. B. F.; Ortiz, J. V.; Cioslowski, J.; Fox, D. J.; Revision A.1 ed.; Gaussian, I., Ed. Wallingford CT., 2009.

(102) Becke, A. D. *Phys. Rev. A* **1988**, *38*, 3098.

(103) Lee, C.; Yang, W.; Parr, R. G. *Phys. Rev. B* **1988**, *37*, 785.

(104) Becke, A. D. *J. Chem. Soc.* **1993**, *98*, 1372.

(105) Hay, P. J.; Wadt, W. R. *J. Chem. Phys.* **1985**, *82*, 270.

(106) Wadt, W. R.; Hay, P. J. *J. Chem. Phys.* **1985**, *82*, 284.

(107) Hay, P. J.; Wadt, W. R. *J. Chem. Phys.* **1985**, *82*, 299.

(108) Cances, E.; Mennucci, B.; Tomasi, J. *J. Chem. Phys.* **1997**, *107*, 3032.

(109) Grigoriev, V. A.; Hill, C. L.; Weinstock, I. A. *J. Am. Chem. Soc.* **2000**, *122*, 3544.

(110) Grigoriev, V. A.; Cheng, D.; Hill, C. L.; Weinstock, I. A. *J. Am. Chem. Soc.* **2001**, *123*, 5292.

(111) Pope, M. T.; Müller, A. *Angew. Chem.* **1991**, *103*, 56.

(112) Hill, C. L.; Prosser-McCartha, C. M. *Coord. Chem. Rev.* **1995**, *143*, 407.

(113) Hill, C. L. *J. Mol. Catal. A: Chem.* **2007 Special Issue**, *262*, 1.

(114) Long, D.-L.; Tsunashima, R.; Cronin, L. *Angew. Chem. Int. Ed.* **2010**, *49*, 1736.

(115) Pradeep, C. P.; Long, D.-L.; Kögerler, P.; Cronin, L. *Chem. Commun.* **2007**, 4254.

(116) Sakai, Y.; Ohta, S.; Shintoyo, Y.; Yoshida, S.; Taguchi, Y.; Matsuki, Y.; Matsunaga, S.; Nomiya, K. *Inorg. Chem.* **2011**, *50*, 6575.

(117) Ibrahim, M.; Lan, Y. H.; Bassil, B. S.; Xiang, Y. X.; Suchopar, A.; Powell, A. K.; Kortz, U. *Angew. Chem. Int. Ed.* **2011**, *50*, 4708.

(118) Mbomekalle, I. M.; Cao, R.; Hardcastle, K. I.; Hill, C. L.; Ammam, M.; Keita, B.; Nadjo, L.; Anderson, T. M. *C. R. Chimie* **2005**, *8*, 1077.

(119) Piepenbrink, M.; Triller, M. U.; Gorman, N. H. J.; Krebs, B. *Angew. Chem. Int. Ed.* **2002**, *41*, 2523.

(120) Hou, Y.; Xu, L.; Cichon, M. J.; Lense, S.; Hardcastle, K. I.; Hill, C. L. *Inorg. Chem.* **2010**, *49*, 4125.

(121) Kortz, U.; Al-Kassem, N. K.; Savelieff, M. G.; Kadi, N. A. A.; Sadakane, M. *Inorg. Chem.* **2001**, *40*, 4742.

(122) Liu, Y.; Liu, B.; Xue, G.; Hu, H.; Fu, F.; Wang, J. *Dalton Trans.* **2007**, 3634.

(123) Kortz, U.; Nellutla, S.; Stowe, A. C.; Dalal, N. S.; Rauwald, U.; Danquah, W.; Ravot, D. *Inorg. Chem.* **2004**, *43*, 2308.

(124) Finke, R. G.; Droege, M. W.; Domaille, P. J. *Inorg. Chem.* **1987**, *26*, 3886.

(125) Bi, L. H.; Huang, R. D.; Peng, J.; Wang, E. B.; Wang, Y. H.; Hu, C. W. *J. Chem. Soc., Dalton Trans.* **2001**, 121.

(126) Bi, L. H.; Wang, E. B.; Peng, J.; Huang, R. D.; Xu, L.; Hu, C. W. *Inorg. Chem.* **2000**, *39*, 671.

(127) Keita, B.; Mbomekalle, I. M.; Nadjo, L.; Contant, R. *Electrochem. Commun.* **2001**, *3*, 267.

(128) Bi, L. H.; Hou, G. F.; Wu, L. X.; Kortz, U. *CrystEngComm* **2009**, *11*, 1532.

(129) Drewes, D.; Limanski, E. M.; Krebs, B. *Eur. J. Inorg. Chem.* **2005**, 1542.

(130) Kikukawa, Y.; Yamaguchi, K.; Mizuno, N. *Inorg. Chem.* **2010**, *49*, 8194.

(131) Kikukawa, Y.; Yamaguchi, K.; Mizuno, N. *Angew. Chem. Int. Ed.* **2010**, *49*, 6096.

(132) Tourné, C. M.; Tourné, G. F.; Zonnevijlle, F. *J. Chem. Soc., Dalton Trans.* **1991**, *1*, 143.

(133) Tan, H. Q.; Zhang, Z. M.; Liu, D.; Qi, Y. F.; Wang, E. B.; Li, Y. G. *J. Cluster Sci.* **2008**, *19*, 543.

(134) Chang, S.; Qi, Y.-F.; Wang, E.-B.; Zhang, Z. *Inorg. Chim. Acta* **2009**, *362*, 453.

(135) Wang, Y. C.; Xu, L.; Jiang, N.; Liu, X. Z.; Li, F. Y.; Li, Y. G. *Inorg. Chem. Commun.* **2010**, *13*, 964.

(136) Zhao, Z.; Zhou, B.; Zheng, S.; Su, Z.; Wang, C. *Inorg. Chim. Acta* **2009**, *362*, 5038.

(137) Niu, J.-Y.; Ma, X.; Zhao, J.-W.; Ma, P.-T.; Zhang, C.; Wang, J.-P. *CrystEngComm* **2011**, *13*, 4834.

(138) Becke, A. D. *J. Chem. Phys.* **1993**, *98*, 5648.

(139) Liu, F.; Concepcion, J. J.; Jurss, J. W.; Cardolaccia, T.; Templeton, J. L.; Meyer, T. J. *Inorg. Chem.* **2008**, *47*, 1727.

(140) Thompson, M. S.; Meyer, T. J. *J. Am. Chem. Soc.* **1982**, *104*, 4106.

(141) Roecker, L.; Meyer, T. J. *J. Am. Chem. Soc.* **1987**, *109*, 746.

(142) Muller, J. G.; Acquaye, J. H.; Takeuchi, K. J. *Inorg. Chem.* **1992**, *31*, 4552.

(143) Binstead, R. A.; McGuire, M. E.; Dovletoglou, A.; Seok, W. K.; Roecker, L. E.; Meyer, T. J. *J. Am. Chem. Soc.* **1992**, *114*, 173.

(144) Hurst, J. K. *Coord. Chem. Rev.* **2005**, *249*, 313.

(145) Huynh, M. H. V.; Meyer, T. J.; Labouriau, A.; Morris, D. E.; White|, P. S. *J. Am. Chem. Soc.* **2003**, *125*, 2828.

(146) Gersten, S. W.; Samuels, G. J.; Meyer, T. J. *J. Am. Chem. Soc.* **1982**, *104*, 4029.

(147) Raven, S. J.; Meyer, T. J. *Inorg. Chem.* **1988**, *27*, 4478.

(148) Quiñonero, D.; Wang, Y.; Morokuma, K.; Khavrutskii, L. A.; Botar, B.; Geletii, Y. V.; Hill, C. L.; Musaev, D. G. *J. Phys. Chem.* **2006**, *110*, 170.

(149) Kuznetsov, A. E.; Geletii, Y. V.; Hill, C. L.; Morokuma, K.; Musaev, D. G. *J. Am. Chem. Soc.* **2009**, *131*, 6844.

(150) Sartorel, A.; Miro, P.; Salvadori, E.; Romain, S.; Carraro, M.; Scorrano, G.; Valentin, M. D.; Llobet, A.; Bo, C.; Bonchio, M. *J. Am. Chem. Soc.* **2009**, *131*, 16051.

(151) Orlandi, M.; Argazzi, R.; Sartorel, A.; Carraro, M.; Scorrano, G.; Bonchio, M.; Scandola, F. *Chem. Commun.* **2010**, *46*, 3152.

(152) Neumann, R.; Khenkin, A. M. *Chem. Commun.* **2006**, 2529.

(153) Hou, Y.; Hill, C. L. *J. Am. Chem. Soc.* **1993**, *115*, 11823.

(154) Joris, L.; Schleyer, P. V. *Tetrahedron* **1968**, *24*, 5991.

(155) Mohanty, J.; Pal, H.; Sapre, A. V. *Bull. Chem. Soc. Jpn.* **2001**, *74*, 427.